FEMTOSECOND LASER PULSE OPTIMIZATION FOR MULTIPHOTON CYTOMETRY AND CONTROL OF FLUORESCENCE

by

Eric Robert Tkaczyk

A dissertation submitted in partial fulfillment
of the requirements for the degree of
Doctor of Philosophy
(Electrical Engineering)
in The University of Michigan
2008

Doctoral Committee:

Professor Theodore B. Norris, Chair
Professor Duncan G. Steel
Assistant Professor Gary D. Luker
Assistant Professor Jennifer P. Ogilvie

To my Family

ACKNOWLEDGEMENTS

Finding a way to express my gratitude to the small army of caring individuals which has helped me to succeed on my very academic life path is probably the most difficult aspect of completing the Ph.D. It has been a great blessing that so many wonderful mentors, teachers, and close friends have invested untellable energy in supporting me and promoting my development and education continuously from an early age. Here, I would like to acknowledge a few individuals and programs in particular, but first, a literature citation[1]:

> A rabbit is happily grazing one day when it is ambushed by a wolf.
>
> "Please don't eat me Mr Wolf," pleads the rabbit, "I haven't completed my Ph.D.!"
>
> The wolf spits out the rabbit and laughs until he almost chokes.
>
> "Yeah right! A rabbit? Doing a Ph.D.? What about? Carrots? Duracell batteries? I just gotta hear this one!"
>
> The rabbit clears its throat and intones: "On the innate superiority of rabbits over wolves."
>
> "That's a crock for a start," scoffs the wolf.
>
> "But I can prove it," says the rabbit. "Come to my hole and I'll show you my results, and if you still don't believe me, then you can eat me. Deal?"
>
> "Sure. Can I have fries with that?" says the wolf, following the rabbit down the hole.
>
> But only the rabbit comes out.
>
> Months later the rabbit is grazing contentedly again when it meets another rabbit.
>
> "How's tricks?" asks the friend.
>
> "Wonderful," says our hero, "I've just submitted my Ph.D. dissertation."
>
> "Congratulations! What's it called?"
>
> "It's called 'On the innate superiority of rabbits over wolves'."
>
> "Unbelievable — I mean, literally. Are you sure?"
>
> "Yes, I thought it was crazy at first too. But I've tested the model rigorously and that's the result I get."
>
> "Wow..."
>
> "Look, if you don't believe me, why not come to my hole and I can show you the results?"
>
> "Of course, I'd love to!"
>
> So the two rabbits scurry down the burrow. In the first chamber is a workstation, covered with and surrounded by piles of books, papers, printouts and half-eaten carrots. In the second chamber are boxes and boxes of wolf bones, all catalogued and annotated. And in the final chamber, in a rocking chair, is a large and very satisfied looking bear.

[1] J. Yewdell, *Nature Reviews of Molecular and Cell Biology*, April 10, 2008.

Moral: do your Ph.D. on any subject you like, provided you have a good supervisor.

Truly, the degree of encouragement, understanding, outstanding physical insight, flexibilty and support Professor Norris has given over the course of my PhD work are unbelievable, ranging from investments in equipment to supporting many trips including the Biophotonics summer school in Sweden last summer. Thank you, Ted! I would also like to thank the other committee members for their contributions to my success, including not only advice, but even excellent biological samples from the lab of Professor Gary and Dr. Kathy Luker. None of the coherent control literature would have made sense without Professor Duncan Steel's year of quantum mechanics instruction. For greater insight into the current work of coherent control, it was very serendipitous to meet Professor Jennifer Ogilvie at the 2006 Photonics West Conference in San Jose. She subsequently gave the excellent suggestion to pursue the time-domain measurement of cross-sections. Dr. Koit Mauring deserves a special thank you for helping me to survive the last dark winter of grad school, his fundamental role in the BFP experiments, numerous fruitful discussions, and insight into computational chemistry from our previous collaboration. He also inspired me to write my first successful grant proposal to fund the international collaboration. My sincere gratitude is extended as well to Alan Tkaczyk for his help and skill in microfluidic and other experimentation.

Many other people have been directly involved in the work presented here, including: Frank Zhong, whose pioneering work largely got me started; Steve Katnik, who rescued me many times when everything went wrong with the lasers; Chuck Divin, for major help in the first tortuous LabView programming endeavors and technical discussions; Dr. Jing Yong Ye for teaching me many experimental techniques; Augustin Mignot, as my first coherent control colleague; Dr. James Baker, Jr. for motivation and the support of his institute; other members of MNIMBS including Dr. Thommey Thomas and Dr. Andrzej Myc. I also thank the members of the Norris lab for being compromising about shared laser time and various other equipment as well as conversations and help: Malakeh Musheinesh, Yu-chung Chang, Yunbo Guo, Guoqing Chang, Moussa Ngom; and last but not least, the very positive recent addition of Meredith Brenner, who with great enthusiasm has taken the torch of continuing the work

outlined in this dissertation, and has been great company during the setting up of the coherent control-flow cytometry fusion experiment underway now, despite her Jackson E & M burden.

For having settled in the field of ultrafast optics, I owe much to NSF REU programs and mentors. Thank you to University of Bordeaux Professors Lionel Canioni, Stephane Santran, Sylvain Rivet, and Laurent Sarger, for first exposing me to multiphoton possibilities amidst the beautiful surrodings of southern France. I am also grateful to Professor Peter So, who took into his MIT lab for the whole summer the random undergraduate he met at a conference, and further nurtured my love of the ultrafast.

It is likely I would have never even bothered to get my first degree in engineering, had my grandmother not challenged me to prove my capabilities as she took care of me abroad during my first year of high school. On a related note, the principal of Hugo Treffneri Gümnaasium in Tartu, Estonia needs to be thanked again for taking in a brash 15-year old American student without the usual high school entrance exams. The Estonian International Math Olympiad training program run through Tartu University also played a crucial role that year in my mathematical development. Other programs to which I am indebted for nurturing my scientific abilities are the NSF Young Scholars Programs at Indiana University and Purdue University, which were an excellent jump start to research for a young adolescent. Carmel High School science teachers Duane Newman, Jack Mayfield, and Mr. Maxim for traveled to almost every university in Indiana with me, sometimes alone, for various science events and competitions, and to National Science Olympiad tournaments even further away.

Next I would like to thank the fantastic teachers and mentors I had at Purdue University, including Dr. Stephen C. Beering, whose named scholarship enabled me the freedom to prepare for combined graduate training in hard science as well as medicine. Math professors Carl C. Cowan, Stephen Bell, Fabio Milner, and Burgess Davis, whose advice and insight helped to solve not only practice Putnam Exam problems, but also to decide life plans. Deserving special thanks is Professor Leslie Geddes, whose physiological measurement techniques course showed the marriage of electrical engineering and medicine from the perspective of a true icon in the field. Not to mention

my first engineering advisor, Professor Robert Montgomery “Dr. Bob,” who first told me my career path with the phrase “you can’t spell ‘geek’ without EE.” He also let me spend time at his pool and wrote the critical letter for the Gates Fellowship. The wonderful letters by all these recommenders may have been the last straw that resulted in the acceptance in the University of Michigan MD/PhD program, which is of course also very high on the thank you list. The NIH funding for medical school cannot be underestimated. Perhaps more importantly, the staff, Operating Committee, and directors Professor Ron Koenig, Penny Morris, and Ellen Elkin, as well as Hilkka Ketola have provided support at a much deeper level, going above and beyond the call of duty. The people at Rackham Graduate School have helped me as well with various programs, including numerous international travel awards. The staff at CUOS including Linda Owens, Bett Weston, and Debra Dieterle has also been very helpful in coordinating countless trips and purchases necessary for this research.

Then there are the individuals who have kept my medical passions alive through the long haul of dual degree training, including acclaimed anatomy professor, author, plastination expert and friend Professor Thomas D. Gest; dedicated pathology Professor Andrew Flint; Dr. Semyon Zarkhin; and Dr. Paul Fine for clinical refresher training in preparation for return to the hospital. I would also like to thank former Ypsilanti Mayor Dr. Cheryl Farmer and Dr. Vangie Spindler for their guidance on the Michigan State Medical Society Bioethics Committee, and all the other outstanding physicians I have met through the AMA and various other medical associations.

On a non-scientific note, much is owed to the Congress-Bundestag Exchange Program and host parents Petra and Uwe as well as Frau Gurtman, the principle of the St. Leonhard French-German Gymnasium, for fostering my independent spirit during the senior year of high school in Aachen. Numerous outstanding piano teachers, rowing trainers, and ballroom dance partners and coaches need to be thanked for teaching me the value of actively pursuing less academic activities as well, including Wayne Applegate and Dan Rutherford in Indianapolis and Stephen and Susan McFerran for the past half-decade in Ann Arbor.

Finally, and most importantly, I would like with my full heart and soul to thank my immediate Family. They have tirelessly made the greatest sacrifices and investments

into my success all along the way, ranging from picking a home far from employment location to have the best school district, and then driving a smart-alec middle school student daily for courses at the high school and numerous extracurricular activities, to instrumental roles editing various applications that have enabled the financing of my education, to alerting me of necessary emergency changes in my travel plans, and generally providing amazing physical, emotional, and spiritual support. In many ways, the achievement of a Ph.D. has as much or more to thank for their work as for my own.

TABLE OF CONTENTS

LIST OF FIGURES

LIST OF TABLES

ABSTRACT

FEMTOSECOND LASER PULSE OPTIMIZATION FOR MULTIPHOTON CYTOMETRY AND CONTROL OF FLUORESCENCE

by

Eric Robert Tkaczyk

Chair: Theodore B. Norris

This body of work encompasses optimization of near infrared femtosecond laser pulses both for enhancement of flow cytometry as well as adaptive pulse shaping to control fluorescence. A two-photon system for *in vivo* flow cytometry is demonstrated, which allows noninvasive quantification of circulating cell populations in a single live mouse. We monitor fluorescently-labeled red blood cells for more than two weeks, and are also able to noninvasively measure circulation times of two distinct populations of breast cancer cells simultaneously in a single mouse. We build a custom laser excitation source in the form of an extended cavity mode-locked oscillator, which enhances the two-photon signal strength several fold relative to a commercial laser. This enables superior detection in whole blood or saline of cell lines expressing fluorescent proteins including the green fluorescent protein (GFP), tdTomato and mPlum. A mathematical model

explains unique features of the signals including: sub-square law scaling of unsaturated two-photon signal; a sigmoidal sensitivity curve for detection under varying excitation powers; and uncorrelated signal strengths in two detection channels.

The ability to distinguish different fluorescent species is central to simultaneous measurement of multiple molecular targets in high throughput applications including the multiphoton flow cytometer. We demonstrate that two dyes which are not distinguishable to one-photon measurements can be differentiated and in fact quantified in mixture via phase-shaped two-photon excitation pulses found by a genetic algorithm. We also selectively enhance or suppress two-photon fluorescence of numerous common dyes with tailored pulse shapes. Using a multiplicative (rather than ratiometric) fitness parameter, we are able to control the fluorescence while maintaining a strong signal. The importance of linear chirp and power scaling checks on the adaptive learning process is investigated in detail. With this method, we control the two-photon fluorescence of the blue fluorescent protein (BFP), which is of particular interest in investigations of protein-protein interactions, and has frustrated previous attempts of control. Implementing an acousto-optic interferometer, we use the same experimental setup to measure two-photon excitation cross-sections of dyes and prove that photon-photon interferences are the predominant mechanism of control.

This research establishes the basis for molecularly tailored pulse shaping in multiphoton flow cytometry, which will advance our ability to probe the biology of circulating cells during disease progression and response to therapy.

CHAPTER 1
INTRODUCTION

The original motivation for this body of work was the need in biomedical research to monitor rare populations of circulating cells. Our group's initial attempts to perform this noninvasively and quantitatively[1,2] achieved some success with femtosecond laser pulses. It seemed at the time that the budding technology would blossom with nourishment only from well-planned biology experiments. The bulk of my doctoral work, however, arose from the hope that even greater advances could be gained by attention to the nature of the pulses used for detection.

This introductory chapter serves as an overview of the relevant scientific background to provide a more cohesive understanding of the individual technical chapters that follow. First, we discuss the potential value of advanced cytometry, tailored pulse shaping, and control of blue fluorescent protein (BFP), the shortest emission wavelength variant of the famous green fluorescent protein (GFP). Next, we review some relevant physical and mathematical themes, including the second-order perturbation theory of fluorescence control as well as the relation of Hilbert transforms to complex basebands of optical fields. This facilitates appreciation of the acousto-optic Fourier transform measurement used repeatedly in the research. Finally, a brief overview of the work is given.

1. Practical Motivations

1.1 Flow cytometry

There is intense interest in analyzing circulating cells in the blood stream, including tumor cells and endothelial cells, to study cancer biology and response to therapy. The number of circulating tumor cells is a predictor of survival in patients with metastatic breast cancer[3]. The genotype of circulating tumor cells appears to be representative of cells in tumor tissue, suggesting that monitoring cancer cells in the blood may reveal genetic changes that occur over the course of disease[4]. Breast cancer cells also can be detected in the circulation of patients without clinical evidence of metastatic disease, although the biologic significance of these cells remains to be established[5]. Furthermore, changes in numbers of circulating endothelial cells have been used to monitor responses to therapy[6]. These data emphasize the significance of circulating cells for cancer biology and treatment and emphasize the need to define molecular features that regulate dynamics of circulating cells in living animals and patients.

One key obstacle to studies of circulating cells in mouse models of cancer and other diseases is the challenge of optically interrogating cells in the vascular system of living mice. Two approaches to so-called *in vivo* flow cytometry have been demonstrated in the vasculature of living mice[7,8]; while these initial studies showed promise, they have been limited to detecting single color biomarkers. However, numbers of circulating cells enumerated with single-color detection may vary in response to changes in an animal's physiology, such as vasoconstriction or fluctuations in heart rate, in addition to intrinsic changes in circulating cells. With single color detection of biomarkers, errors caused by different physiological conditions cannot be compensated. Thus, accurate assessments of circulating cells *in vivo* are difficult to obtain.

To simultaneously enumerate different populations of circulating cells under varying physiological conditions over time in an animal, we developed a novel two-photon flow cytometry system for two-channel detection of fluorescent cells *in vivo*. Although detection of circulating cells *in vivo* has been achieved in a confocal geometry using single-photon excitation[9], that technique has been limited to detection of a single

fluorescent species. In contrast, our two-photon system has the important advantage of simultaneously detecting multiple cell populations because a single femtosecond near infrared (NIR) laser can be used to excite multiple fluorescent dyes via two-photon transitions. The large separation between NIR excitation and emission wavelengths attenuates scattered excitation light while collecting the entire fluorescence spectrum with high efficiency, thereby decreasing detection background[10]. Further, multiphoton excitation brings to *in vivo* flow cytometry all the advantages of multiphoton microscopy, such as reduced photodestruction outside the interrogated region[11].

1.2 Pulse shaping

Something magical happened when the group of Webb applied to microscopy the phenomenon of two-photon excitation, which had been around for a half century since it was theorized in Maria Göppert-Mayer's doctoral thesis of 1931[12]. This marriage of an old and an ancient field has engendered, already by the silver wedding anniversary, uncountable practical applications that have gone on to have very successful independent lives[10,11,13-15]. We consider multiphoton cytometry as one of these children, though even top-level experts of conventional flow cytometry note the technical challenges[16]:

> "Two-photon flow cytometry is relatively impractical for several reasons. First, one needs to use pulsed excitation, which requires a spotting laser upstream of the Ti-sapphire laser and electronics (similar to sort control electronics) to trigger the excitation pulse when the cell of interest reaches the right beam intersection point. Second, even when you get all of that set up, excitation is typically restricted to a very small fraction of the cell volume, as is also the case with two-photon microscopy. However, with two-photon microscopy, you can sample a number of different small volumes within one cell, whereas with flow you're pretty much limited to one shot. "

Many of the advantages of two-photon excitation stem from the nonlinear dependence of the detected signal on the excitation intensity. In particular, the number of absorbed photons by a fluorophore is given by[17]

$$n_a \approx \frac{p_0^2 \delta}{\tau_p f_p^2} \left(\frac{(NA)^2}{2\hbar c \lambda} \right)^2 , \qquad (1)$$

where p_0 is the average laser intensity, τ_p is the pulse duration, f_p is the laser's repetition rate, NA is the numerical aperture of the focusing objective, $\hbar$ and c are Planck's constant and the speed of light, respectively, and δ is the fluorophore's two-photon absorption cross-section at wavelength λ (common dyes typically have cross-sections on the order of

10^{-49} cm^4s/photon around 800nm[18]). The excellent spatial resolution of multiphoton microscopy is a direct result of this nonlinear dependence. The temporal aspect of (1) is equally important, and increasing the peak intensity of pulses will enable major improvement of signal-to-noise for the same average delivered power. This can be achieved by shortening the pulses or increasing the energy per pulse through a lower duty cycle, for example with the reduced-repetition-rate extended laser cavity we built for the investigation of Chapter 3. In this manner, if most of the damage is thermal, one is much less likely to have to burn the sample with the laser to get a quality image. Using only increased peak intensity to improve multiphoton techniques does, however, meet a fundamental limitation if undesirable processes increase nonlinearly as well. Photobleaching, for example, may involve higher-order photon interactions, as evidenced by experiments which reveal a supraquadratic dependence on intensity[19]. Multiphoton processes are also involved probably in some of the damage to the biological specimens that motivate our work. Evidence for this includes the empirically observed P^2/τ dependence of NIR ultrashort laser pulse damage behavior to cells, where P is average power, and τ is pulse duration[20].

On the one hand, compressing laser pulses in time by compensating the phase from dispersion does enable quality two-photon excitation at lower average powers, which reduces photobleaching[21]. On the other hand, at a fixed average power, compressed laser pulses may actually cause *more* photobleaching[20]. This apparent paradox is a fundamental reason to pursue tailored pulse shaping methods, which stretch pulse durations relative to the bandwidth-limited pulse (which is maximally compressed, cf the excellent discussion by Siegman[22]), but might not necessarily reduce two-photon signal. The ability to reduce photobleaching with tailored pulses is, in fact, already demonstrated[23]. Typically, however, search algorithms to improve the ratio of two-photon fluorescence to another multiphoton process converge to a pulse with a significant drop in signal relative to the unshaped pulse. Multiphoton applications like microscopy and cytometry will benefit more from shaped pulses which, despite the lower peak intensities and reduction of undesired multiphoton processes, achieve similar or even improved fluorescent signal relative to the transform-limited pulse. Inspiration for this

goal is obtained from elegant theoretical and experimental work demonstrating the feasibility of shaping to increase two-photon excitation relative to the transform-limit[24].

Ultimately, investigations with molecular specificity have resulted in most of the major advances in our understanding of biology and medicine in the modern era. Traditional spectroscopy has become a standard of the biologist's toolkit. In multiphoton microscopy, changes with tuning of the fundamental laser excitation wavelength can provide information about specific molecules in biological samples[25]. Phase-interferences, however, can achieve orders of magnitude more specificity[26]. It is the dream of tailored pulse shaping to probe and control with great specificity fundamental molecular processes, and thereby enable new realms of technology and discovery.

1.3 Blue fluorescent protein (BFP)

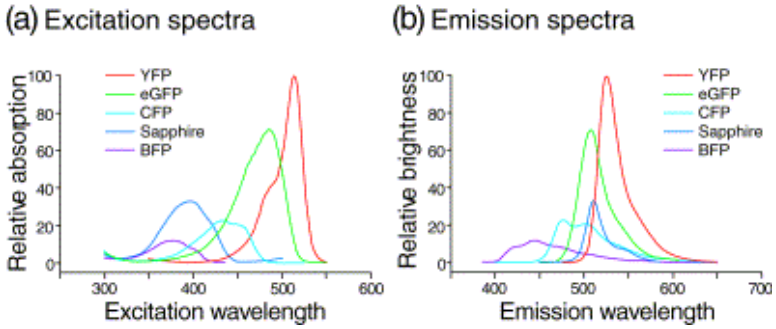

Figure 1.1 Relative excitation (absorption) and emission (brightness) spectra for the five green fluorescent protein (GFP) mutant classes. Purified recombinant protein was used to generate the spectra. Spectra are represented in the following colours: BFP, violet; Sapphire, royal blue; CFP, cyan; eGFP, green; YFP, red. Y-axis values are set relative to YFP (100%). (Reproduced, with permission[27])

BFP, the shortest-wavelength emission fluorescent protein (Figure 1.1), has enabled notable biological discoveries as a fluorescence resonance energy transfer (FRET) donor with the yellow fluorescent protein (YFP). In particular, YFP has significantly greater change in emission upon cleavage from a donor BFP than it does in the next-most common pairing with the cyan fluorescent protein (CFP) (Figure 1.2). BFP is, however, not favored in some investigations at present due to its low quantum yield (Figure 1.1) and high photobleaching. Both the weak signal and photobleaching of BFP could potentially be improved if it were possible for tailored pulse shapes to control the

fluorescence. Therefore there is hope that our approach may re-establish the central role of BFP in pivotal investigations of protein interactions.

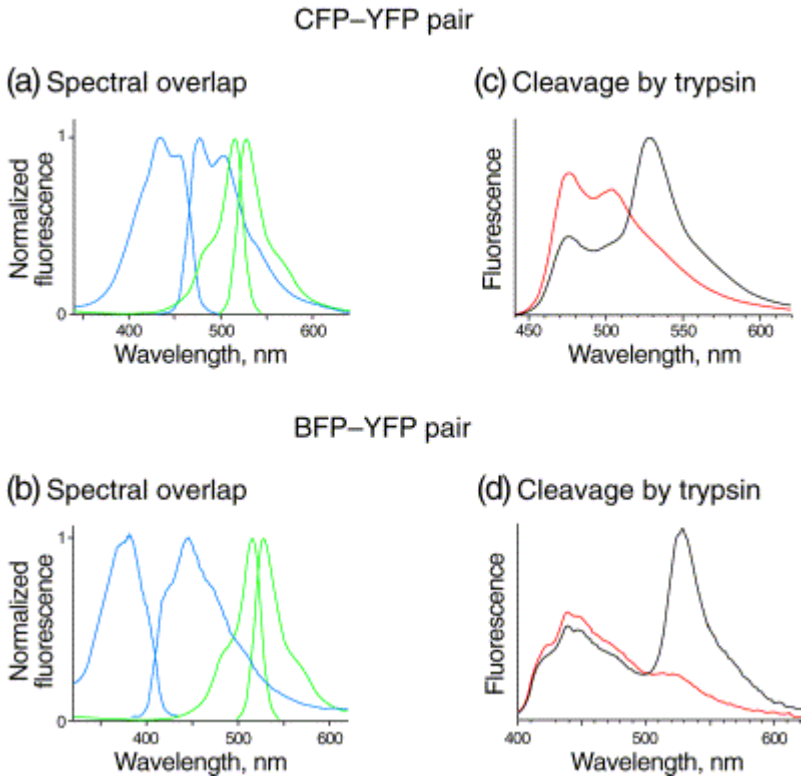

Figure 1.2 Spectra for two tandem green fluorescent protein (GFP) protease reporters, CFP–YFP and BFP–YFP. (a, b) Donor (blue lines) and acceptor (green lines) excitation and emission spectra. These spectra illustrate how the CFP–YFP pair has better overlap for donor emission and acceptor excitation, but poorer separation of donor and acceptor emission spectra, than the BFP–YFP pair. (c, d) Overall emission spectra of each GFP–FRET pair before (black) and after (red) cleavage with trypsin. The more efficient energy transfer in the CFP–YFP pair leads to a larger observed change in the donor CFP emission (425/500 nm peaks). The better emission separation in the BFP–YFP pair, however, gives a greater decrease in the acceptor YFP emission (530 nm peak). A fourfold ratio change for each of the tandem GFP protease substrates is seen with trypsin, showing that FRET readout with two GFPs is a balancing act between several biophysical characteristics of the proteins. These analyses were performed on a SPEX FluoroLog-2 instrument. (Reproduced, with permission[27])

BFP is equally stimulating from the perspective of a physical scientist. The blue shift of BFP has been achieved by mutation of the chromophore of GFP, where the phenolic ring has been replaced by a histidine. Experiments[28-30] and calculations[30-35] have shown that the efficient quenching of the excited state of BFP stems from the excitation-induced isomerization of the chromophore. The highly nonexponential

fluorescence decay has components from some picoseconds up to several nanoseconds, indicating the presence of different chromophore conformations. The equilibrium between the fast-decaying nonfluorescent conformations can be shifted in favor of the fluorescent ones by applying high hydrostatic pressure or by lowering temperature[28].

The nonradiative isomerization makes BFP an interesting target for coherent control. Ideally, control of the evolution of the excited state wavepacket could steer the BFP chromophore away from undesirable isomerization pathways in favor of fluorescence. It is known from quantum chemical calculations[36] that after excitation, the chromophore finds itself in a highly unstable Franck-Condon point on the potential energy surface, where the torque by the nonequilibrium electronic cloud tends to twist the chromophore away from its flat conformation. As a result of this twist, the energy surfaces of the excited and ground states come close to each other, and the fluorescence is quenched. If the electric field of the appropriately tailored femtosecond excitation pulse could drive the electrons in opposite phase to this twisting motion and could efficiently counteract the isomerization, the fluorescence yield could be substantially enhanced.

2. Coherent Control

2.1 Quantum phase in biology

The biological reader has probably already asked the question of whether or not, fundamentally, pulse shaping can really impact biological investigations. Even if the light-matter interaction is treated semiclassically, the quantum world must be considered to understand pulse shaping effects, and this world seems distant from biomedical applications. Nagy *et al.* recently published an excellent review paper[37] in the field of coherent control beginning with the provocative question "Do we live in a quantum world?" where it was pointed out that:

> "…the single most important distinguishing feature that separates quantum mechanics from classical mechanics is the underlying phase of the wave-function."

If the phase of the quantum wavefunction is important for a biological process, it must be completed on such a time scale that phase coherences amongst the participating players are not washed out. This is a very short timescale, indeed; vibrational motions typically have order of picosecond decoherence times, and electronic dephasing times are only in the 10-100 fs range. However, some important biology does happen on comparable timescales, for example energy transfer and barrier crossing events. In fact, it has been shown that low excitation fields can be shaped to significantly affect the outcome of bacteriorhodopsin isomerization, closely related to the primary event of human vision[38]. In this section, we will take a close look at the equally fast process of two-photon excitation, which is the central pillar of the applications considered in this dissertation, and in particular how it can most simply be controlled relative to the instantaneous process of second harmonic generation (SHG) by tuning of the laser's second-harmonic spectrum.

2.2 Schools of coherent control

Traditionally, the ability to control excitation with shaped pulses has been understood in two ways. The Tannor-Rice control scheme relies on the manipulation of vibrational coherences. In the Tannor-Rice control scheme, the laser pulse (or pulse series) is shaped in the time-frequency domain to coherently match the actual trajectory of the excited state wavepacket during its evolution, which is dictated for example by

vibrational relaxation or nuclear motion[39,40]. A classic example is the "pump-dump" explanation of increased stimulated emission with negatively chirped laser pulses[41,42]. The Brumer-Shapiro control scheme, on the other hand, exploits electronic coherences. Energy levels are considered static, and interferences are created between multiple quantum pathways leading to the desired final state. An excellent example is the predictable periodic dependence of the excited state population of cesium on the delay between two optical pulses[43]. In this case, the coherence is between the second pulse and the electrons excited by the first pulse. From a similar vantage point, transform-limited pulses are far from the true optimum to maximize two-photon excitation via a real intermediate level, due to phase differences in the contributions of off-resonant terms[24]. Most of the results in the current dissertation, however, are largely explained without consideration of excited wavepacket motion or molecular coherences. Rather, we interpret them in terms of optical interferences whose major role is to tune the second-harmonic power spectrum of the exciting pulse to the relevant location on the relative two-photon excitation cross-section spectrum of the discriminated dyes.

2.3 Two-photon excitation vs. SHG: theoretical view

Let us consider a quantum system initially in ground state |g>, under a weak femtosecond laser pulse field E(t) not resonant with any intermediate or final state. Using the time-dependent second-order perturbation analysis of Meshulach and Silberberg[44] in the notation of Brixner et *al*.[45], one obtains the amplitude of the final state:

$$a_f(t) = -\frac{1}{\hbar^2}\sum_n \langle f|\mu|n\rangle\langle n|\mu|g\rangle \int_{-\infty}^{t}\int_{-\infty}^{t_1} E(t_1)E(t_2)\exp(i\omega_{fn}t_1)\exp(i\omega_{ng}t_2)dt_2dt_1, \qquad (2)$$

where bracketed terms are dipole matrix elements between final and intermediate states, and intermediate and ground states, respectively. The frequencies are determined by $\hbar\omega_{fn}=(E_f - E_n)$ and $\hbar\omega_{ng}= (E_n - E_g)$, with energy levels applying to final, intermediate, and ground states. As an aside, there is the possibility of further simplification for short pulse excitation, where intermediate levels add coherently for only short time durations (t_1-$t_2 < \omega^{-1}$):

$$\sum_n \langle f|\mu|n\rangle\langle n|\mu|g\rangle \exp[i\omega_{ng}(t_2 - t_1)] \approx \langle f|\mu^2|g\rangle, \quad |t_2 - t_1| < \bar{\omega}^{-1}, \qquad (3)$$

The sum is 0 elsewhere, where ω bar an appropriately weighted average energy.

After a Fourier transform, we find that the final state population (transition probability) after the end of the two-photon absorption process is a simple product:

$$p_{TPA}(\omega) = g_{TPA}(\omega)S_2(\omega), \tag{4}$$

with

$$g_{TPA}(\omega) = \frac{1}{\hbar^4}\left|\sum_n \frac{\langle f|\mu|n\rangle\langle n|\mu|g\rangle}{\omega_{ng} - \omega/2}\right|^2, \tag{5}$$

$$S_2(\omega) = \left|\int_{-\infty}^{\infty} E(\Omega)E(\omega - \Omega)d\Omega\right|^2, \tag{6}$$

where $E(\omega)$ is the Fourier transform of $E(t)$ and $\hbar\omega = (E_f - E_g)$. The first factor (5) depends only on quantum system properties and the transition frequency, whereas the second-harmonic power spectrum $S_2(\omega)$ (6) depends only on the properties of the electric field, and indicates what frequencies are available for two-photon excitation.

The process of second-harmonic generation (SHG) in a crystal has a similar dependence[46] :

$$I_{SHG}(\omega) = g_{SHG}(\omega)S_2(\omega), \tag{7}$$

$$g_{SHG}(\omega) \propto (\chi^{(2)}L)^2\mathrm{sinc}^2[(\upsilon_2^{-1} - \upsilon_1^{-1})(\omega - 2\omega_0) - \Delta kL/2], \tag{8}$$

with $\chi^{(2)}$ the second-order susceptibility, L the crystal length, $\Delta k = 2k_1 - k_2$ the phase mismatch between the fundamental and the second harmonic, υ_2 and υ_1 the group velocities of second-harmonic and fundamental, respectively, and ω_0 the center frequency of fundamental.

We find that for a specific transition, we cannot in this view control the ratio of probability of the two second-order processes, as this is the constant $p_{TPA}(\omega)/I_{SHG}(\omega) = g_{TPA}(\omega)/g_{SHG}(\omega)$, independent of pulse shaping. However, the ratio of the total signal can in fact be changed by tuning of the second-harmonic spectrum. Let us assume a thin enough nonlinear sample to phase-match the whole laser bandwidth and set $g_{SHG}(\omega) = 1$. If we excite to a final state distribution with spectral density of states $\rho(\omega)$, we find that the ratio of the total second-order signals is:

$$\frac{p_{TPA}(\omega)}{I_{SHG}} = \frac{\int g_{TPA}(\omega)\rho(\omega)S_2(\omega)d\omega}{\int S_2(\omega)d\omega}, \tag{9}$$

In some notations, the density of states is included in a single factor which is actually the total two-photon excitation cross-section σ or $g^{(2)}(\omega)$[47,48]. In any case, in this analysis the fundamental quantity for control is the second harmonic spectrum of the field $S_2(\omega)$, which is the power spectrum of $E^2(t)$. The expression (6) can be rewritten for a better physical picture:

$$S_2(\omega) = \left| \int_{-\infty}^{\infty} E(\omega/2 + \Omega) E(\omega/2 - \Omega) d\Omega \right|^2 \tag{10}$$

In other words, two photons of frequency $\omega/2 + \Omega$ and $\omega/2 - \Omega$ add such that the sum of their energies corresponds to the total transition frequency ω. The ability to manipulate this with modulation of amplitude $|E(\omega)|$ or phase $\Phi(\omega) = -\arg E(\omega)$ is even more obvious after expansion[49]:

$$S_2(\omega) = \left| \int_{-\infty}^{\infty} |E(\omega/2 + \Omega)| |E(\omega/2 - \Omega)| \exp\{i[\varphi(\omega/2 + \Omega) + \varphi(\omega/2 - \Omega)]\} d\Omega \right|^2 \tag{11}$$

Theory and experiments both show that linear chirp does affect this spectrum[50], and in fact the reduction of S_2 occurs in a frequency-*dependent* fashion, despite claims of the opposite[51]. However it seems generally true that linear chirp is not a reasonable method of achieving significant control (at low intensities[42]), and in our low-field work, we always interpreted as artifact any change in degree of discrimination with alterations of linear chirp.

If, on the other hand, the excited state population can be manipulated by additional 800 nm photons, the above analysis is no longer sufficient. Rather, the "time ordering" of excitation frequencies becomes important. In this case, the two-photon fluorescence is entering the Tannor-Rice control realm. Cao *et al.*[39] present an excellent theoretical example of precisely this effect and name a few possible underlying mechanisms:

> "Dynamic mechanisms at play in this system include response of solvent to nascent dipole, ultrafast intersystem crossing, and the electronic and structural rearrangements associated with the intraligand electron delocalization in the charge-separated state."

2.4 Example of Brumer-Shapiro control with theory

The Brumer-Shapiro view, perhaps as it deals with time-independent operators and energy levels, seems to be popular especially in the literature reports which merge theory with very quantitative experimental results. Insight into this school of coherent control can be obtained from the theoretical outline by Blanchet *et al.*[43], who were able to distinguish optical (oscillations at the optical period) from quantum interferences (at half the optical period) in the same experiment. The fundamental principle that two pulses are used to create interfering excited state wave packets is closely related to conventional Fourier spectroscopy with a Michelson interferometer[52]. After the first single pulse, there is a constant excited state amplitude, but the phase of the excited state wave function oscillates with time at the frequency corresponding to its eigenvalue. When the second pulse adds to the excited state wave packet, the relative phase of the addition causes interferences which *do* affect the final excited state amplitude. Blanchet puts the matter in its global context[43]:

> Several kinds of control have been investigated. Optimal control consists of shaping the laser pulse in order to reach a well-defined target, but remains mostly inaccessible to the experimentalist, except in very limited cases. In coherent control, quantum interferences between several quantum paths are used to modulate a specific channel. Each quantum path results from the interaction between a laser field and the atomic or molecular system. Variation of the relative phases between these laser fields induces constructive or destructive interferences between quantum paths. Excitation probability of the process is thus coherently controlled.
>
> …
>
> In temporal coherent control, a sequence of two time delayed pulses is used to follow the two quantum paths. The interference phase is related to the time delay between the two pulses. Variation of the time delay results in interferograms which show a high frequency oscillation (corresponding to Ramsey fringes) modulated by a slow envelope resulting from the wave packet motion in the excited state. Various detection schemes have been used to isolate this slow envelope from the rapid oscillations. Three examples are the phase lock technique, the sensitive phase technique, and the random phase technique. These techniques allow extraction of the wave packet motion contribution from the signal. However, to achieve control of the process, the time delay must be fixed with an accuracy much better than the optical period in order to select between constructive or destructive interferences which result in enhancement or weakening of the total cross section of the process. Most of these experiments have been performed in the weak field regime. These quantum interferences persist in the intermediate or high field regime, where higher transfer rates and large control contrasts are observed.

Here we note that despite the discussion of "wave packet motion in the excited state," their analysis nevertheless considers a static energy structure of the excited states manifold and therefore is distinct from the Tannor-Rice scheme. In this consideration, no depletion of the ground state has been assumed, but with high intensity pulses, more interesting effects might occur. The theory begins with the non-resonant second-order

perturbation result of a single two-photon excitation by a short laser pulse $E_0(t)\exp(-\omega_L t)$ with an atomic system of three sets of levels: ground $|g\rangle$, intermediate $|i_l\rangle$, and excited $|e_k\rangle$ with corresponding energies 0, $\hbar\omega_{il}$, and $\hbar\omega_{ek}$. The second pulse is merely a τ time-delayed replica of the first with amplitude-scaling factor β. After interaction with the combined field E(t) of the two pulses there is no population in the intermediate levels (due to non-resonance), but each excited state level is populated with amplitude:

$$a_{e_k}(t) = Q_{g,e_k} e^{-i\omega_{e_k} t} \tilde{E}^2(\omega_{e_k}) \tag{12}$$

where $Q_{g,ek}$ is the two-photon transition operator from $|g\rangle$ to $|e_k\rangle$, calculated from the usual electric dipole moment of the atom μ in the same manner as in (5):

$$Q_{g,e_k} = \sum_l \frac{\langle e_k|\mu|i_l\rangle\langle i_l|\mu|g\rangle}{\hbar(\omega_{i_l} - \omega_L)} \tag{13}$$

Note that the final field term in (12) is not the square of the Fourier transform of the time-domain pulse, but rather the Fourier transform of the squared field, whose square modulus is the second harmonic power spectrum of (6). This important difference accounts for all of the photon-photon interferences which enable phase-only control of the second harmonic power spectrum. Consider Rick Trebino's example[53] of a sinc(t) E-field, which has second harmonic spectrum triangle(ω), not triangle^2(ω).

Direct calculation leads to the final expression of the amplitudes of the different excited state levels, which has a quantum path from each pulse alone, and the combined path with one photon from each pulse:

$$\begin{aligned}
&a_{e_k}(t) = K_1^{e_k} + K_2^{e_k}(\tau) + 2K_{12}^{e_k}(\tau), \quad \textit{with} \\
&K_1^{e_k} = \frac{i}{\hbar} Q_{g,e_k} e^{-i\omega_{e_k} t} \tilde{E}^2(\omega_{e_k} - 2\omega_L) \\
&K_2^{e_k}(\tau) = \beta^2 K_1^{e_k} e^{+i\omega_{e_k}\tau} \\
&K_{12}^{e_k}(\tau) = \frac{i}{\hbar} Q_{g,e_k} \beta e^{-i\omega_{e_k} t} e^{+i\omega_L \tau} \int E_0(t') E_0(t'-\tau) e^{+i(2\omega_L - \omega_{e_k})\tau'} dt'
\end{aligned} \tag{14}$$

At short time scales with nearly complete overlap of the two pulses, the effect is the same as a single pulse whose intensity is determined by the optical interference. At intermediate time scales, all paths contribute and interfere with each other, but the K_{12} path drops monotonically with τ as the pulses cease to overlap. For τ much greater than

the pulse duration, it is relatively impossible for two-photon absorption to occur with one photon of each pulse, and quantum interferences between the two other paths become clear, with the population after the end of the interaction given by:

$$\left|a_{e_k}(\infty)\right|^2 = \sum_k (1+\beta^4+2\beta^2\cos(\omega_{e_k}\tau))\left|K_1^{e_k}\right|^2 \qquad (15)$$

After delays greater than the reciprocal of the excited states energy splittings, the interferograms of each individual excited state $|e_k\rangle$ dephase and beats result. In this manner, Blanchet and colleagues were able to control the ionization probably of Cesium in good agreement with the theory.

2.5 What is "Coherent Control," anyway?

At the time of writing this dissertation, a Google™ Scholar search for the term "coherent control" found 739 000 scientific references. There are multiple books and reviews on the subject from different schools of thought, but it remains somewhat nebulous what exactly qualifies as coherent control, and what does not. One very loose definition might include anything altering a quantum wave function. This would include, for example, excitation of fluorescence by sunlight. At the other end of the spectrum, one might insist upon intentional human manipulation of the evolution of the wave, including quantum phase[54].

A more favored criterion is "the use of coherences of an electromagnetic field to control the state of a wavefunction." These results can often be described semiclassically without regards to actual quantum interferences. As a notable example, the elusive concept of quantum phase can be completely ignored in many "pump-dump" discussions of the time-evolution of an excited population, although coherence of the excitation field with the excited wave packet might be a crucial feature of the control. Coherence of the excitation field with the excited wave packet is not part of our interpretation of most of the results on fluorescence control presented in this dissertation, though intrapulse coherences within the exciting field are essential. A purist might employ a somewhat more stringent definition of coherent control as "the use of coherences between a driving field and a quantum wavefunction to achieve a desired outcome" and thereby exclude most of the work presented here, but we leave the ultimate verdict as an exercise to the reader.

3. Complex Baseband Theory and Acousto-optic Implementation of a Fringe-Resolved Autocorrelation

Due to the enormous separation between the period of light oscillations and the time scales on which light is generally modulated and detected, optical theory and simulations often draw on the electrical engineering concept of a "complex baseband." In this manner, fluctuations can be considered at their native periods and then simply shifted to higher frequency for direct comparison with experimental results. As numerous results in this dissertation are interpreted with the aid of our acousto-optic time-domain measurement of two-photon excitation cross-sections, we present here some of the principles of the complex baseband and apply it in simulation of our measurement. First we discuss the Hilbert transform and use it to define the analytic signal for a real signal. Then we relate this to the optical interferogram and the spectra extracted from a fringe-resolved autocorrelation (FRAC). Finally, we present our acousto-optic implementation of FRAC and simulation thereof.

3.1 Hilbert transforms and the analytic signal

Define the Fourier transform (FT)[55] of a function f(t) as:

$$\mathrm{FT[f]} = F(\omega) \equiv \int_{-\infty}^{\infty} f(t) e^{-i\omega t} dt \tag{16}$$

The original function can be recovered by the usual inverse transform:

$$f(t) = \frac{1}{2\pi} \int_{-\infty}^{\infty} F(\omega) e^{i\omega t} \tag{17}$$

In this work, we will also employ the standard notation that a tilde (~) appearing over a function refers to the FT of that function.

Next, define the Hilbert Transform (HiT) of a function f(t)[56]:

$$\mathrm{HiT[f(t)]} = F_{Hi}(t) \equiv \frac{1}{\pi} p \int_{-\infty}^{\infty} \frac{f(t')dt'}{t'-t} = \frac{-1}{\pi x} \otimes f(t) \tag{18}$$

In the Fourier domain, this is just

$$\tilde{F}_{Hi}(\omega) = H(\omega) F(\omega), \tag{19}$$

where H(ω) = i sign(ω) and F(ω) = FT[f]. As an example, HiT[cos] = -sin, and HiT[sin] = cos. As F(ω) = -H(ω)H(ω)F(ω), the inverse Hilbert transform is thus immediately obvious as the negative of the HiT:

$$f(t) = -\left[\frac{-1}{\pi x} \otimes F_{Hi}(t)\right] \tag{20}$$

Perfect symmetry is sacrificed in favor of maintaining the Hilbert transform of a real function as a real function.

To any real function f(t) w/ FT F(ω), we can in this manner define an *analytic signal* $\hat{f}(t)$ whose real part is f(t).

$$\begin{aligned} \hat{f}(t) &\equiv f(t) - iF_{Hi}(t) = 2g(t) \otimes f(t) \\ g(t) &\equiv \frac{1}{2}\delta(t) + \frac{i}{2\pi t} \end{aligned} \tag{21}$$

In the time domain, we quickly find the analytic signal by dropping the complex conjugate term of the expression $\hat{f}(t)$ + c.c.:

$$f(t) = \frac{1}{2}\,\hat{f}(t) + c.c. = \mathrm{Re}\left[\hat{f}(t)\right] \tag{22}$$

In the Fourier domain, we see that suppressing negative frequencies of F(ω) and then doubling gives the analytic signal immediately. Let the FT of the analytic signal be Y(ω). Then by (21) and (22):

$$\begin{aligned} Y(\omega) &= \tilde{\hat{f}}(\omega) = F(\omega) + \mathrm{sgn}(\omega)F(\omega) \\ F(\omega) &= \frac{1}{2}Y(\omega) + \frac{1}{2}Y^*(-\omega) \end{aligned} \tag{23}$$

As an example, we apply (16)-(23) to relate the cosine function to its analytic signal, the complex exponential:

$$\begin{aligned} f(t) &= \cos(\omega_0 t) = \frac{1}{2}e^{i\omega_0 t} + c.c. = \mathrm{Re}\left[e^{i\omega_0 t}\right] \\ F_{Hi}(t) &= -\sin(\omega_0 t) \\ F(\omega) &= \frac{1}{2}\left[\delta(\omega - \omega_0) + \delta(-(\omega - \omega_0))\right] \\ \hat{f}(t) &= \cos(\omega_0 t) - i\left[-\sin(\omega_0 t)\right] = e^{i\omega_0 t} \\ Y(\omega) &= \delta(\omega - \omega_0) \end{aligned} \tag{24}$$

3.2 The analytic signal and the complex baseband for an optical interferogram

The analytical signal is a useful theoretical tool in optics. Let e(t) be the actual electric field of the optical signal of interest (energy normalized to 1), with FT $\tilde{e}(\omega)$, and ê(t) the corresponding analytic signal. Now define the complex baseband signal E(t) associated with e(t) as a related complex function:

$$E(t) \equiv \frac{1}{2}\hat{e}(t)e^{i\omega_0 t}. \tag{25}$$

Therefore,

$$e(t) = \frac{1}{2}\hat{e}(t) + c.c. = E(t)e^{-i\omega_0 t} + c.c. = \mathrm{Re}\left[2E(t)e^{-i\omega_0 t}\right] \tag{26}$$

We will speak here of three different but related spectra:

- the real measured spectrum $F(\omega) = |\tilde{e}(\omega)|^2$
- the fundamental (complex baseband) spectrum $|\tilde{E}(\omega)|^2$, and
- the analytic spectrum (shifted complex baseband spectrum) Y(ω), which is related to F(ω) as described for analytic signals above in section 3.1.

Consider now the interferogram, which is the square-law detector signal from a Michelson interferometer, which produces a replica of the pulse delayed by τ:

$$S_1(\tau) \equiv \left\langle \left| \frac{e(t)}{2} + \frac{e(t')}{2} \right|^2 \right\rangle, \text{ with } t' = t - \tau \tag{27}$$

Understanding that terms varying at the optical frequency average to 0, we get:

$$S_1(\tau) = (1 + g_1(\tau))/2, \tag{28}$$

where we use the first-order autocorrelation $g_1(\tau)$, whose complex baseband is the second-order coherence function[53] Γ^2:

$$g_1(\tau) \equiv 2\,\mathrm{Re}\left[\Gamma^2(\tau)e^{-i\omega_0 t}\right] \tag{29}$$

$$\Gamma^2(\tau) \equiv \int_{-\infty}^{\infty} E(t)E^*(t-\tau)dt = E(t) \otimes E^*(-t) \tag{30}$$

From this, the fundamental (complex baseband) spectrum is easily extracted (Wiener-Kitchina theorem) by a simple Fourier transform[56]:

$$FT\left[\Gamma^2(t)\right] = \left|\tilde{E}(\omega)\right|^2 \tag{31}$$

Similarly, the real measured spectrum F(ω) is determined as FT[$g_1(\tau)$], with $g_1(\tau)$ the autocorrelation function of the real signal:

$$g_1(\tau) = \int_{-\infty}^{\infty} e(t)e^*(t-\tau)dt = 2\,\mathrm{Re}\left[\Gamma^2(\tau)e^{-i\omega_0\tau}\right] \tag{32}$$

Thus, $\Gamma^2(\tau)\exp(-i\omega_0\tau)$ is the analytic signal to $g_1(\tau)$. How then does the real measured spectrum $F(\omega) = \left|\tilde{e}(\omega)\right|^2 = \mathrm{FT}[g_1]$ relate to the analytic spectrum (shifted complex baseband spectrum) $Y(\omega) = \mathrm{FT}[\Gamma^2(\tau)\exp(-i\omega_0\tau)]$? We showed above that for any analytic pair, F(ω) is obtained from Y(ω) by symmetrization (23). Thus, a real power spectrum is always symmetric about the 0 frequency. This is true because real functions including e(t) Fourier transform to Hermitian symmetric functions[56] $\tilde{e}(-\omega) = \tilde{e}(\omega)^*$. Therefore $F(\omega) = \left|\tilde{e}(\omega)\right|^2 = \left|\tilde{e}(-\omega)\right|^2 = F(-\omega)$. Note however that no such requirement exists for the analytic spectrum Y(ω), which will be 0 for all negative frequencies if ω_0 is larger than the bandwidth of the real measured spectrum F(ω). Thus, the analytic spectrum is generally for positive frequencies the same shape as the real measured spectrum, and we can safely use it in theory and simulation.

3.3 The fringe-resolved autocorrelation (FRAC)

Armed with the knowledge that we can work in the complex baseband, we are now free to follow the development of Naganuma et *al.*[57] in considering the FRAC (also known as the fringe-resolved SHG correlation FRSHG). The FRAC differs from the first-order interferogram (27) by squaring the electric field output of the Michelson:

$$S_2(\tau) \equiv \left\langle \left| \left(\frac{e(t)}{2} + \frac{e(t')}{2} \right)^2 \right|^2 \right\rangle \tag{33}$$

Designate the pulse electric field as in (26):

$$e(t) = E(t)\exp(-i\omega_0 t) + \text{c.c}, \tag{34}$$

We normalize the intensity of the complex baseband signal $I(t) = |E(t)|^2$ to unity integral. Therefore, we can write the FRAC:

$$S_2(\tau) \propto 1 + 2\,G_2(\tau) + 4\,\mathrm{Re}\,[\,F_1(\tau)\exp(-i\omega_0\tau)] + 2\,\mathrm{Re}\,[\,F_2(\tau)\exp(-2i\omega_0\tau)],$$

$$G_2(\tau) \equiv \int_{-\infty}^{\infty} I(t)I(t-\tau)dt = I(t) \otimes I(-t)$$

$$\text{with } F_1(\tau) \equiv \frac{1}{2}\int_{-\infty}^{\infty} \{I(t) + I(t-\tau)\}E(t)E^*(t-\tau)dt \qquad (35)$$

$$F_2(\tau) \equiv \int_{-\infty}^{\infty} E^2(t)E^{*2}(t-\tau)dt$$

Near DC frequency, the G_2 term is simply the intensity autocorrelation, which is commonly used as a quick imperfect assessment of pulse quality by laser manufacturers. The modified interferogram term oscillating at the fundamental frequency, F_1, reduces to the usual interferogram in the limit that distortions of amplitude are slowly varying. At the $2\omega_0$ component, we see F_2, the interferogram of the second harmonic of the field, which contains quite different information from the inteferogram of the fundamental. In the Fourier domain, F_2 yields the second harmonic spectrum we are interested in. Thus, by using the output of a Michelson interferometer for second harmonic generation (SHG), we are able to recover $S_2(\omega)$ by zooming in at the appropriate frequency range of the Fourier transform of the FRAC.

3.4 Acousto-optic implementation

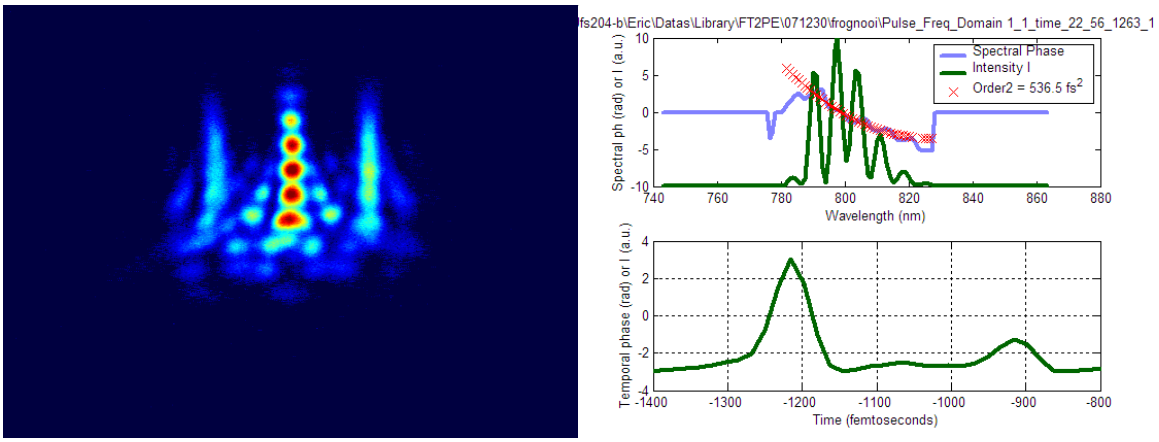

Figure 1.3 Time-delayed duplicate pulse, without phase correction. Left: raw SHG-FROG data of a programmed 300 fs delay from the acousto-optic modulator. Right: frequency and time-domain pulses recovered by the FROG algorithm.

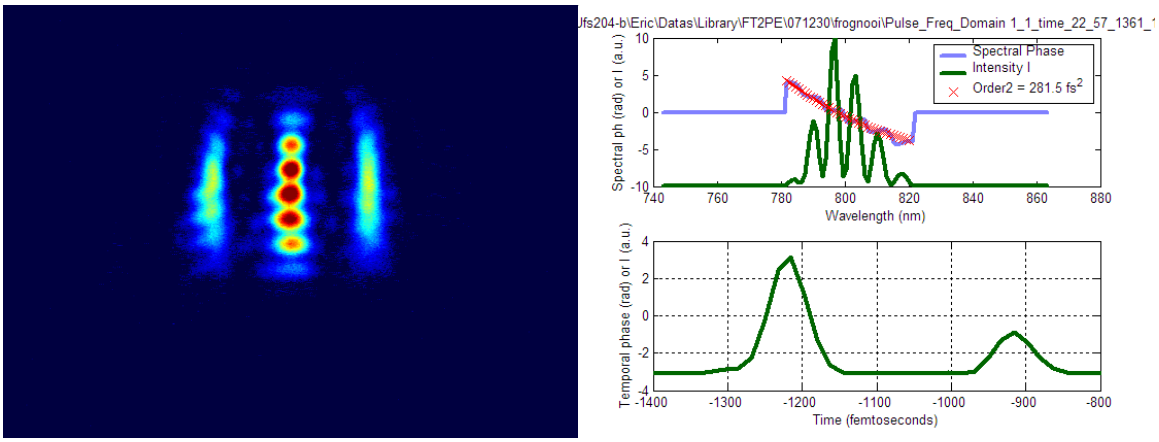

Figure 1.4 Time-delayed duplicate pulse programmed with phase and amplitude correction found by adaptive learning algorithm to maximize SHG. Raw SHG-FROG data with time and frequency-domain recovered pulse by the FROG algorithm.

Our implementation was performed analogously to the description by Ogilvie and colleagues[47]. However, rather than physically delaying a beam-split replica of the pulse, a virtual Michelson interferometer was programmed into the "Dazzler," the acousto-optic modulator we used for pulse shaping. A delay of t_0 between pulses is achieved with simple multiplication by a cosine amplitude mask $\cos(\omega t_0/2)$ in the frequency domain for 150 intervals in an 80 nm bandwidth, corresponding in the conjugate Fourier domain to a time delay of t_0. In practice, due to the non-transform limited nature of the unshaped

pulse (Figure 1.3), superior results were obtained when we first ran an adaptive learning algorithm to maximize SHG efficiency of the pulse to remove phase distortions and ensure an optimal transform-limited pulse (Figure 1.4). When this phase and amplitude was then used as the fundamental pulse for programmed duplication in the time-domain measurement, we were able to significantly improve the bandwidth and accuracy of the measurement (Figure 1.5).

We also note that the 27 nm of bandwidth of the pulses from our regeneratively amplified laser system are at the limits of the commercial Grenouille device (SwampOptics, Atlanta, GA) we use for SHG-FROG reconstruction[58]. While the majority of the pulse is captured within the 50 nm bandwidth limit of the raw data (Figure 1.5), the lost information from the wings is crucial for accuracy of the pulse recovered by the FROG algorithm. For example, while the raw data indicates a pulse near the transform limit in Figure 1.4, we see in Figure 1.6 that the FROG algorithm-recovered pulse in the time domain (in red) appears elongated relative to the theoretical transform-limited duration (in blue) for the measured bandwidth.

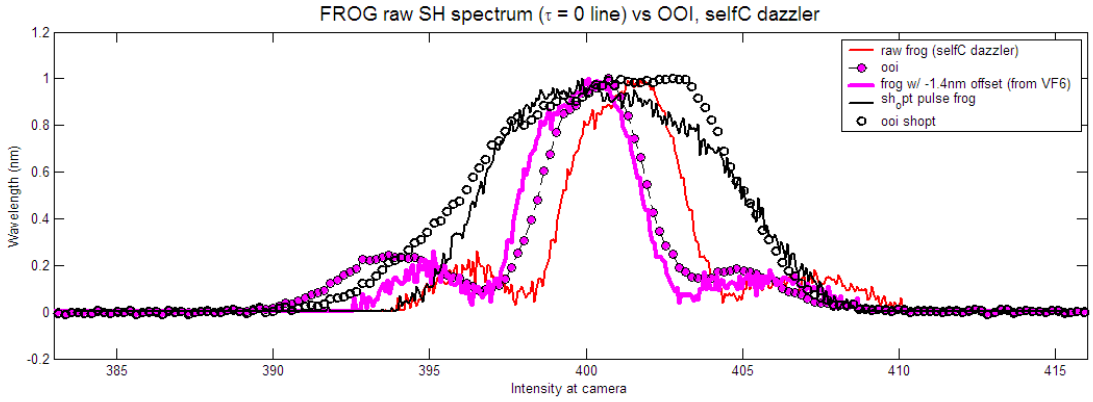

Figure 1.5 Measurement bandwidth added by the adaptive learning algorithm-found pulse (black) relative to the unshaped (magenta) pulse. Solid lines indicate the spectrum extracted from a FROG measurement of the programmed pulse. Agreement with an ocean optics spectrometer (circles), confirms that phase matching issues are not significantly clipping spectral bandwidth. Note that the FROG measurements are shifted to compensate the offset in the dial setting of the Grenouille.

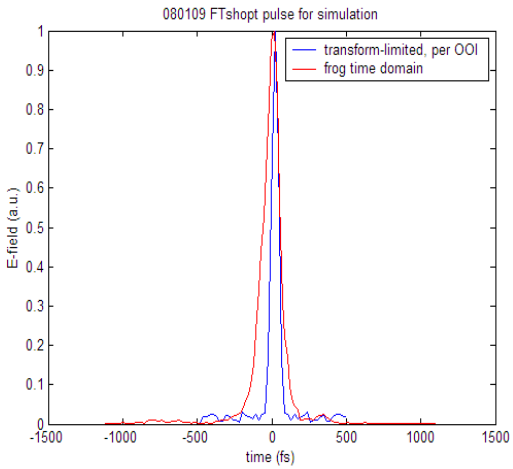

Figure 1.6 Time-domain comparison of FROG-recovered pulse (red) versus theoretical transform-limited pulse calculated with the spectrometer-measured bandwidth (blue).

3.5 Simulated versus measured FRAC

The validity of our acousto-optic implementation of the Fourier transform time-domain FRAC measurement is confirmed by a direct comparison with theory. Figure 1.7 shows the overlay of SHG data (red) for various delay-points with the theoretical calculation (blue), assuming the FROG-recovered pulse amplitude and phase (Figure 1.6). Figure 1.8 shows the same data set, assuming instead for simulation the transform-limited pulse. From this data, we are able to conclude that the actual pulse must be somewhat longer in time than the transform-limit, but not so much as the inaccurate FROG recovery suggests. We also note some noise in the real measurement not predicted by the simulations.

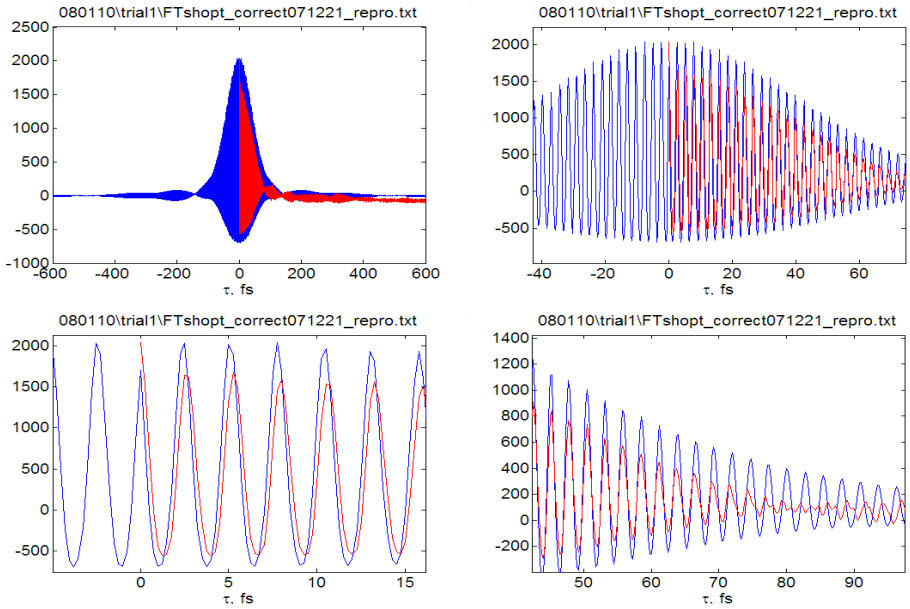

Figure 1.7 Real SHG signal for various pairs of delayed pulses programmed into the Dazzler (red) versus the simulated FRAC with the unshaped pulse form recovered by an SHG-FROG measurement (blue).

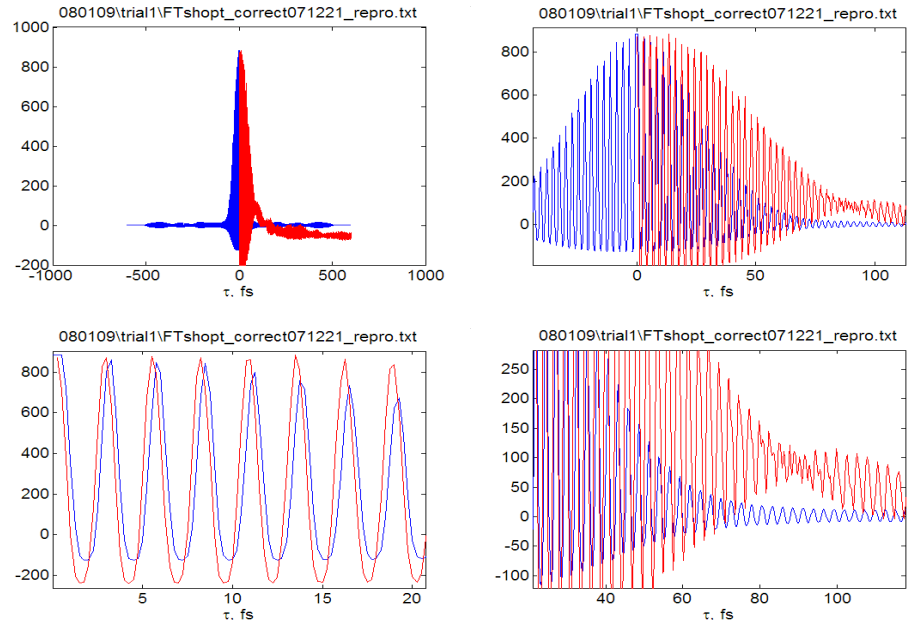

Figure 1.8 Same time-domain data as in Figure 1.7 (red) versus the simulated FRAC with the theoretical transform-limited pulse from the spectrometer-measured fundamental bandwidth (blue).

4. Dissertation Overview

This dissertation work began with a demonstration of the power of multiphoton excitation for flow cytometry[1,59] (Chapter 2). In conjunction, we also devoted some attention to choosing the best fluorescent probes to enhance the detection capabilities. Our next step was to build an extended cavity laser at a reduced repetition to achieve higher energy pulses without increasing average power, and this showed significant improvement in sensitivity. Deeper investigation gave insight into the nature of detection in a flow system with multiphoton excitation, and simple geometrical models explained some counterintuitive results[60] (Chapter 3).

Though achieving stable operation of the custom-built extended cavity laser to directly compare it to a commercial standard system was greatly satisfying, in truth this modification falls far short of the precise manipulation of laser pulses that the relentless advance of technology has enabled. With the advent of rapidly switchable, programmable light modulators, research in molecularly-tailored pulse shaping has advanced the understanding of light-matter interactions and molecular coherences. The term "coherent control" has become an umbrella term for many studies of tailored light pulses, and indeed numerous theoretical and experimental investigations support matched electronic wave packet coherences with electric fields at optical frequency as a mechanism for molecular specificity. With years of research into the pure science of laser pulse shaping, the time is ripe for practical applications of this maturing technology. We wondered, through allegiance with this field, could we eventually achieve molecular specificity in multiphoton flow cytometry and perhaps advance other biomedical research methods? Chapter 4 presents control of the fluorescence of dyes at low and high fields[61] with an adaptive learning algorithm.

As we continued to advance the experimental methods and adaptive learning algorithm, we achieved superior convergence to optimal pulses with molecular specificity. Beyond this, we gained physical insight into the mechanism through a novel acousto-optic Fourier transform measurement of the two-photon excitation cross-sections, concluding that second-harmonic tuning accounts for most of the results. Chapter 5 expands the coherent control studies by describing our attempts to tell apart numerous pairs of common dyes. We also included dyes conjugated to Herceptin or

dendrimers, both of which are very exciting targets for multiphoton cytometry and other biomedical laser applications, given the almost miraculous promise of these macromolecules in biology and medicine. In Chapter 6, we show highly selective excitation of different quantum mechanical systems with similar one-photon absorption properties.[62] Finally, in Chapter 7, we demonstrate excellent control of fluorescence of blue fluorescent protein (BFP), which is a difficult problem that has hitherto frustrated the standard approach. This problem has interested other researchers as well, not only due to the underlying physics, but also due to its biological relevance.

References

1. Tkaczyk ER, Zhong CF, Ye JY, Myc A, Thomas T, Cao Z, Duran-Struuck R, Luker KE, Luker GD, Norris TB and others. In vivo monitoring of multiple circulating cell populations using two-photon flow cytometry. Optics Communications 2008;281(4):888-894.
2. Zhong CF, Tkaczyk ER, Thomas T, Ye JY, Myc A, Bielinska A, Cao Z, Majoros I, Balazs K, Baker JR and others. Quantitative Two-Photon Flow Cytometry – in Vitro and in Vivo. Journal of Biomedical Optics 2008;13(3).
3. Cristofanilli M, Budd GT, Ellis MJ, Stopeck A, Matera J, Miller MC, Reuben JM, Doyle GV, Allard WJ, Terstappen LW and others. Circulating tumor cells, disease progression, and survival in metastatic breast cancer. N Engl J Med 2004;351(8):781-791.
4. Meng S, Tripathy D, Shete S, Ashfaq R, Saboorian H, Haley B, Frenkel E, Euhus D, Leitch M, Osborne C and others. uPAR and HER-2 gene status in individual breast cancer cells from blood and tissues. PNAS 2006;103(46):17361-17365.
5. Meng S, Tripathy D, Frenkel EP, Shete S, Naftalis EZ, Huth JF, Beitsch PD, Leitch M, Hoover S, Euhus D and others. Circulating tumor cells in patients with breast cancer dormancy. Clin Cancer Res 2004;10(24):8152-8162.
6. Mancuso P, Colleoni M, Calleri A, Orlando L, Maisonneuve P, Pruneri G, Agliano A, Goldhirsch A, Shaked Y, Kerbel RS and others. Circulating endothelial-cell kinetics and viability predict survival in breast cancer patients receiving metronomic chemotherapy. Blood 2006;108(2):452-459.
7. Novak J, Georgakoudi I, Wei X, Prossin A, Lin CP. In vivo flow cytometer for real-time detection and quantification of circulating cells. Optics Letters 2004;29:77-79.
8. Zharov V, Galanzha E, Tuchin V. Integrated photothermal flow cytometry in vivo. Journal of Biomedical Optics 2005;10(5).
9. Lee H, Alt C, Pitsillides CM, Puoris'haag M, Lin CP. In vivo imaging flow cytometer. Optics Express 2006;14:7789-7800.
10. Konig K. Multiphoton microscopy in life sciences. J Microsc 2000;200(Pt 2):83-104.
11. Denk W, Svoboda K. Photon upmanship: why multiphoton imaging is more than a gimmick. Neuron 1997;18(3):351-357.
12. Masters B, So P. Antecedents of two-photon excitation laser scanning microscopy. Microscopy Research and Technique 2004;63(1):3-11.
13. Squier J, Muller M. High resolution nonlinear microscopy: A review of sources and methods for achieving optimal imaging. Review of Scientific Instruments 2001;72(7):2855-2867.

14. Zipfel WR, Williams RM, Webb WW. Nonlinear magic: multiphoton microscopy in the biosciences. Nat Biotechnol 2003;21(11):1369-1377.

15. Helmchen F, Denk W. Deep tissue two-photon microscopy. Nature Methods 2005;2(12):932-940.

16. Shapiro HM. Two-photon flow cytometry. Volume 2008: http://www.cyto.purdue.edu/hmarchiv/2004/0273; 2004.

17. Denk W, Strickler J, Webb W. Two-photon laser scanning fluorescence microscopy. Science 1990;248(4951):73-76.

18. Xu C, Webb WW. Measurement of two-photon excitation cross sections of molecular fluorophores with data from 690 to 1050 nm. Journal of the Optical Society of America B Optical Physics 1996;13:481-491.

19. Patterson GH, Piston DW. Photobleaching in two-photon excitation microscopy. Biophys J 2000;78(4):2159-2162.

20. König K, Becker TW, Fischer P, Riemann I, Halbhuber KJ. Pulse-length dependence of cellular response to intense near-infrared laser pulses in multiphoton microscopes. Opt. Lett. 1999;24(2):113-115.

21. Xi P, Andegeko Y, Weisel L, Lozovoy V, Dantus M. Greater signal, increased depth, and less photobleaching in two-photon microscopy with 10 fs pulses. Optics in Life Sciences 2008;281(7):1841-1849.

22. Siegman AE. Lasers. American Journal of Physics 1987;55(9):862.

23. Kawano H, Nabekawa Y, Suda A, Oishi Y, Mizuno H, Miyawaki A, Midorikawa K. Attenuation of photobleaching in two-photon excitation fluorescence from green fluorescent protein with shaped excitation pulses. Biochemical and Biophysical Research Communications 2003;311(3):592-596.

24. Dudovich N, Dayan B, Gallagher, Silberberg Y. Transform-Limited Pulses Are Not Optimal for Resonant Multiphoton Transitions. Physical Review Letters 2001;86(1):47.

25. Laiho L, Pelet S, Hancewicz T, Kaplan P, So P. Two-photon 3-D mapping of ex vivo human skin endogenous fluorescence species based on fluorescence emission spectra. Journal of Biomedical Optics 2005;10(2).

26. Lozovoy VV, Pastirk I, Walowicz KA, Dantus M. Multiphoton intrapulse interference. II. Control of two- and three-photon laser induced fluorescence with shaped pulses. J. Chem. Phys. 2003;118:3187-3196.

27. Pollok BA, Heim R. Using GFP in FRET-based applications. Trends Cell Biol 1999;9(2):57-60.

28. Mauring K, Deich J, Rosell FI, McAnaney TB, Moerner WE, Boxer SG. Enhancement of the fluorescence of the blue fluorescent proteins by high pressure or low temperature. J Phys Chem B Condens Matter Mater Surf Interfaces Biophys 2005;109(26):12976-12981.

29. Kummer A, Wiehler J, SchÃ¼ttrigkeit T, Berger B, Steipe B, Michel-Beyerle M. Picosecond Time-Resolved Fluorescence from Blue-Emitting Chromophore Variants Y66F and Y66H of the Green Fluorescent Protein. ChemBioChem 2002;3(7):659-663.

30. Mena M, Treynor T, Mayo S, Daugherty P. Blue fluorescent proteins with enhanced brightness and photostability from a structurally targeted library. Nat Biotech 2006;24(12):1569-1571.

31. Voityuk A, Michel-Beyerle M-E, Rosch N. Structure and rotation barriers for ground and excited states of the isolated chromophore of the green fluorescent protein. Chemical Physics Letters 1998;296(3-4):269-276.

32. Weber W, Helms V, McCammon JA, Langhoff PW. Shedding light on the dark and weakly fluorescent states of green fluorescent proteins. Proc Natl Acad Sci U S A 1999;96(11):6177-6182.

33. Weber W, Helms V, McCammon A, Langhoff P. Shedding Light on the Dark and Weakly Fluorescent States of Green Fluorescent Proteins. Proceedings of the National Academy of Sciences of the United States of America 1999;96(11):6177-6182.

34. Toniolo A, Olsen S, Manohar L, MartÃ-nez TJ. Conical intersection dynamics in solution: the chromophore of Green Fluorescent Protein. Faraday Discuss 2004;127:149-163.

35. Hasegawa J-Y, Fujimoto K, Swerts B, Miyahara T, Nakatsuji H. Excited states of GFP chromophore and active site studied by the SAC-CI method: Effect of protein-environment and mutations. Journal of Computational Chemistry 2007;28(15):2443-2452.

36. Mauring K, Krasnenko V, Miller S. Photophysics of the blue fluorescent protein. Luminescence and Optical Spectroscopy of Condensed Matter - Proceedings of the 2005 International Conference on Luminescence and Optical Spectroscopy of Condensed Matter, 2005 International Conference on Luminescence and Optical Spectroscopy of Condensed Matter 2007;122-123:291-293.

37. Nagy A, Prokhorenko V, Miller R. Do we live in a quantum world? Advances in multidimensional coherent spectroscopies refine our understanding of quantum coherences and structural dynamics of biological systems. Carbohydrates and glycoconjugates / Biophysical methods 2006;16(5):654-663.

38. Prokhorenko VI, Nagy AM, Waschuk SA, Brown LS, Birge RR, Miller RJ. Coherent control of retinal isomerization in bacteriorhodopsin. Science 2006;313(5791):1257-1261.

39. Cao J, Che J, Wilson KR. Intrapulse Dynamical Effects in Multiphoton Processes: Theoretical Analysis. J. Phys. Chem. A 1998;102(23):4284-4290.

40. Tannor DJ, Kosloff R, Rice SA. Coherent pulse sequence induced control of selectivity of reactions: Exact quantum mechanical calculations. J. Chem. Phys. 1986;85:5805-5820.

41. Bardeen CJ, Wang Q, Shank CV. Femtosecond Chirped Pulse Excitation of Vibrational Wave Packets in LD690 and Bacteriorhodopsin. J. Phys. Chem. A 1998;102(17):2759-2766.

42. Bardeen CJ, Yakovlev VV, Squier JA, Wilson KR. Quantum Control of Population Transfer in Green Fluorescent Protein by Using Chirped Femtosecond Pulses. J. Am. Chem. Soc. 1998;120(50):13023-13027.

43. Blanchet Vr, Nicole Cl, Bouchene M-A, Girard B. Temporal Coherent Control in Two-Photon Transitions: From Optical Interferences to Quantum Interferences. Physical Review Letters 1997;78:2716.

44. Meshulach D, Silberberg Y. Coherent quantum control of multiphoton transitions by shaped ultrashort optical pulses. Phys. Rev. A 1999;60:1287-1292.

45. Brixner T, Damrauer NH, Kiefer B, Gerber G. Liquid-phase adaptive femtosecond quantum control: Removing intrinsic intensity dependencies. The Journal of Chemical Physics 2003;118(8):3692-3701.

46. Weiner A. Effect of group velocity mismatch on the measurement of ultrashort optical pulses via second harmonic generation. Quantum Electronics, IEEE Journal of 1983;19(8):1276-1283.

47. Ogilvie J, Kubarych K, Alexandrou A, Joffre M. Fourier transform measurement of two-photon excitation spectra: applications to microscopy and optimal control. Opt. Lett. 2005;30(8):911-913.

48. Walowicz KA, Pastirk I, Lozovoy VV, Dantus M. Multiphoton Intrapulse Interference. 1. Control of Multiphoton Processes in Condensed Phases. J. Phys. Chem. A 2002;106(41):9369-9373.

49. Lozovoy V, Pastirk I, Dantus M. Multiphoton intrapulse interference.?IV.?Ultrashort laserpulse spectral phase characterization and compensation. Opt. Lett. 2004;29(7):775-777.

50. Broers B, van L, Noordam LD. Large interference effects of small chirp observed in two-photon absorption. Optics Communications 1992;91:57-61.

51. Brixner T, Damrauer NH, Niklaus P, Gerber G. Photoselective adaptive femtosecond quantum control in the liquid phase. Nature 2001;414(6859):57-60.

52. Bellini M, Bartoli A, HÃ¤nsch TW. Two-photon Fourier spectroscopy with femtosecond light pulses. Opt. Lett. 1997;22(8):540-542.

53. Trebino R. Frequency-Resolved Optical Gating: The Measurement of Ultrashort Laser Pulses; 2002.

54. Weinacht TC, Ahn J, Bucksbaum PH. Controlling the shape of a quantum wavefunction. Nature 1999;397:233.

55. Bracewell R. The Fourier Transform and Its Applications. American journal of physics 1966;34(8):712.

56. Bracewell R. The Fourier Transform & Its Applications: {McGraw-Hill Science/Engineering/Math}; 1999.

57. Naganuma K, Mogi K, Yamada H. General method for ultrashort light pulse chirp measurement. Quantum Electronics, IEEE Journal of 1989;25(6):1225-1233.

58. Kane D. conversation. 2008. p "You've hit the limits of the device and the code".

59. Tkaczyk ER, Zhong CF, Ye JY, Katnik S, Myc A, Thomas T, Luker KE, Luker GD, Baker JR, Norris TB. Two-photon, two-color in vivo flow cytometry to noninvasively monitor multiple circulating cell lines. 2007.

60. Tkaczyk ER, Ye JY, Myc A, Katnik S, Luker KE, Luker GD, Baker JR, Norris TB. In Vivo Extended Cavity Laser Enhanced Two-Photon Flow Cytometry. Journal of Biomedical Optics 2008;13(5).

61. Tkaczyk ER, Mignot A, Ye JY, Majoros I, Baker JR, Norris TB. Increasing two-photon fluorescence signals by coherent control. In: Periasamy A, So PTC, editors; 2006. p 165-174.

62. Tkaczyk ER, Tkaczyk AH, Mauring K, Ye JY, Baker JR, Norris TB. Quantitative differentiation of dyes with overlapping one-photon spectra by femtosecond pulse shaping. Nature 2008;submitted.

CHAPTER 2
TWO-PHOTON, TWO-COLOR *IN VIVO* FLOW CYTOMETRY TO NONINVASIVELY MONITOR MULTIPLE CIRCULATING CELL LINES

Abstract. We have developed a new two-photon system for *in vivo* flow cytometry, thereby allowing us to simultaneously quantify different circulating populations in a single animal. The instrument was able to resolve minute-by-minute depletion dynamics of injected fluorescent microspheres at finer time scales than conventional flow cytometry. Also observed were the circulation dynamics of human MCF-7 and MDA-MB-435 breast cancer cells, which have low and high metastatic potential, respectively. After co-injection of both cell types into mice, markedly greater numbers of MCF-7 cells were present in the circulation at early time points. While low metastatic MCF-7 cells were cleared from the vascular system within 24 hours, detectable numbers of metastatic MDA-MB-435 cells in the circulation remained constant over time. We also non-invasively monitored a population of labeled, circulating red blood cells for more than two weeks, demonstrating that this technique can also quantify the dynamics of abundant cells in the vascular system for prolonged periods of time. When we replace the commercial (80-MHz) NIR excitation laser with a reduced-repetition-rate (20-MHz) mode-locked oscillator, the signal is enhanced four-fold, enabling superior detection in blood of cell lines expressing fluorescent proteins tdTomato and mPlum (cross-labeled with DiI and DiD). Detection sensitivity versus incident laser power is understood in terms of detected event photon count distribution, which can be predicted with simple fluorophore distribution assumptions. The technique of two-color, two-photon flow cytometry greatly enhances the capabilities of *ex vivo* flow cytometry to investigate dynamics of circulating cells in cancer and other important diseases.

1. Introduction

While conventional *ex vivo* flow cytometry is a powerful technique for quantitative characterization of single cells, the possibility of performing *in vivo* flow cytometry offers unique opportunities for studying biological events. *In vivo* labeling and detection of cells preserves biologically important signals provided by other circulating cells and vascular endothelium. Furthermore, *ex vivo* flow cytometry eliminates potential adverse effects on cell integrity and function caused by isolation of cells for *ex vivo* analyses. Due to its noninvasive nature, *in vivo* flow cytometry enables the dynamics of circulating cells to be analyzed repetitively in a single animal, thereby providing temporal resolution that cannot be achieved with conventional flow cytometry. Monitoring the same animal over time also allows rare populations of cells to be detected and analyzed. Particularly, the ability to distinguish distinct but infrequent cells in the same animal based on acquisition of multiple channels of fluorescent data is crucial to overcome experimental variability caused by differences in hemodynamics. By allowing multiple fluorophores to be detected simultaneously, we expect two-color, two-photon flow cytometry to greatly advance our ability to investigate biologic processes such as trafficking of immune or tumor cells in the vascular system.

Recent developments in non-invasive fluorescence imaging, such as whole body imaging[1] and fluorescence molecular tomography[2,3] have limited capability to obtain quantitative information on individual cells. Other techniques, such as confocal and two-photon microscopy, are able to image fluorescently labeled cells *in vivo,* but it is difficult to use these methods to quantify specific populations of cells in the blood stream. Although enumeration of circulating cells *in vivo* has been achieved with confocal detection using single-photon excitation[4], the two-photon flow cytometry technique described here offers several advantages for *in vivo* cytometry measurements. To perform multiple color measurements using confocal one-photon excitation requires multiple lasers to excite different dyes that have distinct one-photon absorption spectra. The optical design of such a system becomes complex because of the need to align multiple laser beams to a precise focal point, and the overlap between excitation and emission spectra of different fluorophores presents a technical challenge for discriminating individual signals. By comparison, a single femtosecond near infrared

(NIR) laser can be used to simultaneously excite multiple fluorescent dyes via two-photon transitions, which permits several cell populations labeled with different fluorophores to be monitored simultaneously. In addition, the large separation between NIR excitation and emission wavelengths makes it easier to attenuate scattered excitation light while collecting the entire fluorescence spectrum with high efficiency[5]. Thus, using a NIR femtosecond laser as the excitation source for cytometry allows multi-color measurements with simplified optical filtering and fluorescence background reduction.

In this work, we demonstrate that two-photon excitation enables flow cytometry under conditions of nonuniform flow, such as *in vivo* blood flow. When a train of femtosecond laser pulses from a mode-locked Ti:Sapphire oscillator is focused into a blood vessel beneath the skin, fluorescent tags in circulating cells are excited via two-photon transitions. The nonlinear excitation defines a localized excitation volume within the blood vessel to allow only one cell to be excited at a time. This technique makes it possible to detect and monitor circulating fluorescent microspheres or fluorescently labeled cells injected through the tail vein of living mice. Importantly, two-photon excitation and two-channel detection of fluorescence allowed us to quantify dynamics of two separate populations of breast cancer cells, each of which was labeled with quantum dots that emit at distinct wavelengths. Compared with existing technologies for *ex vivo* and *in vivo* flow cytometry measurements, the *in vivo* two-photon flow cytometer enables enhanced real-time monitoring of distinct populations of circulating cells in the integrated physiology of an intact animal.

2. Materials and Methods

2.1 Two-photon flow cytometer

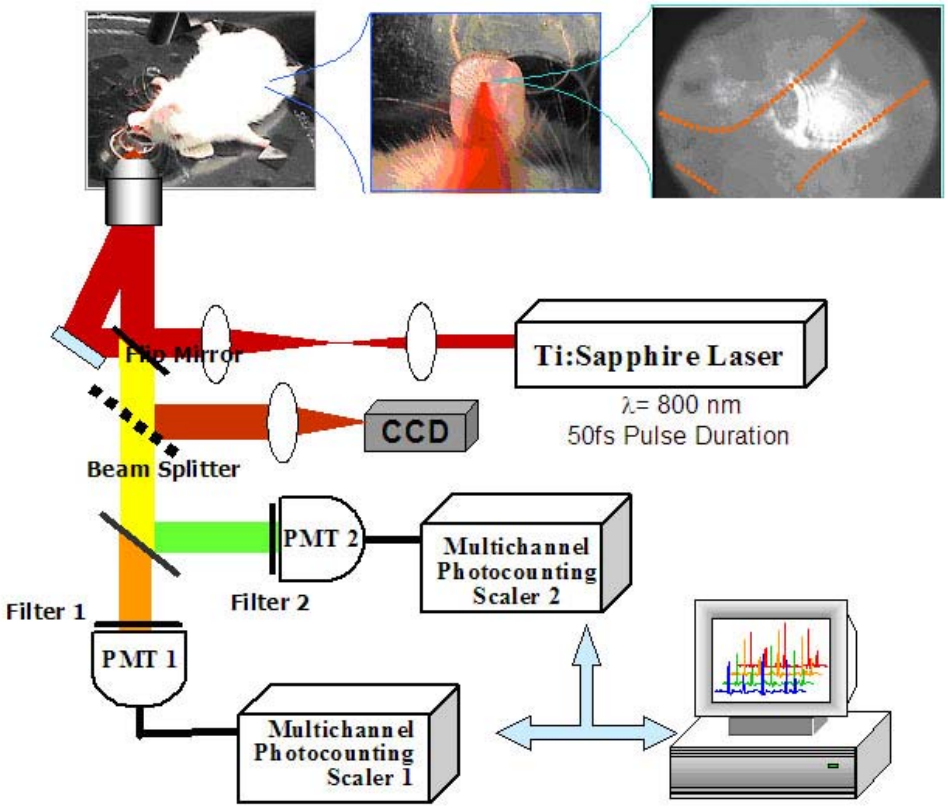

Figure 2.1 Experimental setup for in vivo measurements with mouse. Mouse is replaced by a 100 μm (edge width) square glass capillary for ex vivo experiments.

The two-photon flow cytometry apparatus (Figure 2.1) used a Ti:Sapphire laser (Mira Coherent), which generates 50-fs pulses at 800nm with a repetition rate of 76-MHz. The femtosecond NIR laser beam was focused into the 100 μm wide square glass capillary or a blood vessel of the mouse ear with a long working-distance Olympus 40x objective. A dichroic mirror was used to reflect the laser into the microscope objective while transmitting the collected fluorescence. As a cell stained with fluorescent dye passed through the laser focal volume, the two-photon excited fluorescence was collected back through the same microscope objective. Beam splitters and bandpass filters were used to separate the fluorescence from different dyes into two channels, which were detected with two photo-multiplier tubes (PMT Hamamatsu HC7421-40) and recorded

with two multi-channel photon counting scalers (MCS Stanford Research SR430). The signals were sent to a computer for data analysis.

For *in vivo* measurements, a custom-made heated stage was used to hold anesthetized mice. An 8 mm diameter hole was drilled at the center of the stage, on top of which a glass slide was placed. The vasculature and blood flow of the mouse ear were visualized with a CCD camera from transmitted light of a fiber optic illuminator (EW-41500-50, Cole-Parmer Instrument Company, Vernon Hills, Illinois).

A Matlab (The Mathworks, Inc. Natick, MA) program was used to extract fluorescent peaks above the background noise level from the multi-channel photon counting scaler (MCS) trace signals (Figure 2.2). The background threshold in a detection channel was set above the maximum signal level from control traces. The program scanned the trace signals for fluorescent peaks above the threshold. Once a peak is located, the peak characteristics, such as height (maximum fluorescent signal within the peak), width (number of consecutive bins above the background threshold) and location (the index of the maximum bin) were stored. For two-channel measurements, the data from each channel were analyzed separately. A double-peak event is treated as a single event if the fluorescent signal between the two peaks does not fall below the background threshold value.

2.2 The *in vivo* flow cytometry procedure

Five to six weeks old, specific-pathogen-free female NU/NU CD-1 and CD-1 mice were purchased from Charles River Laboratories (Portage, Michigan) and housed in a specific pathogen-free animal facility at the University of Michigan Medical Center in accordance with the regulations of the University's Committee on the Use and Care of Animals as well as with federal guidelines, including the principles of Laboratory Animal Care.

To conduct *in vivo* two-photon flow cytometry measurements, mice were anesthetized by inhalation of isoflurane. For optical detection, the mice were placed on a heated stage with the left ear on the glass slide window. The femtosecond NIR laser beam was focused into the mouse ear with the objective from below. Microscope immersion oil was placed between the mouse ear and the glass slide to maintain the position of the ear during the cytometry measurement. Switching off the short pass filter

in the fluorescence collection optical path enabled the back-scattered light from the femtosecond NIR laser beam to be visualized on the CCD camera to align the excitation beam with the blood vessel. A blood vessel roughly 50 μm in diameter with ample blood flow was selected for cytometry measurement. Before injection of the solution of fluorescent-dye-labeled microspheres or cells, the background signals in both short wavelength channel (S-channel) and long wavelength channel (L-channel) were recorded as a control. The laser power used was below 20 mW at the focus, and no photodamage to the ear of the mice was observed during or after the experiments. To perform *in vivo* cytometry measurements, solutions containing fluorescent microspheres or fluorescence labeled cells were injected through the tail vein. Typically within 5 minutes following the injection, the two-channel fluorescence signals from a blood vessel were recorded.

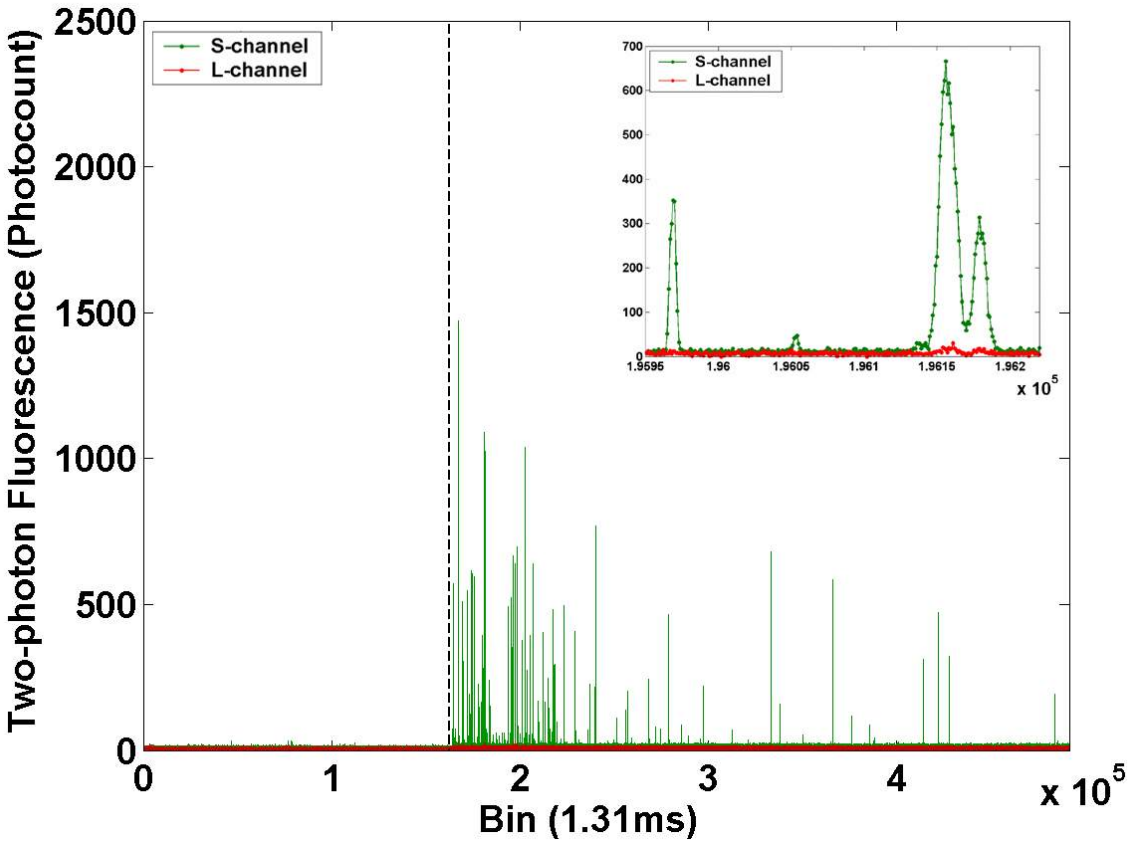

Figure 2.2 Two-channel raw data from the two-channel two-photon flow cytometer. Short wavelength channel (S-channel green) and long wavelength channel (L-channel red) traces from an ear blood vessel of a CD-1 mouse injected with microspheres at time zero (dashed line). The control traces are shown to the left of the dashed line. The data is essentially a histogram showing the number of photons counted by the multichannel scaler in each 1.31 ms bin on the x-axis.

2.3 Flow cytometry of fluorescent microspheres

Before injection of fluorescent microspheres or DeepRed-labeled splenocytes, the background signals in both short wavelength channel (S-channel) and long wavelength channel (L-channel) were recorded with the femtosecond NIR laser beam focused within the mouse ear. The measured background control traces before each injection are shown to the left of the dashed line in Figure 2.2. The thresholds were adjusted so that no peaks existed in the control traces. Two-micron diameter, yellow-green (Ex505/Em515) fluorescent microspheres (Molecular Probes, Inc. Eugene, OR) were washed, resuspended in 200 µl PBS (total number of beads 2.3 x 10^9), and injected via tail vein to CD-1 mice. The two-channel fluorescence signals continued to be recorded for ten or twenty consecutive minutes after the injection.

A parallel experiment was performed with multiple animals for conventional flow cytometry analysis. Blood samples were obtained either from the tail vein or from euthanized premorbid animals by cardiac puncture at different time intervals during the course of the experiment. Blood was collected to heparinized tubes and diluted 10 times with PBS prior to flow cytometry analysis. Samples were acquired on a Coulter EPICS-XL MCL Beckman-Coulter flow cytometer, and data were analyzed using Expo32 software (Beckman-Coulter, Miami, FL).

2.4 *In vivo* flow cytometry of DiD labeled red blood cells

Blood (25-50 µL) was collected from mice by retro-orbital puncture, and 12 µL were centrifuged to remove serum and the buffy coat as described above. Cells were washed once with PBS and then stained with 10 µL 1,1'-Dioctadecyl-3,3,3',3'-tetramethyllindodicarbocyanine perchlorate (DiD, a lipophilic dye that labels membrane bilayers) (Vybrant DiD, Labeling Solution, Invitrogen) in 100 µL PBS for 30 minutes at 37ºC. Cells were washed once in PBS to remove unincorporated DiD and then resuspended in 100 µL sterile 0.9% NaCl. Samples (containing approximately 1 x 10^7 stained RBCs) were injected intravenously into a female NU/J Foxn1nu mouse via a tail vein for *in vivo* flow cytometry experiments. The long channel fluorescence signal was recorded at roughly the same vessel location several times over the next several weeks (0

minutes, 20 minutes, 5 hours, 24 hours, 48 hours, 4 days, and 17 days after injection). The frequency was calculated as the number of peaks in the L-channel within 214 seconds.

For measurements beginning on day 4, the location in the vessel was optimized manually in real time to maximize the amplitude and frequency of the detected events. This was possible since the large number of events enabled a frequency count every few seconds between manual adjustments of the objective. It is noteworthy that this improvement is only possible when the number of detected events is at least several per second, and thus cannot be used in one-color analysis of metastatic cancer cells or other rare populations of cells in the circulation.

2.5 Conventional flow cytometry of red blood cells

Blood samples (50-100 μL) were collected from mice via retro-orbital puncture using heparinized capillary tubes. Blood was transferred to heparinized microfuge tubes and centrifuged for 1 min at 10,000 RPM. Serum and the buffy coat were removed, and the cell pellet was resuspended in 750 μL FACS buffer (PBS with 0.1% sodium azide and 1% heat-inactivated fetal calf serum). Flow cytometry was performed on a FACS Calibur System (BD Biosciences), and data were analyzed with CellQuest software.

2.6 *In vivo* flow cytometry of two cell lines labeled with two color quantum dots

To simultaneously monitor circulating MCF-7 and MDA-MB-435 in the same mouse *in vivo*, cells were labeled with 15 nM or 7.5 nM of Qtracker quantum dots (Invitrogen) that emit at 585 nm (Qdot585) or 655 nm (Qdot655), respectively. Quantum dots were mixed with an equal volume of transfection reagent provided with the Qtracker kit according to the manufacturer's protocol. Breast cancer cells were seeded at 4×10^6 cells/60 mm dish (MDA-MB-435) or 3×10^6 cells per dish (MCF-7) 6 hours prior to labeling with quantum dots mixed with 200 μL of cell culture medium. Cells were rocked every 15 minutes for 1 hour to distribute the quantum dots, and cell culture medium then was added to a final volume of 4 ml to continue labeling overnight. Cells were treated with 2 mM EDTA to release them from the culture dish, washed with PBS, and resuspended in sterile 0.9% saline for injection. Because initial studies with these cells suggested that fewer MDA-MB-435 cells could be detected immediately after

injection, we injected twice as many of these cells: 1 x 10^6 435 cells were coinjected with 0.5 x 10^6 MCF-7 cells in 125 μL PBS. The two-channel fluorescence signals were recorded immediately after each injection and repeated at the same vessel location roughly 2 hours and 1 day after the initial injection.

2.7 Cell preparation for fluorescent protein measurements

We transiently transfected HEK 293T cells with fluorescent proteins tdTomato, DSRed, T4 (a variant of DSRed), or mPlum[6,7,8]. Transfections were performed with Fugene 6 (Invitrogen) according to the manufacturer's directions. We also used MCA-207 cells stably transfected with GFP. Twenty-four hours after transient transfection, cells were labeled with DiI or DiD (Vybrant cell labeling, Invitrogen) according to the manufacturer's protocol. Cells were washed once in PBS to remove unincorporated DiD and then resuspended in 100 μL PBS or heparinized whole blood. Blood samples were diluted 1:3 in PBS with 10 mM EDTA.

Table 2.1 Excitation and emission peaks (nm) and distributions of examined fluorophores for two-photon flow cytometry. Variants of RFP are marked in red.

Fluorophore	Ex	Em	Distribution	Comment
GFP	488	510	cytoplasm and nucleus	fluorescent protein
DiI	549	565	membrane	dye
tdTomato	554	581	cytoplasm	fluorescent protein
DSRed RFP	558	583	cytoplasm and nucleus	fluorescent protein
T4	555	586	cytoplasm and nucleus	fluorescent protein
CellTracker Red CMTPX (CT)	577	602	cytoplasm	dye
mPlum	590	649	cytoplasm and nucleus	fluorescent protein
DiD	644	665	membrane	dye

2.8 *Ex vivo* two-photon flow cytometry measurement

Fluorescent proteins expressed after transfection or fluorescent dyes added to cells are summarized in Table 1 and plotted on a two-photon fluorescence spectrum of human blood in Figure 2.3.

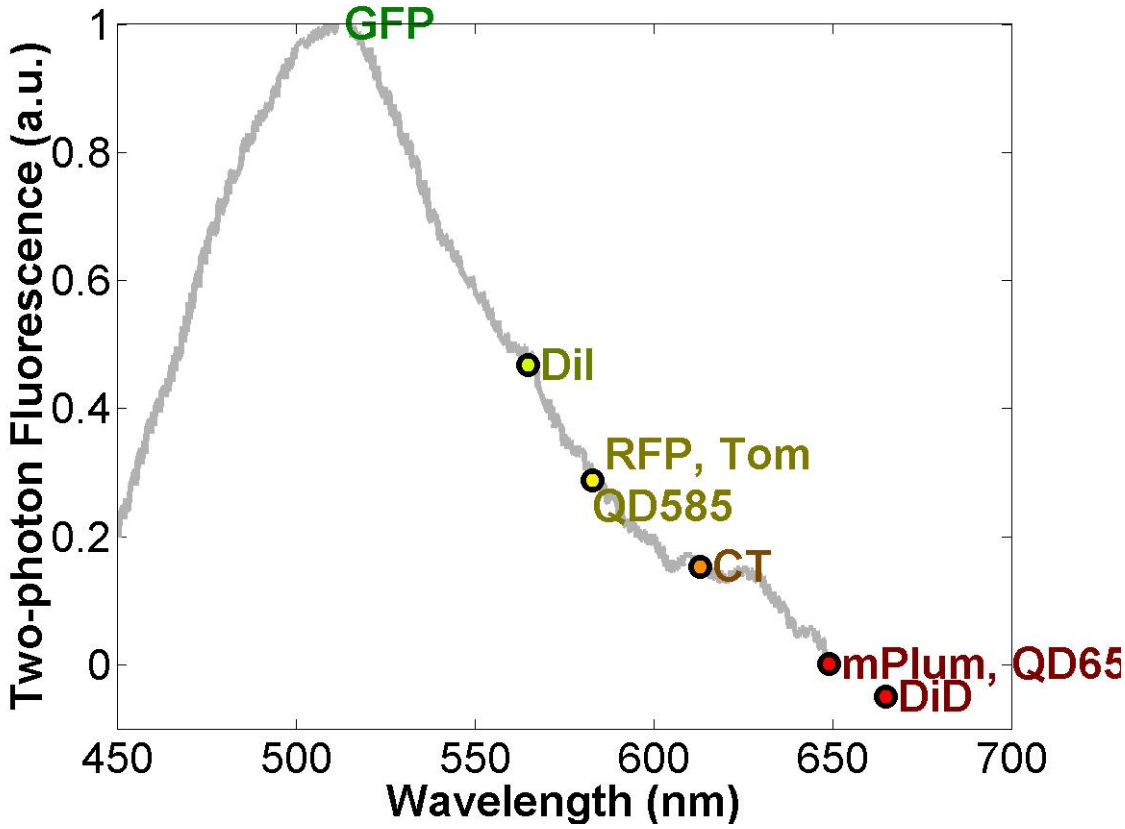

Figure 2.3 Blood autofluorescence spectrum with experimental fluorophores locations marked (T3 and T4 are RFPs, Q represents quantum dots 655).

2.9 Extended cavity laser source

Because the signal levels are generally limited by the average power that can be delivered at focus without damage, we investigated signal improvement with an extended cavity laser[9] (XTND). This home-built laser consists of a Ti:Sapphire crystal optically pumped by a solid-state 532 nm diode laser (Coherent, Verde). A fold mirror routes the beam for three round-trip passes between two large curved multi-pass (MP) mirrors

before the output coupler, achieving a 20 MHz pulse repetition rate and 780 nm center wavelength. This laser delivers a higher peak power for a fixed average power.

For experiments comparing the two lasers, the commercial system (Mira) was tuned to 780 nm emission, and switching between laser sources was accomplished with a flip mirror. Immediately after the flip mirror, before the cytometry system, 3% of the incident laser light is sent via a beamsplitter to a digital power meter for a reference power reading, corresponding to about $1/10^{th}$ of the NIR power at the focal point of the objective due to approximately 30% NIR loss in the objective.

2.10 Calculation of anticipated photocount distributions

In order to understand the histograms (probability distribution functions) of detected event signal strengths, a mathematical model was constructed with simplified geometrical spatial distributions of fluorophores in an idealized spherical cell (radius 10 μm). A solid sphere was used to approximate cytosolic fluorophores (such as GFP), whereas a spherical shell was employed for membrane-bound dyes (DiI, DiD). Gaussian beam propagation was assumed with a laser spot size measured from a calibrated CCD image (measured at 2 μm $1/e^2$ radius w). For each possible origin in the capillary of the idealized cell, the total anticipated signal was calculated to yield a predicted histogram. Further details of the calculation will be published elsewhere[11].

2.11 Trastuzumab targeting.

G5 PAMAM dendrimers conjugated with trastuzumab, a humanized monoclonal antibody to Her2, and 6-Tamra as described previously[10]. SKBR-3 human breast cancer cells, which overexpress Her2, were incubated with 5 ng/μL of Her2-conjugated dendrimer or control dendrimer for 30 minutes on ice. Cells were washed twice with PBS and then used for two-photon flow cytometry.

3. Results and Discussion

3.1 Flow cytometry of fluorescent microspheres

Following intravenous injection of microspheres into CD-1 mice, large fluorescence peaks were detected only in the short wavelength channel, less than 30 seconds after tail vein injection. The frequency dropped to less than 10% within the first 10 to 20 minutes. No fluorescent microspheres were observed at the same location in the mouse ear 2 hours and 1 day after the initial injection. A conventional flow cytometry experiment confirmed that these synthetic microspheres cleared rapidly from the circulation and were not detectable approximately 24 hours after injection. The depletion rate in the first 10 minutes after injection obtained by *in vivo* flow cytometry is larger than the rate over 1.5 hours obtained by *ex vivo* flow cytometry analysis. The difference in depletion rates from *in vivo* and *ex vivo* measurements could be attributed to the different time scales in the depletion process. It could also be the result of systematic error in the *ex vivo* method introduced by the significant delay between blood withdrawal and flow cytometry analysis. In addition, sampling a peripheral artery for *in vivo* flow cytometry versus a tail vein for conventional flow cytometry could contribute to differences in rates of depletion.

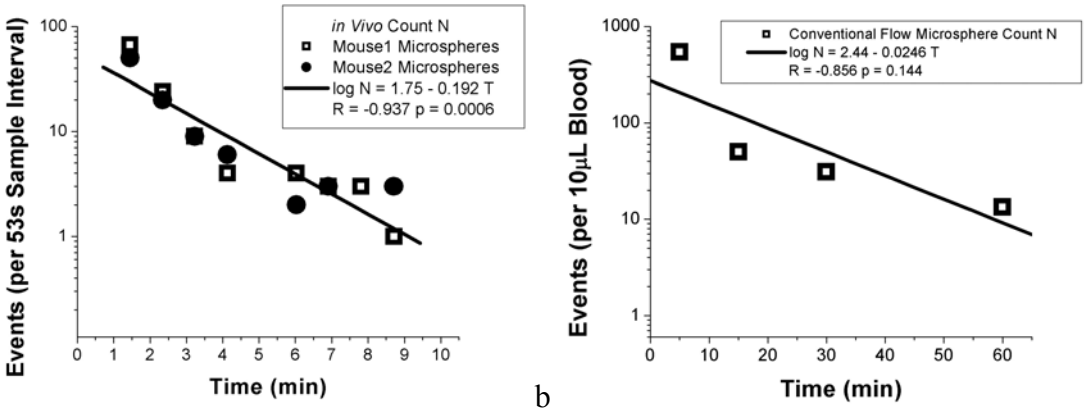

Figure 2.4 Depletion dynamics of circulating fluorescent microspheres. (a) Enumerated *in vivo* with two-photon flow cytometry. Number of detected events (log scale) are plotted over ten minutes after the injection at time 0. (b) Dynamics of microspheres by conventional *ex vivo* flow cytometry.

A similar experiment was performed with injection of splenocytes labeled for detection in the long channel.[11] Overall, these initial studies establish the feasibility of using the two-photon flow cytometer to detect fluorescence in two different detection channels.

3.2 Monitoring of circulating red blood cells *in vivo* for extended periods of time with single cell resolution

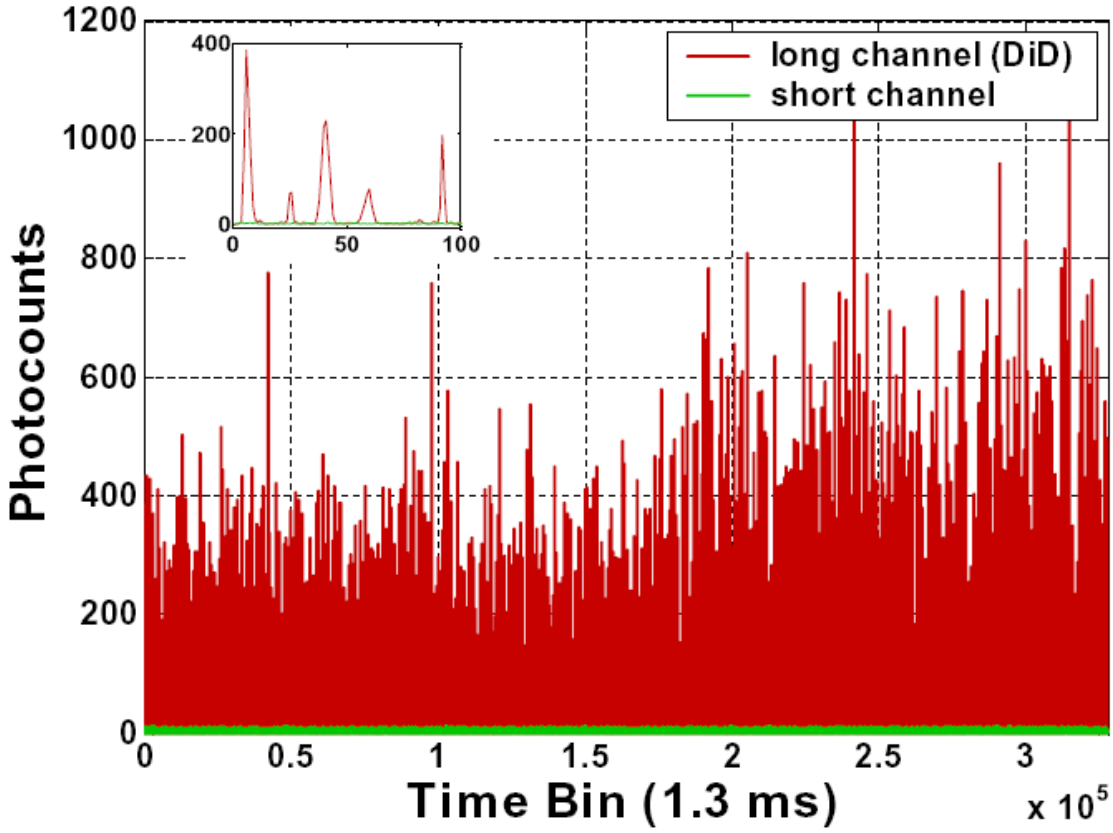

Figure 2.5 Two-channel counts of red blood cells with the two-photon flow cytometer. Short wavelength channel ("S-channel," green line) and long wavelength channel ("L-channel," red line) traces in a mouse injected with DiD-labeled red blood cells. The data is shows the number of photons counted by the multichannel scaler in each 1.31 ms bin on the x-axis. Detail of individual fluorescent peaks are shown in the inset.

To establish that the two-photon flow cytometer could monitor an abundant population of cells for prolonged periods of time, we interrogated red blood cells (RBC) in the circulation of living mice over 17 days. RBC were labeled with the membrane dye 1,1'-Dioctadecyl-3,3,3',3'-tetramethyllindodicarbocyanine perchlorate (DiD) and injected intravenously into nude mice. A representative raw data trace is shown in Figure 2.5, demonstrating the ability to count thousands of cells in a short time period, but at the

same time, resolve them on a single-cell level (inset). Numbers of RBC in repeated measurements were highly variable, despite focusing the laser at the same artery in the ear (Figure 2.6). It was observed that the operator could significantly increase the number of detected events (and therefore sampled volume) by manually adjusting the laser focus during the course of data acquisition, presumably to the maximum flow position in the artery. *In vivo* data for circulating RBC were validated with conventional flow cytometry *ex vivo* on blood drawn on day 18. According to conventional flow, 4.40 % of 1.5 million blood cells counted were labeled with DiD. No labeled cells were detected by either conventional or two-photon flow cytometry 1.5 months after injection, which could be the result of clearance of cells from the circulation or instability of the dye for this period of time in blood.

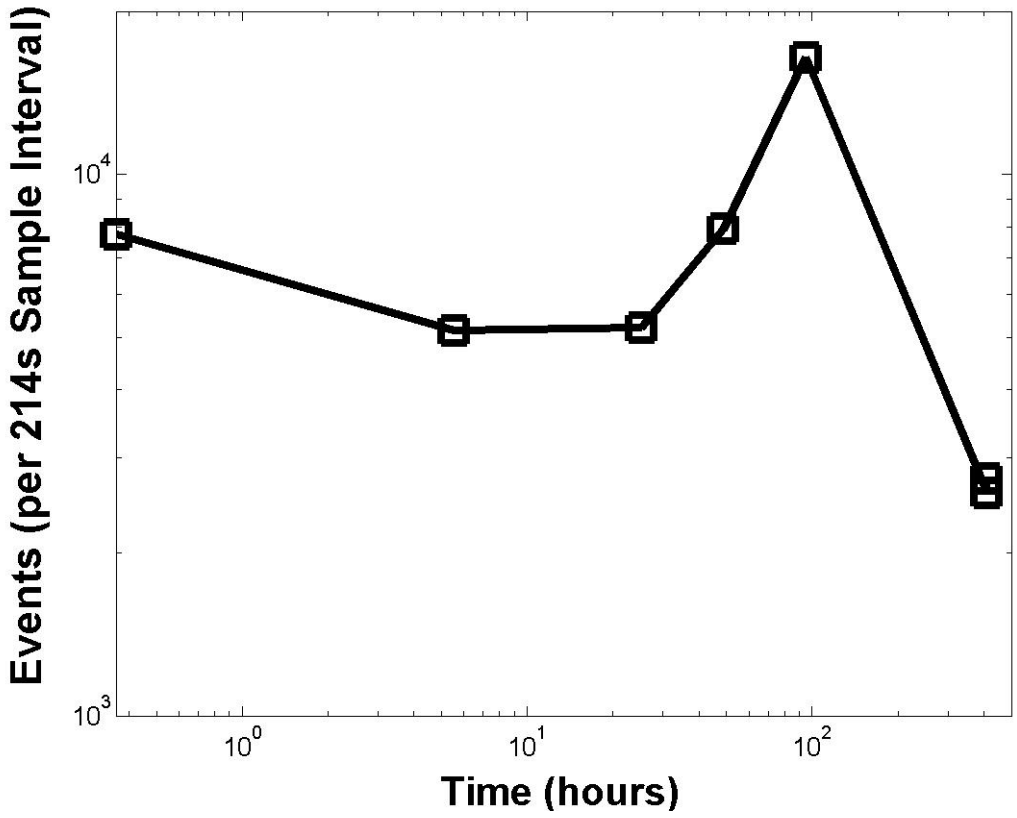

Figure 2.6 Monitoring for extended times in vivo. Number of detected circulating DiD-labeled RBCs are plotted after injection of approximately 1 x 10^7 labeled RBCs at time 0. Focal point in the mouse ear was manually optimized for maximal counts in real time for measurements beginning at 100 hours. Both axes are log scale.

3.3 Simultaneous *in vivo* monitoring of two populations in the circulation of a mouse

To establish the capability of two-photon flow cytometry to enumerate two distinct, rare populations of circulating cells, we measured dynamics of two different breast cancer cell lines in the circulation of living mice. Human MDA-MB-435 studies are known to spontaneously form metastases in mice[12], while MCF-7 cells have very low metastatic potential[13]. Thus, we hypothesized that these cells would show differences in their circulation kinetics based on differences in ability to metastasize.

We enumerated circulating MDA-MB-435 and MCF-7 cells with *in vivo* two-photon flow cytometry at approximately 10, 100, and 1000 minutes after injection. As shown in Figure 2.7, the dynamics of each cell line in the circulation were markedly different. Ten minutes after injection, we detected approximately five hundred MCF-7 cells during a 430-second period of data acquisition. Numbers of MCF-7 cells at this time were more than 10-fold greater than MDA-MB-435 cells, despite the small difference in total numbers of cells injected. These data are similar to those reported by Georgakoudi *et al.*, who showed using single channel *in vivo* flow cytometry that exit of prostate cancer cells from the circulation correlated with relative differences in metastatic potential[14]. Interestingly, MCF-7 cells cleared almost completely from the circulation by 1000 minutes after injection, while MDA-MB-435 cells remained detectable throughout the entire 1000 minutes of the experiment. Thus, the two cell lines had very different circulation kinetics.

To determine the relationship between circulating tumor cells and cells in tissues, we quantified numbers of quantum dot-labeled MDA-MB-435 and MCF-7 cells in excised lungs and liver 48 hours after injection. Microscopic analysis of these organs demonstrated approximately 3-fold greater MDA-MB-435 cells in these organs than MCF-7, based on detection of cells labeled with appropriate quantum dots. These data, in combination with the results of two-photon *in vivo* flow cytometry, suggest that greater numbers of 435 cells arrest in the lungs and liver initially and persist in these organs relative to MCF-7 cells. It is likely that fewer MCF-7 cells are detected by 48 hours because these cells are reported to undergo apoptosis in secondary organs, particularly in the absence of estrogen supplementation that these cells require for proliferation in mice. These data are consistent with previous studies showing that MCF-7 cells do not form

metastases after tail vein injection[15]. Studies *in vitro* showed that the stability of labeling is comparable between 435 and MCF-7 cells, and both remain labeled adequately for detection for over 5-6 days (data not shown). Thus it is doubtful that MCF-7 cells would rapidly lose quantum dots as they circulate and thus be undetectable by flow cytometry and fluorescence microscopy.

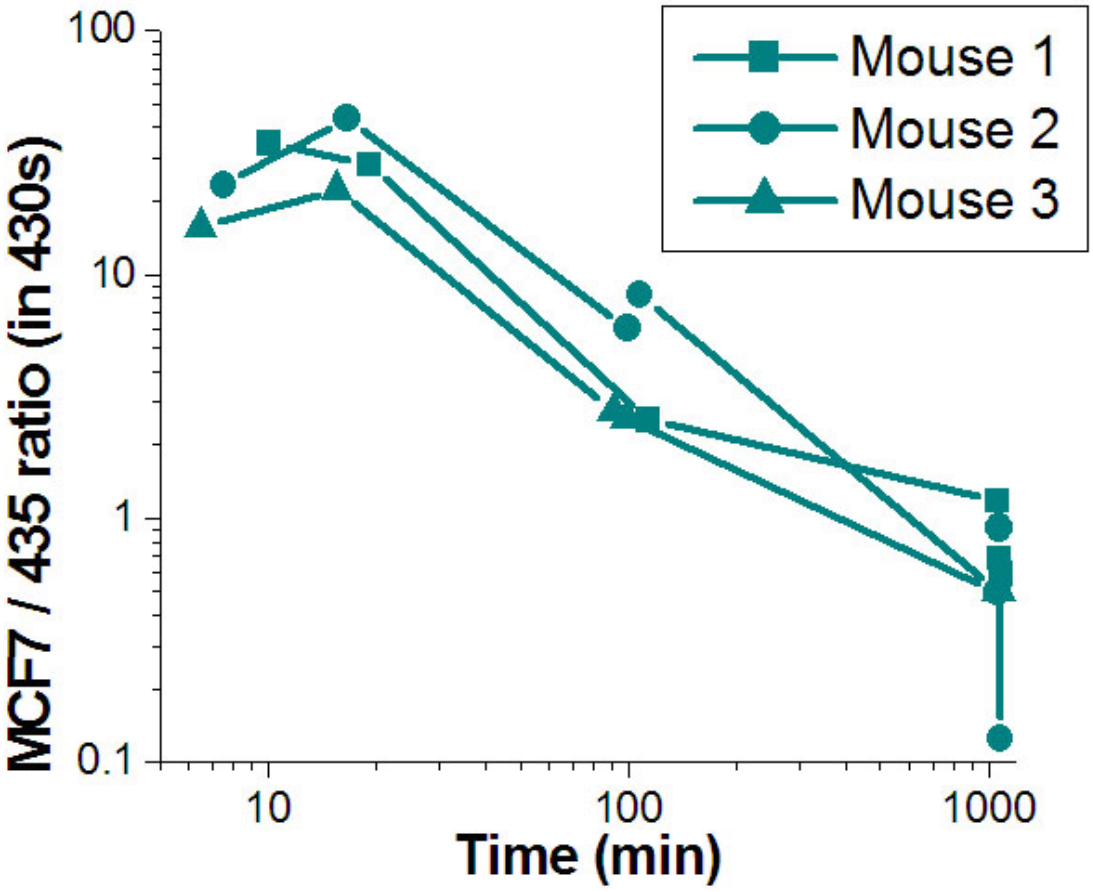

Figure 2.7 Simultaneous monitoring of two populations in each of three mice. The peak frequency dynamics in the artery of three NU/NU mice after the injection of $5x10^5$ low metastatic potential MCF-7 and $5x10^6$ high metastatic potential Qdot665 stained 435 breast cancer cells.

3.4 Evaluation of fluorescent proteins for singly-labeled cell detection in blood

Single-channel evaluation of signal intensity above the blood background for various commercial dyes and fluorescent proteins of Table 1 are shown in Figure 2.8. It is not clear why CellTracker stained dimly in the second experiment (Figure 2.8b). At this exciting light intensity, the enhanced brightness red GFP variant tdTomato is slightly brighter than the commercial dye DiI (cf Figure 2.9). Due to the dense corpuscular

nature of blood, flow in a blood-filled capillary, even under steady syringe pump conditions, has an irregular velocity, and thus single-channel detection does not provide a means to control for the number of cells passing through the laser focus. The number of events detected in a fixed time interval is also not a good measure due to the variation in effective two-photon sampled region detected with variation in the dye intensity due to the minimum photon requirement for peak detection (Figure 2.8b top). Thus, the most reasonable measure of fluorophore signal strength above the variable blood background in a single-channel measurement is the total fluorescent photons counted in all detected events.

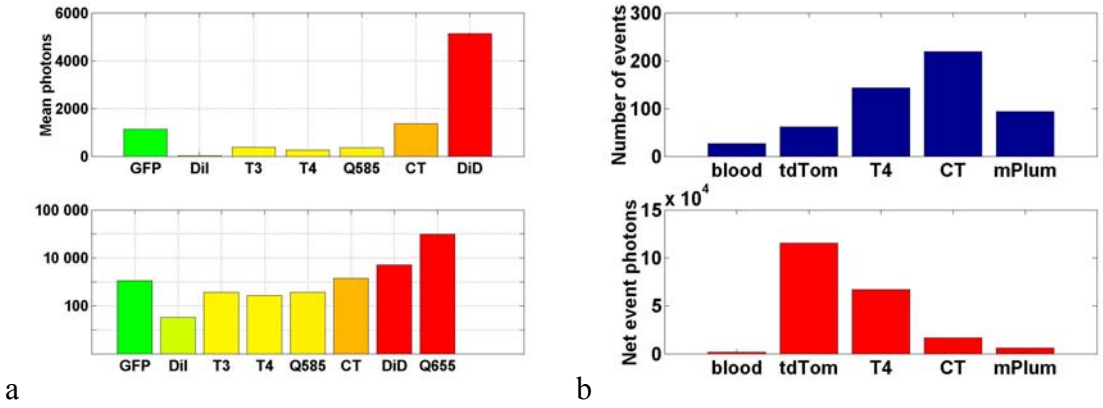

Figure 2.8 Relative strength of two-photon flow signal above blood background from various fluorophores. (a) Mean photons per detected cells with GFP (8 mW at sample), DiI, T3RFP (30 mW), T4RFP (30 mW), 585 nm quantum dots (3 mW), Cell Tracker Red (8 mW), DiD (4 mW), or 655 quantum dots (1 mW), normalized to 16 mW power at the sample in blood suspension via a square-law scaling. (b) Net fluorescent events (top, blue) and net collected photons (bottom, red) in detected events from a single-channel experiment from 8 μL of blood containing nothing, tdTomato, T4, CT or mPlum-expressing cells at 3.3e5 mL^{-1}, with 16 mW laser power from the Mira at the sample.

Two-color evaluation of signal intensity above a blood background is shown in Figure 2.9. Decrease in fluorescence signal from Mira to XTND on T4 was probably caused by poor mode-locking of XTND during that experiment, siphoning power from short pulses to the cw component.

Dual-channel detection offers the advantage of a channel to monitor the number of cells passing through the two-photon excitation region at any given time. A dye fluorescing sufficiently strongly into this additional channel provides an accurate reflection of the number of cells passing through the excitation volume (Figure 2.9 top). DiD was used for cell counting of short wavelength fluorescent proteins GFP, tdTomato,

and T4; DiI was used for the long wavelength fluorescent protein mPlum. Note that DiI has a minimum two-photon cross-section around 800 nm[16], and at lower excitation powers in a whole blood background, it is no longer easily detected with high percentage success, therefore it is not suitable for *in vivo* experiments, which will suffer an even larger blood path contributing to increased background and absorption. Thus, DiI is inferior to redder fluorophores with similar brightness, such as tdTomato. Quantum dots were chosen for the two cancer line *in vivo* experiment due to their superior brightness at emission wavelengths under 600 nm for short channel detection.

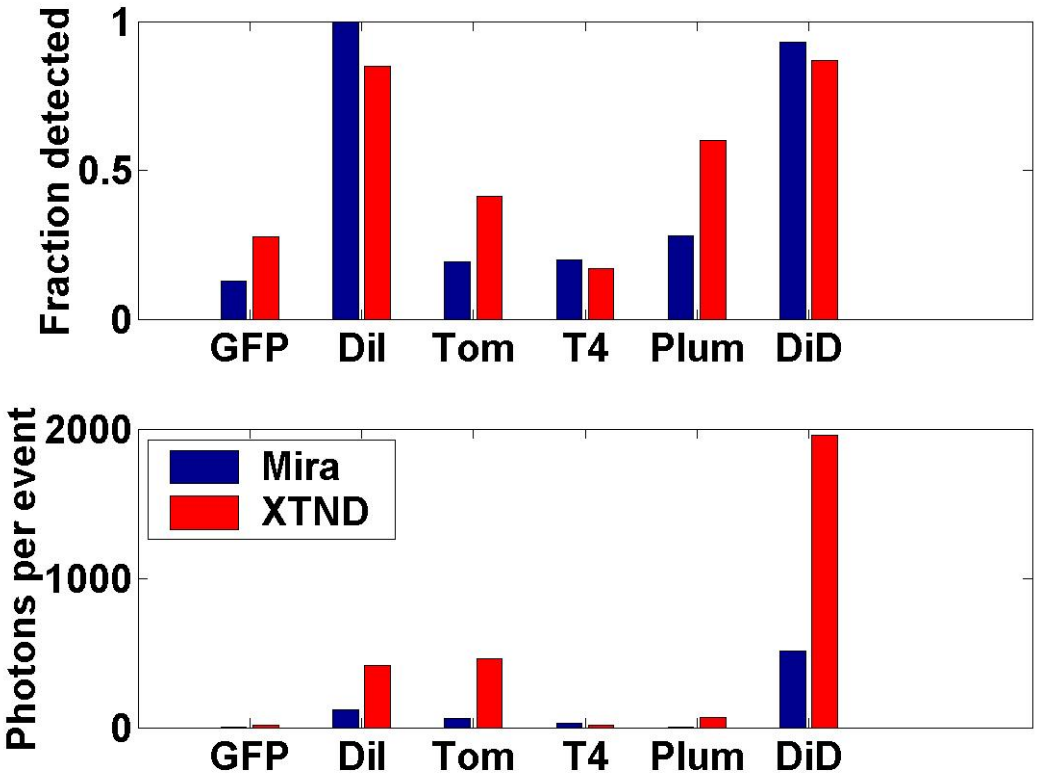

Figure 2.9 Dual-labeled fluorescent protein signal in dilute human blood with different excitation sources. Same conditions as in Figure 2.8 with two-channel detection and dual-labeling of fluorescent protein with DiD in the long wavelength reporter channel (DiI in short wavelength reporter channel in the case of mPlum). (top) Fraction of total reported events detectable in the given detection channel. (bottom) Mean two-photon fluorescent photons per cell passing through laser focus.

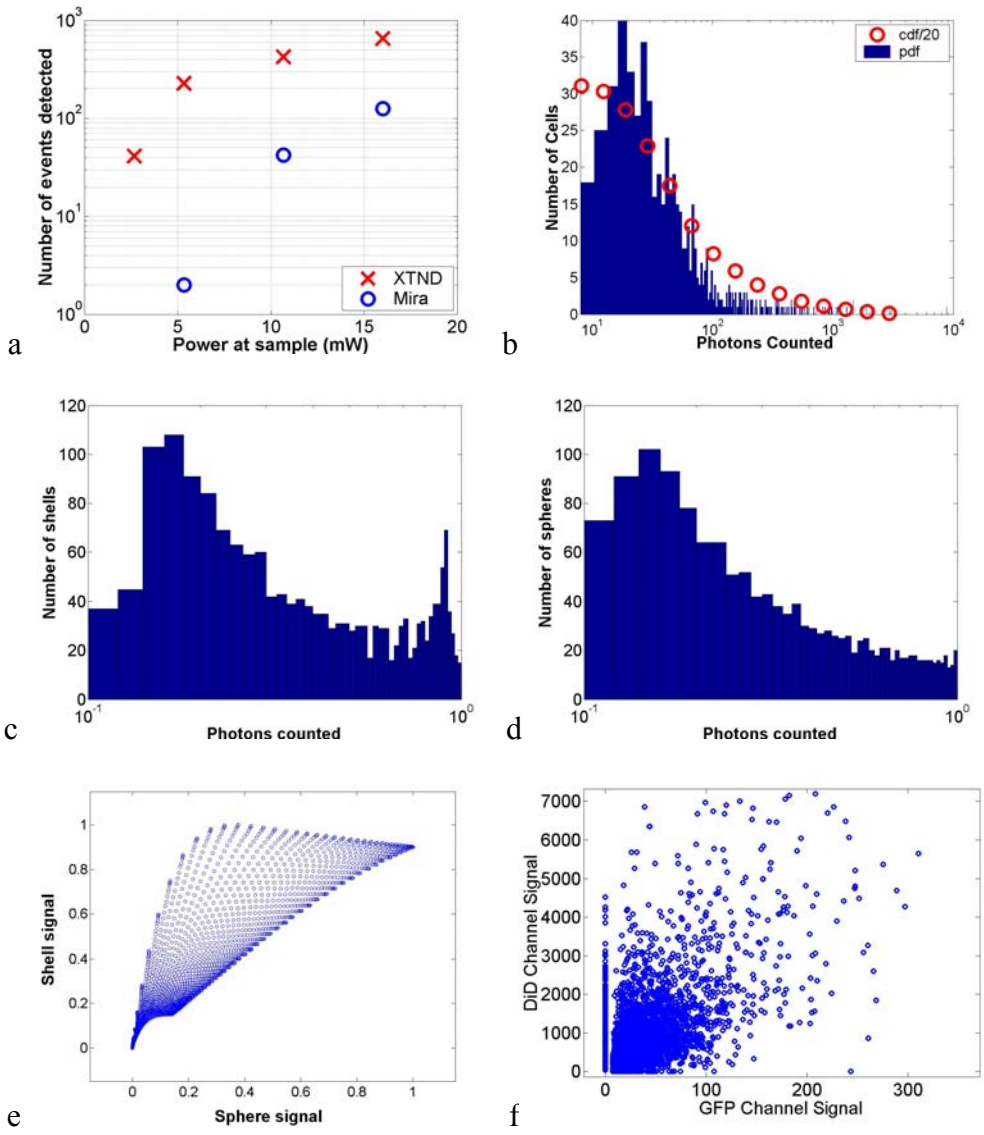

Figure 2.10 (a) Number of Cell-Tracker labeled cells detected in PBS with extended cavity or Mira at varying incident laser power for 13s of a 1e6 mL^{-1} concentration flowing at 0.3 mL/h (b) Probability distribution function (pdf) of detected event energies at 16 mW XTND laser power at sample with cumulative distribution function (cdf) as relative detection threshold moves to dimmer events of the distribution. (c) Simulated histogram (pdf) of a 10 μm radius fluorophore shell flowing through random positions of a 2 micron laser spot size. The cumulative distribution function (cdf) shows how many events would be detected if only events dimmer than the ordinate of the data point (to the left of the given red circle in the figure) are detectable (d) Simulated 10 μm sphere distribution. (e) Correlation between sphere and shell signal. (f) Correlation between cytosolic GFP and membrane DiD signal in real experiment.

3.5 Enhanced sensitivity with increased signal of extended cavity oscillator

While the two-color cancer cell experiment in Figure 2.7 demonstrates the power of the two-photon *in vivo* flow technique, currently the technique is limited by the poor detectability of most conventional fluorophores, which emit at shorter wavelengths than the convenient NIR window[17] and therefore overlap significantly with tissue absorption and autofluorescence peaks (Figure 2.3). Though the strong signal of quantum dots is capable of overcoming this hurdle, a more biocompatible approach would be of major benefit. Due to the direct proportionality of two-photon fluorescent signal with pulsed laser cavity length, an extended cavity laser is introduced as a biocompatible means of increasing signal and detectability of shorter wavelength fluorophores. Figure 2.10 shows the clear increase in detection sensitivity with the extended cavity laser, for CellTracker-labeled cells flowing in PBS. Due to the sigmoidal shape of the detection curve, this causes an enormous difference in detectability, especially at lower excitation powers. For example 5 mW at the sample shows almost no detectable events with the Mira, but a large fraction of the theoretical number of cells flowing through with XTND. The sigmoidal shape of the sensitivity curve can be understood in terms of the event brightness distribution. Decreasing excitation power from p to p' scales the brightness of all events by the same $(p/p')^2$ factor, effectively translating the ordinate position of the detection threshold rightwards on the true distribution. Thus the calculated cumulative distribution function in Figure 2.10b is approximates the detected events curve of Figure 2.10a (flipped left to right as increasing power moves the threshold leftwards). The measured histogram of CellTracker-labeled cells' signal strengths further agrees with the calculated histogram of an idealized cytosolic fluorophore. Clearly, a solid sphere spatial distribution of fluorophore (Figure 2.10d) matches the measured pdf much better than a shell (Figure 2.10c) would. Note also that both idealized calculation and experimental results both demonstrate a lack of correlation between a membrane-dye and cytosolic dye signals (Figure 2.10e and f) due to the different spatial distributions of the dyes.

3.6 Trastuzumab-dendrimer targeting for *in vivo* cancer cell labeling

The ultimate leap of *in vivo* flow cytometry into the realm of clinical applicability for human patients will require successful *in vivo* labeling and detection of endogenously circulating cancer cells. Polyamidoamine dendrimers[18] have shown great promise for precisely this purpose as fluorescently labeled nontoxic targeting molecules. Figure 2.11 shows successful 5 fold increase in 6-Tamra labeling of live cancer cells with trastuzumab-conjugated fluorescent dendrimer over unconjugated fluorescent dendrimer alone, as measured by two-photon flow cytometry.

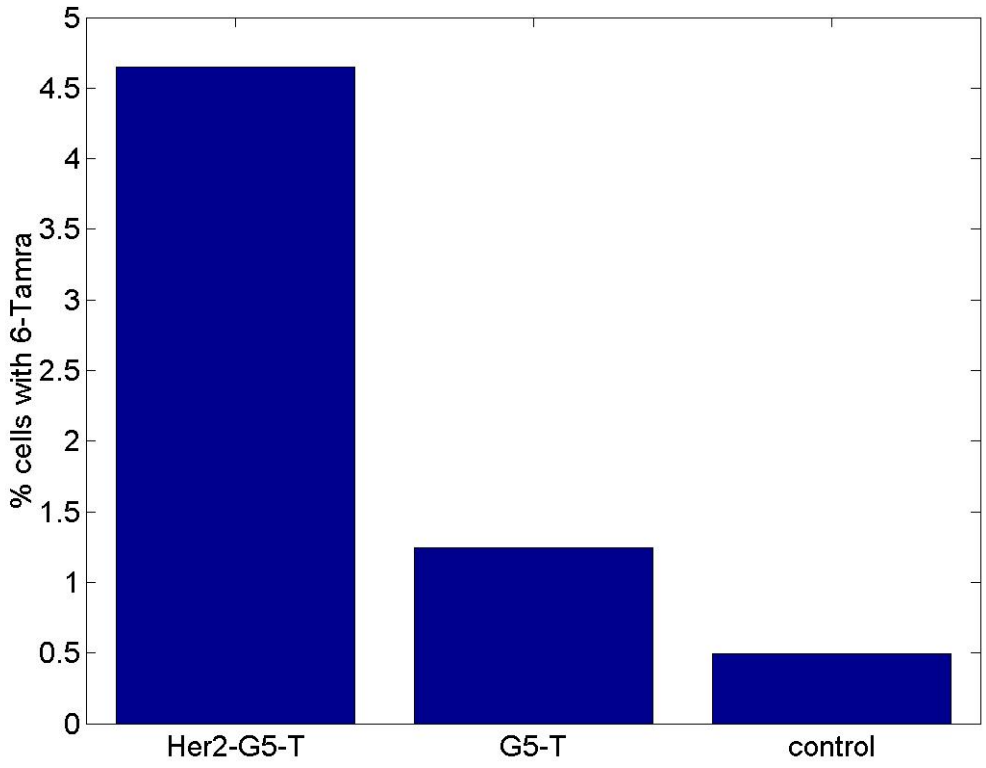

Figure 2.11 Ability to detect targeted molecules. Percent of Her2-overexpressing SKBR3 cells dual-labeled with DiD positive for 6-Tamra by two-photon flow cytometry. Control: DiD-labeled cells only. G5-T: cells tagged with 5th-generation dendrimer conjugated to 6-Tamra (6-T). Her2-G5-T: G5-T conjugated additionally to trastuzumab SKBR3 cells not expressing Her2 was undetectable.

4. Conclusions

Many unique studies are possible with the novel two-photon approach to *in vivo* flow cytometry. With fluorescent microspheres, we have demonstrated the ability of our two-photon *in vivo* flow cytometer to track depletion of fluorescent particles *in vivo* with a time scale beyond the resolution of conventional flow cytometry. Investigations with RBCs show that an abundant population of cells can be monitored for periods of greater than two weeks, thereby establishing that the system can detect single events at high counting rates over extended periods of times. This may be enabled by the limitation of multiphoton absorption to the interrogated region, reducing potential collateral damage to tissues outside of the vessel lumen. Monitoring circulating cells over the course of weeks has not been demonstrated previously with other *in vivo* flow cytometers. Interrogating populations of hematopoietic cells, such as red blood cells (RBCs) or leukocytes, could provide new insights into normal physiology or disease processes, as well as serving as an internal standard for hemodynamics and perfusion. For example, if the dynamics of a cell population, such as RBCs, are well known, this provides a statistically reliable internal control of the interrogated blood volume per unit time, if more than one detection channel is available (as in our unique multiphoton system).

While single channel *in vivo* flow cytometry is sufficient for a qualitative understanding of circulating cell dynamics, it may be limited by variations in event counts in repeated experiments. Between different experiments, the blood flow velocity at the measurement site may vary. This occurs on a short time-scale due to pulsatile flow, but also on a longer time scale due to drift and reproducibility of positioning of the laser focus. During data acquisition, the anesthetized mouse can change position slightly, which results in the laser focusing on a site in the vessel with a different blood flow velocity. Further, time-varying physiological conditions can be highly variable between experiments, whether the same or different mice are used. These factors are compounded by statistical fluctuations when small sample sets are acquired for studies of rare circulating cells. Without a means to determine the volume sampled over a given time interval, these intrinsic problems will complicate analyses of dynamics of different populations of cells injected into separate mice for single color flow cytometry.

With multicolor, two-photon *in vivo* flow cytometry, different populations of cells can be compared simultaneously in a single animal, overcoming many variables intrinsic to *in vivo* experiments. Thus, a specific cell population can be interrogated in reference to a known circulating population (such as RBCs), or the dynamics of two rare cell populations can be compared directly. To exploit the capability of two-photon flow cytometry to enumerate two rare populations of circulating cells, we used this technique to interrogate dynamics of two types of breast cancer cells in the circulation of living mice. Human MDA-MB-435 studies are known to spontaneously form metastases in mice, while MCF-7 cells have very low metastatic potential. Thus, we hypothesized that these cells should show differences in their circulation time based on differences in ability to metastasize.

These studies outline the basis of a two-color two-photon flow cytometry approach for simultaneous *in vivo* detection multiple events in circulating blood cells. This method allows the analysis of many complex physiological phenomena, in intact animal models. An example of this is the monitoring of breast cancer cells in the circulation, which has been reported to have prognostic significance in women[19]. We expect that further studies will allow us to interrogate functions of specific molecules implicated in metastatic breast cancer, such as the chemokine CXCL12 and its receptor CXCR4[20]. This will help to define the kinetics and consistency of these measures to better understand the biology of human breast cancer. Potentially, this approach could also allow the evaluation of drugs targeted against specific molecules or pathways *in vivo*, thereby facilitating clinical therapeutics. The enhanced ability to detect GFP-variants and other fluorophores at lower powers with extended cavity laser excitation and demonstrated targeting of the Her2 receptor with a dendrimer-conjugated dye are significant steps towards these ultimate goals.

One challenge to *in vivo* cytometry is the small number of labeled cells passing through the blood vessel in the detection region. Using the simultaneous injection of labeled RBCs as a control for focal point optimization could enable far more reliable experiments on rare event circulation dynamics. One solution to increase the statistical significance would be to access larger blood vessels with higher flow rates, thereby increasing the number of detected cells. A femtosecond NIR laser source has the

advantage of being able to penetrate much deeper through biological tissue than a one-photon CW laser[21]. In addition, the nonlinear excitation property of a femtosecond NIR laser confines the excitation region to the focal point without requiring the use of a confocal pinhole. This reduces photo damage to the surrounding tissue, which may allow extended monitoring periods in live animals.

We anticipate many novel insights from other applications of this technique. Examples of areas ripe for future development include: 1) monitoring changes in gene expression through imaging probes injected into the mouse or genetically-engineered cell lines with fluorescent reporters; 2) expanding the capability to monitor additional fluorescent channels or more blood per unit time; and 3) studies with mice genetically-engineered with modifications in specific adhesion molecules. These studies will be aided by technical advances such as the real-time imaging of blood vessels to monitor and control the position of the laser beam throughout the experiment and the development of approaches to label specific molecules or cells *in vivo*, rather than *ex vivo*. Given this potential, *in vivo* two-photon flow cytometry will become an important technique for investigating a broad range of issues related to the trafficking of cell populations in living animals, providing new insights into processes as diverse as cancer and host defense.

References

1. Mitsiades CS, Mitsiades NS, Bronson RT, Chauhan D, Munshi N, Treon SP, Maxwell CA, Pilarski L, Hideshima T, Hoffman RM, Anderson KC. 2003. "Fluorescence imaging of multiple myeloma cells in a clinically relevant scid/nod *ex vivo* model: Biologic and clinical implications." *Cancer Research* **63**, 6689-6696.
2. Graves EE, Ripoll J, Weissleder R, Ntziachristos V. "A submillimeter resolution fluorescence molecular imaging system for small animal imaging." *Medical Physics* **30**, 901-911, 2003.
3. Ntziachristos VT, Yodh AG, Schnall M, Chance B. "Concurrent MRI and diffuse optical tomorgraphy of breast after indocyanine green enhancement. *PNAS* **97**, 2762-2772, 2000.
4. Novak J, Georgakoudi I, Wei X, Prossin A, Lin CP. "*Ex vivo* flow cytometer for real-time detection and quantification of circulating cells," *Optics Letters* **29**, 77-79, 2004.
5. Konig K. "Multiphoton microscopy in life sciences." J Microsc (Oxf) 200, 83-104, 2000.
6. Bevis B and Glick BS, "Rapidly maturing variants of the *Discosoma* red fluorescent protein (DsRed)." *Nature Biotechnology* **20**, 83-87, 2002.
7. Wang L, Jackson WC, Steinbach PA and Tsien RY, "Evolution of new nonantibody proteins via iterative somatic hypermutation." *PNAS* **101**, 16745-16749, 2004.
8. Shaner NC, Campbell RE, Steinbach PA, Giepmans BNG, Palmer A and Tsien RY, "Improved monomeric red, orange and yellow fluorescent proteins derived from *Discosoma* sp. red fluorescent protein." *Nature Biotechnology* **22**, 1567-1572, 2004.
9 . Cho SH, Bouma BE, Ippen EP, and Fujimoto, JG, "Low-repetition-rate hih-peak-power Kerr-lens mode-locked TiAl2O3 laser with a multiple-pass cavity." *Optics Letters* **24**, 417-419, 1999.
10. Shukla R, Thomas TP, Peters JL, Desai AM, Kukowska-Latallo J, Patri AK, Kotlyar A, Baker JR, "HER2 specific tumor targeting with dendrimer conjugated anti-HER2 mAb." *Bioconjug Chem*. **17**, 1109-1115, 2006.
11. Tkaczyk, E. *et al*. To be published elsewhere.
12. Price, J., Polyzos, A., Zhang, R. & Daniels, L. "Tumorigenicity and metastasis of human breast carcinoma cell lines in nude mice." *Cancer Res*. **50**, 717-72, 1990.
13. McLeskey, S. et al. "Fibroblast growth factor 4 transfection of MCF-7 cells produces cell lines that are tumorigenic and metastatic in ovariectomized or tamoxifen-treated athymic nude mice." *Cancer Res.* **53**, 2168-2177, 1993.

14 Georgakoudi, I. *et al*. "*In vivo* flow cytometry: A new method for enumerating circulating cancer cells." *Cancer Res*. **64**, 5044-5047, 2004.

15. Panabières, C.A. *et al*. "Characterization and enumeration of cells secreting tumor markers in the peripheral blood of breast cancer patients." *J. Immunol. Methods* **299**, 177-188, 2005.

16. Xu C, Williams RM, Zipfel W and Webb WW, "Multiphoton excitation cross-sections of molecular fluorophores." *Bioimaging*. **4**, 198-207, 2001.

17. Weissleder R, "A clearer vision for *in vivo* imaging." *Nature Biotechnology.* **19**, 316-317, 2001.

18. I. J. Majoros, T. P. Thomas, C. B. Mehta, and J. R. Baker Jr, "Poly(amidoamine) dendrimer-based multifunctional engineered nanodevice for cancer therapy," *J. Med. Chem.* **48**, 5892 -5899, 2005

19. Cristofanilli M, Budd GT, Ellis MJ, Stopeck A, Matera J, Miller MC, Reuben JM, Doyle GV, Allard WJ, Terstappen LWMM and Hayes DF. "Circulating Tumor Cells, Disease Progression, and Survival in Metastatic Breast Cancer." *New England Journal of Medicine.* **351**, 781-791

20. Luker, KE and Luker, GD. "Functions of CXCL12 and CXCR4 in breast cancer." *Cancer Letters.* **238**, 30-41, 2006

21. Gu M, Gan XS, Kisteman A, Xu MG. "Comparison of penetration depth between two-photon excitation and single-photon excitation in imaging through turbid tissue media." *Applied Physics Letters* **77**, 1551-1553, 2000

CHAPTER 3
EXTENDED CAVITY LASER ENHANCED TWO-PHOTON FLOW CYTOMETRY

Abstract. We demonstrate enhanced sensitivity in two-photon flow cytometry with an extended cavity laser excitation source. At low power, the home-built 20 MHz oscillator was able to detect a significantly larger fraction, in either PBS or whole blood, of GFP-expressing MCA-207 cells cross-labeled with the membrane-binding lipophilic dye DiD. A geometrical model is used to explain unique features of the signals resulting from the different spatial distribution of DiD and GFP. These include sub-square law scaling of unsaturated two-photon signal; a sigmoidal sensitivity curve for detection under varying powers for cell detection thresholds as low as a single photon; and uncorrelated signal strengths in two detection channels.

1. Introduction

Recent studies in cancer biology emphasize the importance of detecting and quantifying various types of cells, including rare populations of tumor and endothelial cells, in determining prognosis and response to therapy[1]. Great technological progress has been made in isolating circulating tumor cells, as reviewed by Smerage and Hayes[2]. Modern available assays include combinations of conventional flow cytometry, immunohistochemistry, immunofluorescent microscopy, immunomagnetic separation[3], PCR, RT-PCR[4], high-throughput optical-imaging systems[5] including fibre optic scanning[6], and most recently, microchip technology[7]. The last is the only technology capable of isolating viable cells from whole blood without any additional processing or preparation. As a whole, there remain notable deficiencies with the existing assays that enumerate total malignant cells in a single blood sample[8,9]. The first limitation is specificity. While elevated numbers of circulating tumor cells (CTCs) generally are associated with worse prognosis, not all patients with detectable breast cancer cells in blood progress rapidly[10]. This result suggests that there are subsets of circulating tumor cells that are more biologically relevant for prognosis and response to therapy. The second limitation is sensitivity. Only approximately 50% of patients with metastatic breast cancer have detectable circulating tumor cells at any given time, even though all eventually have progressive disease. These observations suggest that entry of breast cancer cells into the circulation may be intermittent, so analyses based on a single blood sample may give incorrect information. Deficiencies in existing assays for circulating tumor cells potentially have an even greater impact for patients with early stage primary tumors or after adjuvant therapy due to decreased tumor burden. Collectively, limitations of existing assays emphasize the need to develop new tests with the sensitivity and specificity to detect subsets of circulating tumor cells that are linked more directly to prognosis or response to therapy.

To enable *in vivo* investigations of biologically relevant populations of circulating cells in cancer and other disease processes, we previously developed a novel two-color, two-photon flow cytometer[11]. The use of two-photon excitation for *in vivo* flow cytometry permitted us to simultaneously monitor the circulation dynamics of two

distinct populations of breast cancer cells in the same animal in real time[12,13]. Though we were able to enumerate cells labeled with a near infrared fluorescent dye or quantum dots, the system could not as reliably detect dyes with shorter wavelengths, or genetically-encoded fluorescent proteins. While *in vivo* detection of GFP-labeled cells has been achieved with a confocal geometry[14], the ability to detect such dyes and proteins concurrently with longer wavelengths using a single near-infrared excitation source greatly expands the capabilities of *in vivo* flow cytometry. He *et al.* recently showed the feasibility of labeling CTCs in vivo using fluorescein isothiocyanate (FITC) conjugated to folate and monitoring fluorescent cells with two-photon *in vivo* flow cytometry[15]. They also were able to use a folate-AlexaFluor 488 conjuage to detect CTCs in whole blood from ovarian cancer patients, but not in healthy controls. Collectively, these studies emphasize the potential for *in vivo* flow cytometry to overcome limitations of current assays for CTCs and advance the use of CTCs as a biomarker in clinical oncology.

One very promising approach to successful *in vivo* measurements is the development of fluorescent probes with a redder emission wavelength closer to the so-called "NIR window," where autofluorescence, blood and tissue absorption peaks, and Rayleigh scattering are all significantly reduced. Recently, great strides have been made in this area[16,17,18,19,20]. However, two-color measurements have been demonstrated in flow systems as providing superior quantitative ability over one-color measurements[21]. Thus, increased ability to detect short-wavelength fluorescent probes concurrently with long-wavelength ones would further advance molecular imaging.

Thermal damage places a strict upper limit on the average power that can be delivered to any biological specimen. Thus, increasing average laser power is not a feasible method for boosting fluorescent signal. At a fixed average laser power, the integrated two-photon fluorescence signal is directly proportional to the repetition period of the laser[22]. Thus a convenient way of increasing two-photon processes is application of an extended cavity laser, which should increase two-photon signal in proportion with cavity length.

In the current study, we first demonstrate enhanced two-photon fluorescent signal in flowing dye as well as fluorescent polystyrene microspheres with a home-built 20

MHz extended cavity Ti:sapphire oscillator relative to a commercial 76-MHz system. While an approximately four-fold increase in fluorescent signal of both flowing dye and polystyrene microspheres is observed, it is noteworthy that square-law scaling is preserved only in the case of the dye solution. Calculated detection of ideal spheres demonstrates that the power variation in the detection region is the cause of sub-square law scaling in the case of beads. Further, we show enhanced sensitivity with the extended cavity laser for detection of MCA-207 mouse sarcoma cells *via* endogenous expression of GFP (emission maximum 518 nm) in both normal saline and whole blood. The commercially available near infrared membrane dye DiD (1,1'-dioctadecyl-3,3,3',3'-tetramethylindodicarbocyanine,4-chlorobenzenesulfonate, emission maximum 665) is used concurrently to monitor the number of cells interrogated. We also present detailed calculations enabling us to interpret the detection distributions, two-channel signal correlations, and power-sensitivity curves, even under idealized distributions of GFP and DiD.

2. Materials and Methods

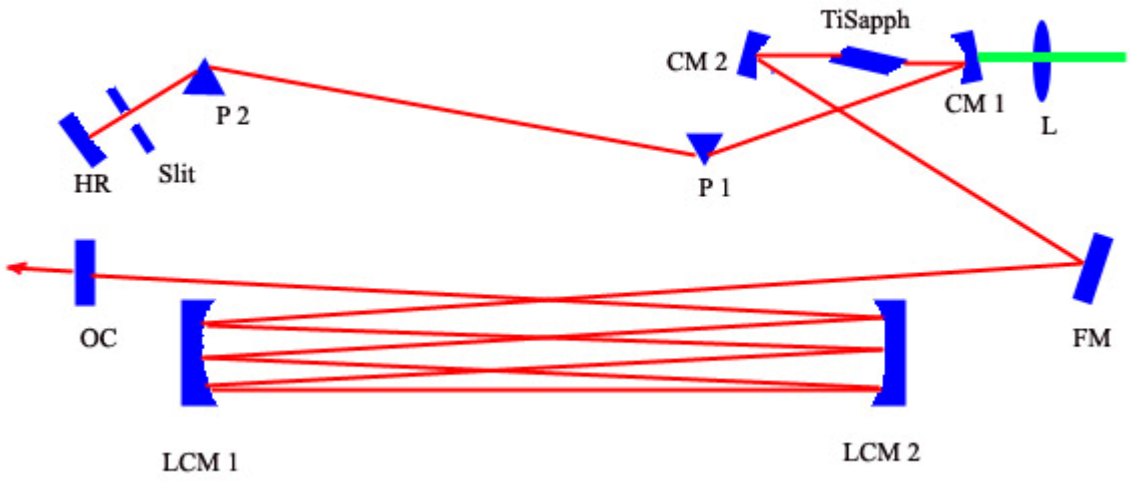

Figure 3.1 Home-built extended cavity laser for 20 MHz repetition rate.

Technical specifications:
CM1/CM2 : 10 cm cc, AR coated for 560-570nm, HR @ 630-1100nm
LCM1/LCM2 : 2m cc, separation: 81.25 cm, # of passes: 3
P1/P2 : fused silica prisms, apex - 63 deg, separation: 50.8 cm
TiSapph : 1 cm long
OC : 10% transmissive 650-1150nm
HR: 99.9% R over 620-1080nm
Total cavity length : 736.6 cm
Period of pulse train : 50 nsec, corresponding to 20 MHz
Pump Power: 3.5w
Output Power: 170 mW cw, 150 mW mode-locked
Bandwidth: ~ 18nm
Pulsewidth (from SHG FROG): ~ 70 fsec

2.1 Laser system

A home-built extended cavity laser was constructed (Figure 4.1), following the design of Cho *et al.*[23], incorporating a 1 cm Ti:Sapphire crystal optically pumped with 3.5 W from a solid-state 532-nm diode laser (Coherent, Verdi). The cavity utilizes concave mirrors (CM1 and CM2) with a 10-cm radius of curvature and 99.9 % reflectivity for 700-900 nm. A fold mirror routes the beam for three round-trip passes between two multi-pass mirrors, which are concave with 2-m radius of curvature and 81.25-cm separation. The output coupler is 10% transmissive at 650-1150nm. The total path length is 736.6 cm. Mode-locking is achieved by selecting for Kerr lensing with an adjustable intracavity slit, and the dispersion is controlled by two fused silica prisms with

apex 63°, separated by 50.8 cm. The pulse train period is 50 ns, corresponding to a 20 MHz pulse repetition rate with a 780 nm center wavelength.

The oscillator is first set up for optimum continuous wave (cw) and mode-locked performance without the multi-pass mirrors (prism separation 48.25 cm, length of output coupler arm (from CM1) 135cm). The multi-pass mirrors are inserted, and the now extended cavity is optimized, and the prisms are separated slightly more to compensate for the dispersion by air from the additional cavity length.

A commercial Ti:Sapphire laser (Coherent Mira), which generates nominally 50-fs pulses at 800 nm with a repetition rate of 76 MHz was tuned to 780 nm for use as the standard for comparison. A flip mirror is used to switch between laser sources. Immediately after the flip mirror, before the cytometry system, 3% of the incident laser light is sent via a beamsplitter to a digital power meter for a reference power reading.

The laser sources are characterized both with a spectrometer (Figure 3.2) as well as a commercial SHG-FROG device (Grenouille, SwampOptics) and software (VideoFROG, Mesaphotonics). The extended cavity reliably produces 80 fs pulses with 12-nm bandwidth and a 0.48 time-bandwidth product. Typical Mira pulse widths are 85 fs with 26-nm bandwidths for a 1.0 time-bandwidth product, and show significantly greater time-frequency structure than the extended cavity pulses (Figure 3.3).

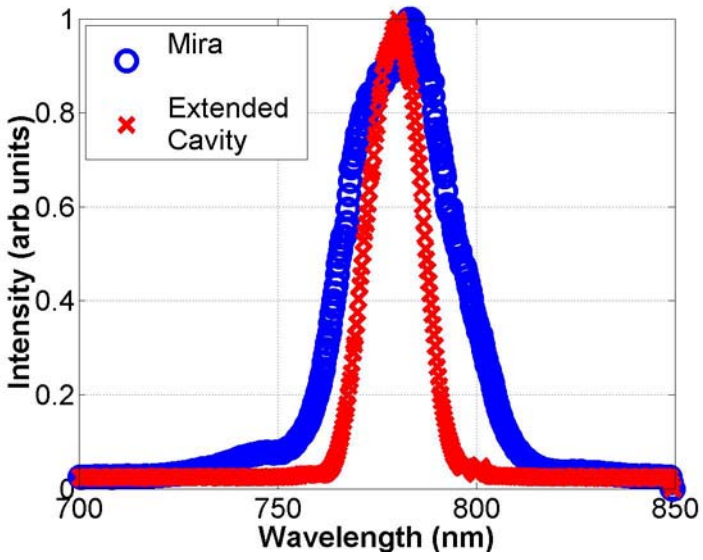

Figure 3.2 Output spectra of extended cavity and commercial (Mira) NIR femtosecond system.

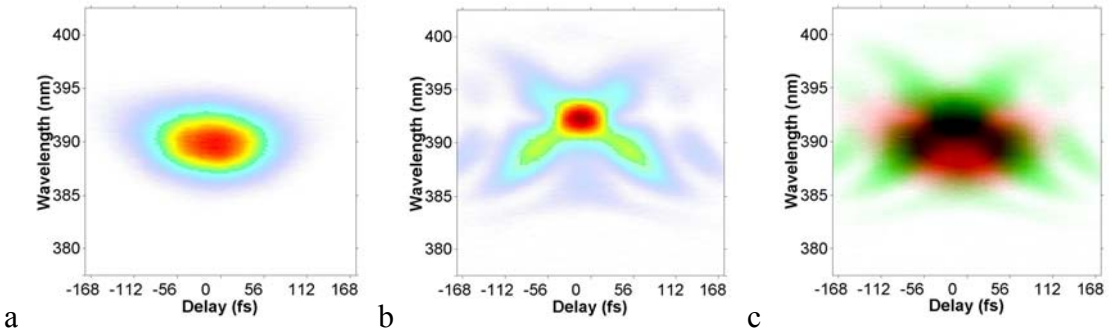

Figure 3.3 Time-frequency characterization of laser pulses with SHG-FROG. (a) Extended Cavity pulse raw SHG-FROG trace (b) Mira (c) Overlay (extended cavity red, mira green)

2.2 Two-photon flow cytometer

The two-photon flow cytometry apparatus is drawn in Figure 3.4. A capillary flow system was employed to emulate flow similar to what is encountered in *in vivo* measurements. Either the home-built extended cavity or Mira laser beam is focused with a long-working distance objective (Olympus 40x, 30% power transmission at 800 nm) into a 100 μm square capillary with a 100 μm fused silica wall (WWP100375, Polymicro Technologies) through which the sample flows at a constant rate (usually 0.3 or 1.0 mL/hr) under the force of a syringe pump (KD Scientific). A dichroic mirror (700 nm cutoff, Melles Griot) directs the laser into the microscope objective while transmitting the fluorescence collected through the same objective. A secondary dichroic mirror (620 nm cutoff) and sharp cutoff interference bandpass filters (530/35nm for GFP, 660/50 for DiD, 525/250 for single channel FITC or beads experiments) are used to separate the fluorescence from different fluorophores into two channels, which are detected with two distinct photomultiplier tubes (PMT Hamamatsu HC7421-40) and recorded with two multichannel photon counting scalers (MCS Stanford Research SR430), which are capable of time resolution as low as 2 ns and have a sharp cut-off in detection at 720 nm. The signals (number of photons counted per each 1.3-ms bin of sampling interval) are sent to a computer for data analysis.

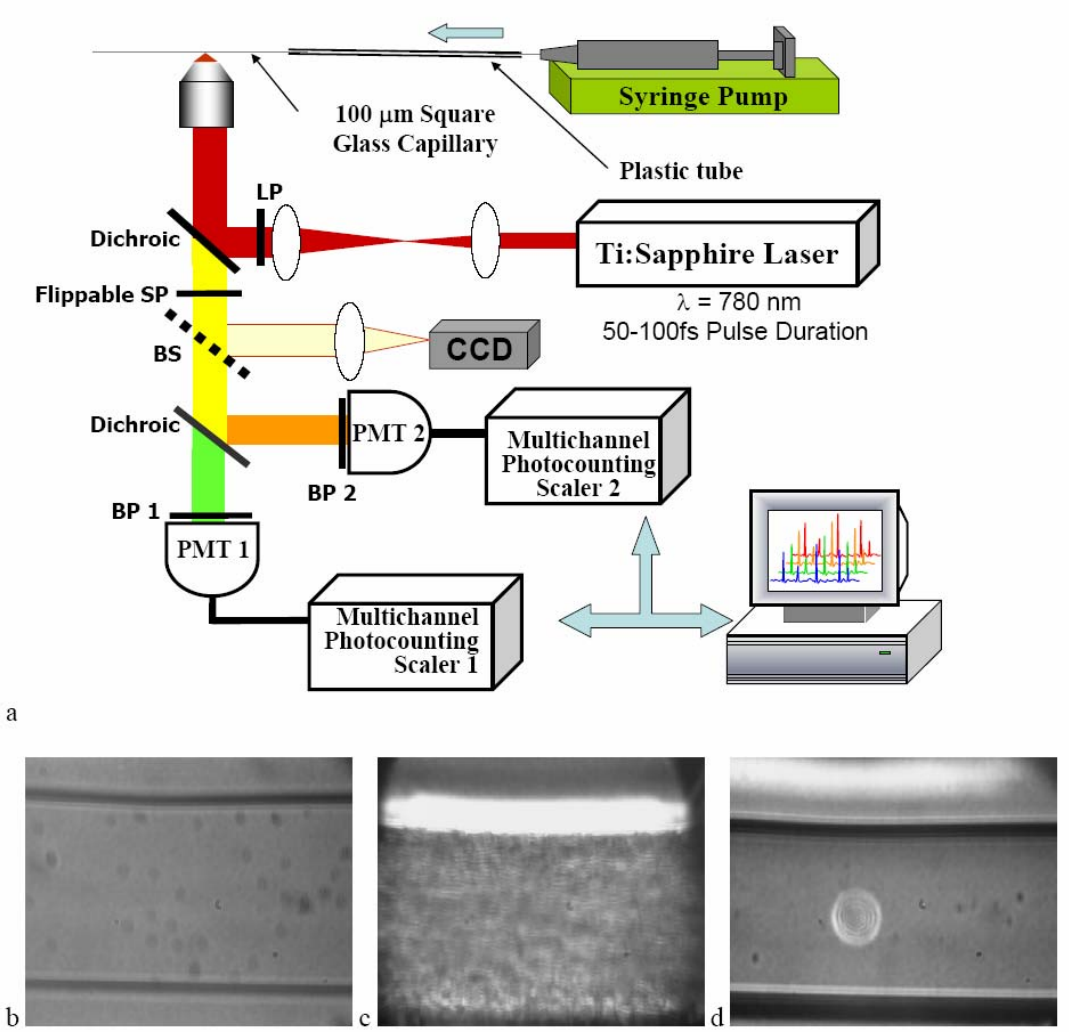

Figure 3.4 (a) Two-photon flow cytometry setup. LP: 760 nm cut-off long-pass filter. SP: 700 nm cut-off short pass filter. Dichroic mirror cutoffs are 750 nm and 620 nm, top to bottom. BP: bandpass filters selected appropriately for the fluorophore of interest (BP1: 525/250 nm for FITC or beads; 520/35 for GFP; BP2: 660/50 for DiD); (b) Typical CCD images of beads and (c) blood flowing through the glass capillary. (d) Newton's rings when the short-pass emission filter is removed. Capillary inner diameter is 100 μm.

Long-pass filtering of the excitation source (760nm cutoff) and short-pass filtering of the emission (700 nm cutoff) are employed to minimize noise on the PMT detectors. When the short-pass filter is removed, back-scattered laser light enables careful positioning of the objective for an optimal laser focal spot at the center of the capillary. Before each data acquisition, the diffraction pattern scattered off the capillary bottom inner surface is examined out-of-focal plane (Figure 3.4d). This ensures proper alignment of the switch mirror between laser sources to minimize aberrations.

The spot size radius (w) at focus of the two-photon cytometer is determined for each laser by matching a Gaussian to the CCD intensity image of backscattered laser radiation Figure 3.5 as well as the image of two-photon volume signal from a drop of concentrated Rhodamine dye.

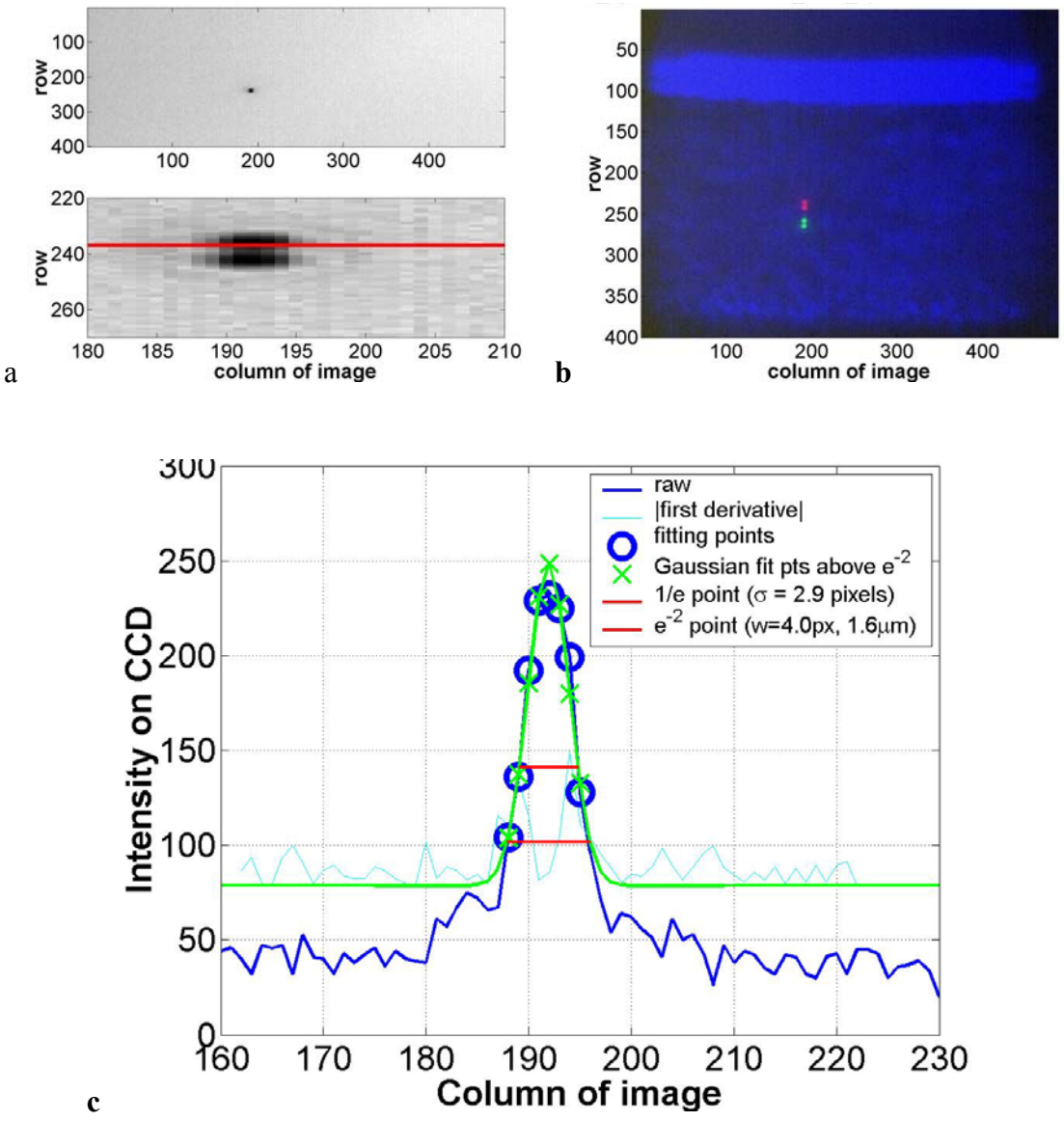

Figure 3.5 (a) CCD image of backscattered laser light from a glass coverslip, at focus, without shortpass filter in place. Red line on magnified image indicates the brightest row. (b) False-color overlay of images of extended cavity spot (red) and mira spot (green) on blood-filled capillary (blue). The double-image of the spot is caused by the two faces of the glass slide beamsplitter to the CCD camera. (c) Analysis of red line row of image from (a) showing Gaussian fit of datapoints between maximum derivative amplitudes to extract beam radius w.

2.3 Peak analysis algorithm

A Matlab program is used to extract fluorescent peaks above the background noise level from the multi-channel photon counting scaler trace signals. The particle detection threshold in a channel is set as the maximum photon count per bin from control traces at the same power, plus one photon. This threshold is typically a few photons per 1.3-ms bin for unlabeled cells flowing in PBS with 12 mW laser power (at the objective focus). For a control run equal in length to the data run, this is generally a stricter requirement than just a mean and five or six standard deviations of the control set photon counts. The program scans the trace signals for fluorescent peaks above the detection threshold. Once a peak is located, the peak characteristics, including height (maximum fluorescent signal within the peak), width (FWHM or number of consecutive bins above the background threshold) and location (the index of the maximum bin) are stored. The beginning and end of a peak are determined by crossings of the background threshold value, set as the mean plus a standard deviation of photon counts from the control run at the corresponding power. A double-peak event is treated as a single event if the fluorescent signal between the two peaks does not fall below the background threshold value. Though resolution of up to 2 ns is achievable on the multichannel scalers, 1.3-ms bins are chosen so that all photons from a single cell fall within the duration of a single bin, for maximal signal-to-noise. For two-channel measurements, the data from each channel are analyzed independently and combined by arrival time.

The flow rate of whole blood in the glass capillary is highly varialbe, which produces a more variable background than the corresponding experiment with cells flowing in PBS. Thus analysis of whole blood data is performed adaptively in one kilobyte intervals (1.34 s of flow for 1.31 ms bins). Initially, background mean $\mathbf{m}_e$ and standard deviation σ_e estimates are calculated from bins with less than half the maximum photon count. Estimated events are then extracted employing background threshold $\mathbf{m}_e + \sigma_e$ and peak detection threshold value an additional 3 σ_e higher. All bins of data outside of estimated events are used to calculate the true background mean $\mathbf{m}$ and true standard deviation σ. A background threshold value $\mathbf{m} + \sigma$ and peak detection threshold of $\mathbf{m} + 4\ \sigma$ are then used to find the actual events.

2.4 Cell preparation

Untransfected MCA-207 cells and MCA-207 cells stably transfected with GFP were kindly provided by Dr. Kevin McDonough at the University of Michigan. They were labeled with DiD (Invitrogen) according to the manufacturer's protocol. After labeling, cells were resuspended in PBS or bovine whole blood with 10 units/mL heparin (Pel-Freeze Biologicals) for two-photon flow cytometry. Cells resuspended in PBS were used for conventional flow cytometry.

2.5 Conventional flow cytometry

Prior to flow cytometry analysis, stained cells were washed three times in phosphate buffered saline (PBS) containing 0.1% bovine serum albumin (BSA) and resuspended in 1 ml of washing buffer. The acquisition was performed on a Beckman-Coulter EPICS-XL MCL flow cytometer. Collected data were analyzed using Expo32 software (Beckman-Coulter, Miami, FL).

2.6 Calculations

Simple geometrical models are used to interpret the signals from the two different laser sources. We calculate the expected fluorescence emission for a cell flowing through the beam focus with different spatial distributions of fluorophore and varying incident laser powers as follows. Let us define a right-handed x-y-z Cartesian coordinate system with z the axial direction of the propagating laser beam and x the direction of laminar fluid flow in the capillary. Let $B(x,y,z)$ be the square intensity of the laser beam at each point in space. We assume this beam is Gaussian. Figure 3.12a shows an example of B as a function of y and z at the x=0 plane (center of the capillary) for a beam waist radius w of 2 μm ($1/e^2$ point). Figure 3.12b shows surfaces of constant intensity in all 3 spatial dimensions for the same Gaussian beam.

Let $S(x,y,z)$ be the distribution function of fluorophores in an object centered at the origin. For GFP expressed uniformly throughout a cell centered on the origin, we can approximate S as unity within a radius R of the origin, 0 elsewhere. For DiD, bound to the membrane, S is modeled as a thin shell of thickness t with outer radius R. The object will not in general be centered at the origin. Let (x0,y0,z0) be a variable for the location of the center of the fluorophore-containing object. Thus, the distribution function of

fluorophore for the object situated in the defined x-y-z coordinate system is *S*(x-x0,y-y0,z-z0*)*. It follows that the instantaneous net two-photon fluorescent signal from the object centered at (x0,y0,z0) is proportional to:

$$\iiint S(x-x_0, y-y_0, z-z_0)B(x,y,z)dxdydz$$

Figure 3.12c shows an example of the spatial distribution of signal from an infinitesimally thin shell situated at (x0,y0,z0) = (5,5,0) μm in the Gaussian beam (waist w = 2 μm).

As an object in the capillary undergoes laminar flow within the x-y-z coordinate system, its center position (x0,y0,z0) will be displaced in the x-direction, and thus the x0 value increases directly with time. During this period, the signal will change. Figure 3.12d shows the anticipated instantaneous signal for a shell centered at y0 = 5 μm, z0 = 0 μm as a function of different points of x0 origin, representing flow through the capillary. The double-peak event with broad base emphasizes the reason for choosing an experimental data collection binwidth which will include all photons from the passing object. Note that the separation between the peaks will depend on the z0 position of the shell, which defines the position of the object relative to the propagation axis z of the laser beam. The total signal obtained from an object flowing through the laser focus is the integral of the instantaneous signal at each traversed position during the period of observation. Thus, we calculate the net observed signal from the object by summing over all the x0 positions that the object traverses as its center translates in the x-direction during flow:

$$Signal = k\iint\iint S(x-x_0, y-y_0, z-z_0)B(x,y,z)dxdydzdx_0 \qquad (1)$$

Here, k is a constant less than 1 taking into account quantum efficiency, collection efficiency, and any other scaling factors.

If the integral is extended over all space (rather than just the capillary volume), then the order of integration can be interchanged, and the integral of S over x_0 will be independent of x. This is a valid assumption since points outside of the capillary do not contribute fluorescent signal. Thus the integration over x_0 and x can be separated for *S* and *B*, and this motivates the definition of new functions freed of these variables through integration, IS^N(y,z) and *IB*(y,z), defined as follows:

$$IB(y,z) \equiv \int B(x,y,z)dx$$

$$\begin{aligned} IS^N(y_0 - y, z_0 - z) &\equiv \int S(x - x_0, y - y_0, z - z_0)dx_0 \\ &= \int S(-x_0, y - y_0, z - z_0)dx_0 \\ &= \int S^N(x_0, y_0 - y, z_0 - z)dx_0 \end{aligned} \quad (3)$$

where the superscript N denotes inversion about the origin of spatial argument coordinates to *S*. Note that the prefix *I* refers to an integrated function, not to intensity. For a Gaussian, *IB* could be written explicitly in terms of the error function. Thus the flowed object's total signal is merely the two-dimensional convolution of the x-integrated functions IS^N(y,z) and *IB*(y,z):

$$\begin{aligned} &k\iint IS^N(y_0 - y, z_0 - z)IB(y,z)dydz \\ &= k\,IS^N \otimes IB\Big|_{(y_0, z_0)} \end{aligned} \quad (4)$$

Representative forms of these integrated functions are shown in Figure 3.13.
In practice, extremely thin shells require prohibitively large matrices to calculate *IB* to sufficient resolution to avoid numerical digital artifacts. In this event, the calculation can be done by either (a) oversampling the periphery of IS^N (near $y0^2+z0^2 = R^2$) or (b) merely recalculating the B matrix at a uniform sampling of points from the shell centered about (y0,z0) and using the original equation (1). The latter calculation is accelerated by assuming a uniform distribution of fluorophore over the thin shell, which removes the product operation in (1).

For each possible origin (y0, z0) in the capillary cross-section, we calculate the anticipated net signal from the flowing object (Figure 3.14). Henceforth, "short channel" will refer to the simulated GFP signal from a uniform distribution of fluorophore over a 10 μm radius sphere, and "long channel" will refer to simulated DiD signal from a uniform distribution of fluorophore over a 10 μm radius, 0.5 μm thick shell. These assumptions of distributions are made from the known expression of GFP throughout the cytoplasm of the cell, and binding of DiD only to the membrane at the irregular surface of the cell. The beam waist, from the spot-size measurement, is

assumed to have a radius w of 2 μm. The signal level is scaled into a photon count by normalization to the brightest single event in the corresponding channel of the two-photon flow cytometry data. The simulated detection threshold can also be taken from the compared two-photon flow data.

3. Results and Discussion

3.1 Dye solution signal enhancement with extended cavity

We begin by checking the enhancement of the fluorescence signal in a dye solution, and indeed we find the expected approximate four-fold improvement for the extended cavity laser relative to the 76-MHz laser. This enhancement is modestly exceeded in the 3.3 μM solution of the biological dye Fluorescein Isothiocyanate (FITC), flowed through the capillary at 0.3 mL/hour (Figure 3.6a). The fluorescence signal is proportional to the square of the exciting power as expected.

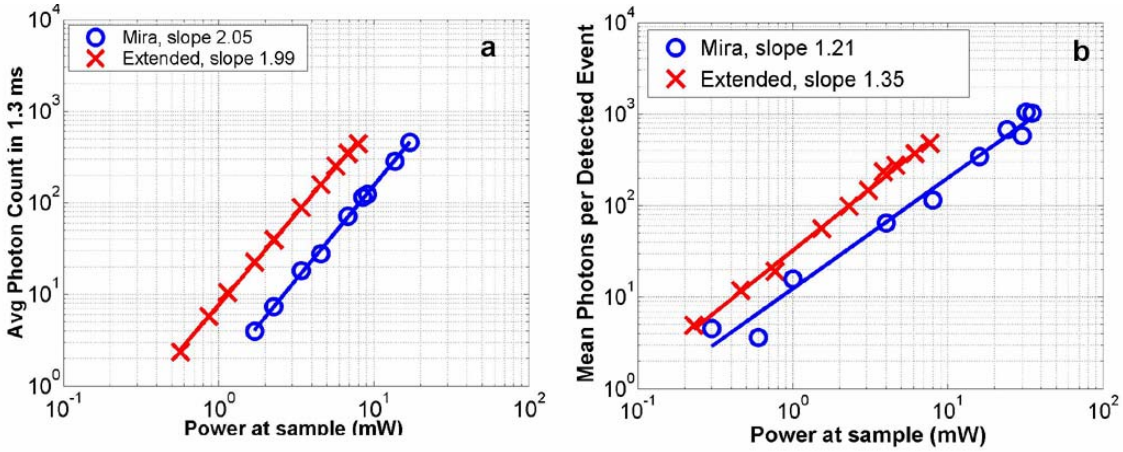

Figure 3.6 (a) Fluorescence emission under extended cavity or Mira laser pulses for a fluorescein-filled capillary, with power-law fits intersecting 10^0 axis at 7.6 (xtnd) or 1.4 (Mira) for a 5.7-fold enhancement. (b) Mean fluorescence of detected 2 μm yellow-green microspheres with 20-MHz or 76-MHz oscillators, with power-law fits intersecting 10^0 axis at 32.7 (xtnd) or 12.4 (Mira) for a 2.6-fold enhancement. Best-fit power laws are 1.4 and 1.7 when only brightest 100 events at each power (of ~800) are selected.

3.2 Fluorescent bead signal enhancement

We next investigate the enhancement of fluorescence in polystyrene beads. We flow a uniform suspension of 2.0 μm yellow-green fluorescent spheres (Ex505/Em515) (Molecular Probes). The mean fluorescence of detected events shows significant sub-square law power scaling with both the 20-MHz and 76-MHz lasers (Figure 3.6b). The difference in best-fit power laws further manifests itself as a less than 4-fold fluorescence signal enhancement at low incident laser power.

We also confirm that the interaction length is consistent with single bead detection. The mean event duration is five 40.96 μs bins (FWHM). At the 0.3 mL/hr

flow rate in the 100 μm square capillary, this corresponds to a 2.4 μm mean interaction length per 2 μm bead. Thus, single fluorescent microspheres are resolved by a two-photon detection region with lateral dimensions on the order of a micron.

3.3 Dual-labeled fluorescent cells

To investigate the enhanced ability of the extended cavity laser to detect cells *via* expressed fluorescent protein, we flow dual-labeled (GFP-expressing and DiD-labeled) MCA-207 cells in PBS and count the number of detected events and mean brightness thereof. The DiD staining serves as a control for the number of cells flowing through the two photon excitation region. We repeat the experiment in whole bovine blood to mimic the autofluorescent background of a noninvasive *in vivo* experiment. We did notice a significant decrease in the average brightness of the detected GFP cells when they were stained with DiD, which further increases the difficulty of detection (Figure 3.7).

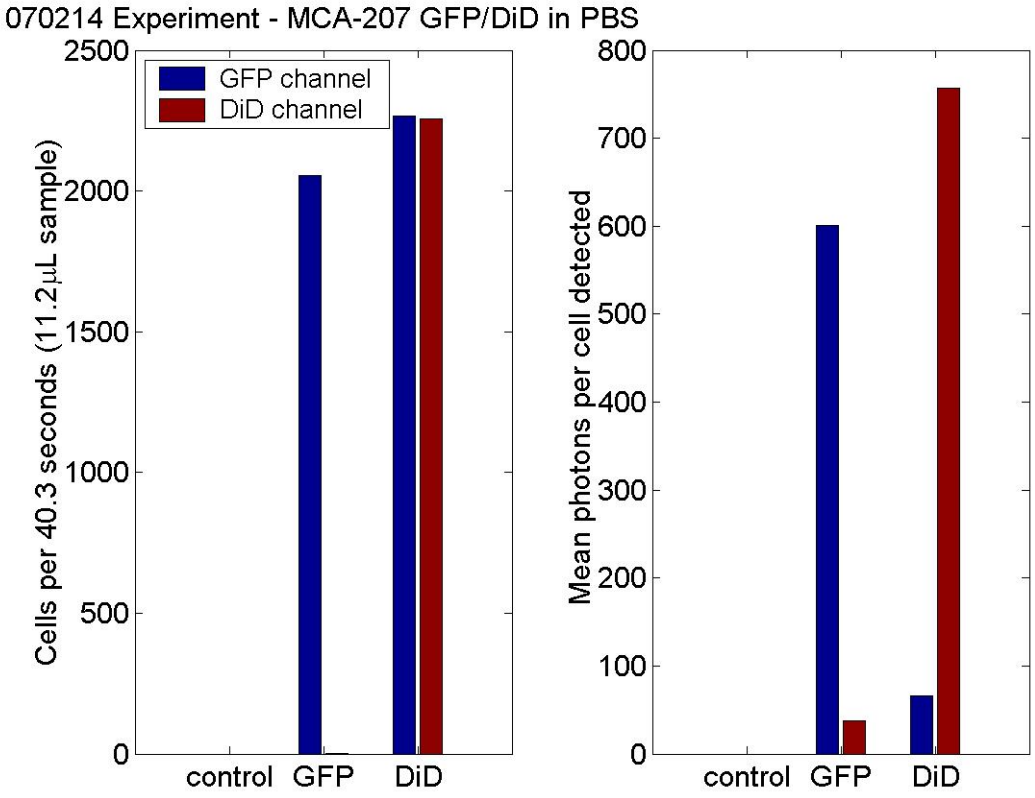

Figure 3.7 Decrease in GFP signal when cells are cross-labeled with DiD. (left) Number of cells detected in each channel for 11 μL of control, GFP, and GFP-DiD cells. (right) Mean brightness (collected photons) for detected cells, under excitation by Mira.

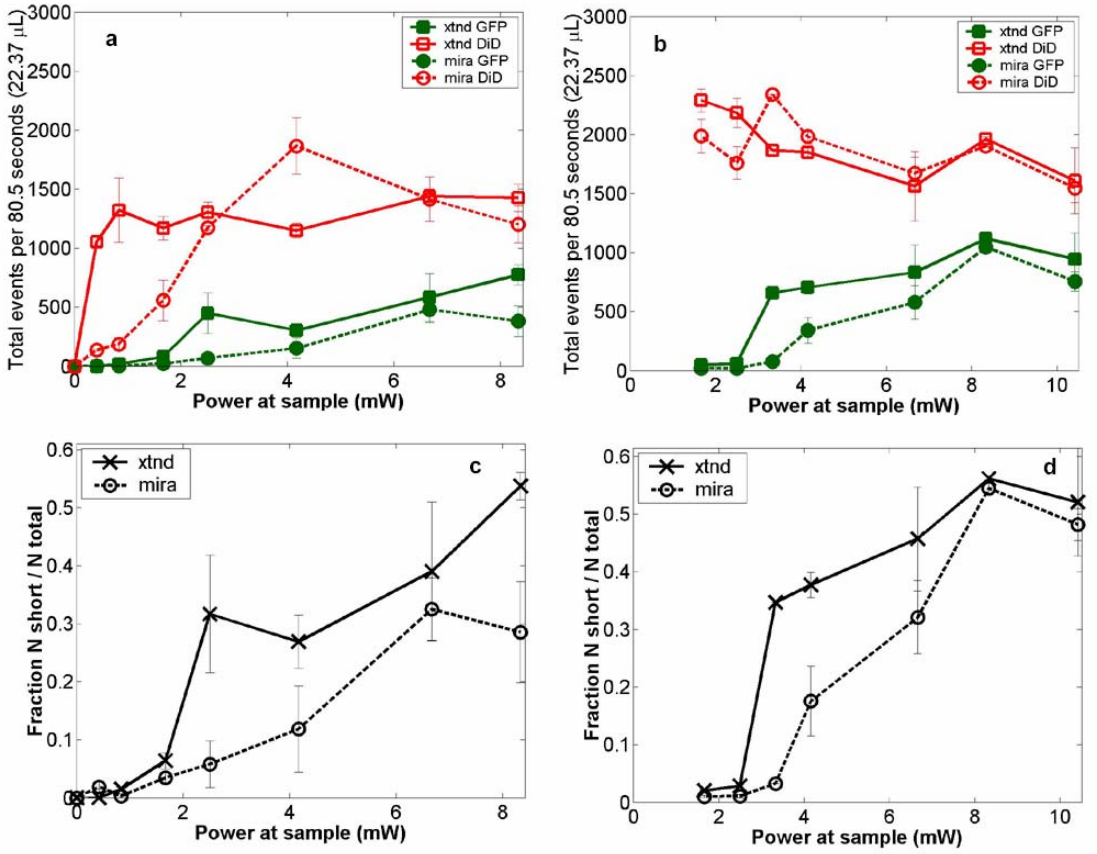

Figure 3.8 The total number of events detected in two channels over 6 repetitions of a 13.4 s two-photon flow cytometry measurement of dual-labeled MCA-207 cells in (a) PBS or (b) blood at varying powers. Error bars are 6 times the standard deviation of these measurements (because summed data over 6 repetitions is shown). Ratio of total counted events (in either or both channels) giving a detectable GFP signal are shown in (c) PBS and (d) blood.

The number of detected events in PBS and blood are plotted versus average incident laser powers for both sources (20-MHz or 76-MHz) in Figure 3.8. The sensitivity of detection *via* GFP is determined as the fraction of total events in either channel which are also detected in the short wavelength channel (into which GFP fluoresces). We observe a sigmoidal (s-shaped) curve of detection sensitivity *via* GFP versus average power in both PBS and blood (Figure 3.8c and Figure 3.8d). At high power, most cells are detected using either laser source. For maximal detection sensitivity near the detection threshold, this highly nonlinear nature implies a dramatic advantage for modest increases in fluorescent signal at low excitation power. We take as the detection threshold the minimum power where over 50% of the maximum fraction of GFP cells detectable is identified. In PBS, this is 2.4 mW for the extended cavity 20-

MHz oscillator and 6.4 mW for the Mira 76-MHz oscillator. In blood, this value increases to 3.2 mW for the extended cavity but remains at 6.4 mW for the Mira, and these values are statistically significant (more than a standard deviation separation).

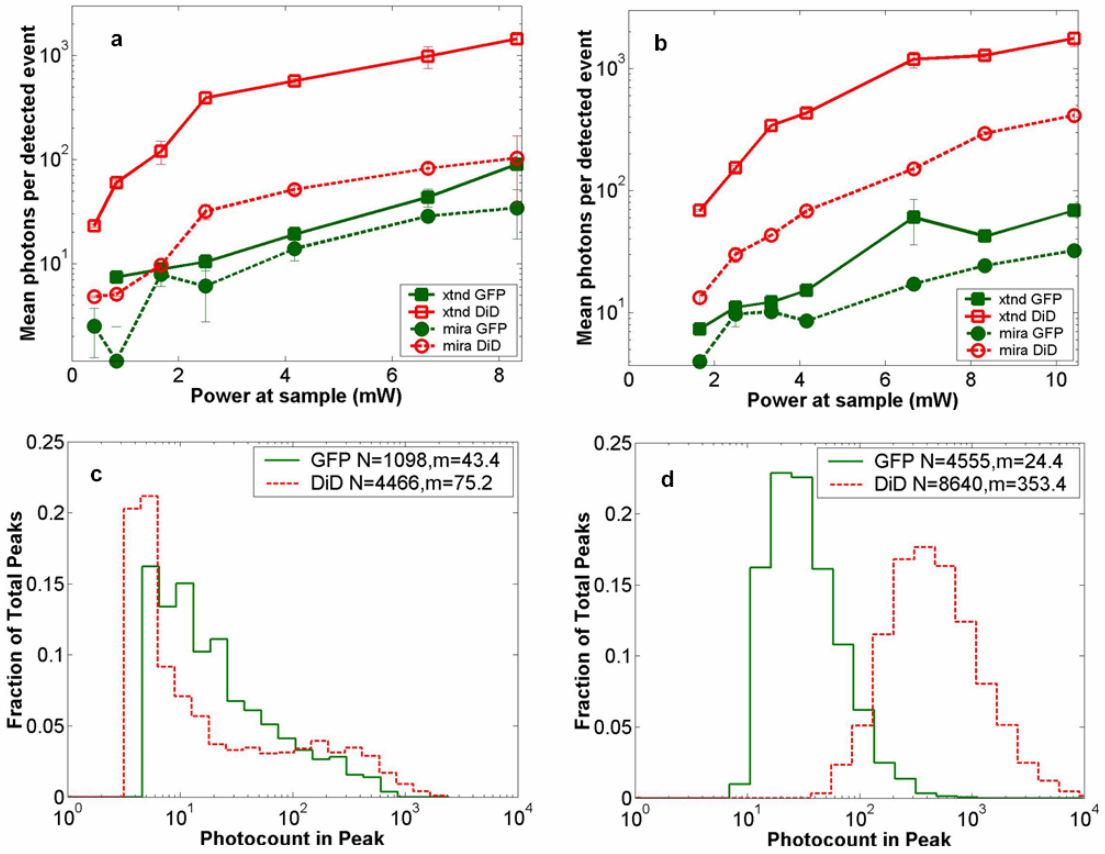

Figure 3.9 Mean photons per event detected in GFP and DiD channels for dual-labeled MCA-207 cells in (a) PBS or (b) blood with varying power. Error bars are a single standard deviation of these measurements. Power law fits are near 1.4 for PBS, 1.9 for blood. Distribution of detected event brightness for the ~8 mW Mira point are shown in (c) for PBS and (d) for blood (combined data of several experiment repetitions). Note detection thresholds of 5 (DiD) and 3 photons (GFP) in PBS, from a background measurement. Detection thresholds of 9 photons (GFP) and 147 photons (DiD) in blood were automatically determined by the processing algorithm, though the control file at the same power never exceeded 15 and 6 photons, respectively.

In all of our two-photon measurements of cells *ex vivo* in PBS, cell settling remains a complicating factor, limiting each sample to a few minutes at most of run time before recycling or replenishing the syringe pump with cells (Figure 3.10). The abnormally large count in the DiD channel at the 4 mW Mira excitation point of Figure 3.8a reflects this difficulty in controlling the flow of cells. Settling effects are abated significantly for cells suspended in the viscous whole blood solution. However, in

exchange, even under constant force of the syringe pump, the flow rate of blood through the long thin capillary is highly variable, often appearing to stop altogether for brief periods of time. Fortunately, we are able to normalize for this with two detection channels, as has also been the case for *in vivo* applications[24, 25].

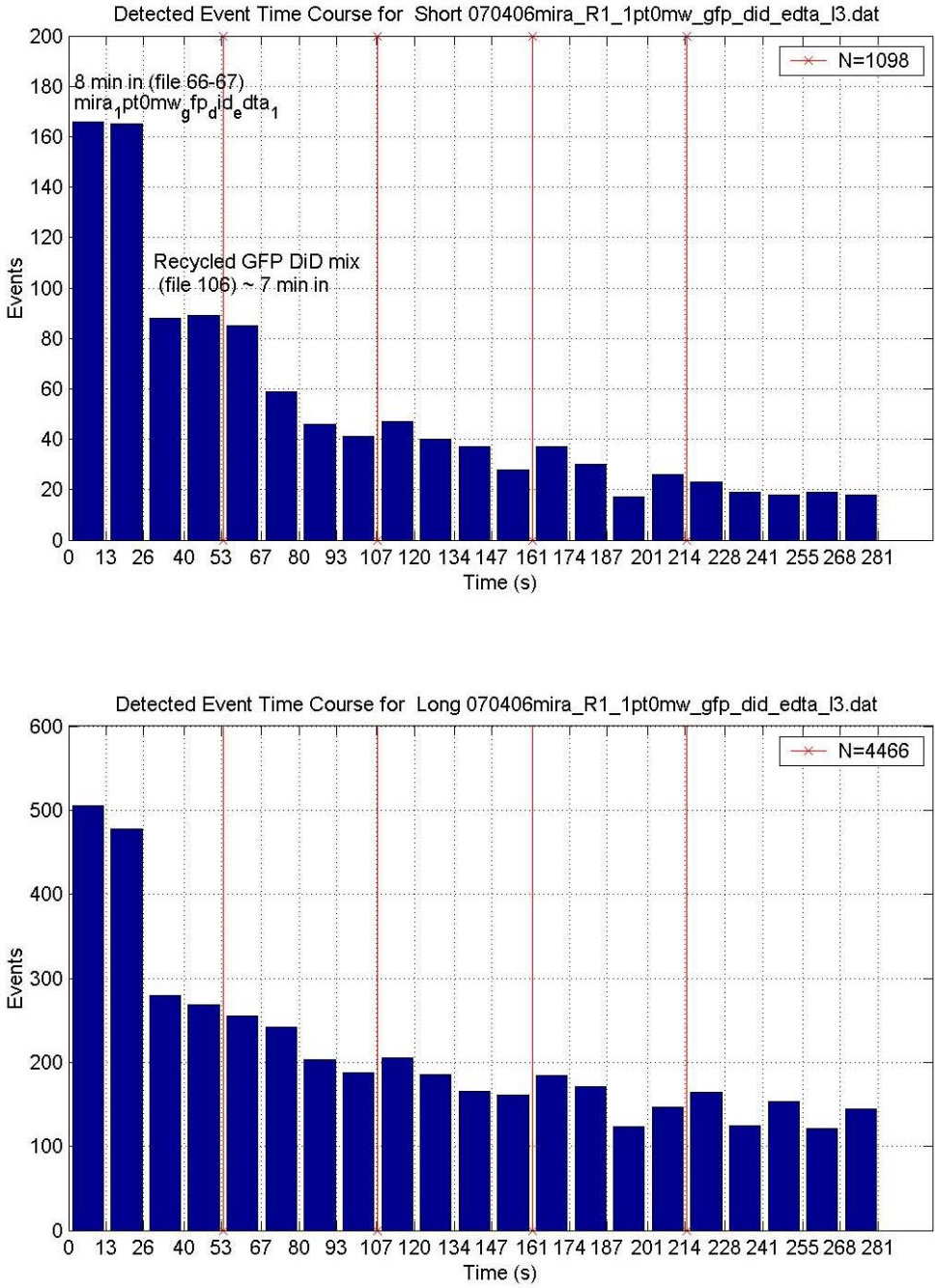

Figure 3.10 Evidence of cell settling during *ex vivo* multiphoton cytometry. Time course of number of events detected in both channels over approximately 20 minutes of steady volumetric flow rate of dual-labeled cells in PBS.

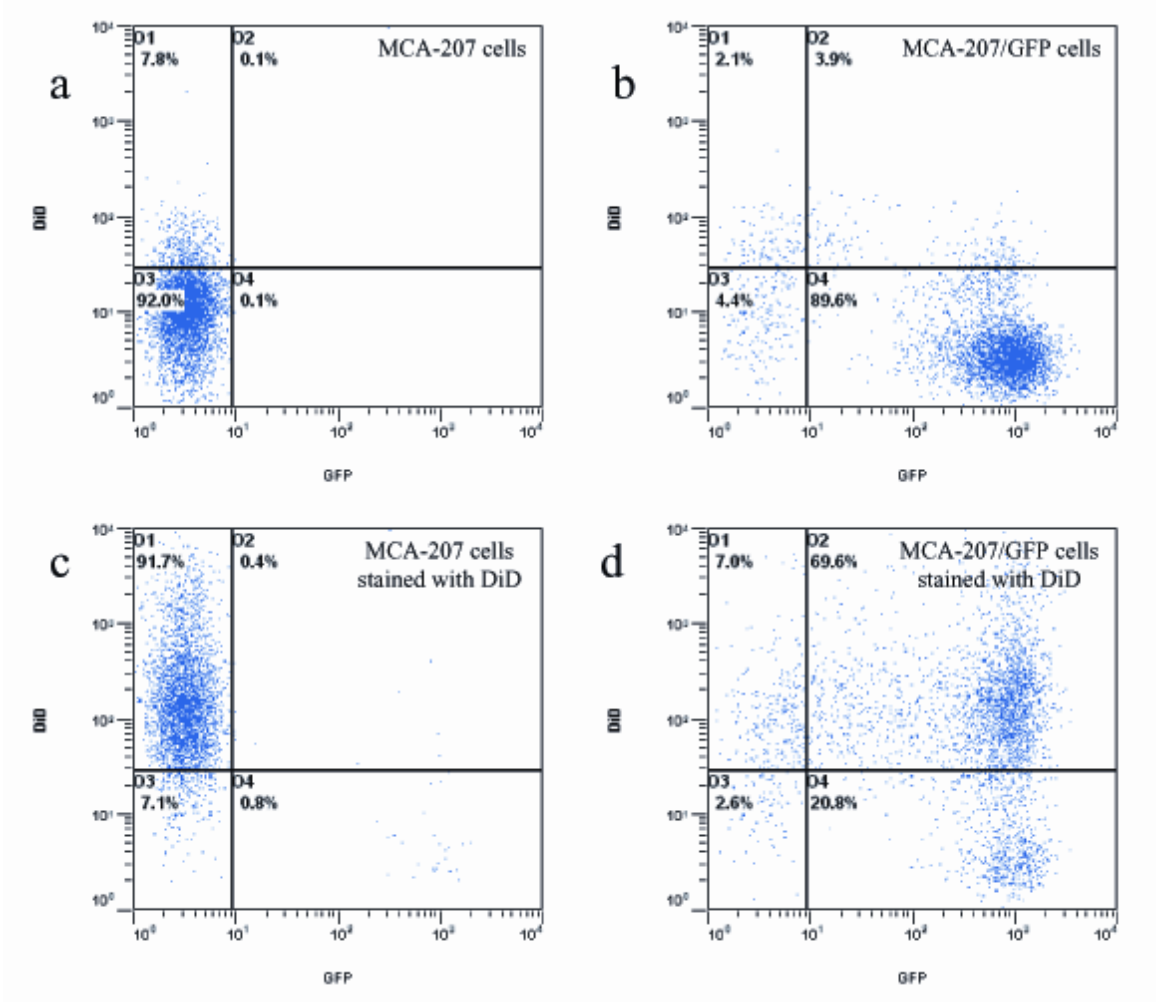

Figure 3.11 Conventional flow cytometry, with signal in GFP channel on the ordinate and DiD channel on the abscissa. (a) MCA-207 cells (b) GFP-expressing MCA-207 cells (c) MCA-207 cells labeled with DiD (d) dual-labeled MCA-207 cells.

That almost all cells passing through the two-photon excitation volume do appear in the DiD channel under all but the smallest excitation powers is corroborated by the data. Firstly, conventional flow cytometry (Figure 3.11) confirms in excess of 90% labeling efficiency of cells with DiD. Secondly, in rough calculation, the observed numbers are consistent with very high detection efficiency. The flowed concentration of cells is known to be near 1000 cells per μL. Assuming a cell diameter of 10 microns and a two-photon excitation region with x-axis 2 microns and z-axis 10 microns (e.g. the 0.3 level curve, Figure 3.12b), we find that on the order of 0.22 x 0.3, or 7 % of the total 100 μm^2 capillary cross-sectional area is interrogated. Therefore, expecting 70 interrogated cells per flowed μL of fluid and calculating flow volumes on the order of 20 μL during

the sampling period, we can confirm an expectation of about 1400 total events for each data point in Figure 3.8. Thus we assume that the DiD channel accurately represents the number of cells interrogated for almost all data points.

In both blood and PBS, mean brightness of detected events (Figure 3.9) shows a sub-square law scaling, with lower power-law fit in PBS (1.4) than in blood (1.9). The average brightness of detected GFP events is significantly greater in blood than in PBS, and this difference is statistically significant. Partly, this is due to periods of congested flow during which particles dwell in the laser focus for longer periods of time. This congestion also causes a variable background and prevents the use of one standard background measurement to determine thresholds in blood, in contradistinction to PBS.

Representative individual channel histograms of detected event brightness are shown for 10 mW incident power in Figure 3.9 (c and d). In PBS, both individual channel histograms peak at the detection threshold, and the DiD channel has an additional peak (near three hundred photons for 10 mW average exciting power). In contrast to those in PBS, dual-labeled cells detected in blood exhibit a single broad peak far above the detection threshold. The much higher adaptively determined detection threshold for DiD (147 photons for 10 mW incident power from the Mira) than GFP (9 photons) occurs despite the significantly lower background in the long channel than short channel on control blood measurements at the same power. This effect is due to biasing by many extremely bright events of DiD. Simply cutting the PBS histogram at these thresholds and spreading somewhat (due to piecewise data analysis) neatly accounts for the blood histograms; these histograms are asymmetric in the GFP channel to much greater extent than the DiD channel, which continues to enjoy its peak far above threshold. Conventional flow cytometry confirms approximately two orders of magnitude variation in cell fluorescent brightness (Figure 3.11).

3.4 Model calculations

Modeled calculations help interpret unique features in the dual-labeled cell experimental results. In particular, we find that the different geometry of fluorophore distribution can account for the histogram of detected event brightness and explain the sigmoidal shape of number of detected events versus average incident power, as well as the sub-square law scaling of mean brightness.

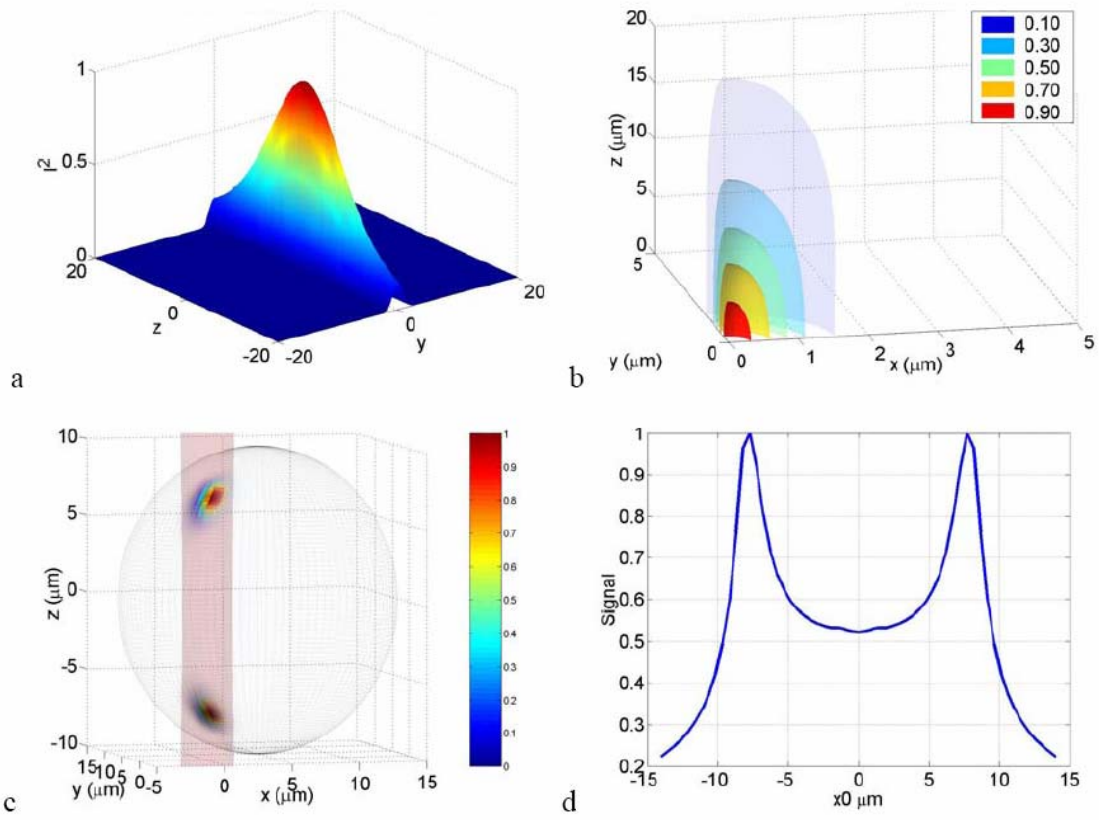

Figure 3.12 Calculation of expected signals. Here we have defined the right-handed x-y-z coordinate system with z the axial direction of the propagating laser beam and x the direction of fluid flow in the capillary. (x0,y0,z0) is a variable for the location of the center of the fluorophore-containing object. (a) Magnitude of the beam squared-intensity function B in the x=0 plane for a beam waist radius w of 2 μm ($1/e^2$ point). (b) Various level sets of B in 3 spatial dimensions. (c) Instantaneous signal (arbitrary units) for a 10 μm infinitesimally thick spherical shell centered at (x0,y0,z0) = (5,5,0) μm in a Gaussian beam (waist w = 2 μm). (d) Signal (arbitrary units) for a shell centered at (x0,y0,z0) = (x0,5,0) μm as a function of x0 origin, which increases as the object flows in the x-direction. Net signal is the integral of the curve.

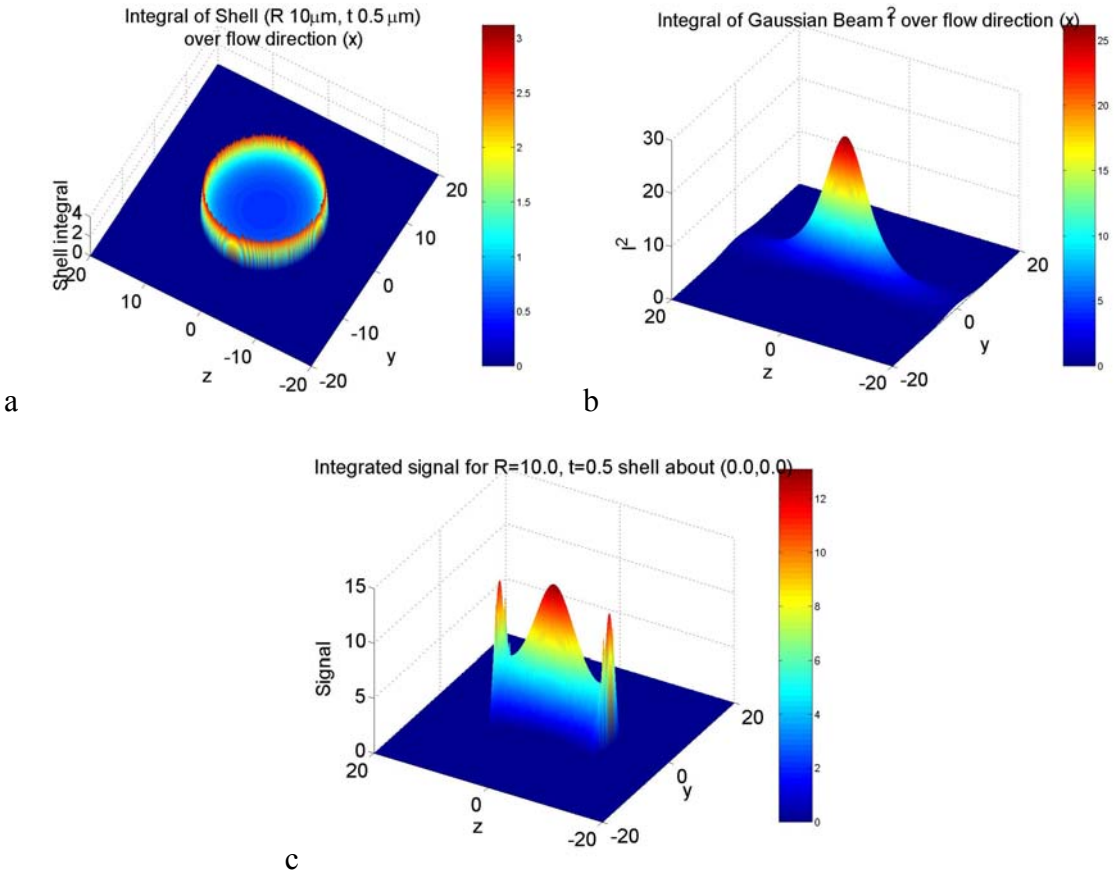

Figure 3.13 (a) Integrated fluorophore distribution function $IS^N(y,z)$ for a 10 μm radius R, 0.5 μm thickness t shell about (y0,z0) = (0,0). (b) Integrated Gaussian beam squared-intensity function $IB(y,z)$ for a 2.0 μm spot size. (c) The integrand for net signal from a shell centered on (y0,z0) is the product of $IS^N(y-y0,z-z0)$ and $IB(y,z)$, drawn here for (y0,z0) = (0,0). This is the integrated projection on the x-axis of Figure 3.12c as the shell flows down x

Calculations on a sphere and shell predict, for each possible origin in the capillary cross-section, the signal level in the GFP channel (Figure 3.14c, sphere) or DiD channel (Figure 3.14d, shell). The calculated distribution of signal in these two channels (Figure 3.15) essentially maps the area between various level sets of the curves in Figure 3.14. For a sphere, there is a large peak in events near the minimum signal level, and a second minor peak at moderately low signals, whereas for a shell, the primary peak is at slightly higher signals than the minimum, and there is a pronounced second peak at higher signals, in reasonable agreement with the experimental results for dual-labeled cells in PBS (Figure 3.9c). This heterogeneity of distributions manifests itself as a lack of correlation between the intensities of both channels on a scatter plot (Figure 3.14c), which is confirmed experimentally (Figure 3.14d).

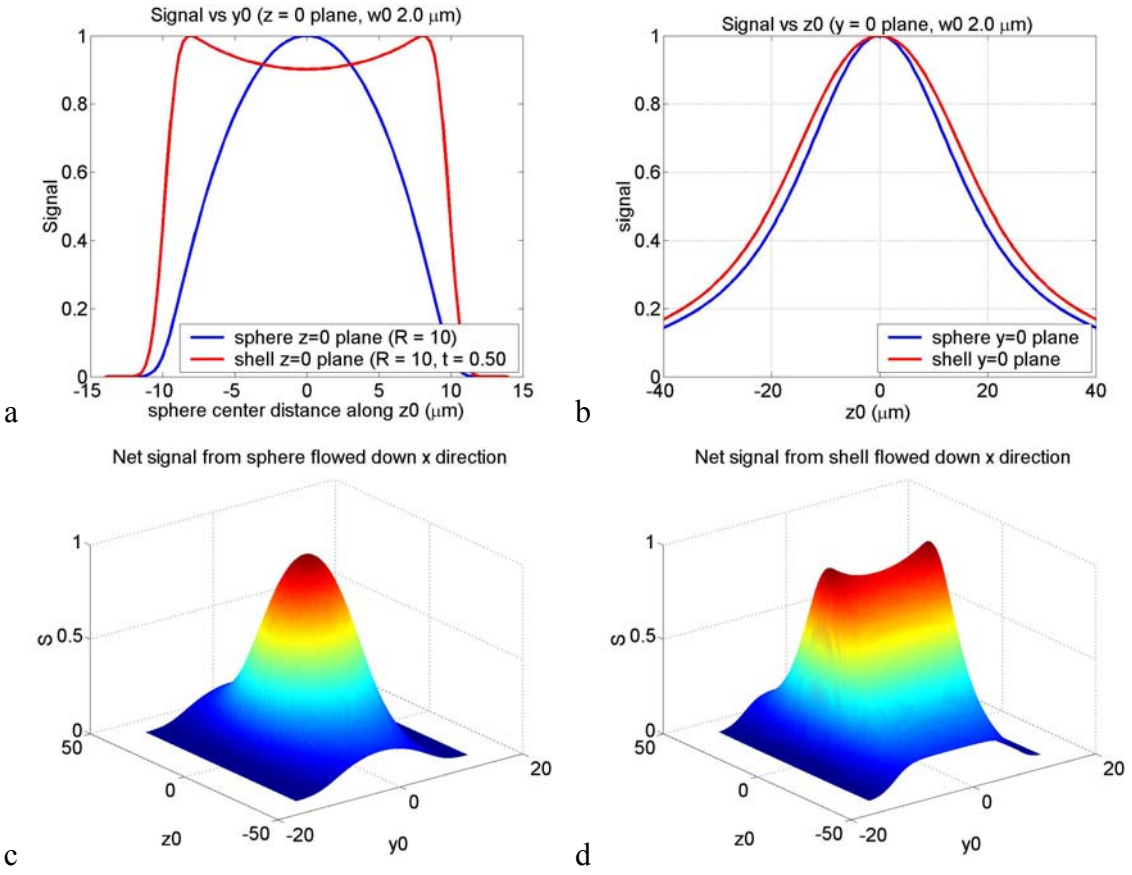

Figure 3.14 Net signal (arbitrary units) from 10.0 μm radius sphere (blue) or shell (t = 0.5 μm, red) with different origins (y0,z0) in the capillary cross-section, flowed down the x direction. Beam propagates in z direction with a 2.0 μm spot size. (a) Signal vs y0 for z0 = 0. (b) Signal vs z0 for y0 = 0. (c) Signal from all possible origins for sphere. (d) Signal from all possible origins for shell.'

The sigmoidal curve for fraction of cells detectable via the weak fluorescent protein signal is realized theoretically by assuming a signal which varies with squared-laser-power from 0 to a set maximum, and a fixed minimum threshold for detection. For example, by assuming heuristically from experimental results that the Mira can generate up to 1000 photons from a DiD shell but only 100 from a GFP sphere, and also assuming background-determined detection thresholds of 10 and 4 photons, respectively, the curve of circles in Figure 3.16a is derived. Assuming five fold higher signals for extended cavity excitation (from Figure 3.6a), but the same detection thresholds, yields the left-shifted curve of x's in Figure 3.16a. In Figure 3.16b, an analogous calculation demonstrates that even with a GFP signal precisely as strong as the DiD signal, and a

single photon detection threshold, the sigmoidal curve shape of detectability will be preserved for the same geometrical reasons. For no detection thresholds, including one single photon, will 100% of detected events be found in the sphere channel. Effectively, the detectable fraction is the area of the y0-z0 plane in Figure 3.14 above a certain finite signal level S, which with increasing incident power falls at a lower level relative to the maximum S. Nonlinearities are inherited from this signal landscape, leading to the observed sub-quadratic scaling of the two-photon signal. These nonlinearities can also lead, under different conditions, to more interesting features in the detection plots, as seen in Figure 3.17.

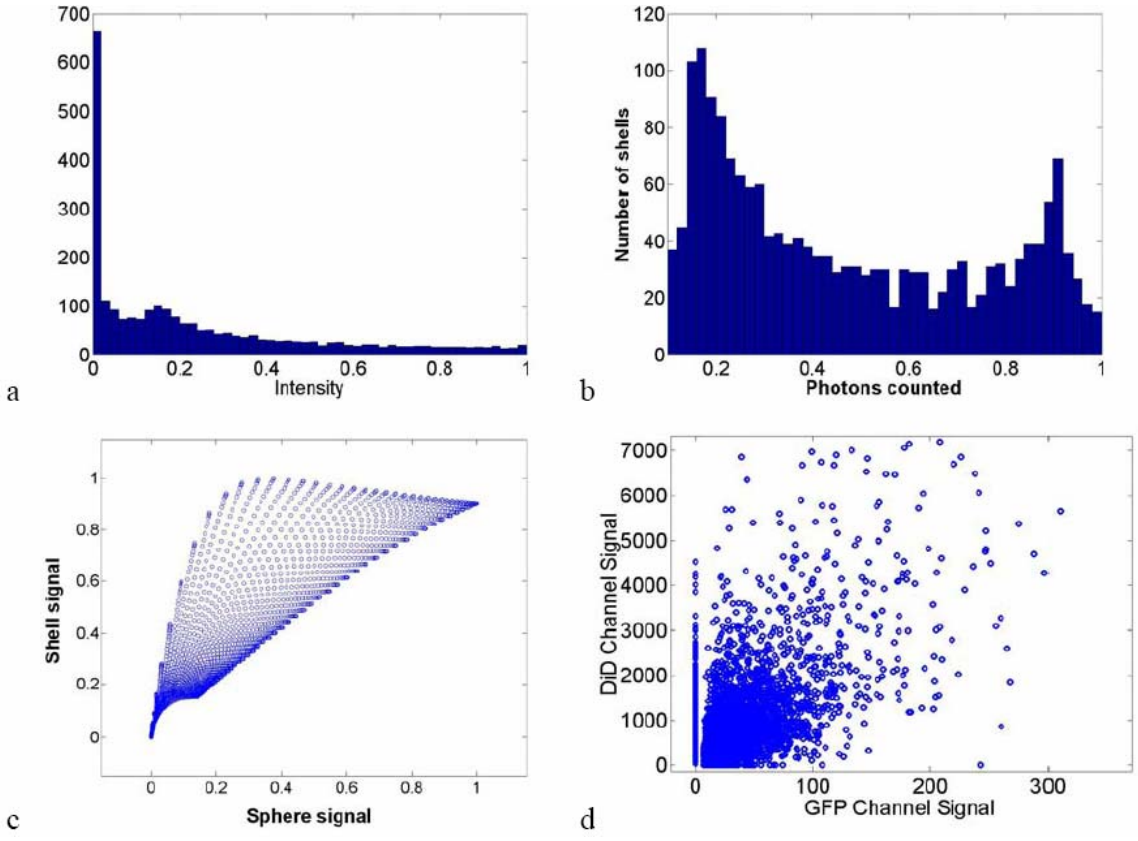

Figure 3.15 Signal intensity distributions extracted for (a) sphere (GFP channel), (b) shell (DiD channel), and (c) scatter plot between the two channels. (d) Scatter plot of GFP vs DiD detected events in 4(d), under 8 mW average excitation power from the Mira.

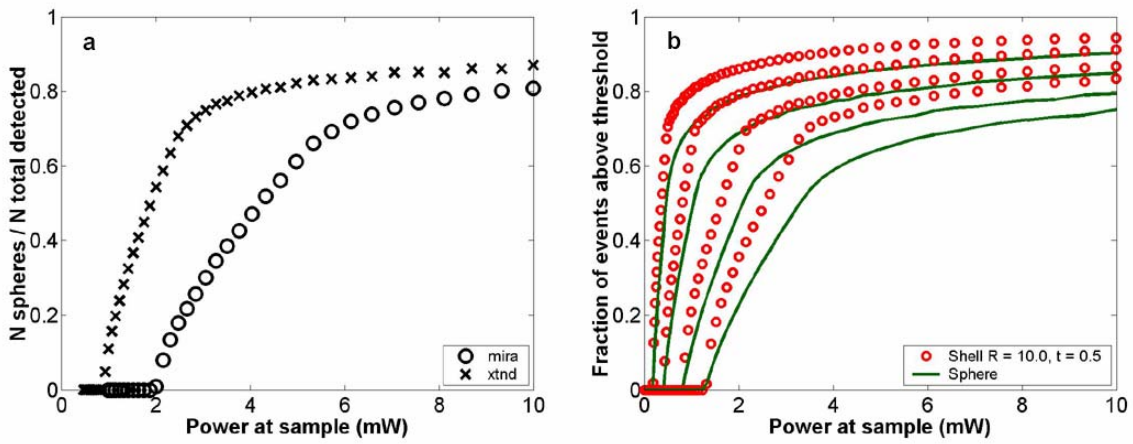

Figure 3.16 (a) Simulated fraction of total detectable events identified in the GFP channel for a fixed detection threshold of 4 photons for GFP, 10 photons for DiD, at varying laser powers (signal levels). Maximum signal produced at the highest incident laser power from the Mira is 100 photons for GFP, 1000 photons for DiD (circles), or five times higher maximum signal strength for the same incident laser power from the extended cavity (x's). (b) Simulated fraction of total detected events appearing above threshold in the DiD (circles) or GFP (lines) channel for a 3000 photon maximum achievable signal at highest incident laser power and a fixed detection threshold of 1, 5, 20 or 50 photons.

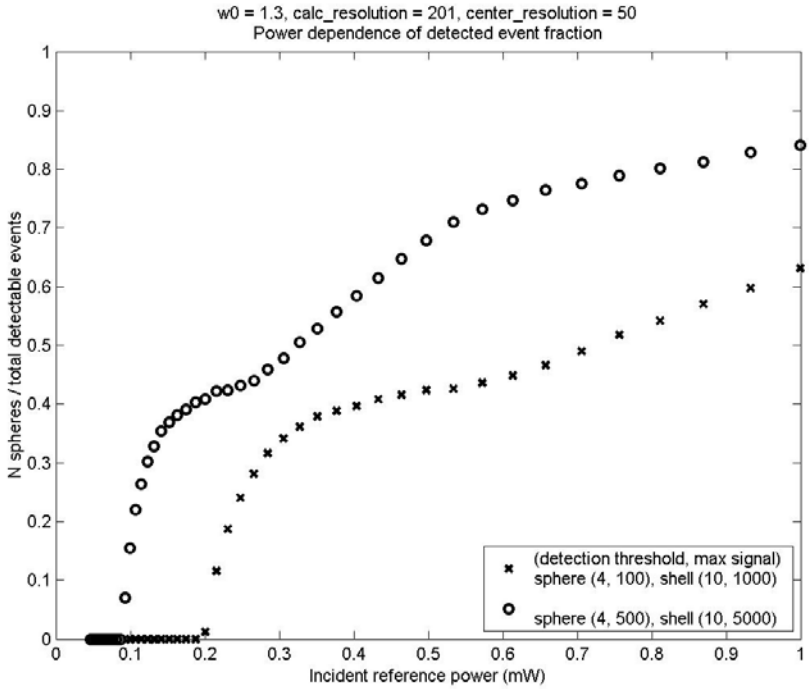

Figure 3.17 Repetition of simulation of Figure 3.16 with laser spot size reduced to 1.3 microns.

Figure 3.18 shows the anticipated GFP sphere (solid line) and DiD shell (open circles) fluorescent signal power-dependence based on the same heuristically determined maximum signals, in excellent qualitative agreement with the observed curves in Figure 3.9 (a and b). Detected solid sphere median brightness also shows a strong sub-square law fit as observed in the original fluorescent microsphere experiments (Figure 3.6b).

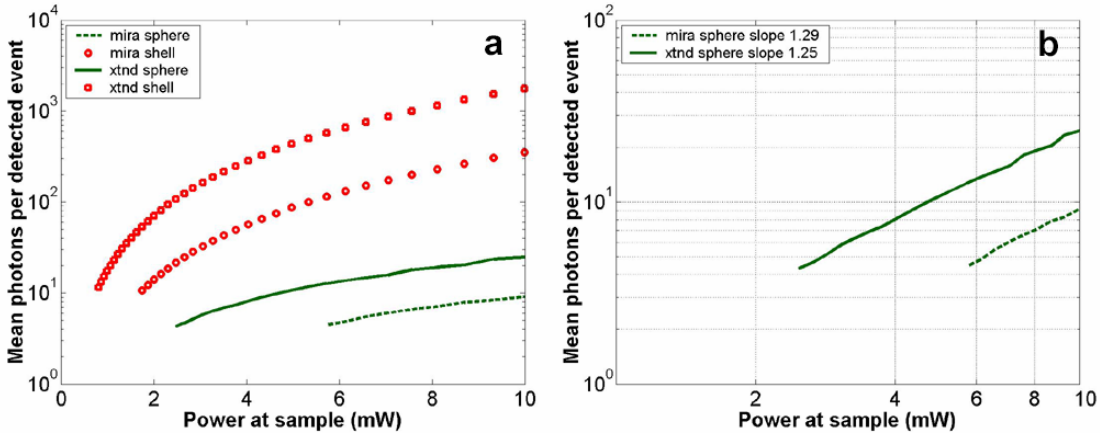

Figure 3.18 (a) Simulated median brightness of detected GFP spheres (line) or DiD shells (open markers) for Mira or extended cavity laser source. Calculation parameters as in Figure 3.15. (b) Note that the best-fit power-curve on a log-log scale exhibits a slope of 1.25 (1.29) for spheres with the extended cavity (Mira).

4. Conclusions

Traditionally, the major limitation on optical detection methods has been the average power that can be delivered to the sample at focus without damage. The present investigation demonstrates an extended cavity oscillator as a useful modification to enhance fluorescent signal from live biological samples in a two-photon flow cytometer at fixed power.

In a simple flowing fluorescent dye solution, the anticipated four-fold signal enhancement by the 20-MHz oscillator relative to a 76-MHz system is met, and anticipated square-law power scaling is followed. However, the signal for flowing fluorescent microspheres obeys a sub-square power law, which can be understood as a geometrical effect (Figure 3.16). For increasing excitation intensity, the detectable two-photon excitation region becomes larger, subsuming more dim events (in the cooler-colored regions of Figure 3.12b). It is noteworthy that this effect will be present even without any noise or background, due to the requirement of at least an entire fluorescent photon emission for object detection. Similar geometrical effects, though less pronounced, would similarly affect the power-scaling of detection signal for any multiphoton or even single photon fluorescence detection scheme whereby the entire capillary cross-sectional area is not uniformly excited above threshold.

For GFP-expressing cell detection, the fraction of all flowed cells (determined with the aid of DiD in the long channel) which can be detected in the short (GFP) channel displays a sigmoidal shape. This curve can be derived heuristically from simple geometrical models (Figure 3.16), which also help account for the lack of correlation in signal strength between the two detection channels (Figure 3.15c). The highly nonlinear detection curve results in a critical detection threshold, where even a modest improvement in signal via innovations such as an extended cavity laser can dramatically enhance the sensitivity of the system. GFP-expressing cells were chosen for detection explicitly for this reason: due to their emission in the highly absorbing region of blood, overlapped as well with blood's autofluorescence, they lie at the threshold of detection for single cell *in vivo* measurements.

Multiphoton approaches have proven to be very useful for noninvasive microscopy applications[26,27]. Recent work of He *et al.* also underscores the utility of the multiphoton methodology as well for monitoring CTCs arising spontaneously from a tumor xenograft and labeled *in vivo* with folate-FITC. Whereas in their study, 200 fs pulses with 80 mW (35 mW) average power enabled detection of Rhodamine (DiI) tags *in vivo*, shorter pulses (85 fs) can successfully detect circulating cells *in vivo* at average powers below 20 mW. It should also be noted that NIR ultrashort laser pulse damage behavior to cells has empirically been observed to obey a P^2/τ dependence, where P is average power, and τ is pulse duration, pointing to a two-photon damage process[28]. Damage induced by the defocused beam outside of the interrogation region remains a matter of speculation. However, studies of the viability of embryos through two-photon microscopy, but not confocal, have indicated likely confinement of damage to the interrogated region in any nonlinear microscopy system[29].

The significantly improved sensitivity of the two-photon flow cytometer with the extended cavity oscillator laser excitation source could open new avenues of biomedical investigation. Enhanced ability to detect GFP in whole blood will further empower cancer metastasis investigations in mouse tumor models. Enhanced sensitivity to shorter wavelength dyes will also assist the ultimate goal of noninvasive *in vivo* human monitoring.

References

1. S. Meng, D. Tripathy, E. P. Frenkel, S. Shete, E. Z. Naftalis, J. F. Huth, P. D. Beitsch, M. Leitch, S. Hoover, D. Euhus, B. Haley, L. Morrison, T. P. Fleming, D. Herlyn, L. W. Terstappen, T. Fehm, T. F. Tucker, N. Lane, J. Wang and J. W. Uhr, "Circulating tumor cells in patients with breast cancer dormancy," *Clin. Cancer Res.* **10**, 8152-8162 (2004).
2. J.B. Smerage and D.F. Hayes, "The measurement and therapeutic implications of circulating tumour cells in breast cancer." *Br. J. of Cancer* **94**, 8-12 (2006).
3. L.W. Terstappen *et al.*, "Flow cytometry-principles and feasibility in transfusion medicine. Enumeration of epithelial derived tumor cells in peripheral blood," *Vox Sang.* **74** (suppl. 2), 269-274 (1998)."
4. V. Ziegelschmid, C. Hollman and O. Bocher, "Detection of disseminated tumor cells in peripheral blood." *Crit. Rev. Clin. Lab. Sci.* **42**, 155-196 (2005).
5. S. Kraeft *et al.*, "Reliable and sensitive identification of occult tumor cells using the improved rare event imaging system," *Clin. Cancer Res.* **10**, 3020-3028 (2004).
6. R. T. Krivacic, *et al.* "A rare-cell detector for cancer," *Proc. Natl Acad. Sci. USA* **101**, 10501-10504 (2004).
7. S. Nagrath *et al.*, "Isolation of rare circulating tumour cells in cancer patients by microchip technology," *Nature* **450**, 1235-1239 (2007).
8. A.G.J. Tibbe, M.C. Miller, L.W.M.M. Terstappen, "Statistical considerations for enumeration of circulating tumor cells," *Cytometry A* **71**, 154-162 (2007).
9. G. Vona, A. Sabile, M. Louha, V. Sitruk, S. Romana, K. Schütze, F. Capron, D. Franco, M. Pazzagli, M. Vekemans, B. Lacour, C. Brechot and P. Paterlini-Brechot, "Isolation by size of epithelial tumor cells: a new method for the immunomorphological and molecular characterization of circulating tumor cells," *Am. J. Path.* **156**, 57-63 (2000).
10. M. Cristofanilli, G. T. Budd, M. J. Ellis, A. Stopeck, J. Matera, M. C. Miller, J. M. Reuben, G. V. Doyle, W. J. Allard, L. W. Terstappen and D. F. Hayes, "Circulating tumor cells, disease progression, and survival in metastatic breast cancer," *N Engl J Med* **351**, 781-791 (2004).
11. C.F. Zhong, J.Y. Ye, A. Myc, T.P. Thomas, A.U. Bielinska, J.R. Baker, Jr., and T.B. Norris. "Two-photon Flow Cytometry," *Proceedings of SPIE*, **5700**, 78-89 (2005)
12. E. R. Tkaczyk, C. F. Zhong, J. Y. Ye, S. Katnik, A. Myc, K. E. Luker, G. D. Luker, J. R. Baker, Jr., and T. B. Norris, "Two-photon, Two-color *in Vivo* Flow Cytometry to Noninvasively Monitor Multiple Circulating Cell Lines," *Proceedings of SPIE*, **6631-31**, (2007).

13. E. R. Tkaczyk, C. F. Zhong, J. Y. Ye, A. Myc, T. Thomas, Z. Cao, R. Duran-Struuck, K. E. Luker, G. D. Luker, T. B. Norris and J. R. Baker, Jr., "*In Vivo* Monitoring of Multiple Circulating Cell Populations Using Two-photon Flow Cytometry," *Optics Communications*, **281**, 888-894 (2008).

14. S. Boutrus, C. Greiner, D. Hwu, M. Chan, C. Kuperwasser, C. Lin and I. Georgakoudi, "Portable two-color in vivo flow cytometer for real-time detection of fluorescently-labeled circulating cells," *J. Biomed. Optics* **12**, 020507 (2007).

15. W. He, H. Wang, L. Hartmann, J. Cheng and P. Low, "*In vivo* quantitation of rare circulating tumor cells by multiphoton intravital flow cytometry," *PNAS* **104**, 11760-11765 (2007).

16. L. Wang, W.C. Jackson, P.A. Steinbach and R.Y. Tsien, "Evolution of new nonantibody proteins via iterative somatic hypermutation," *PNAS* **101,** 16745-16749 (2004).

17. N. Shaner, R.E. Campbell, P.A. Steinbach, B.N.G. Giepmans, A.E. Palmer and R.Y. Tsien, "Improved monomeric red, orange and yellow fluorescent proteins derived from Discosoma sp. Red fluorescent protein," *Nature Biotech.* **22**, 1567-1572 (2004).

18. N. Shaner, P.A. Steinbach and R.Y. Tsien, "A guide to choosing fluorescent proteins," *Nature Meth.* **2**, 904-909 (2005).

19. T. Kogure, S. Karasawa, T. Araki, K. Saito, M. Kinjo, and A. Miyawaki, "A fluorescent variant of a protein from the stony coral *Montipora* facilitates dual-color single-laser fluorescence cross-correlation spectroscopy," *Nature Biotech.* **24**, 577-581 (2006).

20. D. Shcherbo, E.M.M. Merzlyak, T.V.V. Chepurnykh, A.F.F. Fradkov, G.V.V. Ermakova, E.A.A. Solovieva, K.A.A. Lukyanov, E.A.A. Bogdanova, A.G.G. Zaraisky, S. Lukyanov and D.M.M. Chudakov, "Bright far-red fluorescent protein for whole-body imaging," *Nature Methods* **4**, 741-746 (2007).

21. C. F. Zhong, E. R. Tkaczyk, T. Thomas, J. Y. Ye, A. Myc, A. U. Bielinska, Z. Cao, I. Majoros, B. Keszler, J. R. Baker, Jr. and T. B. Norris, "Quantitative Two-Photon Flow Cytometry – *in Vitro* and *in Vivo*," *Journal of Biomedical Optics*, in press.

22. M.T. Myaing, J. Urayama, A. Braun, and T.B. Norris, "Nonlinear Propagation of Negatively Chirped Pulses: Maximizing the Peak Intensity at the Output of a Fiber Probe," *Optics Express* **7**, 210 (2000).

23. S. H. Cho, B. E. Bouma, E. P. Ippen and J. G. Fujimoto. "Low-repetition-rate high-peak-power Kerr-lens mode-locked TiAl2O3 laser with a multiple-pass cavity." *Opt. Lett.* **24**, 417-419 (1999).

24. C. F. Zhong, E. R. Tkaczyk, J. Y. Ye, A. Myc, T. Thomas, Z. Cao, R. Duran-Struuck, K. E. Luker, G. D. Luker, T. B. Norris and J. R. Baker, Jr., "*In Vivo* Monitoring of Two Circulating Cell Lines Using Two-color Two-photon Cytometry," in CLEO/QELS and PhAST 2006 (OSA, Long Beach, CA, May 21-26, 2006), CMH3.

25. E. R. Tkaczyk, J.Y. Ye, S. Katnik, A. Myc, K. E. Luker, G. D. Luker, J. R. Baker, Jr. and T. B. Norris, “Enhanced Two-photon in Vivo Flow Cytometry with an Extendeed Cavity Laser,” in CLEO/QELS and PhAST 2007 (OSA, Long Beach, CA, May 7-11, 2007), CTuP.

26. W. R. Zipfel, R. M. Williams and W. W. Webb, "Nonlinear magic: multiphoton microscopy in the biosciences," *Nat. Biotechnol.* **21**, 1369-1377 (2003).

27. K. König, "Multiphoton microscopy in life sciences," *J. Microsc.* **200**, 83-104 (2000)

28. K. König, T. W. Becker, P. Fischer, I. Riemann and K. J. Halbhuber, "Pulse-length dependence of cellular response to intense near-infrared laser pulses in multiphoton microscopes," *Opt. Lett.* **24**, 113-115, (1999).

29. J. M. Squirrell, D. L. Wokosin, J. G. White and B. D. Bavister, "Long-term two-photon fluorescence imaging of mammalian embryos without compromising viability," *Nat. Biotechnol.* **17**, 763-767 (1999)

CHAPTER 4
INCREASING TWO-PHOTON FLUORESCENCE SIGNALS BY COHERENT CONTROL

Abstract. Two-photon excitation fluorescence of complex solvated molecules was successfully controlled using adaptive pulse shaping. We were able to maximize and minimize the ratio of fluorescent yield to average incident power or second-harmonic generation (SHG) in a thin optical crystal. The optimal excitation pulse shape was found experimentally using a genetic learning algorithm and no *a priori* knowledge. Pulses were shaped with an acousto-optic programmable dispersive filter (Dazzler AOPDF) controlling phase and amplitude of 20 individual frequency components. Convergence occurred over the order of 100 generations of experiments from an original set of 50 random individual pulses. Femtosecond laser pulses (~75 fs, 76 MHz repetition, 800 nm center wavelength, 3nJ without shaping) selected to maximize fluorescence yield / SHG were found to be complementary to those minimizing this ratio when visualized with a SHG-frequency resolved optical gating (SHG-FROG) device. At these powers, linear chirp of the pulse was far less significant in establishing coherent control than the more complex pulse shape. Regeneratively amplified pulses (~150 fs, 20 kHz repetition, 795 nm center wavelength, 0.2 μJ before shaping) were selected for maximum efficiency of fluorescent yield relative to incident power. The peak intensity, as determined by SHG, did not change significantly for optimal pulses when compared to early generations. This indicates that the improved two-photon fluorescent signal was not the result of simple convergence to a transform limited pulse, and suggests that the dye molecule excited state population is being coherently controlled. We are currently investigating the application of this result to enhancing signal in flow-cytometry and improved discrimination for multi-photon microscopy.

1. Introduction

Multiphoton fluorescence is widely used for biomedical microscopy, *in vivo* sensing, and more recently, flow cytometry.[1] At present, discrimination of different fluorescent species is accomplished mainly by differences in emission spectra, and it is difficult to distinguish different fluorophores with significant spectral overlap. In principle, different fluorophores should be distinguishable based on their optimal control (excitation) pulses. For well-characterized hypothetical[2] and even some real quantum systems such as Cs gas[3], the optimal pulses to control transitions between two levels can be precisely predicted and applied. However, the interest in complex systems such as those commonly found throughout biology has lead to the advent of closed-loop adaptive learning algorithms to crack coherent control problems with no *a priori* knowledge. Recently, Pastirk *et al.* were able to demonstrate pH-sensitive two-photon microscopy based on coherent control with such an adaptive learning algorithm.[4]

Highly selective excitation of different quantum mechanical systems with similar one-photon absorption properties could also find medical applications. Poly(amidoamine) (PAMAM) dendrimers are an emergent technology showing great promise in cancer therapy and diagnostics. These dendrimers have been shown to alter the physical properties of many systems, including the common dye fluorescein isothiocyanate (FITC) conjugated to a fifth generation dendrimer (G5-FITC).[5] Towards such applications, we investigate here the possibility of performing coherent control at low and high intensity adaptively shaped femtosecond laser pulses on unconjugated FITC, G5-FITC, and Rhodamine dyes.

As Brixner *et al.*[6,7] have already achieved on other systems, we were able with unamplified oscillator pulses to control the ratio of fluorescence to second-harmonic generation (SHG) emission, with a similar degree of control. Maximization and minimization of the fluorescence to SHG ratio in our investigations resulted in complementary pulses when these experiments are run in parallel. This is somewhat consistent with the investigation of $[Ru(dpb)_3]^{2+}$ by Brixner *et al.*, who found many complementary areas for optimal pulses with a peak intensity on the order of 10^{11} W/cm^2. They, however, found that minimization of fluorescence to SHG resulted predominantly in a nearly transform-limited pulse with removed frequency components. At incident

fluences estimated at 5 x 10^{-4} J/cm^2 per pulse, we found as Brixner *et al.* that maximization of fluorescence yield to incident power converged on a short pulse maximizing peak intensity (estimated on the order of 10^{10} W/cm^2 for a diffraction-limited, transform-limited pulse). However, with regeneratively amplified pulses at two orders magnitude higher intensity, maximization of fluorescence yield appeared to occur without any increase in peak intensity as reflected by SHG from a thin optical crystal.

The limiting factor in the degree of coherent control we achieve is the tendency of the genetic algorithm to converge to low powers to truly minimize the measurement selected against in the ratiometric fitness parameter. To curtail this process, we set a lower bound that the genetic algorithm can approach for the minimized measurement before the fitness is penalized. By adjusting the limit of what we define as a legitimate fitness parameter ratio denominator, we are able to achieve arbitrarily high increases in fitness of our coherent control experiments. The trade-off between signal level and the ability to selectively suppress an undesired multiphoton process has been insightfully explored through a variably nonlinear cost function by Midorikawa *et al.*[8] They used a similar oscillator setup to our own to improve two-photon fluorescence from EGFP while suppressing three-photon fluorescence from the essential amino acid L-Tryptophan.

For one-photon transitions in dyes like LD690 and LDS750, Cerullo *et al.*[9] have previously shown the ability of positively chirped pulses at intensities of 10^9 W / cm^2 to enhance excited state populations by approximately a factor of two, and, conversely, negatively chirped pulses to deplete these populations via the "pump-dump" mechanism. Extrapolating this to our investigation of two-photon fluorescence, we would expect a positive chirp to enable strong improvement of fluorescence to SHG ratio by enhancing fluorescence while stretching the pulse and thereby decreasing SHG. This is in marked contrast to our finding that adjustments in polynomial phase and in particular linear chirp contribute relatively little to coherent control of this ratio. Cerullo *et al.* found no chirp-related improvement at estimated intensities of 10^7 W / cm^2. We are currently in the process of following this work with a comprehensive study at high power.

2. Materials and Methods

2.1 Experimental setup

Concentrations of ~ 1 x 10^{-5} M Rhodamine 590 BF4 (Exciton chemical company) in deionized water, Fluorescein (FITC) in 100% ethanol, and G5-dendrimer-conjugated FITC (G5-FITC) were prepared as described previously.[5] The experimental setup is shown in Figure 4.1. The laser system consists of a homebuilt Ti:sapphire oscillator providing ~75 fs, 3 nJ pulses at a center wavelength of 800nm, approximately 15nm FWHM bandwidth, and a repetition rate of 76 MHz. For high power experiments, the pulses are regeneratively amplified on a homebuilt "regen" system previously described[10] to 0.2 μJ pulses at 20 kHz with a center wavelength of 795nm and 15nm FWHM bandwidth. The "Dazzler," an acousto-optic programmable dispersive filter[11,12] (AOPDF) (Fastlite, Palaiseau, France), then is used to shape the laser pulses. Typical optimally shaped pulse energies after the Dazzler are estimated at 5e-10 J for the oscillator and 2e-8 J for the regen. A glass coverslip acting as a 4% splitter enables a reference reading of incident power I_{ref} by photodiode PD1. After 50% beamsplitting, one arm of the beam is focused by a 15 mm focal length, 6.3 mm diameter achromatic doublet lens into the dye sample, and the fluorescence signal I_{flr} is detected by a photomultiplier tube (PMT1). The other arm is focused by a duplicate lens into a thin BBO crystal for second-harmonic generation (SHG), which is detected by another PMT to read I_{shg}. All three signals I_{flr}, I_{ref}, and I_{shg} are read in parallel by a 250 kHz DAQ board, which is also set to trigger the Dazzler at 20 kHz. Each data point for the regeneratively amplified pulses comes from precisely one laser pulse, whereas multiple oscillator pulses arrive within the response time of the electronics for the lower fluence experiments. 1000 data points, all at the same time delay after Dazzler triggering, are averaged together to give a single reading. Thus, each measurement of a specific dazzled pulse requires 50 ms. After completion of the averaged reading for a specific individual pulse shape, the controlling genetic algorithm (GA) programs the Dazzler for the next individual, closing the loop for the iterative improvement of the laser pulse shape by the adaptive learning algorithm.

Assuming a diffraction-limited beam waist, we estimate a fluence on the order of 5 x 10^{-4} J/cm^2 (peak intensity ~10^{10} W/cm^2 transform-limited) at the laser focus in the dye sample for the oscillator pulses, and 5 x 10^{-2} J/cm^2 (peak intensity ~10^{12} W/cm^2 transform-limited) for the regeneratively amplified pulses. These are high end estimates, and we expect that the actual power at the sample could be significantly lower if the diffraction limit is not achieved.

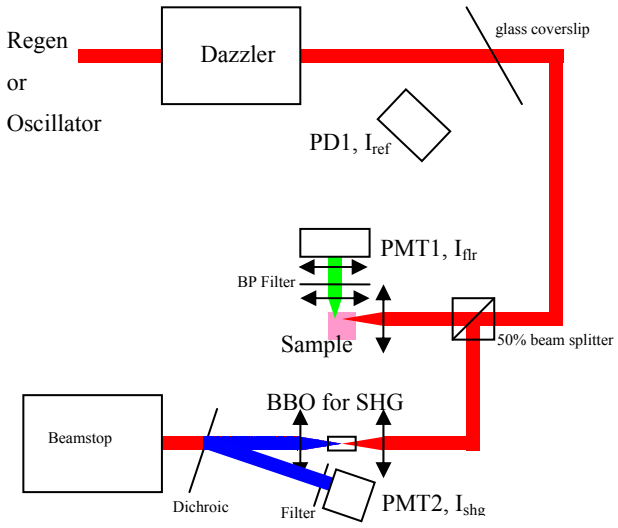

Figure 4.1 Experimental Setup. The dye sample is contained in an optical glass fluorescence cuvette (Cole Palmer). Incident laser power I_{ref} is measured by photodiode PD1 (PDA55, Thorlabs). After filters to remove all pump laser and exciting 800 nm light, the fluorescence signal I_{flr} in the perpendicular direction is collected and focused with a two lens system for detection by PMT1 (H5784-01, Hamamatsu). SHG from the thin BBO crystal is detected by PMT2 (R2066, Hamamatsu). Optimal pulses were later reconstructed by replacing the glass coverslip with a commercial SHG-FROG device (Grenouille, SwampOptics). Lenses are depicted as double-arrowed lines.

2.2 Genetic algorithm

A genetic learning algorithm is used to find an optimal shaped pulse for coherent control. The results of the experiment are very different depending on what fitness parameter is picked (Table 1). If one looks simply at two-photon excited fluorescence, the I_{flr} signal for low incident fluences is always maximized by a transform-limited pulse. In order to investigate the possibility of genuine coherent control of a molecule and not just maximizing excitation by increasing peak pulse intensity, we employ as a fitness parameter the ratio of two second-order processes: two-photon fluorescence and second-harmonic generation SHG.

Table 4.2 Notations for experiments optimizing different fitness parameters.

Detected Signal Name	Description	Experiment name	Fitness parameter optimized
I_{flr}	two-photon fluorescence	flr	I_{flr} / I_{ref}
I_{ref}	incident laser beam intensity	shg	I_{shg} / I_{ref}
I_{shg}	SHG emission	flrshg	I_{flr} / I_{shg}
		shgflr	I_{shg} / I_{flr}

The genetic algorithm relies on two-point crossover and mutation operators. Briefly, for each of 20 frequency components, the Dazzler was programmed to vary phase from 0 to 2π and amplitude from 0 to 1 depending on the corresponding gene. Four additional redundant genes modify 4^{th} order polynomial phase within the Dazzler's limits. Finally, there is also a gene controlling the power of the diffracted beam, for a total of 45 genes creating a single chromosome, which corresponds to exactly one shaped pulse and completely describes an individual in the population.

One of the possible fitness parameters in Table 4.1 is picked for a given experiment. For the first generation, an initial population of 50 random individuals is created and sequentially expressed by the Dazzler for measurement. The top 10 individuals, as determined by the fitness parameter, are passed from the old generation on to the next generation unchanged. The remaining individuals of the new generation are determined by a two-point crossover mating of individuals picked from the old generation with probability equal to their relative scaled fitness. This mating is implemented in the same manner as Pearson *et al.* have described[13], with a slight modification of chromosome circularization. To prevent location on the chromosome from favoring any genes or groups of genes, the first gene is treated as the adjacent neighbor of the last gene of the chromosome. After two-point crossover, each gene of an offspring is mutated (i.e. replaced with a completely random gene uniformly distributed in the possible range) with a certain probability mp. To keep this process in check, there is a probability 1-mp that the offspring will not be given the chance for mutation at all. The new population is then sequentially expressed by the Dazzler and measured, and the algorithm thus continues iteratively in pursuit of an optimal pulse shape.

For the purposes of these experiments, we discovered that a mutaton percentage mp of about 20% provided an optimal balance between quickly exploring the vast phase space while not easily losing outstanding individuals to excessive mutation. Noting the limitation of homogeneity in the population to progression of the algorithm out of a local minimum, for each generation we actually scaled the mutation percentage by the standard deviation of the population in the preceding generation to ensure a fairly random population with a variance in genes of 1/12 (the variance of uniformly distributed random variables).

As a check of stability of the laser and experimental conditions, for each population at every generation, two additional unvarying individuals, the "noise_individual" and the "test_individual," were tested. The test_individual's chromosome encodes for a pulse exactly self-compensating the Dazzler, which is the only major dispersive element in the optical system before the sample, and thus the test-individual provides an approximation of the transform-limited pulse. The noise_individual encodes for a zero power pulse from the Dazzler, thus providing a background offset to subtract from the measurements if necessary.

For maximum concurrence of experimental conditions, as many as four different populations were interleaved into the experimental sequence and tracked with different fitness parameters independently to allow parallel processing of multiple experiments.

Finally, to ensure tolerable SNR of the readings, a noise_limit parameter was set for any divisor in the fitness parameter. Any individual whose actual divisor reading fell below this value, usually defined as 5% of the corresponding reading in that generation of the transform-limited test_individual, was penalized by adjusting this value to the noise_limit, thereby denying it the fitness gained by going to low signals. The noise_limit was almost invariably reached by the optimal individuals of each generation.

2.3 Pulse retrieval

It should be noted that the Dazzler's expression of genes for phase and amplitude of each frequency component is not pure in that modification of either phase or amplitude prescriptions can affect *both* phase and amplitude of surrounding wavelengths. As we were thus unable to precisely predict the pulse that a given set of genes would produce, we characterized pulses with a commercial SHG-FROG unit[14] (Grenouille from

SwampOptics, VideoFrog software from MesaPhotonics). Our attempts to perform phase-only modulation merely resulted in slower convergence of the algorithm to similar pulses as phase and amplitude modulation achieved. This is one regard in which our study differs from the similar liquid-phase control experiments existing in the literature.

SHG-FROG was typically performed within 8 hours of termination of the experiment to ensure maximum similarity of the pulse reproduced with the selected individual's genes to that actually employed in the experiment. However, it was noted that even several days later, the SHG-FROG traces did not vary perceptibly for reproduction of a fixed set of genes, with reproducibility of the actual measurements being somewhat more finicky.

3. Results and Discussion

The algorithm as implemented here is robust to laser instabilities. Although we only present results for stable experimental conditions, the GA has reproducibly and steadily converged upon significant coherent control of flrshg and shgflr even under greater than 20% fluctuations in I_{shg} and I_{flr} for the test_individual.

A typical result for G5-FITC is shown in Figure 4.2 and Figure 4.3. Analogous results were obtained for Rhodamine and unconjugated FITC as well. Equivalently for a fitness parameter of either flr (I_{flr} / I_{ref}) or shg (I_{shg} / I_{ref}), convergence occurred within several dozen generations to a short pulse (Figure 4.2). For shg or flr, our initial algorithm did not absolutely achieve the conversion efficiency of a transform-limited pulse. This indicated that in searching the full parameter space, the algorithm did not discover the obvious possibility of selecting the four genes for a perfect polynomial phase to compensate the chirp of dispersive elements in the optical system. All subsequent runs of the algorithm relied on an improved graded search algorithm which always achieved the transform-limited pulse for either fitness parameter.

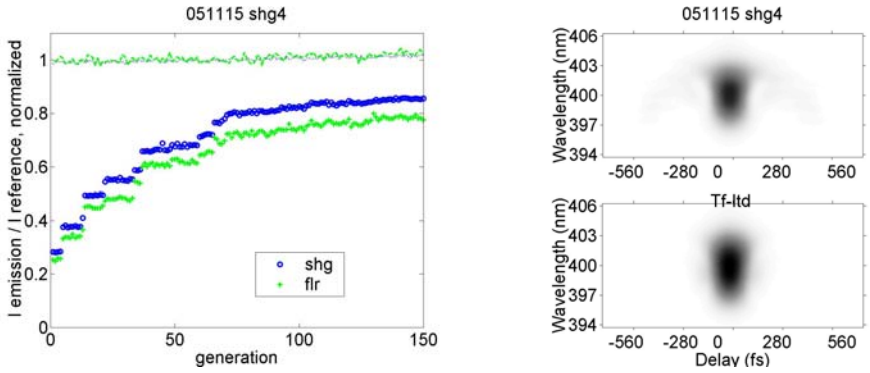

Figure 4.2 Maximization of SHG conversion efficiency as fitness parameter for initial genetic algorithm applied to G5-FITC. Left: learning curve for shg experiment. For best individual of each generation, blue circles show shg (I_{shg} / I_{ref}) and green plusses show flr (I_{flr} / I_{ref}). The dotted blue line and dashed green line show the same measurement at each generation of the test_individual, whose genes encode an approximately transform-limited pulse. All measurements are normalized to the corresponding test_individual measurement at generation 75. On the right top is the SHG-FROG trace from the optimum pulse at the last generation, with the transform-limited pulse on the bottom for comparison (grayscale, arbitrary units)

The modified algorithm employed a graded strategy to ensure that the forty remaining genes were not being wasted in trying to achieve the proper polynomial phase controlled by four genes. First, 5-10 generations were run with a restricted search that permitted variation only in the polynomial phase genes; after this the entire 45-degree parameter space was opened for searching. Typically, for experiments of the flr or shg fitness parameter alone, the optimum polynomial phase was reached already in the first or second generation. After this instantaneous convergence to optimal polynomial chirp, the best individual of all following generations in the algorithm achieved the maximum possible efficiency and remained transform-limited in the SHG-FROG reconstruction.

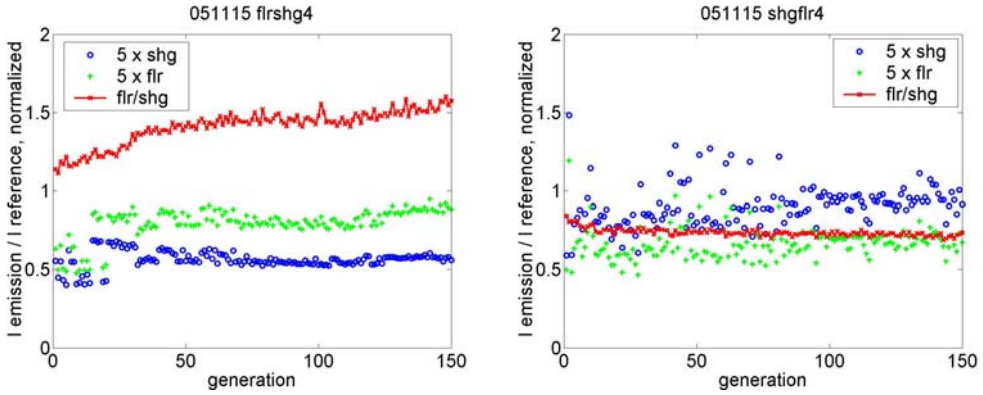

Figure 4.3 Maximization of fluorescence / SHG (left) or SHG / fluorescence (right) as fitness parameter for G5-FITC. For best individual of each generation, open blue circles show 5 times shg

(Ishg / Iref) and green plusses show 5 times flr (Iflr / Iref). Red line with x's shows the flrshg ratio (Iflr / Ishg). All measurements normalized to test_individual of generation 75.

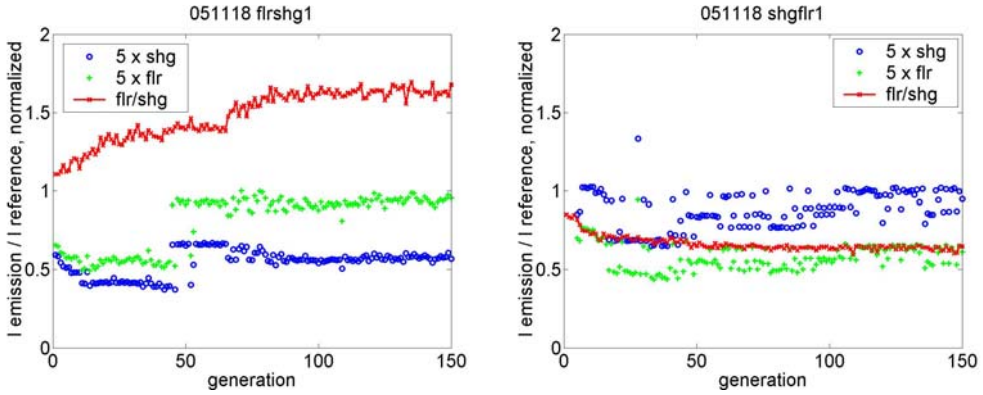

Figure 4.4 Repetition of experiment from Figure 4.3 maximizing Iflr / Ishg (left) or Ishg / Iflr (right) from G5-FITC with graded search algorithm searching only polynomial phase space for first 4 generations.

Figure 4.4 shows the results of the graded algorithm in coherent control of the two-photon fluorescence to SHG ratio. The sudden jumps occasionally observed in the flr and shg efficiencies correspond to the introduction of a new individual into the population. The flrshg or shgflr fitness parameter optimized in the experiment however nonetheless follows a smooth course, reflecting the independence of the selective coherent control from the efficiency alone of each underlying process. Notably, the course and final degree of control achieved by the algorithm is not perceptibly affected by the optimization of polynomial phase. Independent experiments of twenty generations confirmed that polynomial phase alone as a parameter is unable to significantly control the fluorescence to SHG at this power.

Essentially the same learning curves as for G5-FITC were obtained in the experiments repeated on unconjugated FITC and Rhodamine, with approximately the same degree of coherent control. In these runs, the normalized ratio of I_{flr}/I_{shg} is maximized near 1.7 and minimized near 0.6, consistent with the result of Brixner *et al.*[6]

As invariably the algorithm sought the lowest permissible signal for the measurement in the denominator, the degree of coherent control enumerated here is actually a somewhat arbitrary figure. For a ratiometric fitness parameter, there is no upper bound on the achievable result when the measurement of the divisor is driven to zero. We were able to dramatically affect the flrshg fitness by adjusting our noise_limit

threshold defined in the Methodology section 2.2 above. For example, when we set the noise_limit to 0% to remove any penalization on fitnesses for individuals with an I_{shg} orders of magnitude lower than the maximum transform-limited signal (I_{shg} for the test_individual), we were able to see several hundred percent improvement (relative to the test_individual) of the fitness parameter flrshg at these low powers. On the other hand, when we demanded an I_{shg} at least 50% of the test_individual measurement, we saw less than 10% improvement of the flrshg fitness from the test_individual.

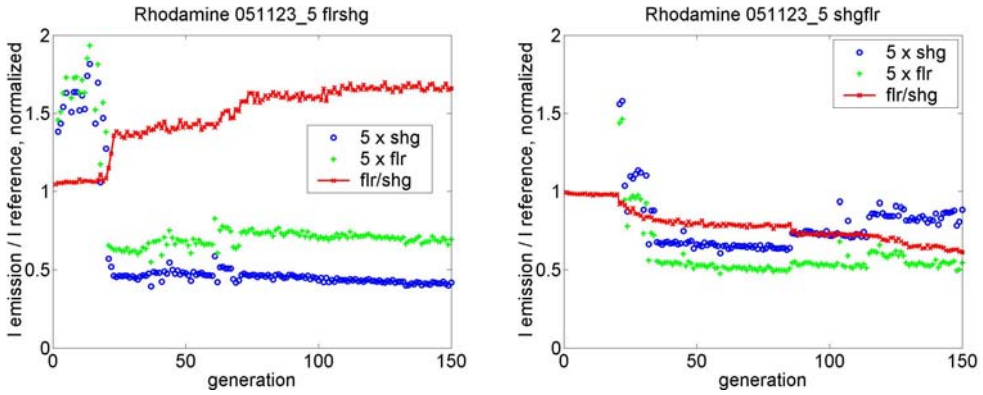

Figure 4.5 Flrshg and shgflr experiments on Rhodamine. Only polynomial phase is modified for the first 20 generations. The algorithm performs the full-dimensional search for generations 21 to 150.

Table 4.3 Φ''(ω) in fs2. The chirp gene indicates the linear chirp the dazzler should theoretically produce from a transform-limited input pulse. The chirp was extracted from the SHG-FROG as the 2nd order coefficient from a fourth-degree polynomial fit to the phase recovered by the FROG algorithm.

Dye	Optimized fitness parameter	Chirp gene (fs^2)	Chirp from SHG-FROG (fs^2)
G5-FITC (Figure 4.3)	flr	2695	568
	shg	305	565
	flrshg	-6 725	-3 365
	shgflr	-7 545	-2 826
G5-FITC (Figure 4.4)	flr	-2 590	-788
	flrshg	-11 625	-1 584
	shgflr	-10 890	-6 244
FITC	flr	-2 205	-734
	flrshg	34 530	1 215
	shgflr	-9 250	-2 247
Rhodamine	flr	-1 835	-783
	flrshg	-12 545	-2 133
	shgflr	-3 185	-4 366

Learning curves for Rhodamine, seen in Figure 4.5, emphasize the relatively limited degree of coherent control achievable with polynomial phase adjustment on two-photon fluorescence normalized to another second order process (SHG). At generation 20, there is a marked improvement in fitness parameters of either the flrshg or shgflr experiment when the graded search algorithm undergoes the switch from a polynomial phase only search to the full-dimensional search. Linear chirps of optimal pulses were not consistent between experiments (even those performed in succession on the same day), as shown in Table 4.2. This further reflects the irrelevance of polynomial phase and chirp to our coherent control experiments at the powers achieved in unamplified oscillator experiments.

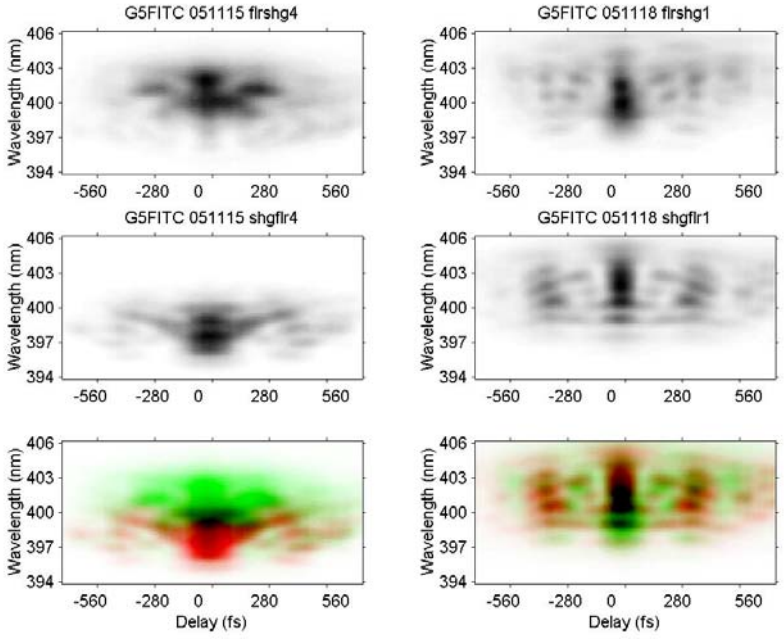

Figure 4.6 SHG-FROG traces (arbitrary grayscale units on CCD camera) of best pulse in last generation for experiments with fitness curves in Figures 3 (left) and 4 (right). First row shows optimal pulse for improvement of flrshg (Iflr / Ishg), second for shgflr (Ishg / Iflr), and the last row is a false-color overlay of the two with green for flrshg, red for shgflr, and common areas black. The left side traces (performed three days after experiment) are from the experiment using the original unmodified algorithm with learning curve depicted in Figure 4.3. The right side shows frog traces corresponding to Figure 4.4 (performed one week after experiment).

As can be seen in Figure 4.6, experiments performed on the same dye (G5-FITC) at different times with very similar fitness evolution curves and measurements could produce markedly different optimal pulse shapes. One possible explanation for this finding, which was also seen in control of $[Ru(dpb)_3]^{2+}$ by Brixner *et al.*,[6] is the presence

of numerous equivalently local minima that are the optimal pulses. Selected optimal pulses for experiments on unconjugated FITC and Rhodamine are shown in Figure 4.7. We consistently found that the variability between experiments of SHG-FROG traces for optimal pulses, even for those performed sequentially, was greater than the variability between dyes. A consistent finding in the oscillator experiments is the complementary nature of optimal pulses obtained for parallel experiments to maximize (flrshg) or minimize (shgflr) the ratio of fluorescence to SHG. The SHG-FROG traces of the pulses are complementary in the sense that the regions of maximal intensity for flrshg fall in regions of low intensity for the shgflr pulses, and vice versa.

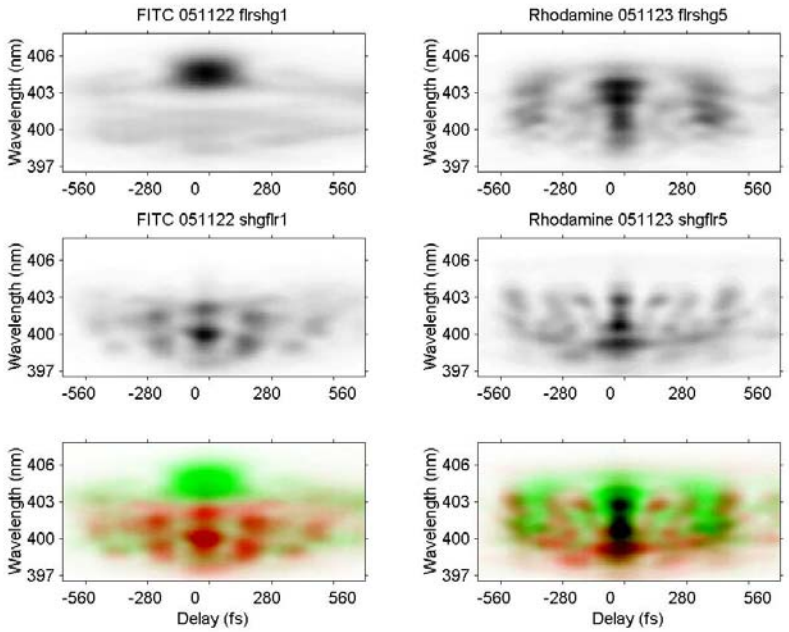

Figure 4.7 SHG-FROG traces of best pulse in last generation for low power coherent control experiments on FITC (left) and Rhodamine (right). First row shows optimal pulse for improvement of flrshg (Iflr / Ishg), second for shgflr (Ishg / Iflr), and the last row is a false-color overlay.

Fluorescence optimization for Rhodamine at high intensities is shown in Figure 4.8. No SHG-FROG trace was obtained of the optimal pulses due to laser malfunction shortly after completion of the experiment. The unnormalized absolute I_{flr} signal in these experiments approached but never quite reached the I_{flr} measurement for a transform-limited pulse (approximated by the test_individual). Nonetheless, optical saturation of the fluorophore transitions cannot be completely ruled out. In the case of saturation, we would expect the algorithm to simply increase pulse duration to reduce peak intensity and

saturation. However, there is no clear concomitant decrease in SHG conversion efficiency evident during the learning curve. The improvement of fluorescence efficiency to almost double that of a transform-limited pulse (at the input of the focusing lens) without an increase in peak intensity (as measured by SHG) may be an indication of strong coherent control of the excited state population. Indeed, without actually optimizing flrshg, this high fluence experiment yielded individuals with close to 400% of this fitness parameter relative to the approximate transform-limited pulse.

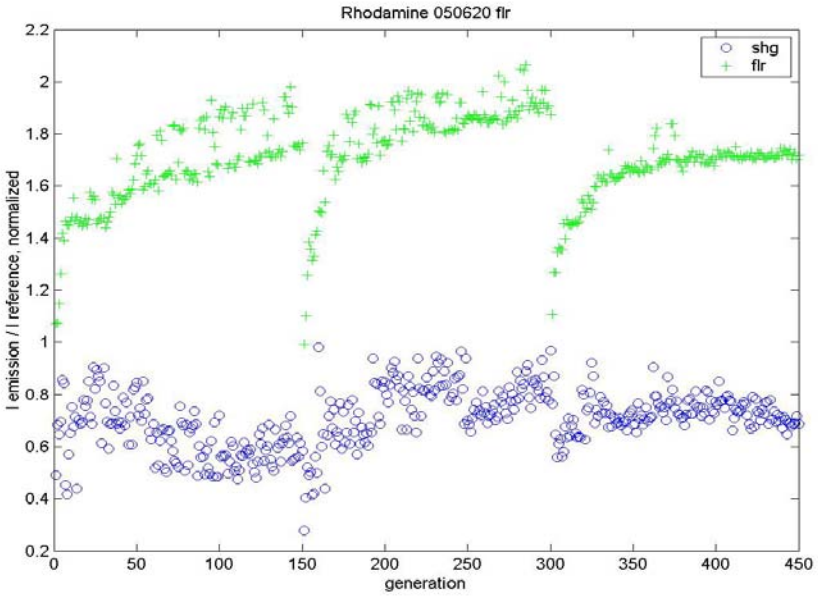

Figure 4.8 Learning curves of three consecutive experiments for maximization of flr (I_{flr} / I_{ref}) in Rhodamine by shaping regeneratively amplified laser pulses. Estimated intensity at sample: ~ 1 x 10^{13} W/cm^2. For best individual of each generation, blue circles show shg (I_{shg} / I_{ref}) and green plusses show flr (I_{flr} / I_{ref}). All measurements are normalized to the corresponding test_individual measurement (~transform-limited pulse).

4. Conclusions

We have developed and tested a robust genetic algorithm to coherently control two-photon fluorescence relative to incident laser power or normalized to SHG. It converges predictably to optimal pulse shapes which are complementary for maximization and minimization, even under unstable experimental conditions. One of the most interesting aspects of the low fluence experiments using the oscillator is that the polynomial phase, including linear chirp, is far less significant in achieving coherent control between two-photon processes than the other parameters of our genetic algorithm.

The greater experimental variability of optimal pulses as compared to variability between dyes at low laser fluences of the oscillator experiments is a blow to the potential usefulness of this method in biological applications. At high fluence, strong field control may still enable a useful degree of coherent control. It is also encouraging that similar implementations have been successfully able to directly discriminate dyes.[15,16] Experiments with the unamplified oscillator reveal marked broadening and weakening of the optimally shaped pulse by the Dazzler AOPDF in the flrshg and shgflr experiments relative to an approximately transform-limited test individual. The significant decrease in absolute fluorescence and actual fluorescence efficiency (I_{flr}/I_{ref}) relative to the transform-limited signal is a major hindrance to implementation of the current results to improve SNR in an actual biological imaging system. The key to overcoming this is expected to lie in regeneratively-amplified shaped pulses that greatly improve two-photon fluorescence at peak intensities significantly lower than a regeneratively-amplified transform-limited pulse.

In contrast to our low fluence results, experiments at the high fluences of regeneratively-amplified pulses evidence improvement of fluorescence efficiency as well as the ratio I_{flr}/I_{shg} without significant reduction in absolute I_{flr} signal strength relative to a transform-limited pulse. The marked enhancement of flr by the learning algorithm without concomitant improvement of shg efficiency is unique from previous investigations, which always converged upon a transform-limited pulse for this circumstance. The several fold increase in flrshg ratio while surpassing the transform-limited fluorescence efficiency may indicate a strong degree of coherent control for example due to saturation of the excited state population at the focal point.

References

1. C.F. Zhong, T.P. Thommey, J.Y. Ye, Z. Cao, A. Myc, J.R. Baker Jr., and T.B. Norris, "Multiphoton in vivo flow cytometry," paper CFF1 presented at the Conference on Lasers and Electroptics (OSA, Washington, DC), 2005.

2. D. J. Tannor and S.A. Rice, "Control of selectivity of chemical reaction via control of wave packet evolution," J Chem Phys, **83**, 5012-5018, 1985.

3. D. Meshulach and Y. Silberberg, "Coherent quantum control of two-photon transitions by femtosecond laser pulse," Nature, **396**, 239-242, 1998.

4. I. Pastirk, J.M. Dela Cruz, K. Walowicz, V. Lozovoy, and M. Dantus, "Selective two-photon microscopy with shaped femtosecond pulses," Optics Express, **11**, 1695-1701, 2003.

5. I. J. Majoros, T. P. Thomas, C. B. Mehta, and J. R. Baker Jr, "Poly(amidoamine) dendrimer-based multifunctional engineered nanodevice for cancer therapy," J. Med. Chem., **48**, 5892 -5899, 2005

6. T. Brixner, N.H. Damrauer, B. Kiefer, and G. Gerber, "Liquid-phase adaptive femtosecond quantum control: Removing intrinsic intensity dependencies," J Chem Phys, **118**, 3692-3701, 2003.

7. T. Baumert, T. Brixner, V. Seyfried, M. Strehle, and G. Gerber, "Femtosecond pulse shaping by an evolutionary algorithm with feedback," Applied Physics B: Lasers and Optics, **65**, 779-782, 1997.

8. K. Midorikawa, J. Chen, H. Kawano, Y. Nabekawa, A. Suda, H. Mizuno, and A. Miyawaki, "Coherent control of Multiphoton excitation process for biological fluorescence imaging," Commercial and Biomedical Applications of Ultrafast Lasers V, Proceedings of SPIE, **5714**, 99-107, 2004.

9. G. Cerullo, C.J. Bardeen, Q. Wang, and C.V. Shank, "High-power femtosecond chirped pulse excitation of molecules in solution," Chem Phys Lett, **262**, 362-368, 1996.

10. T.B. Norris, "Femtosecond pulse amplification at 250 kHz with a Ti:sapphire regenerative amplifier and application to continuum generation," Optics Letters, **17**, 1009-1011, 1992.

11. F. Verluise, V. Laude, Z. Cheng, Ch. Spielmann, and P. Tournois, "Amplitude and phase control of ultrashort pulses by use of an acousto-optic programmable dispersive filter: pulse compression and shaping," Optics Letters, **25**, 575-577, 2000.

12. D. Kaplan and P. Tournois, "Theory and performance of the acousto optic programmable dispersive filter used for femtosecond laser pulse shaping," J. Phys. IV France, **12**, Pr5-69 75 1-7, 2002.

13. B.J. Pearson, J.L. White, T.C. Weinacht, and P.H. Bucksbaum, “Coherent control using adaptive learning algorithms,” Phys Rev A, **63**, 63412-1-12, 2001.
14. R. Trebino, K. DeLong, D. Fittinghoff, J. Sweetser, M. Krumbügel, B. Richman, and D. Kane, “Measuring ultrashort laser pulses in the time-frequency domain using frequency-resolved optical gating,” Rev Sci Inst, **68**, 3277-3295, 1997.
15. J.M. Dela Cruz, I. Pastirik, M. Comstock, and M. Dantus, “Multiphoton Intrapulse Interference 8. Coherent control through scattering tissue,” Optics Express, **17**, 4144-4149, 2004.
16. T. Brixner, N.H. Damrauer, P. Niklaus, and G. Gerber, “Photoselective adaptive femtosecond quantum control in the liquid phase,” Nature, **414**, 57-60, 2001.

CHAPTER 5
CONTROL OF TWO-PHOTON FLUORESCENCE OF COMMON DYES AND CONJUGATED DYES

1. Introduction

Multiphoton fluorescence is widely used for biomedical microscopy, *in vivo* sensing, and more recently, flow cytometry[1-7]. Generally, multiple dyes are employed for simultaneous measurements of multiple targets, and these dyes are discriminated by spectral filtering in essentially all high-throughput applications. Laser pulse shaping offers a new avenue of fluorescence discrimination by manipulating the phase and amplitude of an excitation pulse to selectively enhance specific electronic transitions or follow in time the excited state on evolving molecular energy levels. In addition to microscopy, tailored pulse shapes have been successfully applied in spectroscopy[8]. It has already been demonstrated that laser pulse shaping is a successful tool to distinguish fluorescent species[7,9,10].

Traditionally, the ability to control fluorescence with shaped pulses has been understood in two ways. The Tannor-Rice control scheme relies on the manipulation of vibrational coherences. The laser pulse is shaped to coherently match the actual trajectory of the excited state wavepacket during its evolution, which is dictated for example by vibrational relaxation or nuclear motion[11,12]. A classic example is the pump-dump explanation of increased stimulated emission with negatively chirped laser pulses[13]. The Brumer-Shapiro control scheme, on the other hand, exploits electronic coherences. Energy levels are considered static, and interferences are created between multiple quantum pathways leading to the desired final state. An excellent example is the predictable periodic dependence of the excited state population of cesium on the delay between two optical pulses[14]. In this case, the coherence is between the second pulse and the electrons excited by the first pulse. From a similar vantage point, transform-limited pulses are far from the true optimum to maximize two-photon excitation via a real

intermediate level, due to phase differences in the contributions of off-resonant terms[15]. The results we present here, however, are largely explained without consideration of excited wavepacket motion or molecular coherences. Rather, we interpret them in terms of optical intrapulse interferences whose major role is to tune the second-harmonic power spectrum of the exciting pulse to the relevant location on the relative two-photon excitation cross-section spectrum of the discriminated dyes. We thus refrain from the term "coherent control," as coherences in the molecules of interest presumably do not contribute significantly to the selectivity.

One of the primary reasons existing multiphoton applications have already and will continue to benefit from pulse shaping is the enhanced specificity to the targeted processes. It has already been shown that simply tuning the fundamental laser excitation wavelength can provide significant information about biological samples in two-photon microscopy[16]. Phase-interferences, however, can achieve far greater specificity[17]. Also, the reduced peak power that generally accompanies shaping of pulses away from the suboptimal transform-limit reduces photobleaching and other undesired multiphoton processes[18].

In the current study, we demonstrate selective excitation of two-photon fluorescence from various pairs of dyes and dyes in different conjugation states with tailored pulse shapes found with a genetic algorithm. We are particularly interested in the application of coherent control to promising platforms for addressing biological problems with molecular specificity. To this end, we include in the investigation a conjugate to trastuzumab (Herceptin®), which has proven itself as transformative not only in the scientific understanding, but also in the treatment of cancer. Trastuzumab is a humanized monoclonal antibody to the HER2/neu member of the epidermal growth factor receptor, whose overexpression in breast cancer patients is associated with worse prognosis[19,20]. Poly(amidoamine) (PAMAM) dendrimers are another emergent technology showing great promise in cancer therapy and diagnostics[21,22]. We also consider tailored pulse shaping to discriminate dyes with significant spectral overlap, which could find practical application.

In this paper, we first present an overview of our procedure for adaptive pulse shaping, including power-law and chirp-scaling checks to ensure that trivial

convergences do not obscure the possibility of true discrimination. Then we describe the details of the genetic algorithm (GA) which, via a multiplicative fitness parameter in a graded search method, converges on pulse shapes that not only differentiate two-photon processes, but do so in a high signal regime. For interpretation of the results, we use a time-domain acousto-optic measurement of two-photon excitation cross-section spectra. Before looking to discriminations of dye pairs, we first examine the ability to control fluorescence relative to the simpler same-order process of second harmonic generation (SHG). We consider the results in terms of not only the absolute maximum ratio of discrimination achieved, but also present the evolutionary course of the GA and compare the improvement to a quantitative measure of the noise level.

2. Materials and Methods

2.1 Samples

Samples are purchased from Invitrogen Corpororation (Carlsbad, CA) or Excimer Laser Dye Company, as listed in Table 5.4, with the exception of the dendrimer- and Herceptin- conjugates, which are prepared in house. Fifth generation PAMAM dendrimers are prepared and conjugated to folic acid (FA) and 6-Tamra as described previously[22], to create the G5-6T-FA sample.

Table 5.4 Dyes used in two-photon fluorescent control experiments. All samples were purchased from Invitrogen corporation except rhodamine B, which was purchased from Exciton, and BFP, which was purchased from QBioGene.

Sample	One-photon peak (nm)		Catalog Number	Solvent	Concentration (μM)
	Absorption	Emission			
Fluorescein Isothiocyanate (FITC)	495	520	F-143	water	3.33
Calcium Green	506	531	C-3010MP	water	10
6-TAMRA	540	564	C-6123	water	3.33
G5-6T-FA				water	3.33
DiI	549*	565*	V-22885	DMSO	20
Rhodamine B (Rhodamine 610)	556	578	6102	water	1
TXR-Phalloidin	583	603	T-7471	methanol	~2.2
Texas Red (TXR)	596	615	T-353	methanol	5
Alexa Fluor 594	590	617	A-20004	water	6
Herceptin-AF594				PBS	3
DiD	644*	665*	V-22887	DMSO	20

***DiI and DiD absorption and emission are provided for the membrane-bound dyes.**

The Herceptin-Alexa Fluor 594 conjugate is prepared as follows. 5 mg Herceptin (148 kDa) is dissolved in 3.4 ml phosphate-buffered saline for a 10 μM concentration. To the antibody solution is added 34 μl of 5 mM AF594-SE (*Invitrogen* A20005; AF594 carboxylic acid, succnimidyl ester) in DMSO. The reaction mixture is mixed overnight at room temperature and purified by gel filtration with a Sephadex G25 column (1cm X

30 cm), which is equilibrated with 10 mM phosphate buffer pH 7.0. The fraction that absorbs both at 280 nm and 590 nm is collected and concentrated with a Centricon device (10K MWCO). An average of 4 or 5 Alexa-Fluor molecules are present per Herceptin in the final mixture.

2.2 Experimental setup

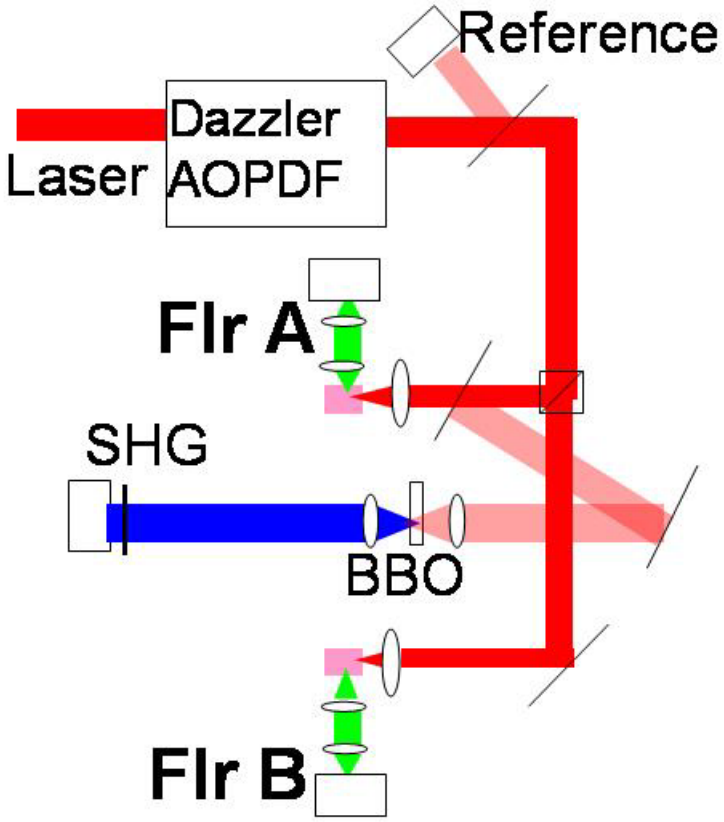

Figure 5.1 Experimental Setup. The dye sample is contained in a disposable fluorescence cuvette (Cole Palmer). Incident laser power I_{ref} is measured by photodiode PD1 (R2066, Hamamatsu). After filters to remove all pump laser and exciting 800 nm light, the fluorescence signals FlrA and FlrB are measured in the perpendicular direction by a PMT (H5784-01, Hamamatsu). SHG from the BBO crystal is detected by another PMT (R2066, Hamamatsu). Lenses are depicted as ovals.

The experimental setup is shown in Figure 5.1. The laser system consists of a regeneratively amplified Ti:sapphire system (RegA, Coherent, Santa Clara, CA) providing up to 4 μJ, 50 fs pulses at 250 kHz with a center wavelength of 800 nm and 27 nm FWHM bandwidth. The "Dazzler," an acousto-optic programmable dispersive filter (AOPDF) (Fastlite, Palaiseau, France), is used to shape the laser pulses. The Dazzler modulates the diffracted output pulse by way of an acousto-optic interaction with an RF

wave launched into a TeO_2 crystal[23,24]. The controlling electronics of the Dazzler read the diffracted power, center wavelength, bandwidth, and polynomial phase to fourth order from a text file, which in our experiments is automatically generated by the algorithm. Additionally, an amplitude file can be read to spectrally shape the diffracted pulse, and the phase in different frequency bins can be read from a phase file for complete control of the pulse shape. The Dazzler is triggered by every twelfth RegA pulse for an approximately 20 kHz repetition rate. SHG-FROG measurements confirm that the approximately 6 shaped pulses falling within the 50% duty cycle of the Dazzler give precisely the same average two-photon time-frequency characteristics as are obtained when the RegA is operated at 20 kHz. Thus, the effective shaping of all 6 diffracted pulses per launched RF waveform has the same effect in our experiment as if each were synchronized to the center of separate identical acoustic waves in the TeO_2 crystal.

A glass-coverslip beamsplitter enables a reference reading of incident power I_{ref} by a photodiode (FFD-100, Perkin-Elmer Optoelectronics, Fremont, CA). We define the efficiency of each two-photon fluorescence signal S as the ratio S/I_{ref}. The excitation beam is then divided into two arms with a beamsplitter, and the relative power in each arm is controlled with a variable reflective attenuator. Each arm is focused into a cuvette holding the dye sample, and the fluorescence signal A or B is collected in the perpendicular direction through an appropriate bandpass filter for detection by a photomultiplier tube (PMT) (H5784-01, Hamamatsu, Bridgewater, NJ). Immediately preceding the lens, the A arm additionally has another glass-coverslip beamsplitter to create a third arm of the experiment. In the third arm, a 500-micron thick beta barium borate (BBO, β-BaB_2O_4) crystal is used for second-harmonic generation, which is read through a blue absorptive filter by another PMT (R2066, Hamamatsu, Bridgewater, NJ) to give the signal SHG. All four signals I_{ref}, A, B, and SHG are read in parallel as root-mean-square voltage for 2500 samples by a 250 kHz DAQ board (M-series, National Instruments, Austin, TX), which is synchronized by the Dazzler trigger.

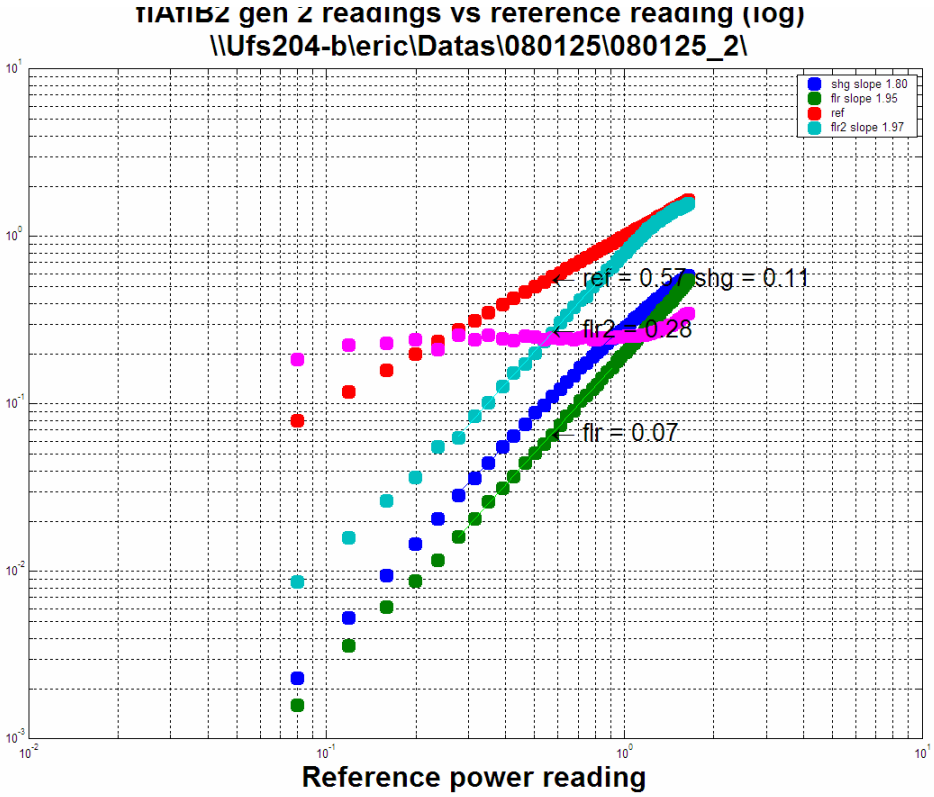

Figure 5.2 Power scaling of two-photon signals relative to I_{ref}. Magenta squares show the dependence of the ratio FlA/FlB on power. Axes are in log scale. Slopes of a least-squares linear fit through the center of the data are marked in the legend. SHG sub-quadraticity results from detector saturation at the higher powers, whereas perfect quadratic scaling is seen at lower powers.

Before each experiment, the incident power is scanned to ensure quadratic scaling of the discriminated two-photon processes, as shown in Figure 5.2, to avoid artefactual results which might disappear under changing laser power. There are three possible causes for subquadratic behavior: saturation of molecular transitions, detector saturation, or scattered excitation light leakage into the detector. Shaped pulse energies after the Dazzler used during experiments are near 2 nJ. Assuming a diffraction-limited beam waist, we estimate a typical fluence at the laser focus during experiments of 0.5 mJ/cm^2 (peak intensity on the order of a GW/cm^2 transform-limited), which is too low to saturate the molecular transitions. Detector saturation is ruled out by an independent calibration demonstrating linearity at the measured signal levels. Scattered light is minimized with bandpass filters and beam dumps. As long as both signals used in the fitness parameter have the same degree of deviation from quadratic scaling, scattered light is not noted to affect the convergence of the algorithm. However, if one dye for example is approaching

saturation of the molecular transition while the other is still in the quadratic region, this trivializes the convergence to mere pulse stretching. Photobleaching with a recovery time of several seconds is also generally noted for repeated measurements anywhere near the saturation region (Figure 5.3). Thus, the power scaling check in each experiment is extremely important.

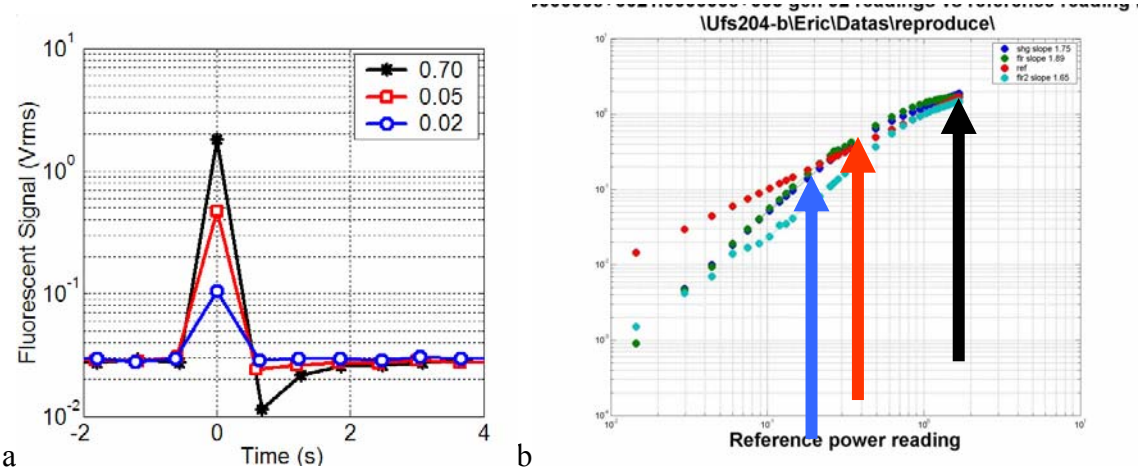

Figure 5.3 Photobleaching coincident with saturation. (a) Net two-photon fluorescent signal from a mixture of DiI and RhodB versus time. At time 0, incident power of 2, 5, or 70% of the maximum was sent to the sample. All other time points had 1% of maximum power incident. (b) Average two-photon fluorescence from mixture versus pulse power (as % of maximum). Applied powers in (a) are marked with circles.

Even if the incident laser power is unvarying in the course of the adaptive learning algorithm, true control possibilities could still be masked by uninteresting convergences with simple linear chirp (second order polynomial phase) adjustments. Under increasing chirp, two-photon fluorescence in the saturation region for example would not decrease, while the unsaturated SHG signal would decrease with the increased pulse duration[25]. In fact, if the two-photon fluorescence emission has a short enough lifetime to be saturated by peak laser intensity rather than the pulse fluence, the two-photon signal could actually increase with the increased group delay dispersion. Another case in which linear chirp could mask control is when the dispersion in the different materials in the two optical paths is not exactly matched. In this case, the optimal pulse shape would discriminate simply by tuning to compensate dispersion in the appropriate path.

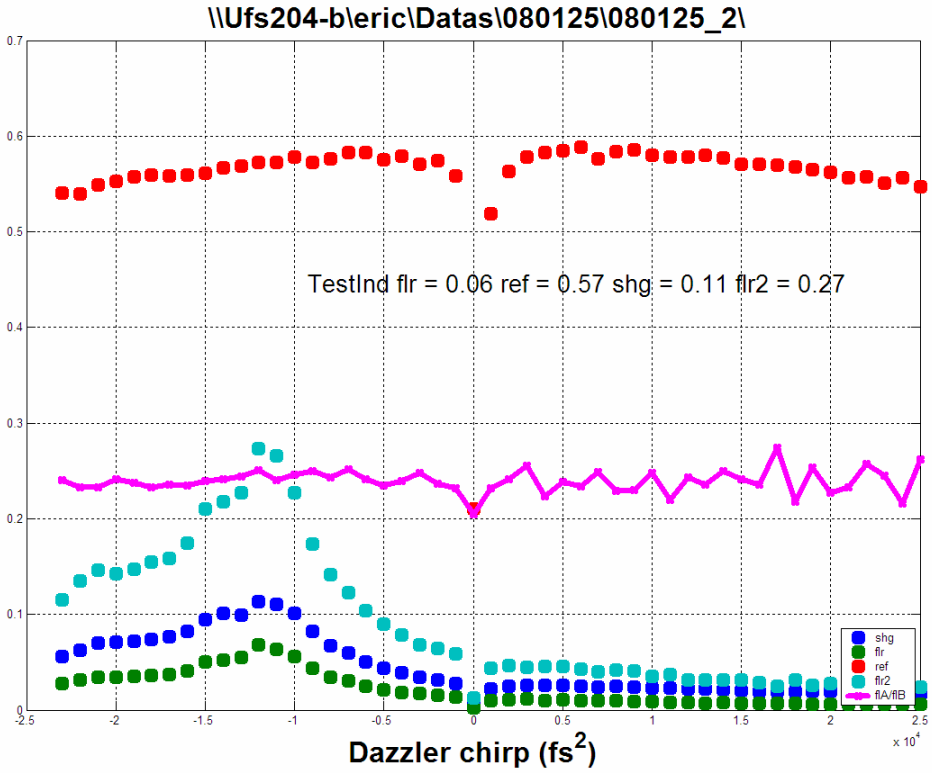

Figure 5.4 Lack of discrimination with linear chirp scaling. Scaling of same signals as Figure 5.2 with variation in linear chirp (2nd order polynomial phase). Note the drop in diffraction efficiency of the Dazzler when little second-order polynomial phase is applied (0 chirp).

As shown in Figure 5.4, when we have carefully set up our experiments, we find little discrimination of two-photon processes by linear chirp adjustment applied by the Dazzler. While it is true that some investigations[13,26] have shown true coherent control based only on chirp variation, these have generally been at saturating fluences and shown asymmetry with positive versus negative chirp.

2.3 Genetic algorithm

The genetic algorithm (GA) relies on two-point crossover and mutation operators inspired by the work of Pearson and colleagues[27]. From an initially random set of pulses, evolutionary improvement follows the fitnesses assigned to the measurements for each pulse, reflecting proximity to the desired outcome. In addition to implementing the GA in an acousto-optic modulator, several modifications we have added include a multiplicative fitness parameter, chromosome circularization, a variable mutation rate, a graded search method, and an unvarying individual in each generation to measure laser stability.

Gene interpretation

Each individual laser pulse in a generation of the GA is defined by a chromosome consisting of 45 or more genes, all of which can vary between 0 and 1. One gene controls the power of the diffracted beam by setting the energy of the acoustic wave, and four genes modify 4^{th} order polynomial phase. Additionally, for each of 20 frequency components, there is an amplitude gene and a phase gene. The number of frequency components for some experiments is increased to as many as 100 to access higher resolution frequency information. The genes are interpreted linearly within prescribed physical limits specified for each experiment, which are generally in line with the constraints of the Dazzler's capabilities. For example, the linear chirp was allowed to vary between -50 000 and +50 000 fs^2. The amplitude in a particular frequency bin is simply the direct value of the corresponding amplitude gene. If physical constraint programming is not used, each phase gene is multiplied by 2π to give the programmed phase in that frequency bin.

A more advanced feature that can be employed in the algorithm is physical constraint programming, which limits the interpretation of phase genes to ensure that the shaped pulse falls within an absolute time window $[T_{MIN}, T_{MAX}]$. These are typically 1 ps and 2 ps to ensure that the trailing edges of the pulse still fall within the 3.6 ps maximal programmable duration within the TeO_2 crystal of the Dazzler. The feature is generally used to obtain the results shown in this paper. Exact implementation is as follows. The derivative of polynomial phase is used to determine the time delay $\tau_{polynomial}$ which a frequency bin would experience in the absence of further phase modulation. This might be less than T_{MIN}, or possibly even a negative number. From this, we set the minimum permissible delay the phase file can add (via its derivative with respect to frequency) as $\tau_{min} = T_{MIN} - \tau_{polynomial}$. Similarly, the maximum permissible delay is set as $\tau_{max} = T_{max} - \tau_{polynomial}$. The range $[\tau_{min}, \tau_{max}]$ then determines the limits of interpretation for the individual frequency bin genes, which are set such that their derivative adds a delay linearly scaled in this interval. Thus, the combined delay of the frequency bin including both polynomial phase and direct phase will fall in the range $[T_{MIN}, T_{MAX}]$. One further nuance of our implementation is that genes from 0 to 0.5 are linearly scaled to positive additional delays in the range $[\max(0, \tau_{min}) \tau_{max}]$, and genes from 0.5 to 1 are linearly

scaled to negative additional delays in the range [τ_{min} min(τ_{max},0)]. This ensures that the unshaped pulse can be directly programmed as all ones or zeros. This nuance also requires that, in order to properly exert their effect, the limits [T_{MIN}, T_{MAX}] must be chosen to completely contain the pulse with only polynomial phase modification.

Fitness parameters

The results of the experiment depend heavily on the exact form of the fitness parameter assigning the fitness F to each individual in a population. As shown previously[29], SHG and two-photon excited fluorescence of common dyes, both second-order processes, are generally (but not necessarily) maximally efficient with a transform-limited pulse. As an alternative to blind maximization attempts, one can remove the intrinsic nonlinear dependence of the two-photon fluorescent signal A by controlling it relative to the signal B from SHG or another process of the same order. This inspires a ratiometric fitness parameter $F = A/B$[9,18]. However, as the two-photon signals can drop significantly for example with changing pulse chirp, we have found that this approach leads to low signal levels with degree of discrimination dictated primarily by the arbitrarily set acceptable low-signal limit[29]. In this regime, true discrimination can be confounded by slight nonlinearities in the detectors or mismatches in optical components of the excitation path. Thus in the current investigation, to optimize a ratio A/B, we employ instead the fitness parameter $F = (A-c)(c^{-1}-B)$, where values of A and B are normalized to the unshaped pulse measurement. We have found that setting c to 0.8 yields the better convergence in our experimental conditions, as opposed to the original implementation of unity for c[30]. If both multiplicands are negative, an infinite negative fitness is given to the pulse. If either multiplicand alone falls below 0, the inverse of the other taken instead to ensure for example that if B exceeds c^{-1}, further decreases in the optimized signal A from c result in a decreased (more negative) fitness. This division-free fitness ensures that the optimized signal surpasses or at least is near the signal for an unshaped pulse.

The algorithm considers the array of all raw fitnesses **F** at a population level. To protect the algorithm from domination by a noise-spiked individual, we linearly map the fitnesses so that the median individual is about half as likely to produce offspring as the

best individual in the population. In particular, for an individual k with raw fitness F(k), we calculate a scaled fitness $F_{scaled}(k)$ as:

$$F_{scaled}(k) = 2 + [\max(\mathbf{F}) - F(k)] / [\text{median}(\mathbf{F}) - \max(\mathbf{F})] \quad (1)$$

Thus the median individual has a scaled fitness of 1 whereas the best individual has a scaled fitness of 2. Negative scaled fitnesses are set to 0 and result in non-reproducing individuals.

Evolution, mating and mutation

For the first generation, an initial population of fifty random individuals is created and sequentially expressed by the Dazzler for measurement. The top ten individuals, as determined by the fitness parameter, are passed from the old generation on to the next generation unchanged to ensure elitism. The remaining forty individuals of the new generation are determined by twenty two-point crossover matings of individuals picked randomly from the old generation with probability proportional to their relative scaled fitness. In a two point cross-over of individuals, the two offspring are produced by exchange of all genes of the parents between two random cut points[27]. To prevent location on the chromosome from favoring any genes or groups of genes, we treat the first gene as the adjacent neighbor of the last gene of the chromosome in this process. In other words, the chromosome is circularized by permitting the first cut to occur immediately before the first gene.

In the absence of mutation, there would be no source of genetic variation in our population. Therefore, we permit mutation of each gene of a new offspring by replacing it with probability mp by a completely random value uniformly distributed in the possible range. To keep this process in check, there is a probability 1-mp that the offspring will not be given the chance for mutation at all. For these experiments, we use mp near 0.2 to provide an optimal balance between quickly exploring the vast search space while protecting outstanding gene sets from excessive mutation. One limitation of standard implementations of a genetic algorithm with a low mutation rate is progression to a local minimum once homogeneity takes over the population. Therefore, in our algorithm we vary the mutation rate from one generation to the next. In particular, we scale mp by 1/12 of the variance of the population in the preceding generation. As the variance of

uniformly distributed random variables is precisely 1/12, mp will be set at 0.2 in the first generation, but will increase to balance the degree of population homogeneity that occurs in the search.

The new population is then sequentially expressed by the Dazzler and measured, and the algorithm thus continues iteratively in pursuit of an optimal pulse shape. Typically the search is divided into the first twenty or thirty generations modifying only the polynomial phase search space, followed by full freedom of the GA to manipulate all genes. We have previously shown that this graded search method converges more quickly for problems like SHG maximization alone[29].

Laser stability evaluation

When we consider the results of multiple GA runs, we would like to know how the extent of improvement compares with possible variation of laser conditions between the experiments. To ensure that maximization and minimization curves for discrimination of an individual dye against SHG or another dye meet with identical experimental conditions, we perform these optimizations in parallel. As many as four different populations are interleaved to evolve simultaneously but independently with different fitness parameters. Further, in each generation, two common additional unvarying individuals are added which do not participate in the evolutionary process. The first of these is a zero power pulse from the Dazzler, thus providing a background offset to subtract from the measurements if necessary, and also reflecting any changes in noise due to electronics or dark-room conditions. The other constant individual encodes an unshaped pulse, which additionally gives a measure of the pulse-to-pulse laser fluctuations. This individual expresses genes only of polynomial phase roughly self-compensating the Dazzler, which is the major dispersive element in the optical system before the sample, and thus provides an approximation of the behavior of the transform-limited pulse.

2.4 Pulse characterization

We characterize pulses with a commercial SHG-FROG unit[31] (Grenouille 8-50 from SwampOptics, Atlanta, GA) and software (VideoFrog, MesaPhotonics, Santa Fe, NM). SHG-FROG is typically performed within 24 hours of termination of the

experiment to ensure maximum fidelity of the reproduced pulse to that actually measured in the course of the experiment.

As the Grenouille has a 50 nm bandwidth range, the 27 nm FWHM bandwidth RegA pulses are slightly beyond the limit of accurate phase recovery from the raw data by the FROG algorithm. However, we confirm for most experiments with a spectrometer (S1024DW, Ocean Optics, Dunedin, FL) that the t=0 point from the raw Grenouille image corresponds well to the shaped pulse second harmonic spectrum measured from the BBO crystal in our experimental setup. This also serves as independent verification that despite the thickness of the crystal, phase-matching does not significantly limit the spectral bandwidth of second-harmonic generation[32]. It is however possible that both SHG-FROG and the thick BBO crystal have a similar spectral bandwidth limitation.

2.5 Time-domain two-photon excitation cross-section measurement

Using the same experimental setup, we implement a time-domain measurement of the two-photon excitation cross-section spectrum of dyes in the region of interest. This is performed analogously to the description by Ogilvie and colleagues[33]. However, rather than physically delaying a beam-split replica of the pulse, a virtual Michelson interferometer is programmed into the Dazzler. A delay of t_0 between pulses is achieved with simple multiplication by a cosine amplitude mask $\cos(\omega t_0/2)$ in the frequency domain for 150 intervals in an 80 nm bandwidth, corresponding in the conjugate Fourier domain to a time delay of t_0. Note that we only use binary coding of the phase file to be at 0 or pi corresponding to the sign of the cos function, as absolute and linear phase (absolute time delay) are physically irrelevant when the information is actually contained in the interarrival period of the two pulses [34]. When the data is Fourier transformed, the two-photon excitation cross-section is extracted with relatively good accuracy in the frequency domain as the divisor of the fluorescent signal by the second-harmonic signal in the region of the $2\omega_0$ component. For detailed mathematical proof of this, the reader is referred to the article by Naganuma *et al*.[35] or Trebino's discussion[36].

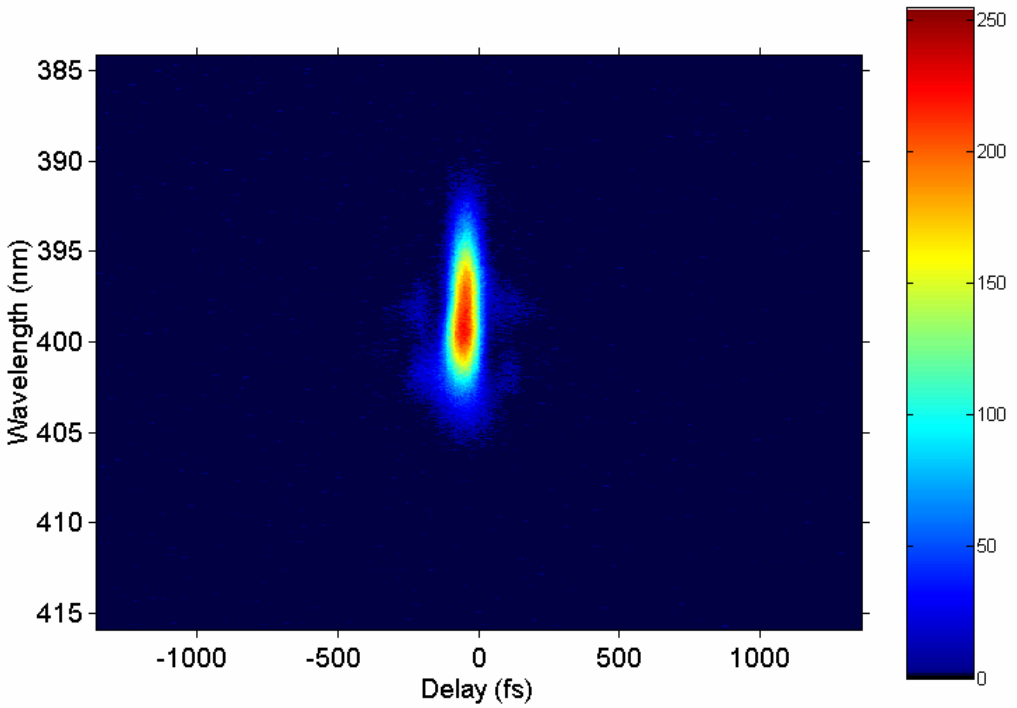

Figure 5.5 Optimal pulse from a GA run to maximize SHG/I_{ref}, as measured by SHG-FROG.

In practice, due to the non-transform limited nature of the unshaped pulse, superior results are obtained when the GA was first run to maximize SHG efficiency to ensure an optimal transform-limited pulse, as shown in Figure 5.4. This phase and amplitude is then used as the fundamental pulse for programmed duplication in the time-domain measurement.

Representative data concurrently measuring two dyes in is shown in Figure 5.5 in both time and frequency domain.

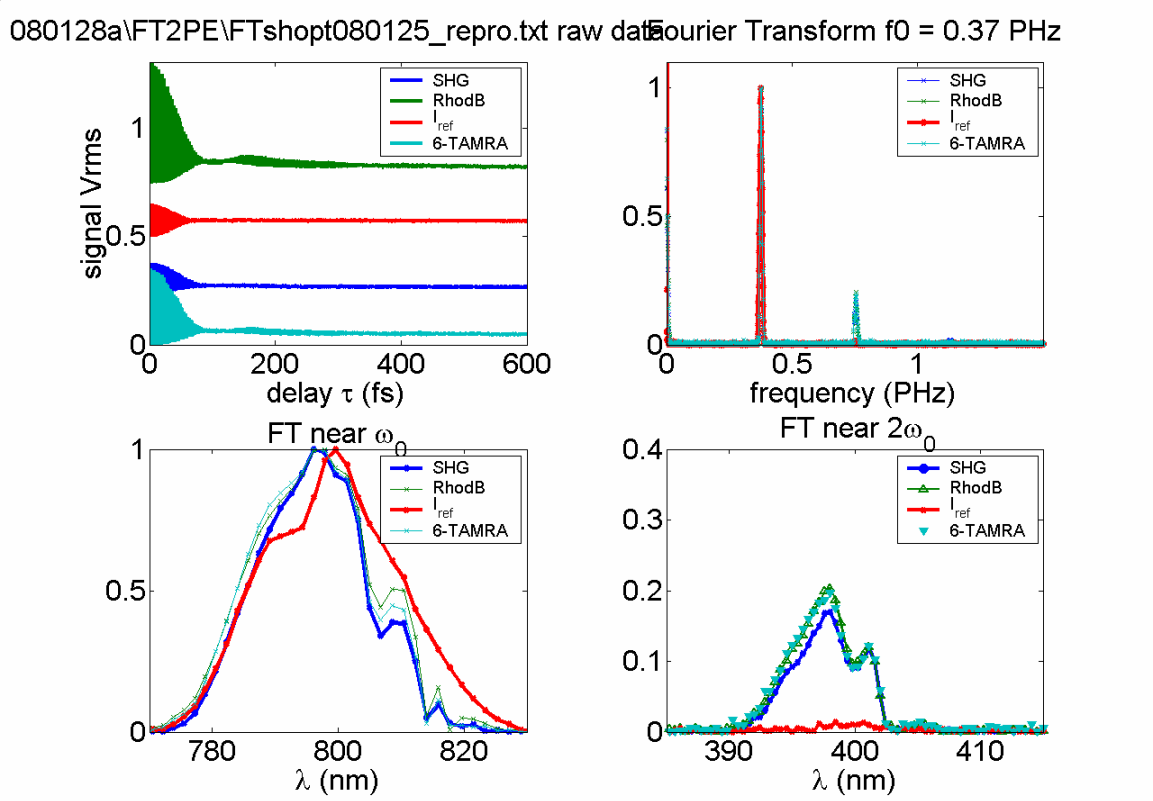

Figure 5.6 Time domain measurement of two-photon excitation cross sections of rhodamine B and 6-TAMRA. (a) Absolute signal strength versus programmed delay between the replicated pulses. (b) Fourier transform view. The fundamental frequency of our 800 nm excitation is 0.37 PHz. (c) Detail of peak at the fundamental optical carrier frequency. (d) Detail of second harmonic peak of the signals.

3. Results and Discussion

One potential practical application of tailored pulse shaping might be the assessment of delivery success of targeted compounds like the G5 dendrimer to specific cell types or cells in a tissue. If multiple fluorescent molecules are used, traditional methods may be frustrated by spectral overlap between the markers or with an autofluorescent background. Further, conjugation state usually does not affect one photon spectra, and therefore differentiating specific uptake of targeted molecules conjugated to a reporter dye from nonspecific uptake of these molecules is not generally possible by simple spectral filtering. We find in our investigation that shaped pulses can enhance or suppress the fluorescence of many common reporter dyes relative to SHG, which could be a significant source of fluorescent background for example in a collagen-dense tissue. We also control the relative fluorescence of dye pairs with variable success, proving that our tailored pulse shapes are sometimes, but not always, a useful discrimination technique. Further, the degree of discrimination achieved with shaped two-photon excitation pulses is not correlated with one-photon spectral distinction or overlap. Rather, the predominant mechanism of discrimination is found to be tuning of the second-harmonic spectrum of the excitation laser pulse to the relative maxima and minima of the two-photon excitation cross-sections of the target dyes. These cross-sections do not change within the bandwidth of our measurement with conjugation of AlexaFluor 594 to Herceptin or 6-TAMRA to a dendrimer, and therefore we are unable to distinguish these conjugation states in our experiments. To change the two-photon excitation cross-section of a fluorophore, we believe that a strong electronic interaction must occur. An example of a conjugation sufficient for this result is Texas Red to phalloidin, which our method is able to successfully detect.

Compiled results are summarized in Table 5.5, showing the ratio of two-photon signal achieved for the maximizing and minimizing pulses. It is important not only to look at the absolute ratio of control achieved, but also details of the GA run that are also included in Table 5.5. For example, if the best degree of control is very high but little or no improvement occurs after the generations of polynomial-only search, this may indicate noise of excessive laser pulse-to-pulse variation or other instabilities. The degree of

fluctuations in measurements of the unshaped pulse between generations reflects the degree of laser stability, and it is quanitified as the standard deviation of the unshaped laser pulse, normalized to the mean. Generally this was less than 5% per channel. An example with greater fluctuations is the discrimination experiment with Herceptin-conjugated AlexaFluor 594. That particular experiment, which had approximately 10% total noise from both channels, but only 7% improvement after the polynomial search portion of the search. By comparison, the BFP to SHG discrimination had 111% increase in control after the end of polynomial search, with only 4.2% total noise between the two channels.

Table 5.5 Summary of experimental results for discrimination of two-photon processes. The maximum discrimination is the ratio A/B for the maximizing pulse divided by the ratio for the minimizing pulse. The relative increase is the maximum discrimination divided by the maximum discrimination achieved in the first 20 generations of the GA, during polynomial-only modification. "Noise" is the standard deviations of the measurement of the unshaped pulse, normalized to the mean measurement.

Signal A	Signal B	Maximum A/B	Minimum A/B	Maximum Discrimination	Relative Increase	Noise A	Noise B
BFP	SHG	1.42	0.44	3.27	2.11	0.029	0.013
RhodB	SHG	1.43	0.58	2.48	1.93	0.014	0.017
Her-AF594	SHG	1.17	0.63	1.87	1.36	0.034	0.034
TXR	SHG	1.22	0.64	1.89	1.28	0.021	0.041
G5-6T-FA	SHG	1.10	0.80	1.38	1.18	0.023	0.015
DiI	FITC	1.90	0.67	2.82	1.94	0.037	0.022
BFP	DiI	1.21	0.41	2.98	1.79	0.024	0.044
DiI	RhodB	1.76	0.62	2.83	1.57	0.047	0.034
DiI	DiD	1.61	0.70	2.31	1.55	0.031	0.029
DiI	RhodB	1.28	0.62	2.08	1.10	0.027	0.027
Ca Green	Rhod B	1.23	0.81	1.51	1.07	0.050	0.020
TXR	AF594	1.14	0.91	1.24	1.06	0.041	0.042
Rhod B	6-TAMRA	1.12	0.90	1.25	1.02	0.029	0.028
TXR-phal	TX Red	1.23	0.85	1.45	1.13	0.035	0.016
Her-AF594	AF594	1.14	0.87	1.31	1.07	0.063	0.026
G5-6T-FA	6-TAMRA	1.10	0.90	1.22	1.06	0.048	0.035

3.1 Control of two-photon fluorescence relative to SHG

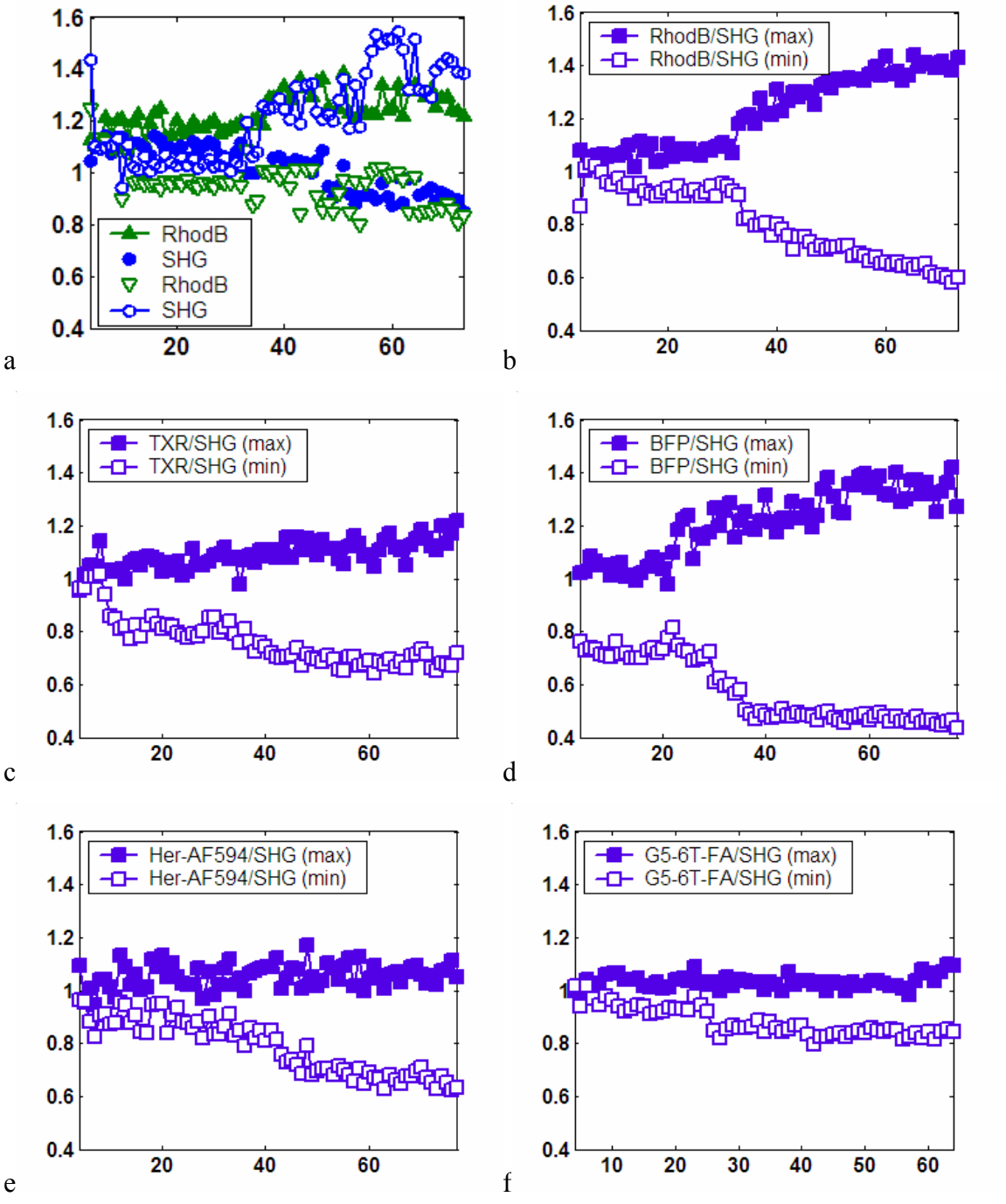

Figure 5.7 Control of the ratio of two-photon fluorescence to SHG versus generation of GA for various dyes. Measurements of each generation's best individuals for maximization are shown with closed markers, whereas results of the parallel minimization experiment are shown with open markers. (a) rhodamine B / SHG. Blue circles show SHG efficiency (SHG/I_{ref}). Green triangles show rhodamine B fluorescence efficiency. (b) Ratio of rhodamine B fluorescence to SHG for the same experiment pair. (c) control of Texas Red / SHG ratio (d) BFP (e) Herceptin-conjugated AlexaFluor 594 (f) Fifth-generation-dendrimer with conjugated 6-TAMRA and folic acid.

For all dyes, tailored pulses met with varying degrees of success in controlling the ratio of two-photon fluorescence to SHG (Figure 5.7). At the same time as controlling this ratio, there is no drop in the maximized signal relative to the unshaped pulse. An example is the maximization of two-photon fluorescence of rhodamine B, marked with closed green triangles of Figure 5.7a, at the expense of SHG (closed blue circles). These measurements are plotted normalized to the unshaped pulse and clearly never drop below one. This is in distinction from previous results, where the algorithm with a ratiometric fitness parameter generally converged to the minimum permissible signal level[29]. The consistent high signal levels found with a multiplicative fitness parameter are a great advantage if the pulses are to subsequently be applied in signal-limited situations.

In some cases, both maximization and minimization experiments converge on significant discrimination (e.g. rhodamine B Figure 5.7b or BFP Figure 5.7d). More commonly, the fluorescence can be only modestly improved relative to SHG, but significantly decreased. For example, the folic acid (FA)-G5-dendrimer-conjugated 6-TAMRA fluorescence can be decreased 20% relative to SHG, but improved by under 10% (Figure 5.7f).

3.2 Discriminability is not necessarily correlated with one-photon spectral distinction

Many of the dyes we have controlled have significant overlap in one-photon spectra (Figure 5.8).

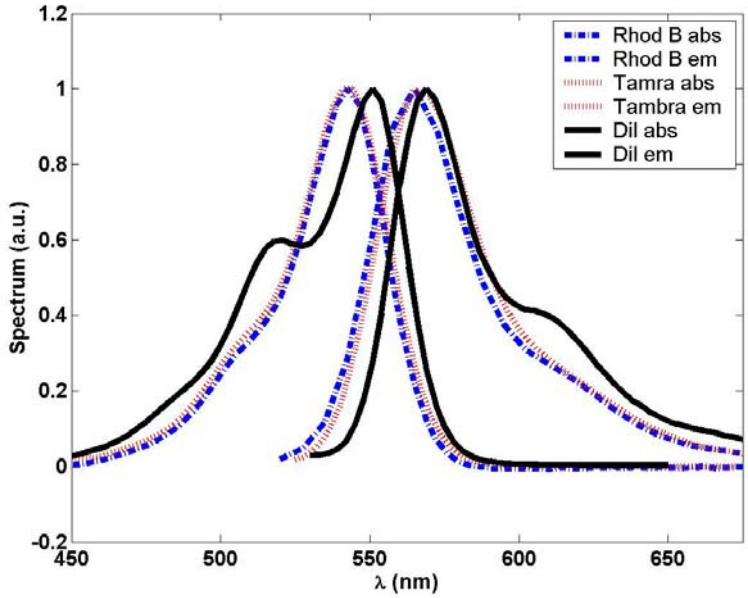

a

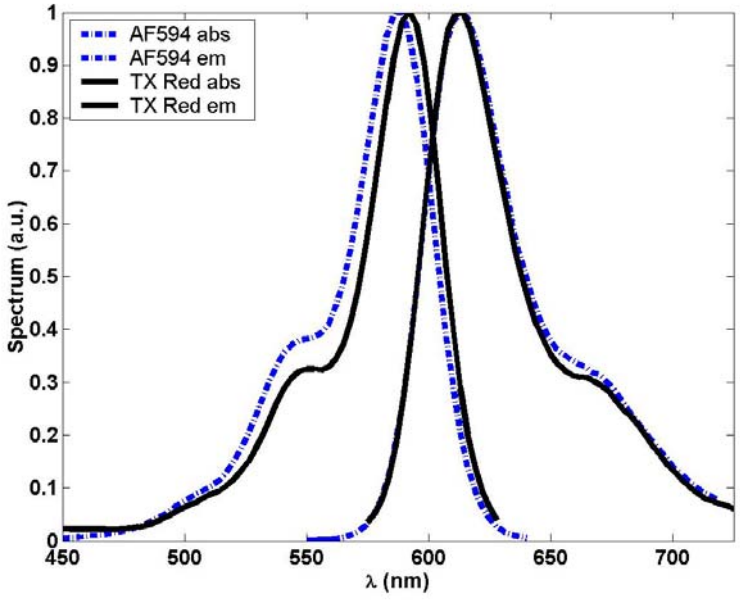

b

Figure 5.8 Overlapping absorption and emission spectra of (a) rhodamine B, 6-TAMRA, and DiI and (b) Alexa Fluor 594 and Texas Red.[41,42]

Figure 5.9 shows convergence of the GA to discriminate various dye pairs with tailored pulses. We discover that the degree of control is not predictable by that achieved relative to SHG for each individual dye. For example, both 6-TAMRA (conjugated to G5-FA) and rhodamine B had significant control relative to SHG (Figure 5.7b and Figure 5.7f), yet discrimination of rhodamine B from 6-TAMRA met with limited success (Figure 5.9c). The difficulty in using one-photon excitation or emission (Figure 5.8a) to differentiate the pair of rhodamine B and 6-TAMRA is thus not significantly ameliorated by the application of tailored two-photon excitation pulses. This is also the case for the one-photon spectrally indistinguishable pair Texas Red and AlexaFluor 594 (Figure 5.8b, Figure 5.9b). On the other hand, some dyes which are easily discriminated by means of their one-photon spectra, for example DiI and FITC, are quite amenable to differentiation by our GA (Figure 5.9h).

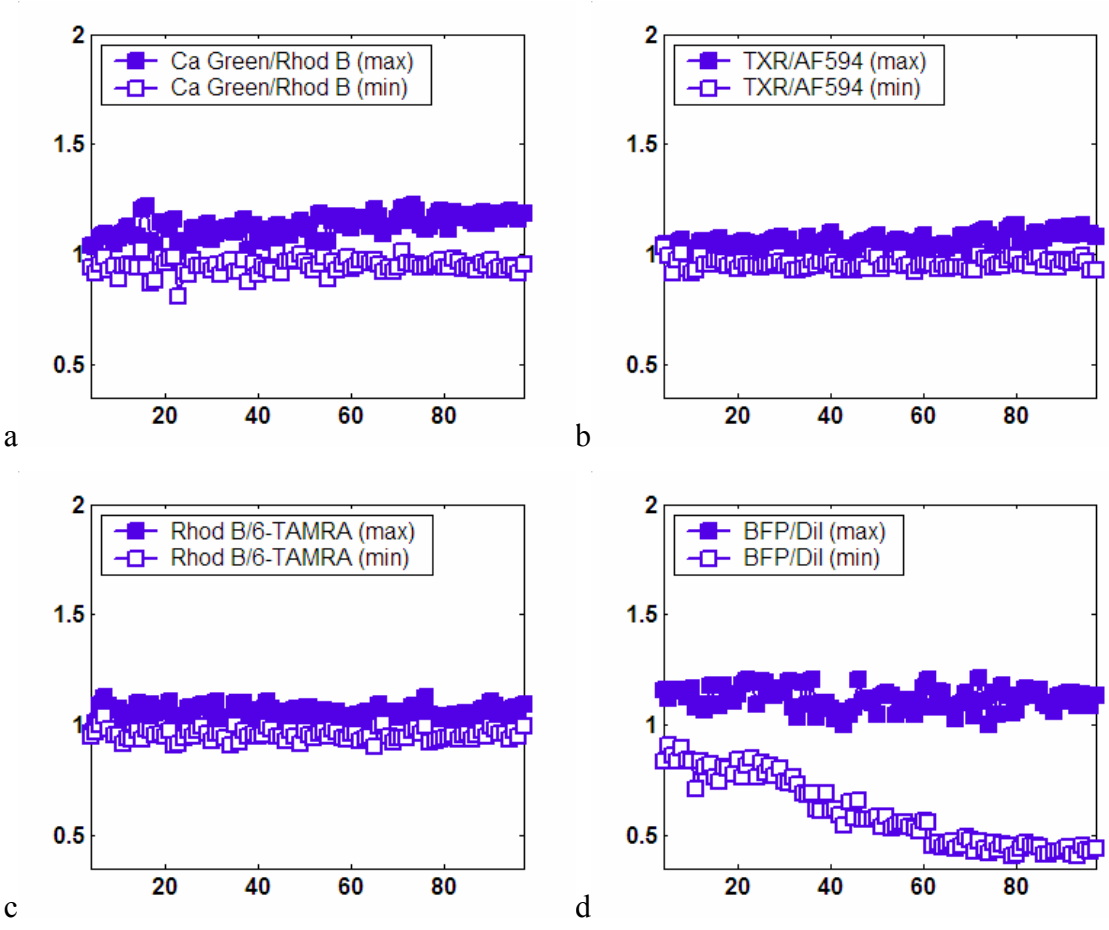

Figure 5.9 Control of the ratio of two-photon fluorescence from various dye pairs versus generation of GA. Closed squares show maximization of the ratio, and open squares mark the parallel experiment minimizing the same ratio (optimizing the inverse ratio).

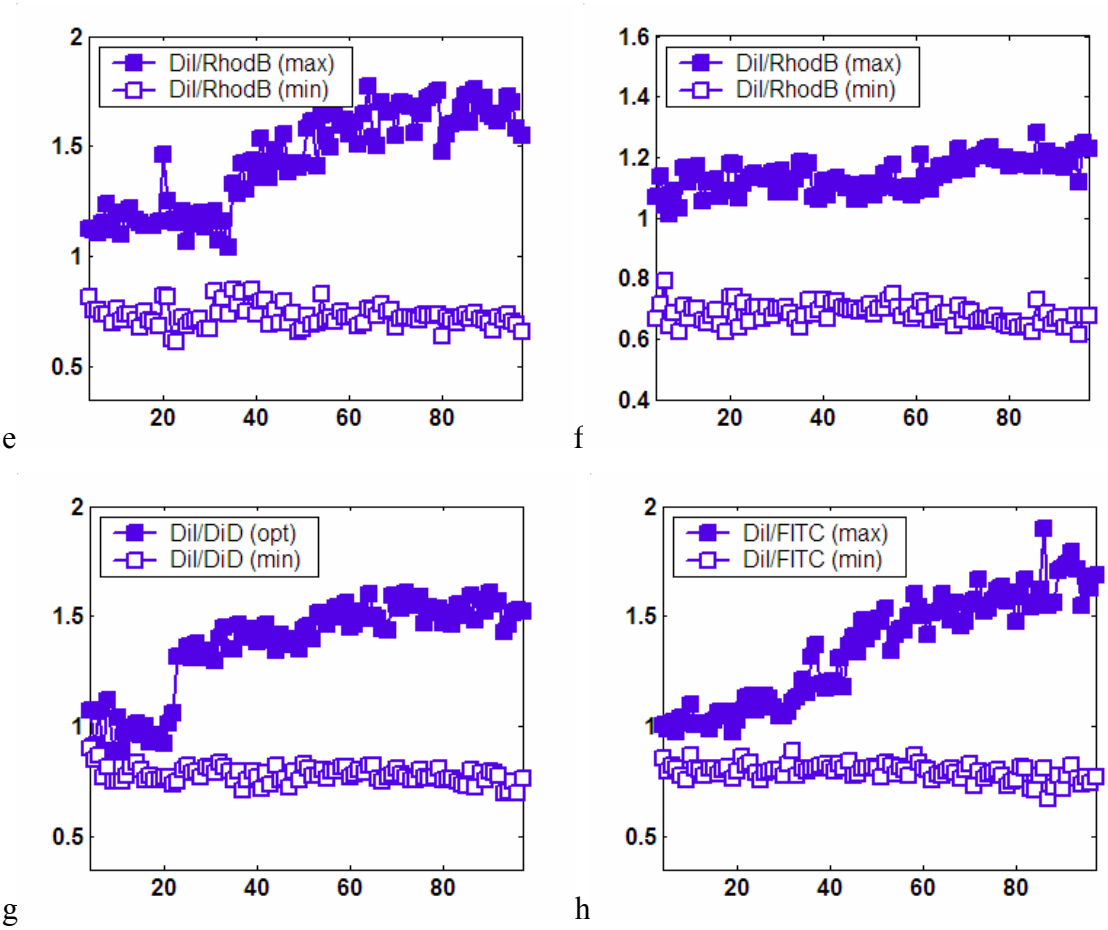

Figure 5.9 continued. Control of the ratio of two-photon fluorescence from various dye pairs versus generation of GA. Closed squares show maximization of the ratio, and open squares mark the parallel experiment minimizing the same ratio (optimizing the inverse ratio).

Identical one-photon spectra do not preclude two-photon distinction via pulse shaping, since two-photon processes obey different quantum selection rules[37-39]. For example, rhodamine B and DiI are distinguished by our GA to a significant extent (Figure 5.9e) despite almost complete overlap of both one-photon excitation and emission spectra, though the exact amount of discrimination found by the GA varies (Figure 5.9f). We are even able to use this capability to quantify the concentration of DiI and rhodamine B in a mixture of the two dyes[40].

Finally, dyes with different one-photon spectra are not necessarily more distinguishable with our method than the overlapping dyes. For example, rhodamine B and calcium green have distinguishable one-photon spectra, but are more poorly differentiated (Figure 5.9a) by our shaped pulses than the rhodamine B and DiI pair.

3.3 Determination of the conjugation states of dyes

Figure 5.10 summarizes attempts to discriminate two-photon fluorescence of free from conjugated dyes. For both the dendrimer and Herceptin conjugates, the degree of improvement in control after polynomial phase search by the GA is smaller than the combined error of the two signals (Table 5.5). However, for the F-actin-binding protein phalloidin, the differentiation of free versus bound Alexa Fluor 594 dye is significant by this measure.

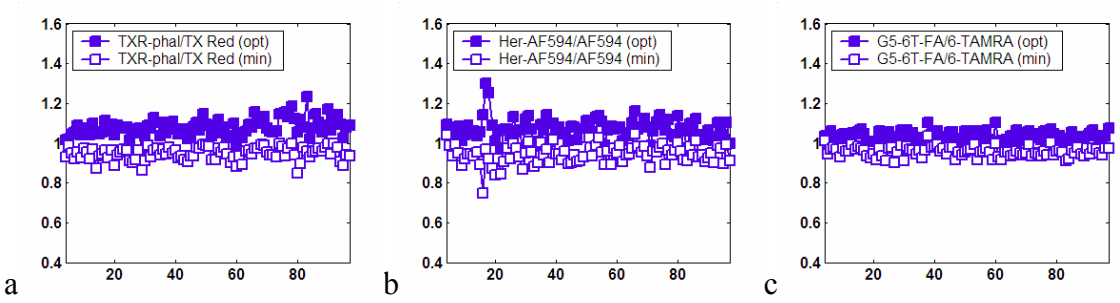

Figure 5.10 Control of the ratio of two-photon fluorescence from conjugated to free dye versus generation of GA. Closed squares show maximization of the ratio, and open squares mark the parallel experiment minimizing the same ratio (optimizing the inverse ratio).

In general, we believe that the conjugation state of a dye can only be determined with pulse shaping if there is a reasonably strong electronic interaction between the excited state orbital of the dye and the molecular orbitals of the conjugate molecule. Good evidence for such an interaction is a significant change of two-photon excitation cross-section spectrum for the dye upon binding, which has previously been shown to occur when Texas Red is conjugated to phalloidin[43].

3.4 Mechanism of fluorescence control

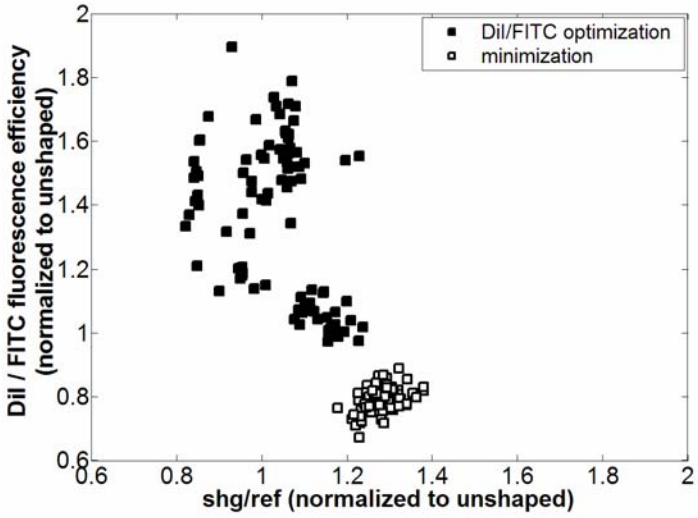

Figure 5.11 Correlation analysis of DiI vs FITC discrimination experiment from Figure 5.9h. DiI/FITC fluorescence efficiency ratio of the best individual for each of 100 generations is plotted against the corresponding SHG efficiency (SHG/I_{ref}). Closed squares show the maximization of the ratio, and open squares mark the parallel minimization experiment.

A common practice in the investigation of tailored pulse shaping is to look at the correlation of the outcome of the experiment with SHG (a surrogate for pulse compression), with the assumption that presence or absence of good correlation is a measure of the complexity of the control problem. For example, a simple problem like multiphoton ionization of a molecule might translate into maximizing the peak pulse energy. As the problem of SHG maximization also maps to the same underlying mechanism, a strong correlation is seen between multiphoton ionization and SHG in an adaptive search to maximize either[44]. Figure 5.11 shows this analysis for the DiI / FITC discrimination. No noticeable correlation is evident between the degree of discrimination of the pulse shapes and the SHG efficiency. This demonstrates that the discrimination mechanism does not map directly onto the simple problem of maximizing peak laser intensity. Despite the lack of correlation of the discrimination problem with SHG, second harmonic spectral tuning will be seen to provide an adequate explanation for the control.

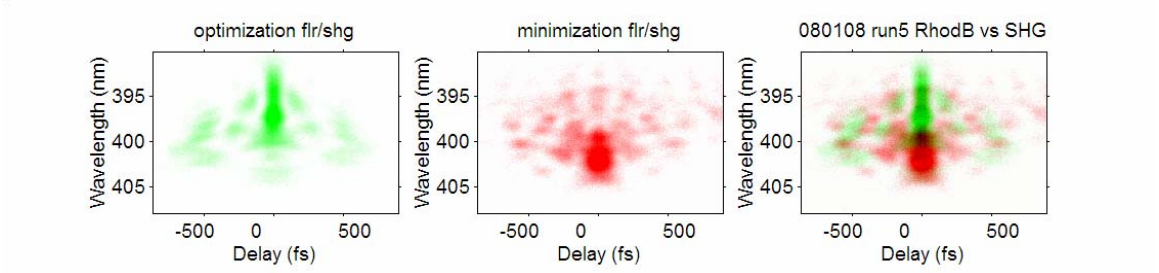

Figure 5.12 Optimal pulses measured by SHG-FROG for (a) maximization and (b) minimization of ratio of rhodamine B two-photon fluorescence to SHG from the experiment (shown in Fig. 6a and Fig. 6b), and (c) overlay.

Detailed information for optimal discriminating pulses is revealed in a time-frequency picture. Figure 5.12 shows the SHG-FROG traces in the case of rhodamine B and SHG. The complementary nature of the pulses for maximization and minimization is consistent with our previous observations[29]. Often, part of the exciting laser field is broken down into a series of pulses, characteristic of control of an excited state wavepacket's motion in coherence with vibrational energy level changes[45]. However, most of the pulse energy is nevertheless confined to short delay times. Thus, a second order perturbation analysis gives significant insight into the underlying mechanism of discrimination[44]. The essential parameters are the second harmonic spectrum $S_2(\omega)$ of the pulse and the two-photon excitation cross-section $\sigma^{(2)}(\omega)$ of the dye. The spectrum at zero time delay on the SHG-FROG trace is in fact $S_2(\omega)$. Whereas the SHG signal is the total integral of $S_2(\omega)$, the fluorescent signal is the integral of the product of S_2 and $\sigma^{(2)}$. Thus, the pulse optimizing the fluorescence to SHG ratio is achieved by tuning $S_2(\omega)$ to peak in the region where $\sigma^{(2)}(\omega)$ peaks as well, whereas minimization is achieved by tuning $S_2(\omega)$ to peak away from this region. Figure 5.13 reveals this tuning of $S_2(\omega)$ (extracted from the traces of Figure 5.12) relative to the rhodamine B cross-section spectrum we measured in the time-domain. Also shown is the spectrum of $\sigma^{(2)}$ for 6-TAMRA, which was simultaneously measured from the other arm of the setup. Noting the similar shape of these cross-sections, it becomes clear why our GA was unable to distinguish these two dyes despite their individual fluorescence controllability relative to SHG (Table 5.5). Thus, our acousto-optic time-domain cross-section spectrum measurement yields a prediction of the success or failure of our method to distinguish any attempted dye pair.

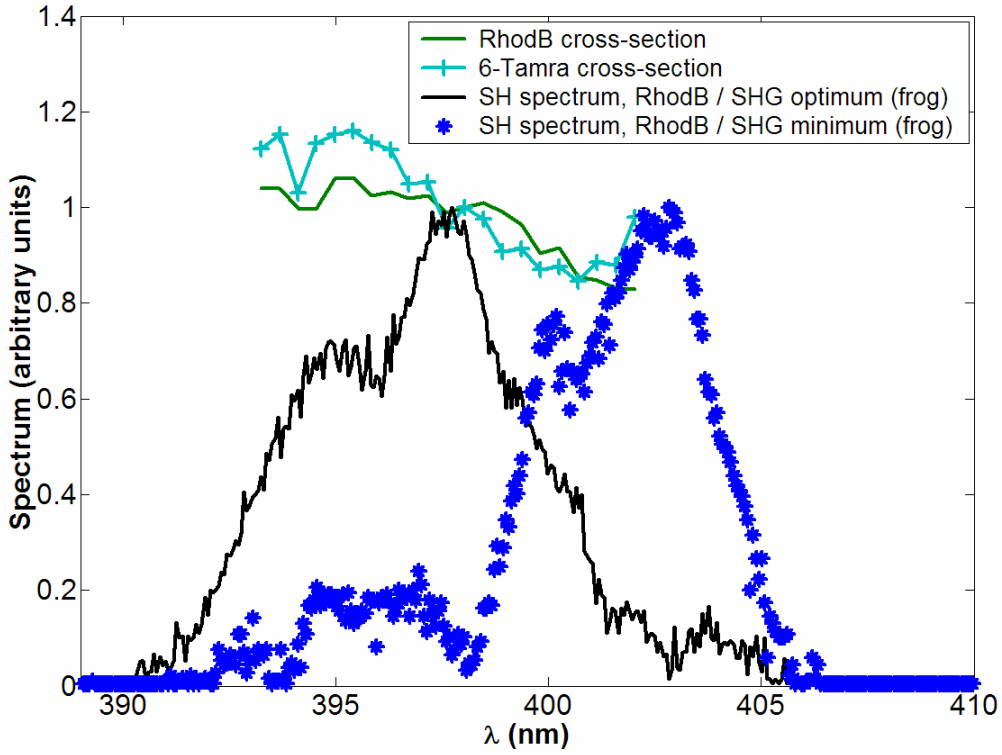

Figure 5.13 Tuning of pulse second harmonic spectrum relative to cross-section. Time domain measured two-photon excitation cross-sections of rhodamine B (green line) and 6-TAMRA (cyan line with plusses). Also shown are the second harmonic spectrum of optimal pulses for maximization (black line) or minimization (blue asterixes) of Rhod B fluorescence / SHG ratio, determined from FROG traces in Figure 5.12.

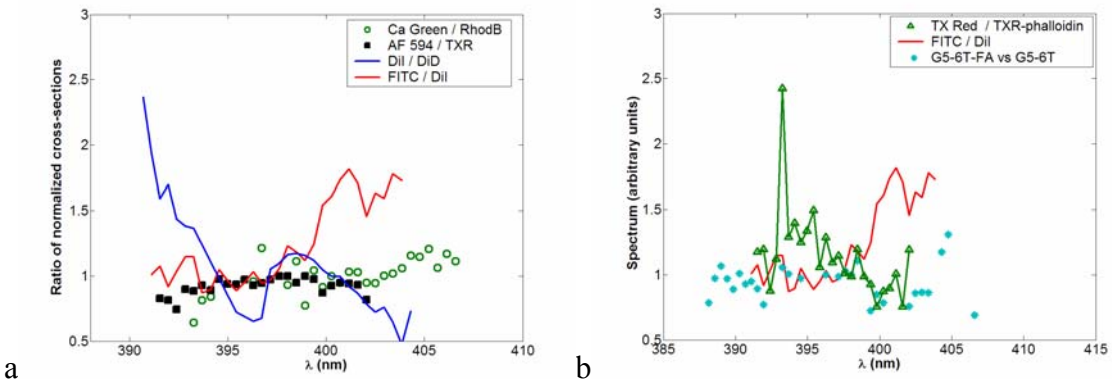

a b

Figure 5.14 Relative two-photon excitation cross-sections of several dye pairs, as measured acousto-optically in the time-domain.

Several ratios of cross-sections we measured are plotted in Figure 5.14. Within the second harmonic spectral bandwidth of the laser pulses, we measured strikingly flat

curves for the pair of Texas Red vs. Alexa Fluor 594 (Figure 5.14a). The G5-FA-conjugated vs. free 6-TAMRA pair also seems quite flat (Figure 5.14b), though the measurement suffers greater noise. As our experiment operates in the same spectral range, it is not able to discriminate the two dyes by a simple tuning of the second-harmonic spectrum $S_2(\omega)$. The under 25% total control (Table 5.5) in differentiating these pairs is thus the result of a fundamental physical limitation. The direction of tuning of $S_2(\omega)$ we measured was always consistent with the relative cross-section in successful discriminations.

4. Conclusion

We have used tailored femtosecond pulses to control two-photon fluorescence of several common dyes relative to second harmonic generation, which fundamentally has the same nonlinear dependence. We have further studied the ability of our evolutionary learning algorithm to find pulses which selectively enhance or suppress two-photon fluorescence of one dye or dye-conjugate relative to another. While the controllability of individual dyes against SHG does not predict the success of the latter trials, we find that the ratio of two-photon excitation cross-section spectra for the dyes is always consistent with the tuning of the second harmonic spectrum of the excitation pulses. Therefore, we conclude that photon-photon interferences play the major role in discrimination. These interferences are best accessed with arbitrary phase modulation beyond the fourth order polynomial phase, and therefore typical GA runs experience the most significant improvement after the period of restriction to polynomial modulation is passed in our graded search algorithm. Interestingly, the ability to distinguish these dye pairs was uncorrelated with the utility of one-photon spectra to discriminate the dyes, due to the fundamentally different processes responsible for one- vs. two-photon excitation.

Systematic errors from mismatches in different arms of the experiment including dispersion, saturation, or other causes of subquadratic scaling can be removed by examining the improvement of the GA after the graded search has progressed to full phase modulation. Further comparing the degree of enhancement to laser instabilities reflected in repeated measurements of the unshaped pulses lends insight into the true extent of discrimination achieved in our experiments.

Considering the relative improvement compared to the noise in the measurements, the evolutionary search was unable to recognize Herceptin or PAMAM dendrimer-conjugation in our experiments. This is not surprising considering the lack of change upon conjugation of two-photon excitation spectra we measured with the acousto-optic time domain method in the bandwidth of our exciting laser pulse. In the event of a strong electronic coupling to the dye molecule upon conjugation, as reflected in a change of two-photon excitation spectrum, our method is more likely to succeed. This is evidenced in the case of discrimination of phalloidin-bound from free Texas Red dye. Another

example of a strong interaction with a dye would be an antibody binding to the dye. In the future we hope to exploit this to develop molecular assays based on detection of precisely these binding events.

There are several aspects of the work presented here which may prove valuable in the eventual practical application. Firstly, the multiplicative fitness parameter of our genetic algorithm is able achieve significant discrimination without a drop in signal of the favored fluorophore, which is very advantageous for signal-to-noise ratio limited measurement techniques. Secondly, the lack of positive or negative correlation of one-photon differentiation with two-photon tailored pulse distinguishability will help us to validate systems relying on tailored pulse shaping with spectrally distinct dyes, and then subsequently apply it to differentiate dyes which are otherwise indistinguishable, for example rhodamine B and DiI. Finally, the exciting pulse phase can be rapidly modulated in an acousto-optic programmable dispersive filter like the Dazzler for high throughput applications. In these cases, the reconfiguration time for one or more laser sources and emission filters traditionally used for discrimination would be prohibitive. Even compared to the standard liquid crystal pulse shaping for selective excitation, the acousto-optic method enables reduction of typical switching times of tens of milliseconds[46,47] into the submillisecond regime[7].

References

1. Zipfel WR, Williams RM, Webb WW. Nonlinear magic: multiphoton microscopy in the biosciences. Nat Biotechnol 2003;21(11):1369-1377.
2. König K. Multiphoton microscopy in life sciences. J Microsc 2000;200(Pt 2):83-104.
3. Squirrell JM, Wokosin DL, White JG, Bavister BD. Long-term two-photon fluorescence imaging of mammalian embryos without compromising viability. Nat Biotechnol 1999;17(8):763-767.
4. Zhong C, Ye J, Myc A, Thomas T, Bielinska A, Jr, Norris T. Two-photon flow cytometry. In: Periasamy A, So P, editors; 2005. SPIE. p 78-89.
5. Tkaczyk ER, Zhong CF, Ye JY, Myc A, Thomas T, Cao Z, Duran-Struuck R, Luker KE, Luker GD, Norris TB, Baker Jr JR. In vivo monitoring of multiple circulating cell populations using two-photon flow cytometry. Optics Communications 2008;281(4):888-894.
6. Zhong CF, Tkaczyk ER, Thomas T, Ye JY, Myc A, Bielinska A, Cao Z, Majoros I, Balazs K, Baker JR, Norris TB. Quantitative Two-Photon Flow Cytometry – in Vitro and in Vivo. Journal of Biomedical Optics 2008;13(3).
7. Ogilvie JP, D D, Solinas X, Martin JL, Beaurepaire E, Joffre M. Use of coherent control for selective two-photon fluorescence microscopy in live organisms. Optics Express 2006;14:759-766.
8. Dudovich N, Oron D, Silberberg Y. Single-pulse coherently controlled nonlinear Raman spectroscopy and microscopy. Nature 2002;418(6897):512-514.
9. Brixner T, Damrauer NH, Niklaus P, Gerber G. Photoselective adaptive femtosecond quantum control in the liquid phase. Nature 2001;414(6859):57-60.
10. Lozovoy V, Pastirk I, Walowicz K, Dantus M. Multiphoton intrapulse interference. II. Control of two- and three-photon laser induced fluorescence with shaped pulses. The Journal of Chemical Physics 2003;118(7):3187-3196.
11. Cao J, Che J, Wilson KR. Intrapulse Dynamical Effects in Multiphoton Processes: Theoretical Analysis. J Phys Chem A 1998;102(23):4284-4290.
12. Tannor DJ, Kosloff R, Rice SA. Coherent pulse sequence induced control of selectivity of reactions: Exact quantum mechanical calculations. J Chem Phys 1986;85:5805-5820.
13. Bardeen CJ, Yakovlev VV, Squier JA, Wilson KR. Quantum Control of Population Transfer in Green Fluorescent Protein by Using Chirped Femtosecond Pulses. J Am Chem Soc 1998;120(50):13023-13027.
14. Blanchet Vr, Nicole Cl, Bouchene M-A, Girard B. Temporal Coherent Control in Two-Photon Transitions: From Optical Interferences to Quantum Interferences. Physical Review Letters 1997;78:2716.

15. Dudovich N, Dayan B, Gallagher Faeder SM, Silberberg Y. Transform-Limited Pulses Are Not Optimal for Resonant Multiphoton Transitions. Phys Rev Lett 2001;86(1):47-50.

16. Laiho L, Pelet S, Hancewicz T, Kaplan P, So P. Two-photon 3-D mapping of ex vivo human skin endogenous fluorescence species based on fluorescence emission spectra. Journal of Biomedical Optics 2005;10(2).

17. Lozovoy V, Dantus M. Systematic Control of Nonlinear Optical Processes Using Optimally Shaped Femtosecond Pulses. ChemPhysChem 2005;6(10):1970-2000.

18. Kawano H, Nabekawa Y, Suda A, Oishi Y, Mizuno H, Miyawaki A, Midorikawa K. Attenuation of photobleaching in two-photon excitation fluorescence from green fluorescent protein with shaped excitation pulses. Biochemical and Biophysical Research Communications 2003;311(3):592-596.

19. Yarden Y. The EGFR family and its ligands in human cancer: signalling mechanisms and therapeutic opportunities. European Journal of Cancer 2001;37(Supplement 4):3-8.

20. Mendelsohn J, Baselga J. Status of Epidermal Growth Factor Receptor Antagonists in the Biology and Treatment of Cancer. J Clin Oncol 2003;21(14):2787-2799.

21. Majoros IJ, Thomas TP, Mehta CB, Baker JR. Poly(amidoamine) dendrimer-based multifunctional engineered nanodevice for cancer therapy. J Med Chem 2005;48(19):5892-5899.

22. Thomas T, Ye JY, Chang Y-C, Kotlyar A, Cao Z, Majoros I, Norris TB, Baker JR. Investigation of tumor cell targeting of a dendrimer nanoparticle using a double-clad optical fiber probe. Journal of Biomedical Optics 2008;13(1):014024.

23. Verluise F, Laude V, Huignard JP, Tournois P, Migus A. Arbitrary dispersion control of ultrashort optical pulses with acoustic waves. Journal of the Optical Society of America B Optical Physics 2000;17:138-145.

24. Kaplan D, Tournois P. Theory and performance of the acousto optic programmable dispersive filter used for femtosecond laser pulse shaping. Journal de Physique IV 2002;12:69-75.

25. Siegman AE. Lasers. American Journal of Physics 1987;55(9):862.

26. Bardeen CJ, Wang Q, Shank CV. Femtosecond Chirped Pulse Excitation of Vibrational Wave Packets in LD690 and Bacteriorhodopsin. J Phys Chem A 1998;102(17):2759-2766.

27. Pearson BJ, White JL, Weinacht TC, Bucksbaum PH. Coherent control using adaptive learning algorithms. Physical Review A 2001;63(6):063412.

28. Laarmann T, Shchatsinin I, Stalmashonak A, Boyle M, Zhavoronkov N, Handt J, Schmidt R, Schulz CP, Hertel IV. Control of Giant Breathing Motion in C[sub 60] with Temporally Shaped Laser Pulses. Physical Review Letters 2007;98(5).

29. Tkaczyk ER, Mignot A, Ye JY, Majoros I, Baker JR, Norris TB. Increasing two-photon fluorescence signals by coherent control. In: Periasamy A, So PTC, editors; 2006. p 165-174.

30. Laarmann T, Shchatsinin I, Singh P, Zhavoronkov N, Gerhards M, Schulz CP, Hertel IV. Coherent control of bond breaking in amino acid complexes with tailored femtosecond pulses. The Journal of Chemical Physics 2007;127(20).

31. Trebino R, Delong K, Fittinghoff D, Sweetser J, Krumbugel M, Richman B, Kane D. Measuring ultrashort laser pulses in the time-frequency domain using frequency-resolved optical gating. Review of Scientific Instruments 1997;68(9):3277-3295.

32. Weiner A. Effect of group velocity mismatch on the measurement of ultrashort optical pulses via second harmonic generation. Quantum Electronics, IEEE Journal of 1983;19(8):1276-1283.

33. Ogilvie J, Kubarych K, Alexandrou A, Joffre M. Fourier transform measurement of two-photon excitation spectra: applications to microscopy and optimal control. Opt Lett 2005;30(8):911-913.

34. Bellini M, Bartoli A, HÃ¤nsch TW. Two-photon Fourier spectroscopy with femtosecond light pulses. Opt Lett 1997;22(8):540-542.

35. Naganuma K, Mogi K, Yamada H. General method for ultrashort light pulse chirp measurement. Quantum Electronics, IEEE Journal of 1989;25(6):1225-1233.

36. Trebino R. Frequency-Resolved Optical Gating: The Measurement of Ultrashort Laser Pulses; 2002.

37. So P, Dong C, Masters B, Berland K. TWO-PHOTON EXCITATION FLUORESCENCE MICROSCOPY. Annual Review of Biomedical Engineering 2000;2(1):399-429.

38. Xu C, Zipfel W, Shear J, Williams R, Webb W. Multiphoton fluorescence excitation: New spectral windows for biological nonlinearÂ microscopy. PNAS 1996;93(20):10763-10768.

39. Denk W, Svoboda K. Photon upmanship: why multiphoton imaging is more than a gimmick. Neuron 1997;18(3):351-357.

40. Tkaczyk ER, Tkaczyk AH, Mauring K, Ye JY, Baker JR, Norris TB. Quantitative differentiation of dyes with overlapping one-photon spectra by femtosecond pulse shaping. Nature 2008;submitted.

41. Du H, Fuh R-CA, Li J, Corkan LA, Lindsey JS. PhotochemCAD: A Computer-Aided Design and Research Tool in Photochemistry. Photochemistry and Photobiology 1998;68(2):141-142.

42. Invitrogen. http://probes.invitrogen.com/servlets/spectra. Invitrogen Website; 2008.

43. Bestvater F, Spiess E, Stobrawa G, Hacker M, Feurer T, Porwol T, Berchner-Pfannschmidt U, Wotzlaw C, Acker H. Two-photon fluorescence absorption and emission spectra of dyes relevant for cell imaging. J Microsc 2002;208(Pt 2):108-115.

44. Brixner T, Damrauer NH, Kiefer B, Gerber G. Liquid-phase adaptive femtosecond quantum control: Removing intrinsic intensity dependencies. The Journal of Chemical Physics 2003;118(8):3692-3701.

    Brixner T, Kiefer B, Gerber G. Problem complexity in femtosecond quantum control. Chemical Physics 2001;267(1-3):241-246.

45. Prokhorenko VI, Nagy AM, Miller RJD. Coherent control of the population transfer in complex solvated molecules at weak excitation. An experimental study. J Chem Phys 2005;122:4502.

46. Pastirk I, Dela Cruz J, Walowicz K, Lozovoy V, Dantus M. Selective two-photon microscopy with shaped femtosecond pulses. Opt Express 2003;11(14):1695-1701.

47. Delacruz JM, Pastirk I, Lozovoy VV, Walowicz KA, Dantus M. Multiphoton Intrapulse Interference 3: Probing Microscopic Chemical Environments. J Phys Chem A 2004;108(1):53-58.

CHAPTER 6
DIFFERENTIAL QUANTIFICATION OF DYES WITH OVERLAPPING ONE-PHOTON ABSORPTION AND EMISSION SPECTRA BY PULSE SHAPING

Abstract. The ability to distinguish different fluorescent species is central to simultaneous measurement of multiple molecular targets. At present, high throughput applications rely primarily on spectral filtering of emission, and it is difficult to tell apart fluorophores with significant spectral overlap. We demonstrate that DiI and Rhodamine B, which are not distinguishable to one-photon measurements, can be differentiated and in fact quantified in mixture via tailored two-photon excitation pulses found by a genetic algorithm (GA). A nearly three-fold difference in the ratio of two-photon fluorescence of the two dyes is achieved, without a drop in signal of the favored fluorophore. A mixture of 25% Rhodamine B and 75% DiI solution was measured with fractional concentrations of 0.27 +/- 0.08 and 0.64 +/- 0.54 for the two dyes, respectively. Implementing an acousto-optic interferometer, we were able to use the same experimental setup to measure two-photon excitation cross-sections of Rhodamine B and DiI in the time domain. These prove that the mechanism of discrimination is second-harmonic tuning by the phase-shaped pulses to the relative maxima and minima of these cross-sections.

1. Introduction

Multiphoton fluorescence is widely used for biomedical microscopy, *in vivo* sensing, and more recently, flow cytometry [1-5]. Generally, multiple dyes are employed for simultaneous measurements of multiple targets, and in almost all high-throughput applications, these dyes are discriminated by spectral filtering. Laser pulse shaping offers a new avenue of fluorescence discrimination. In addition to microscopy, tailored pulse shapes have been successfully applied in spectroscopy [6]. It has already been demonstrated that laser pulse shaping is a successful tool to distinguish fluorescent species [7-9], but several years have elapsed since the proposal of optical dynamic discrimination (ODD) [10] with limited practical application [11]. In the current letter, we investigate the discrimination of the dyes DiI and Rhodamine B. Simple spectral filtering of one-photon excitation or emission light is not sufficient to distinguish this dye pair [12], but we are able to successfully differentiate them with tailored pulse shapes found in a genetic algorithm (GA) search. We also demonstrate the capability to use pulse shaping to quantitatively measure a mixture of the dye pair.

For phase- and amplitude-shaped femtosecond laser pulses, two-photon fluorescence of the dyes was collected concurrently, and the pulse shapes were adaptively improved in a closed-loop manner to maximize the discrimination. In parallel, a second harmonic generation (SHG) signal for the pulse reflected the pulse compression. This was found to be uncorrelated to the discriminating ability of the pulses created by the algorithm. All three signals were maintained within the quadratic scaling regime with power to avoid trivial convergences which might hinder or mask discrimination. A multiplicative fitness parameter in the search prevented drop in signal during the course of the algorithm. A time-domain measurement of the two-photon excitation cross-section of each dye $\sigma_{RhodB}(\omega)$ and $\sigma_{DiI}(\omega)$ was implemented acousto-optically by the pulse shaper in order to interpret the results. The convergence of the algorithm is interpreted in terms of tuning of the laser pulse second harmonic spectrum $S_2(\omega)$ to the maximum or minimum of the ratio $\sigma_{DiI}(\omega)/\sigma_{RhodB}(\omega)$.

In section 2 of this paper, we present the detailed experimental setup and procedure, including a description of the GA and acousto-optic time-domain $\sigma(\omega)$

measurement. Section 3 demonstrates discrimination of DiI from Rhodamine B, which is discussed in relation to SHG. Also, we present evidence for second harmonic spectral tuning as the mechanism. Finally, we demonstrate quantitative measurement of a mixture of the two dyes based only on the signal of the mixture under different pulse shapes.

2. Materials and Methods

2.1 Samples

DiI was purchased from Invitrogen Corpororation (Carlsbad, CA) and diluted to 20 μM in DMSO solvent. Rhodamine B (Rhodamine 610) was purchased from Exciton (Dayton, OH) and mixed to a 1 μM solution in water.

2.2 Experimental setup

The experimental setup is shown in Figure 6.1. The laser system consists of a regeneratively amplified Ti:sapphire system (RegA, Coherent, Santa Clara, CA) providing up to 4 μJ, 50 fs pulses at 250 kHz with a center wavelength of 800 nm and 27 nm FWHM bandwidth. The "Dazzler," an acousto-optic programmable dispersive filter (AOPDF) (Fastlite, Palaiseau, France), is used to shape the laser pulses. The Dazzler modulates the diffracted output pulse by way of an acousto-optic interaction with an RF wave launched into a TeO_2 crystal [13, 14]. The controlling electronics of the Dazzler read the diffracted power, center wavelength, bandwidth, and polynomial phase to fourth order from a text file, which in our experiments is automatically generated by the algorithm. Additionally, an amplitude file can be read to spectrally shape the diffracted beam, and the phase in different frequency bins can be read from a phase file for complete control of the pulse shape. The Dazzler is triggered by every twelfth RegA pulse for an approximately 20 kHz repetition rate. SHG-FROG measurements confirm that the approximately 6 shaped pulses falling within the 50% duty cycle of the Dazzler give precisely the same average two-photon time-frequency characteristics as are obtained when the RegA is operated at 20 kHz. Thus, the effective shaping of all 6 diffracted pulses per launched RF waveform has the same effect in our experiment as if each were synchronized to the center of separate identical acoustic waves in the TeO_2 crystal.

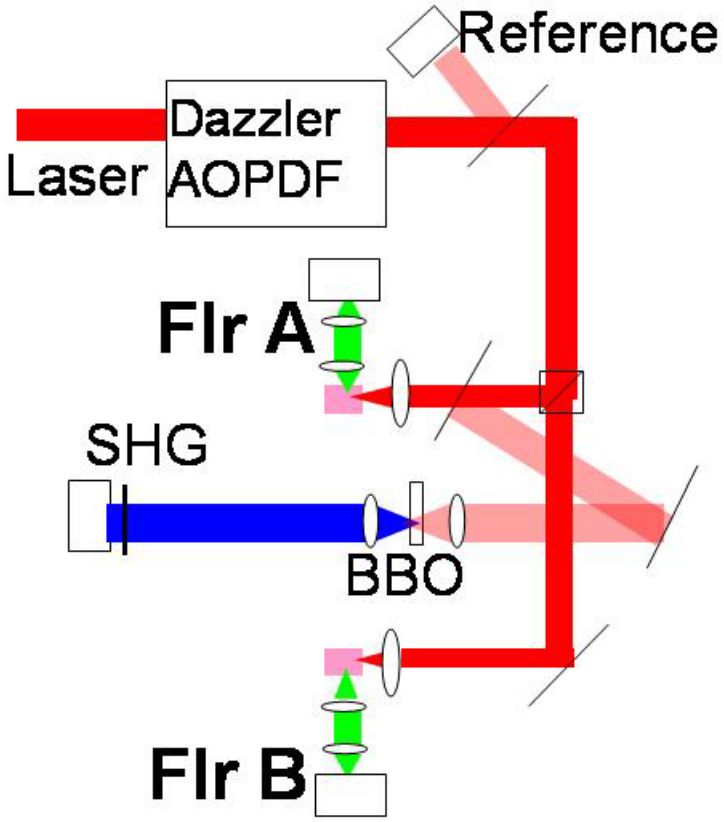

Figure 6.1 Experimental Setup. The dye sample is contained in a disposable fluorescence cuvette (Cole Palmer). Incident laser power I_{ref} is measured by photodiode (R2066, Hamamatsu). After filters to remove all pump laser and exciting 800 nm light, the two-photon fluorescence signal FlrA or FlrB is measured in the perpendicular direction by a PMT (H5784-01, Hamamatsu). SHG from the BBO crystal is detected by another PMT (R2066, Hamamatsu). Lenses are depicted as ovals.

A glass-coverslip beamsplitter enables a reference reading of incident power I_{ref} by a photodiode (FFD-100, Perkin-Elmer Optoelectronics, Fremont, CA). We define the efficiency of each two-photon fluorescence signal S as the ratio S/I_{ref}. The excitation beam is then divided into two arms with a beamsplitter, and the relative power in each arm is controlled with a variable reflective attenuator. Each arm is focused into a cuvette holding the dye sample, and the fluorescence signal FlrA or FlrB is collected in the perpendicular direction through an appropriate bandpass filter for detection by a photomultiplier tube (PMT) (H5784-01, Hamamatsu, Bridgewater, NJ). Immediately preceding the lens, the FlrA arm additionally has another glass-coverslip beamsplitter to create a third arm of the experiment. In the third arm, a 500-micron thick beta barium borate (BBO, β-BaB_2O_4) crystal is used for second-harmonic generation, which is read

through a blue absorptive filter by another PMT (R2066, Hamamatsu, Bridgewater, NJ) to give the signal SHG. All four signals I_{ref}, FlrA, FlrB, and SHG are read in parallel as root-mean-square voltage for 2500 samples by a 250 kHz DAQ board (M-series, National Instruments, Austin, TX), which is synchronized by the Dazzler trigger.

2.3 Pulse search method

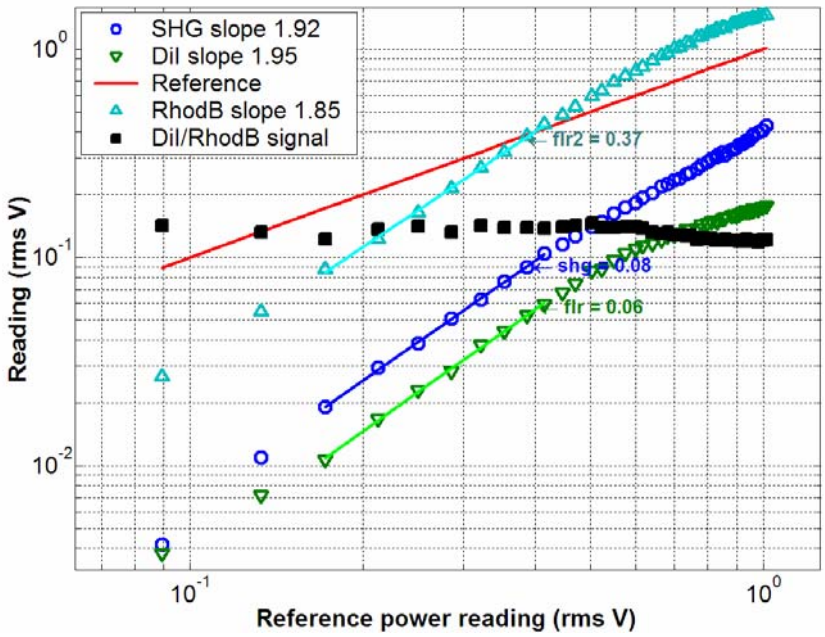

Figure 6.2 Power scaling of two-photon signals relative to I_{ref}. Blue circles show the SHG signal (typically 0.08 Vrms in the experiments), green downwards triangles show the DiI signal (20 μM in DMSO, typically 0.06 Vrms), cyan upwards triangles show the Rhodamine B signal (1 μM in H_2O, typically 0.37 Vrms), and the red line shows I_{ref} (typically 0.39 Vrms). Axes are in log scale. Filled black squares show the dependence of the ratio DiI/Rhodamine B fluorescent signal on power. Slopes of a least-squares linear fit through the center of the data are marked in the legend.

Before each experiment, the incident power was scanned to ensure quadratic scaling of the discriminated two-photon processes, as shown in Figure 6.2, to ensure that apparent discrimination of dyes is not merely an artifact which would disappear when the laser power is changed. There are three possible causes for subquadratic behavior: saturation of molecular transitions, detector saturation, or scattered excitation light leakage into the detector. Typical shaped pulse energies after the Dazzler used during experiments are typically on the order of 2 nJ. Assuming a diffraction-limited beam waist, we estimate a typical fluence at the laser focus during experiments on the order of 0.5 mJ/cm^2 (peak intensity on the order of a GW/cm^2 transform-limited), which is too

low to saturate the molecular transitions. Detector saturation is ruled out by an independent calibration demonstrating linearity to much higher signal levels. Scattered light is minimized with bandpass filters and beam dumps. As long as both signals used in the fitness parameter have the same degree of deviation from quadratic scaling, scattered light was not noted to affect the convergence of the algorithm. However, if one dye for example is approaching saturation of the molecular transition while the other is still in the quadratic region, this trivializes the convergence to mere pulse stretching. Photobleaching with a recovery time of several seconds was also noted for repeated measurements anywhere near the saturation region of Rhodamine B or DiI. Thus, the power scaling check in each experiment is extremely important.

A genetic learning algorithm (GA) is used to find the optimal pulse shape, with implementation similar to that already described by Pearson *et al*. [15]. Briefly, the polynomial controls and amplitude and phase file settings to the Dazzler are used as genes of a single circular chromosome to define a specific individual laser pulse. After measuring all four signals for an individual, the adaptive learning algorithm programs the next individual. Though each measurement of a specific pulse shape lasts only 50 ms, about 500 ms are typically required for the electronics to implement the acoustic wave of a novel pulse shape in the TeO_2 crystal of the Dazzler. Once RF waves for the shapes have been saved for the Dazzler, switching between them is possible in sub-millisecond time. A random population of 50 individuals is ranked via a fitness parameter, and the best 10 individuals are passed unmodified to the next generation. Remaining individuals of the new generation are created by mating and mutation of fitness-preferenced individuals of the preceding generation. In each generation, signals are also measured for the unshaped pulse, which is obtained by programming polynomial phase exactly compensating the dispersion from the Dazzler TeO_2 crystal (but not from elsewhere in the optical path).

While our goal is to optimize a ratio A/B, we seek a fitness parameter which does not preference A and B near 0. At the same time either increasing A or decreasing B alone should improve the fitness monotonically. This can be accomplished via the multiplicative fitness parameter $(A-c)(c^{-1}-B)$, where values of A and B are normalized to the unshaped pulse measurement. We have found that setting the constant c to 0.8 yields

better convergence in our experimental conditions, relative to the original implementation of unity for c [16].

We characterized pulses with a commercial SHG-FROG unit [17] (Grenouille 8-50 from SwampOptics, Atlanta, GA) and software (VideoFrog, MesaPhotonics, Santa Fe, NM). SHG-FROG was performed as soon as possible after the end of the GA experimental run to ensure maximum fidelity of the reproduced pulse to that actually measured in the course of the experiment.

2.4 Time-domain two-photon excitation cross-section measurement

Using the same experimental setup of Figure 6.1, we implemented a time-domain measurement of the two-photon excitation cross-section spectra of DiI and Rhodamine B in the region of interest. This was performed analogously to the description by Ogilvie and colleagues [18]. However, rather than physically delaying a beam-split replica of the pulse, a virtual Michelson interferometer was programmed into the Dazzler. A delay of t_0 between pulses is achieved with simple multiplication by a cosine amplitude mask $\cos(\omega t_0/2)$ in the frequency domain for 150 intervals in an 80 nm bandwidth, corresponding in the conjugate Fourier domain to a time delay of t_0. Note that we only use binary coding of the phase file to be at 0 or pi corresponding to the sign of the cos function, as absolute and linear phase (absolute time delay) are physically irrelevant when the information is actually contained in the interarrival period of the two pulses [19]. When the data is Fourier transformed, the two-photon excitation cross-section is extracted with relatively good accuracy in the frequency domain as the divisor of the fluorescent signal by the second-harmonic signal in the region of the $2\omega_0$ component. For detailed mathematical proof of this, the reader is referred to the article by Naganuma *et al*. [20] or Trebino's discussion [21].

3. Results and Discussion

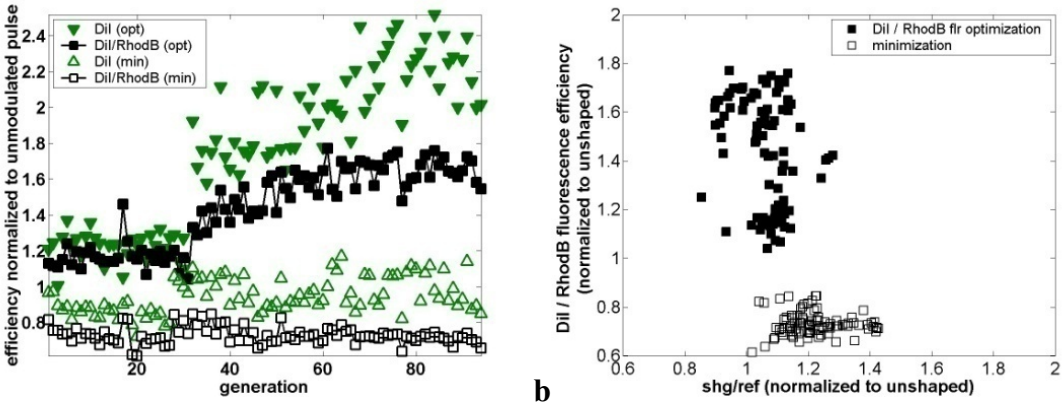

Figure 6.3 Control of fluorescence ratio for 1 μM Rhodamine B in H_2O (FlA) versus 20 μM DiI in DMSO (FlB). Only polynomial phase was adjusted until generation 30. After this, both amplitude and phase files were used, with 20 frequency bins in each over 60 nm of bandwidth for a total of 45 genes. The phase manipulation was constrained for delays between 1000 and 3000 fs. (a) Measurements for each generation's best individuals in the maximization of DiI / Rhodamine B fluorescence efficiency experiment are shown with filled markers, whereas the parallel minimization experiment is shown with open markers. Black squares show the ratio of DiI / Rhodamine B fluorescence efficiency and green triangles show the DiI fluorescence efficiency for the same individual. (b) Correlation analysis of DiI / Rhodamine B fluorescence efficiency plotted against the corresponding SHG efficiency, for the best individuals of the experiment. All measurements are normalized to the unshaped pulse (with polynomial phase compensating the dispersion of the Dazzler TeO_2 crystal).

3.1 Demonstration of discrimination

Figure 6.3a shows the convergence of the GA to optimize the ratio of two-photon fluorescence from DiI to Rhodamine B in parallel with the minimization experiment. The highest achieved ratio of DiI to Rhodamine B fluorescence is 1.769 whereas the minimum in the parallel experiment is 0.614 (normalized to the unshaped pulse). Most of the improvement in fluorescence discrimination occurs only after phase beyond the 4th order polynomial is allowed to be modified after generation 30. Notably, the discrimination control closely follows the two-photon fluorescent signal of DiI. When the number of frequency bins of the GA was increased from 20 to 100, almost precisely the same level of control (1.770 and 0.655) resulted in a repetition of the same experiment on a different day. Thus the result is not dependent on high frequency resolution in the pulse shaping. Any possible detector-specific bias of the experiment is excluded by a repetition with swapped samples, which yielded again the same level of

control (1.682 and 0.683). It is notable that in all cases the multiplicative fitness parameter ensures that the fluorescence of the favored fluorophore is comparable to, or significantly higher than that with the unshaped pulse. This is important for practical applications where signal-to-noise is a typical limiting factor.

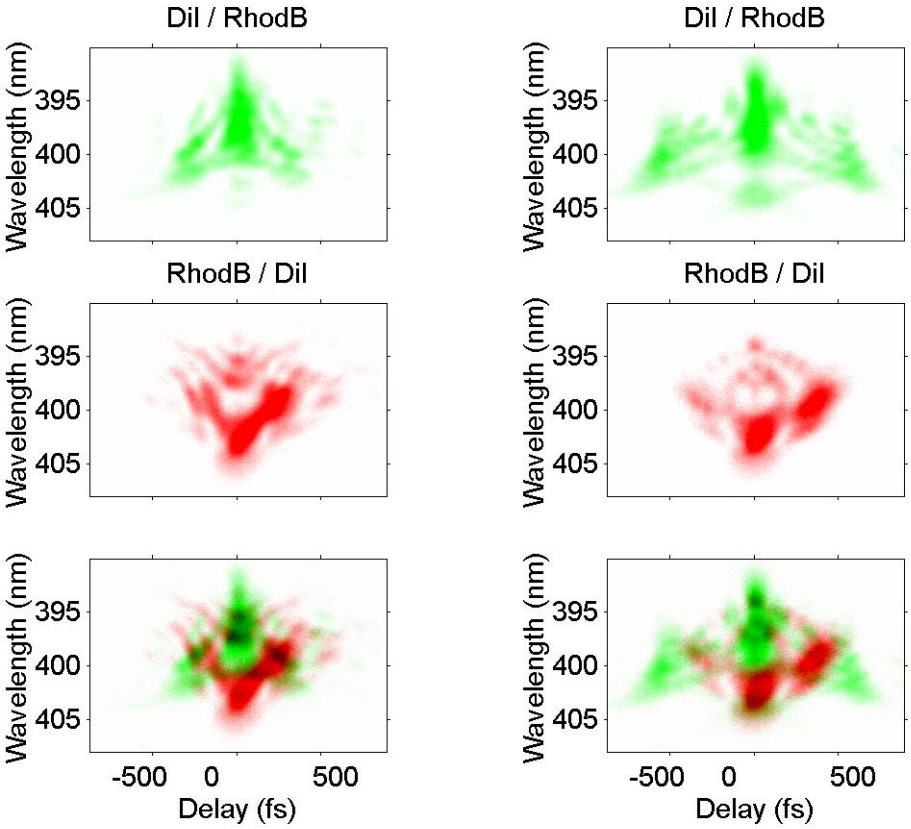

Figure 6.4 SHG-FROG trace of optimal pulse for maximization (top row) and minimization (middle row) of DiI / Rhodamine B fluorescence ratio, with overlay on bottom (maximization in green, minimization in red) for pulses from experiments on two consecutive days (left and right). Abscissa is delay in fs and ordinate is the second-harmonic wavelength.

A common practice in the investigation of tailored pulse shaping is to look at the correlation of the outcome of the experiment with SHG (a surrogate for pulse compression), with the assumption that presence or absence of good correlation is a measure of the complexity of the control problem. For example, a simple problem like multiphoton ionization of a molecule might translate into maximizing the peak pulse energy. As the problem of SHG maximization also maps to the same underlying mechanism, a strong correlation is seen between multiphoton ionization and SHG in an

adaptive search to maximize either [22, 23]. Figure 6.3b shows this analysis for the DiI / Rhodamine B discrimination. No noticeable correlation is evident between the degree of discrimination of the pulse shapes and the SHG efficiency. This demonstrates that the discrimination mechanism does not map directly onto the simple problem of maximizing peak laser intensity. Despite the lack of correlation of the discrimination problem with SHG, second harmonic spectral tuning will be seen to provide an adequate explanation for the control.

3.2 Mechanism of discrimination

SHG-FROG traces for the optimal and anti-optimal pulses to control the DiI to Rhodamine B two-photon fluorescence ratio are shown in Figure 6.4. The complementary nature of pulses converged upon in parallel experiments are consistent with our previous investigations in laser pulse-shaping [24].

More intuition is gained by focusing attention on the 0 delay point of these traces to obtain the second-harmonic spectrum $S_2(\omega)$ of the shaped pulse. The results can be interpreted especially simply by considering the relation to the spectrum of the two-photon excitation cross-section $\sigma^{(2)}(\omega)$. Assuming no intermediate resonant levels between the ground and excited state, the two-photon fluorescent signal will be proportional to the overlap integral of $\sigma^{(2)}(\omega)$ and $S_2(\omega)$ [25]. This can be derived in second-order perturbation analysis of a two-level system [23, 26] or from stationary analysis of two-photon absorption in a three-level model by assuming that the nuclear wave packet motion is frozen in the short time duration of the pulse [27]. Using the overlap integral, Ogilvie and colleagues demonstrated excellent quantitative agreement between the time-domain measurement of $\sigma^{(2)}(\omega)$ for coumarin and the degree of control relative to SHG achieved in a closed-loop search [18].

Figure 6.5 shows the ratio of $\sigma^{(2)}(\omega)$ for DiI / Rhodamine B we measured as described in the Methods overlain with the second harmonic spectrum of the optimal pulses for maximization and minimization of the two-photon fluorescence ratio of the two dyes. Clearly, maximization tunes $S_2(\omega)$ to regions where the DiI / Rhodamine B cross-section ratio is maximal, whereas the minimization algorithm converges in the opposite direction. As the photon-photon interferences for second-harmonic tuning are

best accessed with arbitrary, rather than mere 4th order polynomial phase control, it becomes clear why the GA result improves drastically at the algorithmic switch at generation 30 (Figure 6.3a). Although in that particular experiment, the spectrum of the fundamental laser pulse was also adjusted in the algorithm via the Dazzler amplitude file, this is by no means a prerequisite for tuning of $S_2(\omega)$. Second harmonic tuning can be performed via phase-only control of photon-photon interferences, as commonly achieved with spatial light modulators [28, 29]. When we reduced the search space by excluding amplitude file control, we found that the GA converged on a comparable result (1.860 and 0.721) without whatsoever modifying the fundamental laser pulse spectrum. In our similar experiments to differentiate the two-photon processes of fluorescence and SHG, the direction of tuning of $S_2(\omega)$ is always consistent with the measured cross-section for both maximizing and minimizing pulses.

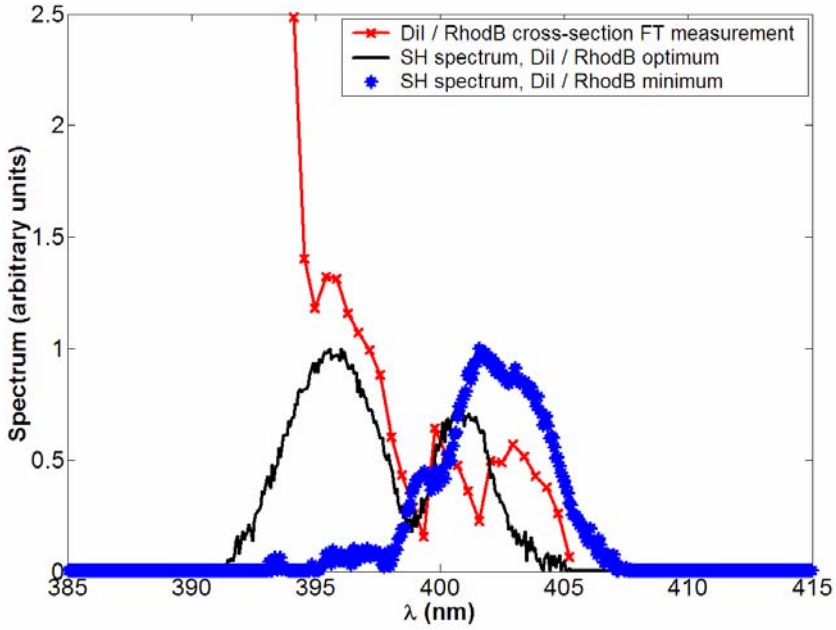

Figure 6.5 Time-domain measured relative two-photon cross-section of DiI versus Rhodamine B (red line with crosses) with second harmonic power spectra $S_2(\omega)$ of the optimal pulses for maximization (black line) and minimization (blue asterixes) of the two-photon fluorescence ratio.

Further evidence for photon-photon interferences and $S_2(\omega)$ tuning as the mechanism of discrimination is provided by the independence of the degree of control from the number of frequency bins used. High frequency information from the shaped pulse is not crucial to control, implying that long time scales are not accessed by the

shaped pulse. The 60 nm bandwidth over 20 bins corresponds to 3 nm or 1.4 PHz resolution at our 800 nm operating wavelength. In other words, only coherences less than a picosecond in duration need to be accessed for the optimal result. The containment of the optimal pulse shape to less than 500 fs of delay is also seen in the SHG-FROG traces of optimal pulses from different days (Figure 6.4). True molecular energy level quantum interferences have been generally accessed in the picosecond or longer realm [19, 22, 30]. We also note the lack of a pulse series visible in the optimal shape (Figure 6.4), which might be expected from previous investigations [6, 24]. Thus, the second harmonic spectra of Figure 6.5 explain the mechanism of discrimination by optimal pulses found by the algorithm, and we conclude that discrimination has been achieved without control of an excited state population by vibrational coherences.

The $\sigma^{(2)}(\omega)$ interpretation also explains why the discrimination result so closely follows the two-photon fluorescent signal of DiI (Figure 6.3a). Published excitation spectra show a sharp spectral feature, almost a cliff, in the two-photon excitation cross-section for DiI near 800 nm [31, 32], which is unmatched by any other dye whose cross-sections we were able to find in the current literature. Thus, tuning $S_2(\omega)$ will affect the DiI two-photon fluorescence far more significantly than that of any other dye. Indeed, in additional experiments we observed significantly improved ability to control the ratio of two-photon fluorescence of DiI to SHG when compared to the same experiment in Rhodamine B. We observed this and the aforementioned results in a similar series of experiments to differentiate DiI from fluorescein isothiocyanate fluorescence.

3.3 Quantitative measurement with pulse shaping

Consider the optimal discriminating pulses 1 and 2 found by the algorithm. Under pulse 1, let S_{1DiI} be the signal from the pure solution of DiI, and let S_{1RhodB} be the signal from the pure solution of Rhodamine B. Similarly, under pulse 2 we have signals S_{2DiI} and S_{2RhodB}. Barring chemical reaction between the dyes, the total signal S_1 under pulse 1 or S_2 under pulse 2 from a mixture of these two solutions is simply the linear superposition of signals from the unmixed solution, weighted by the concentration in the mixture (measured relative to the pure solution):

$$S_1 = S_{1DiI} \times [DiI] + S_{1RhodB} \times [RhodB]$$

$$S_2 = S_{2DiI} \text{ x } [DiI] + S_{2RhodB} \text{ x } [RhodB] \quad (1)$$

This may be rewritten in matrix format:

$$\mathbf{S} = \mathbf{M} \text{ x } \mathbf{C},$$

$$\text{with } \mathbf{S} = \begin{pmatrix} S_1 \\ S_2 \end{pmatrix} \quad \mathbf{M} = \begin{pmatrix} S_{1DiI} & S_{1RhodB} \\ S_{2DiI} & S_{2RhodB} \end{pmatrix} \quad \mathbf{C} = \begin{pmatrix} [DiI] \\ [RhodB] \end{pmatrix} \quad (2)$$

From this we can extract the concentrations of the dyes by simple matrix inversion:

$$\mathbf{C} = \mathbf{M}^{-1} \text{ x } \mathbf{S} \quad (3)$$

Thus it is possible to use tailored pulses to perform quantitative measurements by first measuring reference solutions. Note that this analysis can be extended to an arbitrary number of dyes and pulse shapes by using the pseudoinverse rather than the inverse of **M**. Measurement errors in **S** will be multiplied by the condition number of the matrix **M** for a larger error in the concentrations **C**.

We performed precisely this experiment using our 20 μM DiI and 1 μM Rhodamine B as our reference solutions. We then repeated eight measurements of a mixture of 75% of the DiI solution and 25% of the Rhodamine B solution with each pulse from Figure 6.6. This indicated a fractional mixture of 0.6438 of DiI and 0.2697 of Rhodamine B, with standard deviations of 0.5383 and 0.0809, respectively. The relatively large standard deviation of the recovered concentrations results from the error amplification by the condition number of **M**.

4. Conclusions

With tailored pulse shapes found by a genetic algorithm, we have demonstrated the ability to control the two-photon fluorescence ratio to nearly a factor of three of Rhodamine B and DiI, a dye pair which is practically indistinguishable to traditional one-photon excitation and emission spectroscopy. Modulation of the pulse on time scales less than a picosecond is sufficient for this high degree of control. The degree of discrimination closely parallels control of the fluorescent signal from DiI, which is known to have a sharp feature in the two-photon absorption spectrum near our 800 nm excitation wavelength. While the result does not map in correlation analysis to the simple problem of SHG optimization, the second harmonic spectrum of the optimal pulse through repetitions of the experiment with a full or reduced search-space is consistently tuned to the appropriate location in the relative two-photon excitation cross section of the dyes. We are thus lead to the conclusion that photon-photon interferences are the predominant mechanism of control, and it seems unlikely that the GA has been able to manipulate the excited state population with additional photons after initial excitation. Evolution of wavepackets on molecular energy levels at least in this investigation does not seem to play a fundamental role in selective two-photon fluorescence excitation.

The high degree of fluorophore discrimination achieved by second harmonic tuning without a drop in fluorescent signal of the favored fluorophore demonstrates the practical value of tailored pulse shaping. The ability to accurately quantify spectrally overlapping dyes in a mixture is but one application. Multiphoton microscopy and spectroscopy will also continue to see advances based on the specificity and reduced photobleaching concomitant with the reduced peak power [33] of tailored pulse shaping. The implementation here in an acousto-optic modulator further has the advantage of rapid switching capabilities between pulse forms, which will enable higher throughput than that achievable via slower liquid-crystal based pulse shapers [9] and far greater than could be achieved with straightforward tuning of a narrowband laser pulse. In the future, we look forward to many applications of truly quantitative techniques of discrimination based on tailored pulse shaping.

References

1. K. König, "Multiphoton microscopy in life sciences," J Microsc **200**, 83-104 (2000).
2. W. R. Zipfel, R. M. Williams, and W. W. Webb, "Nonlinear magic: multiphoton microscopy in the biosciences," Nat Biotechnol **21**, 1369-1377 (2003).
3. J. M. Squirrell, D. L. Wokosin, J. G. White, and B. D. Bavister, "Long-term two-photon fluorescence imaging of mammalian embryos without compromising viability," Nat Biotechnol **17**, 763-767 (1999).
4. E. Tkaczyk, C. Zhong, J. Ye, A. Myc, T. Thomas, Z. Cao, R. Duran-Struuck, K. Luker, G. Luker, T. Norris, and Baker, "In vivo monitoring of multiple circulating cell populations using two-photon flow cytometry," Optics Communications **281**, 888-894 (2008).
5. Zhong CF, Tkaczyk ER, Thomas T, Ye JY, Myc A, Bielinska A, Cao Z, Majoros I, Balazs K, Baker JR, Norris TB. Quantitative Two-Photon Flow Cytometry – in Vitro and in Vivo. Journal of Biomedical Optics 2008;13(3).
6. N. Dudovich, D. Oron, and Y. Silberberg, "Single-pulse coherently controlled nonlinear Raman spectroscopy and microscopy," Nature **418**, 512-514 (2002).
7. T. Brixner, N. H. Damrauer, P. Niklaus, and G. Gerber, "Photoselective adaptive femtosecond quantum control in the liquid phase," Nature **414**, 57-60 (2001).
8. V. Lozovoy, I. Pastirk, K. Walowicz, and M. Dantus, "Multiphoton intrapulse interference. II. Control of two- and three-photon laser induced fluorescence with shaped pulses," The Journal of Chemical Physics **118**, 3187-3196 (2003).
9. J. P. Ogilvie, D. D, X. Solinas, J. L. Martin, E. Beaurepaire, and M. Joffre, "Use of coherent control for selective two-photon fluorescence microscopy in live organisms," Optics Express **14**, 759-766 (2006).
10. B. Li, G. Turinici, V. Ramakrishna, and H. Rabitz, "Optimal Dynamic Discrimination of Similar Molecules through Quantum Learning Control," J. Phys. Chem. B **106**, 8125-8131 (2002).
11. F. c. Courvoisier, V. e. Boutou, V. Wood, A. Bartelt, M. Roth, H. Rabitz, and J. Wolf, "Femtosecond laser pulses distinguish bacteria from background urban aerosols," Applied Physics Letters **87** (2005).
12. Invitrogen. http://probes.invitrogen.com/servlets/spectra. Invitrogen Website; 2008.
13. F. Verluise, V. Laude, J. P. Huignard, P. Tournois, and A. Migus, "Arbitrary dispersion control of ultrashort optical pulses with acoustic waves," Journal of the Optical Society of America B Optical Physics **17**, 138-145 (2000).
14. D. Kaplan, and P. Tournois, "Theory and performance of the acousto optic programmable dispersive filter used for femtosecond laser pulse shaping," Journal de Physique IV **12**, 69-75 (2002).

15. B. J. Pearson, J. L. White, T. C. Weinacht, and P. H. Bucksbaum, "Coherent control using adaptive learning algorithms," Physical Review A **63**, 063412 (2001).

16. Laarmann et. al., *J Chem Phys* **127**, 2011101 (2007)

17. R. Trebino, K. Delong, D. Fittinghoff, J. Sweetser, M. Krumbugel, B. Richman, and D. Kane, "Measuring ultrashort laser pulses in the time-frequency domain using frequency-resolved optical gating," Review of Scientific Instruments **68**, 3277-3295 (1997).

18. J. Ogilvie, K. Kubarych, A. Alexandrou, and M. Joffre, "Fourier transform measurement of two-photon excitation spectra: applications to microscopy and optimal control," Opt. Lett. **30**, 911-913 (2005).

19. M. Bellini, A. Bartoli, and T. W. Hänsch, "Two-photon Fourier spectroscopy with femtosecond light pulses," Opt. Lett. **22**, 540-542 (1997).

20. K. Naganuma, K. Mogi, and H. Yamada, "General method for ultrashort light pulse chirp measurement," Quantum Electronics, IEEE Journal of **25**, 1225-1233 (1989).

21. R. Trebino, *Frequency-Resolved Optical Gating: The Measurement of Ultrashort Laser Pulses* (2002).

22. T. Brixner, B. Kiefer, and G. Gerber, "Problem complexity in femtosecond quantum control," Chemical Physics **267**, 241-246 (2001).

23. T. Brixner, N. H. Damrauer, B. Kiefer, and G. Gerber, "Liquid-phase adaptive femtosecond quantum control: Removing intrinsic intensity dependencies," The Journal of Chemical Physics **118**, 3692-3701 (2003).

24. E. R. Tkaczyk, A. Mignot, J. Y. Ye, I. Majoros, J. R. Baker, and T. B. Norris, "Increasing two-photon fluorescence signals by coherent control," in *Multiphoton Microscopy in the Biomedical Sciences VI. Edited by Periasamy, Ammasi; So, Peter T. C. Proceedings of the SPIE, Volume 6089, pp. 165-174 (2006).* A. Periasamy, and P. T. C. So, eds. (2006), pp. 165-174.

25. K. A. Walowicz, I. Pastirk, V. V. Lozovoy, and M. Dantus, "Multiphoton Intrapulse Interference. 1. Control of Multiphoton Processes in Condensed Phases," J. Phys. Chem. A **106**, 9369-9373 (2002).

26. D. Meshulach, and Y. Silberberg, "Coherent quantum control of multiphoton transitions by shaped ultrashort optical pulses," Phys. Rev. A **60**, 1287-1292 (1999).

27. J. Cao, J. Che, and K. R. Wilson, "Intrapulse Dynamical Effects in Multiphoton Processes: Theoretical Analysis," J. Phys. Chem. A **102**, 4284-4290 (1998).

28. V. Lozovoy, and M. Dantus, "Systematic Control of Nonlinear Optical Processes Using Optimally Shaped Femtosecond Pulses," ChemPhysChem **6**, 1970-2000 (2005).

29. A. M. Weiner, "Femtosecond pulse shaping using spatial light modulators," Review of Scientific Instruments **71**, 1929-1960 (2000).

30. V. r. Blanchet, C. l. Nicole, M.-A. Bouchene, and B. Girard, "Temporal Coherent Control in Two-Photon Transitions: From Optical Interferences to Quantum Interferences," Physical Review Letters **78**, 2716 (1997).

31. C. Xu, and W. W. Webb, "Measurement of two-photon excitation cross sections of molecular fluorophores with data from 690 to 1050 nm," Journal of the Optical Society of America B Optical Physics **13**, 481-491 (1996).

32. C. Xu, W. Zipfel, J. Shear, R. Williams, and W. Webb, "Multiphoton fluorescence excitation: New spectral windows for biological nonlinearÂ microscopy," PNAS **93**, 10763-10768 (1996).

33. H. Kawano, Y. Nabekawa, A. Suda, Y. Oishi, H. Mizuno, A. Miyawaki, and K. Midorikawa, "Attenuation of photobleaching in two-photon excitation fluorescence from green fluorescent protein with shaped excitation pulses," Biochemical and Biophysical Research Communications **311**, 592-596 (2003).

CHAPTER 7
CONTROL OF BFP: IMPORTANCE OF ALGORITHMIC AND EXPERIMENTAL ASPECTS FOR COMPLEX EVOLUTIONARY PULSE SHAPING PROBLEMS

Abstract. We demonstrate control of the two-photon fluorescence of the blue fluorescent protein (BFP), which is of particular interest in investigations of protein-protein interactions. In addition to biological relevance, BFP represents an interesting target for coherent control from a physicist's perspective due to its many components of highly nonexponential fluorescence decay and low quantum yield resulting from excited state isomerization. Using a genetic algorithm (GA) with a multiplicative (rather than ratiometric) fitness parameter, we are able to control the ratio of BFP fluorescence to second harmonic generation without a considerable drop in the maximized signal. The importance of linear chirp and power scaling on the discrimination process is investigated in detail.

1. Introduction

Amongst the large variety of visually fluorescent proteins, blue fluorescent protein (BFP) stands out as the one with the shortest-wavelength absorption and fluorescence emission, with maxima at 383 nm and 447 nm, respectively[1]. This has enabled the use of BFP to study protein interactions as a fluorescence resonance energy transfer (FRET) donor for the green fluorescent protein (GFP). In this manner, biologists have gained deep insight into fundamental processes including protease cleavage, calcium signaling, phosphorylation, and programmed cell death[2,3]. Unfortunately, in live cells the excitation of a fluorophore with UV light entails stronger interfering autofluorescence as well as higher toxicity than visible light. BFP also has the lowest fluorescence quantum yield (20%) as well as the strongest photobleaching of all GFP variants. Thus, most investigators now favor the red-shifted pair of cyan fluorescent protein (CFP) and yellow fluorescent protein (YFP), which suffers lower sensitivity to FRET changes due to CFP's extended tail on the emission spectrum. In the words of Pollok and colleagues[4]:

> "To date, two GFP pairs have been used in FRET-based biological systems. BFP is often employed as the donor, and eGFP as the acceptor. Although this GFP pair has experienced the broadest use (due in part to their availability from commercial suppliers), BFP is only weakly fluorescent. This is a serious limitation for its use in applications outside of those employing microscopy or flow cytometry for fluorescence detection. An alternative GFP–FRET pair that has been used successfully in a variety of situations is the CFP–YFP combination[1]. CFP is significantly brighter than BFP, permitting accurate ratiometric measurement of both donor and acceptor GFPs by a variety of fluorescence detectors, including plate-type readers. However, a limitation of the CFP–YFP FRET system is the extenuated tail for the right end of the CFP emission spectrum (Figure 7.1). Bleeding of the CFP emission into the emission spectrum of YFP compromises the independent measurement of fluorescence derived from the donor and acceptor GFPs, thus decreasing the efficiency of detecting FRET changes. Judicious choice of filter sets for fluorescence detection helps to minimize this problem."

The first difficulty of BFP, UV excitation, is instantly solved by moving to two-photon excitation[5]. However, the photobleaching and low quantum yield will continue to frustrate applications without an innovative new approach to BFP fluorescence. It has already been shown that shaping of two-photon excitation pulses is able to reduce the photobleaching rate of various GFP variants[6]. If it would be possible to control the fluorescence of BFP in this manner without a reduction of its already weak signal, this could restore the role of BFP in the field of cell biology.

The blue shift of BFP has been achieved by mutation of the chromophore of GFP, where the phenolic ring has been replaced by a histidine. Experiments[7-9] and calculations[10-13] have shown that the efficient quenching of the excited state of BFP stems from the excitation-induced isomerization of the chromophore. The highly nonexponential fluorescence decay has components from some picoseconds up to several nanoseconds, indicating the presence of different chromophore conformations. The equilibrium between the fast-decaying nonfluorescent conformations can be shifted in favor of the fluorescent ones by applying high hydrostatic pressure or by lowering temperature[7].

The nonradiative isomerization makes BFP an interesting target for coherent control. Ideally, control of the evolution of the excited state wavepacket could steer the BFP chromophore away from undesirable isomerization pathways in favor of fluorescence. It is known from quantum chemical calculations[14] that after excitation, the chromophore finds itself in a highly unstable Franck-Condon point on the potential energy surface, where the torque by the nonequilibrium electronic cloud tends to twist the chromophore away from its flat conformation. As a result of this twist, the energy surfaces of the excited and ground states come close to each other, and the fluorescence is quenched. If the electric field of the appropriately tailored femtosecond excitation pulse could drive the electrons in opposite phase to this twisting motion and could efficiently counteract the isomerization, the fluorescence yield could be substantially enhanced.

Though genetic learning algorithms are commonly used in coherent control problems to explore a vast phase space, there is still concern as to the susceptibility of the search to convergence on local minima in the face of noise. In theory, under reasonable assumptions for any controllable quantum system with no constraints placed on the controls, the only allowed extrema of the transition probability landscape correspond to perfect or no control[15]. No suboptimal local extrema exist. In the laboratory, however, lack of total controllability, field fluctuations, noise in observations, the statistical state of initial distribution, decoherence, and constraints on control can limit the validity of this theory. In particular, weak noise acts like a filter providing a lower resolution view of the ideal quantum control landscape, reducing the value of non-robust solutions. Further, various systematic errors can exist in the experiment which might bias convergence to a

pulse irrelevant for the desired target. These could include phase-matching in multiphoton processes, saturation of molecular transitions, dispersion differences in different paths, or even simple detector variations or saturation. Thus experimental and algorithmic aspects of searches for optimal coherent control pulses can strongly affect the solutions found, as illustrated here.

In the present study, we first made an attempt to enhance the fluorescence quantum yield of BFP by shaped femtosecond excitation pulses. At low pulse energies avoiding photobleaching and saturation of fluorescence, this fitness parameter in the adaptive learning algorithm converges to transform-limited pulses, consistent with results of dyes investigated previously[16]. Thus, we follow the tradition of employing an additional two-photon process, second harmonic generation (SHG), in the fitness parameter[17]. This control problem proves to be quite a difficult one, and a ratiometric fitness two-photon fluorescence / SHG has already been shown to be incapable of discriminating the two second-order processes in BFP[6]. However, employing a multiplicative fitness parameter and controlling for factors like power-scaling differences, dispersion mismatches in different arms of the experiment, and photobleaching, we are able to differentiate the two processes to nearly a factor of three. Though we are able to effectively control the fluorescence of BFP in our investigation, we find that the substantial contribution to the control is by tuning of the second harmonic spectrum of the laser to the maximum or minimum of the two-photon excitation cross-section of BFP, rather than manipulation of the excited state wavepacket and the ensuing isomerization.

2. Experimental Setup

2.1 Samples

BFP was purchased from QBiogene ("superglo" sgBFP, Montreal, Canada), thawed, and immediately used in its original concentration of 0.5 μg/μL in TE buffer, pH 8.0. The total sample volume used was 75 μL. A spectrophotometer measurement after all experiments agreed with the published one-photon absorption spectrum[18].

2.2 Optical layout

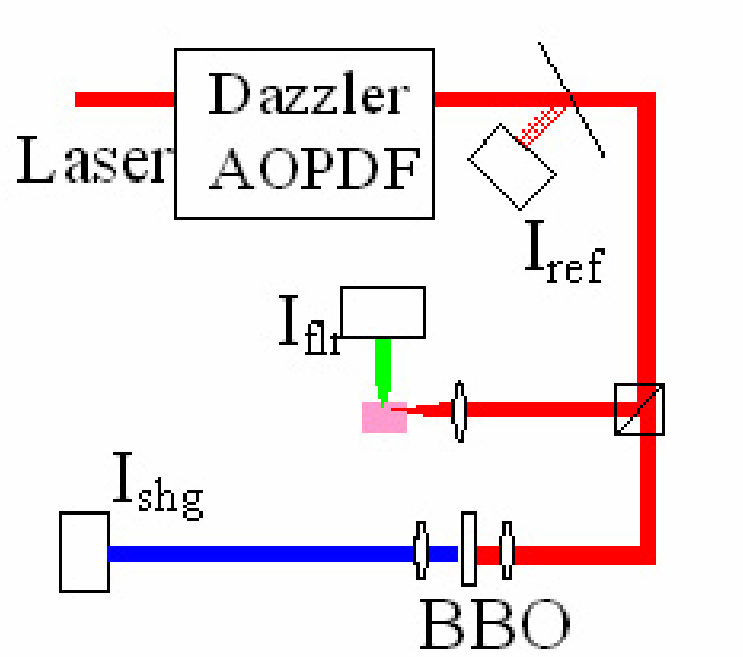

Figure 7.1 Experimental Setup. The dye sample is contained in a plastic fluorescence cuvette (Cole Palmer). Incident laser power Iref is measured by a photodiode (R2066, Hamamatsu). After filters to remove scatted pump light at 800 nm, the two-photon fluorescence signal Iflr is measured in the perpendicular direction by a PMT (H5784-01, Hamamatsu). The second-harmonic signal ISHG from the BBO crystal is detected by another PMT (R2066, Hamamatsu). Lenses are depicted as ovals.

The experimental setup is shown in Figure 7.1. The laser system consists of a regeneratively amplified Ti:sapphire system (RegA, Coherent, Santa Clara, CA) providing up to 4 μJ, 50 fs pulses at 250 kHz with a center wavelength of 800 nm and 27 nm FWHM bandwidth. The "Dazzler," an acousto-optic programmable dispersive filter (AOPDF) (Fastlite, Palaiseau, France), is used to shape the laser pulses. The Dazzler

modulates the diffracted output pulse by way of an acousto-optic interaction with an RF wave launched into a TeO_2 crystal[19,20]. Diffracted power and polynomial phase to fourth order are the most basic control parameters. Additionally, arbitrary amplitude and phase modulation can be accomplished by binning the pulse spectrum into numerous (typically 20 to 100) frequency bins and giving each bin an arbitrary amplitude and phase. The Dazzler is triggered by every twelfth RegA pulse for an ~20 kHz repetition rate. SHG-FROG measurements confirm that the approximately 6 shaped pulses falling within the 50% duty cycle of the Dazzler give precisely the same average two-photon time-frequency characteristics as are obtained when the RegA is operated at 20 kHz. Thus, the shaping of all 6 diffracted pulses per launched RF waveform has the same effect in our experiment as if each were synchronized to the center of separate identical acoustic waves in the TeO_2 crystal.

A reference value for incident power I_{ref} was measured by reflecting laser beam from a glass coverslip onto a photodiode (FFD-100, Perkin-Elmer Optoelectronics, Fremont, CA. We define the efficiency of each two-photon process signal S as the ratio S/I_{ref}. The beam is then divided into two arms with a beamsplitter, and the relative power in each arm is controlled with a variable reflective attenuator. The first arm is focused by a 2.4 f# achromatic doublet lens into the cuvette holding the dye sample, and the fluorescence signal I_{flr} is collected in the perpendicular direction through an appropriate bandpass filter for detection by a photomultiplier tube (PMT) with internal conversion to a voltage source (H5784-01, Hamamatsu, Bridgewater, NJ). In the other arm, a 500 micron beta barium borate (BBO, β-BaB2O4) crystal is placed at the center of a telescope consisting of two 2.4 f# achromatic doublet lenses for SHG, read through a blue absorptive filter by another PMT (R2066, Hamamatsu, Bridgewater, NJ) to give the signal I_{SHG}. All three signals I_{ref}, I_{flr}, and I_{SHG} are read in parallel as root-mean-square voltage for 2500 samples by a 250 kHz DAQ board (M-series, National Instruments, Austin, TX), which is synchronized by the Dazzler trigger.

After measuring fitness with a specific individually shaped pulse, the adaptive learning algorithm programs the next individual, closing the loop for the iterative improvement. Though each measurement of a specific pulse shape lasts only 50 ms, about 500 ms are typically required for the electronics to implement the acoustic wave of

a novel pulse shape in the TeO_2 crystal at the heart of the Dazzler. Once parameters for generation of the pulse shapes have been saved in the computer, switching between them is possible in sub-millisecond time.

2.3 Pulse characterization

We characterized pulses in the time-frequency domain with a commercial SHG-FROG unit[21] (Grenouille 8-50 from SwampOptics, Atlanta, GA) and software (VideoFrog, MesaPhotonics, Santa Fe, NM). SHG-FROG measurement was typically performed within 24 hours of termination of the experiment to ensure maximum fidelity of the reproduced pulse to that actually measured in the course of the experiment. As the Grenouille has a total 50 nm bandwidth range, the 27 nm FWHM bandwidth RegA pulses are slightly beyond the limit of accurate phase recovery from the raw data by the FROG algorithm. However, we independently confirmed for most experiments with a spectrometer (S1024DW, Ocean Optics, Dunedin, FL) that the t=0 cross-section from the raw Grenouille image corresponds well to the shaped pulse second harmonic spectrum measured off of the BBO crystal in our experimental setup. This also served as independent verification that despite the thickness of the crystal, phase-matching does not significantly limit the spectral bandwidth of second-harmonic generation[22].

2.4 Time-domain two-photon excitation cross-section measurement

In order to interpret the coherent control results, we implemented a time-domain measurement of the two-photon excitation cross-section spectrum of BFP in the region of interest using the same experimental setup. This was performed analogously to the description by Ogilvie and colleagues[23]. However, rather than physically delaying a beam-split replica of the pulse, a virtual Michelson interferometer was programmed into the Dazzler. Where ω is the center frequency of the laser, a delay of t0 between pulses is achieved with simple multiplication by a cosine amplitude mask $\cos(\omega t0/2)$ in the frequency domain, for 150 intervals in an 80 nm bandwidth, corresponding in the conjugate Fourier domain to a time delay of t0. Note that we only use binary coding of the phase file to be at 0 or pi corresponding to the sign of the cos function, as absolute and linear phase (absolute time delay) are physically irrelevant when the information is actually contained in the interarrival period of the two pulses[24]. When the data is Fourier

transformed, the two-photon excitation cross-section is extracted with relatively good accuracy in the frequency domain as the divisor of the fluorescent signal by the second-harmonic signal in the region of the 2ω0 component. For detailed mathematical proof of this, the reader is referred to the article by Naganuma *et al*.[25] or Trebino's discussion[26].

2.5 Experimental considerations for adaptive learning convergence

Power scaling

Before each experiment, the optical system and laser power were adjusted to ensure quadratic scaling of discriminated two-photon processes with I_{ref}. Scattered excitation light reaching the fluorescence-detecting PMT, for example would result in subquadratic scaling. As another example, if I_{flr} is approaching saturation while I_{SHG} is still in the quadratic region, then this can trivialize the convergence to mere pulse stretching. For other dyes, we have also noted photobleaching for repeated measurements anywhere near the saturation region. Thus, the power scaling check in each experiment is extremely important to assure proper experimental conditions. Typical diffracted pulse energies after the Dazzler used during experiments were estimated to be 2 nJ. Assuming a diffraction-limited beam waist, we estimate a typical fluence on the sample at the laser focus on the order of 0.5 mJ/cm^2 (peak intensity on the order of a GW/cm^2 transform-limited).

Chirp scaling

Even if the incident laser power is unvarying in the course of the adaptive learning algorithm, true control possibilities could still be masked by uninteresting convergences with simple linear chirp (second order polynomial phase) adjustments. For example under increasing chirp, two-photon fluorescence in the saturation region would not decrease, while the unsaturated SHG signal would decrease with the increased pulse duration[27]. In fact, if the two-photon fluorescence emission has a short enough lifetime to be saturated by peak laser intensity rather than the pulse fluence, the two-photon signal could actually increase with the increased group delay dispersion. Another case in which linear chirp could mask control is when the dispersion in the different materials in the

two optical paths is not exactly matched. In this case the optimal pulse shape would be found simply by tuning to compensate dispersion differences.

2.6 Algorithmic considerations for adaptive learning convergence

A genetic learning algorithm (GA) is used to find the optimal pulse shape. The adjustable parameters which determine the pulse shape are amplitude and phase settings for the Dazzler. These are used as genes to define a specific individual laser pulse. The algorithm usually is set to place physical constraints on the allowable phases, i.e. the derivative of phase with respect to frequency is limited so the length of the acoustic wave is shorter than the crystal length. At the beginning, the algorithm generates a random population of 50 individuals. This population is ranked via a fitness parameter, and the best 10 individuals are passed unmodified to the next generation. Remaining individuals of the new generation are created by mating and mutation of fitness-preferenced individuals of the preceding generation. Our implementation relies on two-point crossover and mutation operators similar to those already described by Pearson *et al*.[28]. We additionally scale the mutation rate by the homogeneity of the preceding generation to help avoid local minima and use a circular chromosome to avoid edge effects.

To use pulse shaping to discriminate different two-photon processes, many investigators use as a fitness parameter the ratio of two second-order processes A/B, for example with A as two-photon fluorescence and B as SHG[6,17]. As the two-photon signals can drop significantly for example with changing pulse width, as affected by chirp[29-31], this approach can easily lead to low signal levels with degree of discrimination dictated primarily by the arbitrarily set acceptable low-signal limit[16]. In order to avoid suboptimal solutions, it is important to pick a fitness parameter which is not biased towards the low-signal regime by noise-dominated measurements. Thus in the current investigation, to maximize a ratio A/B, we rather employ the fitness parameter $(A-c)(c^{-1}-B)$, where values of A and B are normalized to the unshaped pulse measurement. We have found that setting c to 0.8 yields better convergence relative to the original implementation of unity for c[32]. If both multiplicands are negative, an infinite negative fitness is given to the pulse. If either multiplicand alone falls below 0, the inverse of the other is taken. This will ensure for example that if B exceeds c^{-1} by a fixed amount, decreases in the maximized signal A towards c result in a decreased (more negative) fitness. As a

negative fitness will result whenever the maximized signal A falls below c, the search is strongly biased to enable the maximized signal to surpass that of an unshaped pulse, which is beneficial for practical applications.

As a check of stability of the laser and experimental conditions, for each population at every generation, two additional unvarying individuals, the "noise_individual" and the "test_individual," were tested. The noise_individual encodes for a zero power pulse from the Dazzler, thus providing a background offset to subtract from the measurements. The test_individual's chromosome encodes for a pulse roughly self-compensating the Dazzler's dispersion. As the TeO_2 crystal of the Dazzler is the major dispersive element in the optical system before the sample, the test_individual thus provides an approximation of the transform-limited pulse. We also refer to the "test_individual" in this letter as the "unshaped" pulse. All measurements of I_{flr} or I_{SHG} in this paper (unless explicitly in units of Vrms) are normalized to the unshaped pulse of the corresponding generation.

For maximum concurrence of experimental conditions, as many as four different populations were interleaved into the experimental sequence and tracked with different fitness parameters independently to allow parallel processing of multiple experiments.

3. Results and Discussion

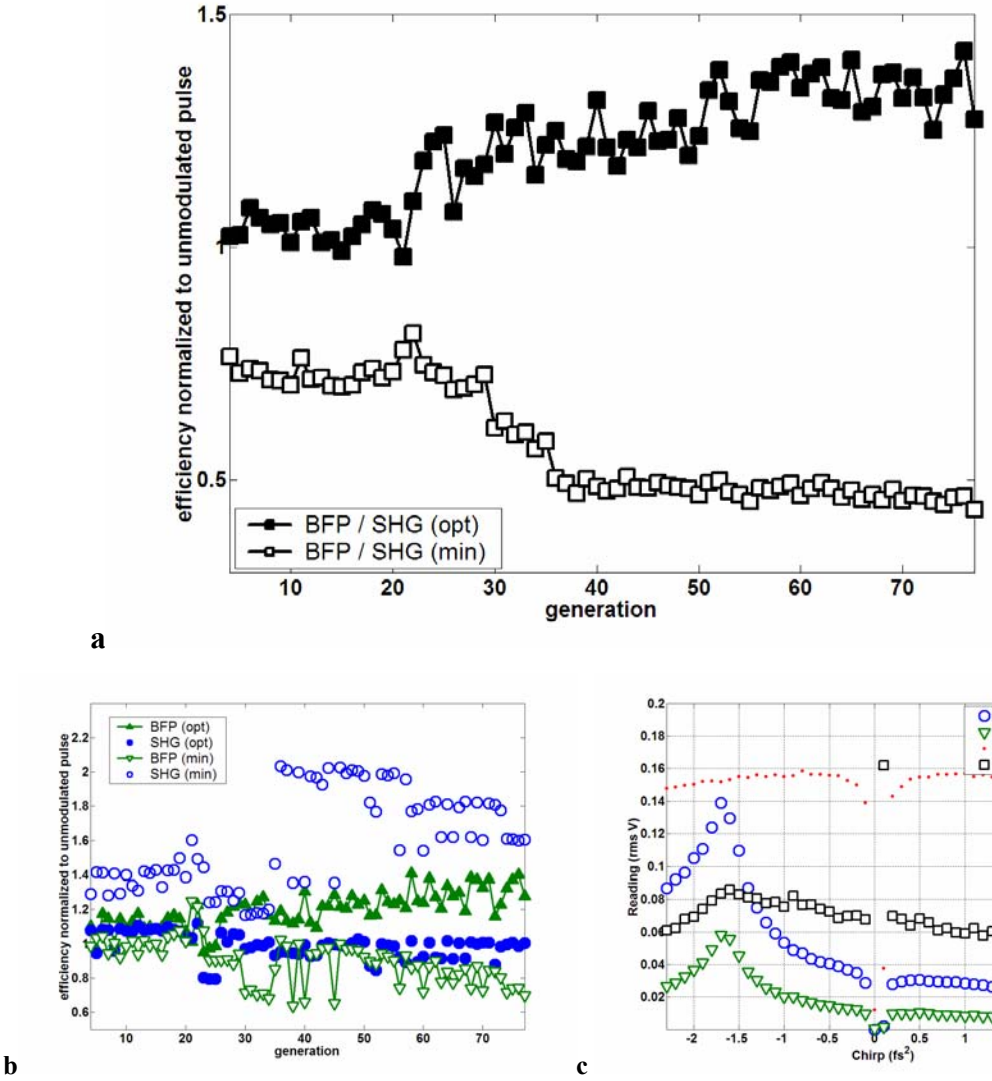

Figure 7.2 (a) Control of ratio of BFP fluorescence efficiency to SHG efficiency. Only polynomial phase was adjusted until generation 20. After this, arbitrary phase (and no amplitude) adjustments were permitted to the adaptive learning algorithm, with 20 frequency bins over 60 nm of bandwidth. The phase manipulation was constrained for delays in the TeO2 crystal between 1000 and 3000 fs. Measurements for each generation's best individuals in the maximization are shown with filled markers, whereas the parallel minimization experiment is shown with open markers. All measurements are normalized to the unshaped pulse. Black squares show the ratio Iflr / ISHG. (b) For the same experiment, green triangles show the BFP fluorescence efficiency Iflr / Iref whereas blue circles mark the SHG efficiency ISHG / Iref. (c) Linear chirp dependence of two-photon signals in the same experiment. Blue circles show ISHG (typically 0.05 Vrms in the experiment), green triangles show the Texas Red fluorescent signal Iref (typically 0.26 Vrms), red dots show Iref (typically 0.15 Vrms), and black squares show the dependence of the ratio Iflr/ISHG ratio on the

chirp. Note the drop in diffraction efficiency of the Dazzler when little second-order polynomial phase is applied (0 chirp).

3.1 Control of BFP

Taking into account all of the aforementioned considerations, we attack the problem of maximizing two-photon fluorescence of BFP relative to SHG. Figure 7.2 shows the convergence of the GA for the parallel maximization and minimization experiments. The highest achieved ratio of the two-photon processes (normalized to the unshaped pulse) is 1.42 whereas the minimum in the parallel experiment is 0.44. Most of the improvement in discrimination occurs only after generation 20, when phase beyond the 4th order polynomial is allowed to be modified. Figure 7.2c confirms consistency of the I_{flr}/I_{SHG} ratio with linear chirp adjustment. Excluding the points adjacent to 0 chirp (with almost no diffracted power), the ratio can be controlled at most by a factor of 1.45 over the full range of this one-parameter scan. Arbitrary phase shaping by the genetic algorithm, however, was able to control the ratio of two-photon fluorescence from BFP to SHG to a factor of 3.27 (maximum to minimum).

We also wanted to understand how applicable and reproducible our method of excitation might be after several experiments on the same BFP sample at room temperature. Thus we repeated the initial experiment and variations thereof for almost continuous excitation over the course of more than 24 hours. A comparable degree of control (maxima and minimum I_{flr}/I_{SHG} 1.38 and 0.49 for a total control factor of 2.83) was still achieved in the repetition of the original experiment two days later, despite realignment of the system causing slight differences in the power-law and chirp-dependences (maxima and minima 1.383 and 0.489 for a total control factor of 2.83). Thus we conclude that our control attempts are very reproducible, both from the standpoint of the pulse search convergence, but also from the standpoint of possible physical changes in BFP during extended investigations.

We tried many variations of the GA to see how details of our implementation influence the result. The most complicated aspect of the GA programming is the constraint on the control parameters of the Dazzler.which ensure that the acoustic wave wavelength does not exceed the crystal dimensions. An immediate repetition of the initial experiment in the same alignment condition without imposing physical constraints

on the phase weakened the result noticeably (maximum and minimum I_{flr}/I_{SHG} 1.31 and 0.54 for a control factor of 2.43). Immediate repetition with the original (physically constrained) algorithm and with the added ability for amplitude modulation had a somewhat smaller but also appreciable negative effect on the final result (ratios 1.42 and 0.57 for a control factor of 2.52). We note that adding amplitude modulation doubles the search space of the GA. The most deleterious effect to control was seen by maintaining the optimal experimental conditions of Figure 7.2, but quintupling the GA search space by increasing only the number of frequency bins of phase control from 20 to 100 over the 60 nm programmed bandwidth. This brought the control factor down to 2.166. Thus we conclude that while tying into physical reality in the search is important, the most important factor in our success was keeping the lowest possible search space for the algorithm.

These observations are consistent with our investigations in other systems and emphasize the difficulty of the control problem in BFP. The control landscape in the presence of noise of BFP discrimination from SHG is evidently dominated by suboptimal solutions, and all the described modifications to the search algorithm spread the parameter space to include more regions of inferior control. Pulse shapes not physically confined within the crystal have little probability of successful control. Phase adjustments are known to offer better control of the second harmonic spectrum of the laser pulse than amplitude modulation[33], so the decreased control with the addition of the latter is understandable. Finally, high frequency resolution in the two-photon fluorescence problem at hand does not offer a benefit sufficient to outweigh the disadvantages of the expanded phase space, as it does for example, in the problem of selective bond breaking[34].

As further evidence of the low density of optimal solutions to the BFP control problem, Figure 7.3a shows the results of the GA search experiment with algorithm almost identical to that for Figure 7.2. Slightly more scattered excitation light from the cuvette results in a drop in the power scaling factor of the BFP signal I_{flr} relative to I_{ref} from 1.63 to 1.51. As a result, the control is eliminated. The best control factor of 1.57 (1.14 and 0.73 maximizing and minimizing pulse I_{flr}/I_{SHG} ratios, respectively) at the end of the run are almost the same as that seen in the first generation. In the failed

experimental alignment, linear chirp adjustment made the optimal minimizing pulse's I_{flr}/I_{SHG} ratio identical to that of the maximizing pulse. For control problems with a robust solution, the increased scattering does not, however, hurt convergence. Immediately following the failed experiment, the SHG arm was routed via a flip mirror to focus tightly in a cuvette of DiI, with a power-law scaling of two-photon fluorescence to I_{ref} at 1.81, not far from the 1.83 power law scaling in our SHG detector. As shown in Figure 7.3b, maximization of the ratio of two-photon fluorescences of BFP to DiI yielded a factor of three-fold discrimination for this robust discrimination problem (1.21 vs 0.41). As seen in the first 30 generations of the experiment, this problem does not map to polynomial phase modulation.

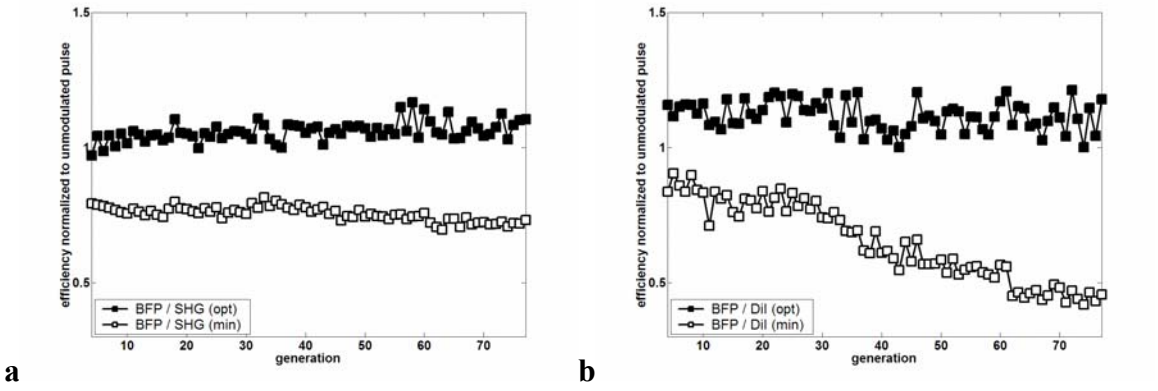

Figure 7.3 (a) Failed control of ratio of BFP fluorescence efficiency to SHG efficiency. The ratio of BFP fluorescence efficiency / SHG efficiency is plotted, normalized to the unshaped pulse. Measurements for each generation's best individuals in the maximization are shown with filled markers, whereas the parallel minimization experiment is shown with open markers. Only polynomial phase was adjusted until generation 30. After this, arbitrary phase and amplitude file adjustments were permitted to the adaptive learning algorithm, with 20 frequency bins over the 60 nm of bandwidth. The phase manipulation was constrained for delays in the TeO_2 crystal between 1000 and 3000 fs. (b) Same experimental conditions, with I_{SHG} replaced by two-photon fluorescent signal from DiI.

It is notable that in all cases the multiplicative fitness parameter ensures that the signal of the favored two-photon process is comparable to, or significantly higher than that with the unshaped pulse. For example, in Figure 7.3b, for the maximization of BFP / SHG signal, the value of BFP two-photon fluorescence efficiency I_{flr}/I_{ref} normalized to the unshaped pulse converges on values above one (closed green triangles). In the parallel minimization experiment, however, I_{SHG}/I_{ref} exceeds one when thus normalized (open blue circles). This is important for practical applications where signal-to-noise

ratio (SNR) is a typical limiting factor. The large generational variations in the signal level of the best pulse (Figure 7.3b) concurrently with a consistent trend in the ratio of the discriminated processes (Figure 7.3a) emphasize the independence of the GA search result from signal strength. We were unable to elicit control of BFP with identical experimental conditions when we substituted the ratiometric for the multiplicative fitness parameter. In those experiments, using either the I_{flr}/I_{SHG} or I_{SHG}/I_{flr} fitness parameter, the maximized signal dropped well below that of the unshaped pulse, consistent with our previous findings in other dyes[16]. This distinction underscores the value of the multiplicative fitness parameter for practical SNR-limited applications.

3.2 Mechanism of BFP control

The mechanism of control of BFP becomes evident by considering the relation of the second-harmonic spectrum $S_2(\omega)$ of the shaped pulse to the spectrum of the two-photon excitation cross-section $\sigma^{(2)}(\omega)$ of BFP (Figure 7.4). Assuming no intermediate resonant levels between the ground and excited state, the two-photon fluorescent signal will be proportional to the overlap integral of $\sigma^{(2)}(\omega)$ and $S_2(\omega)$[35]. This can be derived in second-order perturbation analysis of a two-level system[17,36] or from stationary analysis of two-photon absorption in a three-level model by assuming that the nuclear wave packet motion is frozen in the short time duration of the pulse[37]. Using the overlap integral, Ogilvie and colleagues demonstrated excellent quantitative agreement between the time-domain measurement of $\sigma^{(2)}(\omega)$ for coumarin and the fitness converged on in a GA-led discrimination experiment[23].

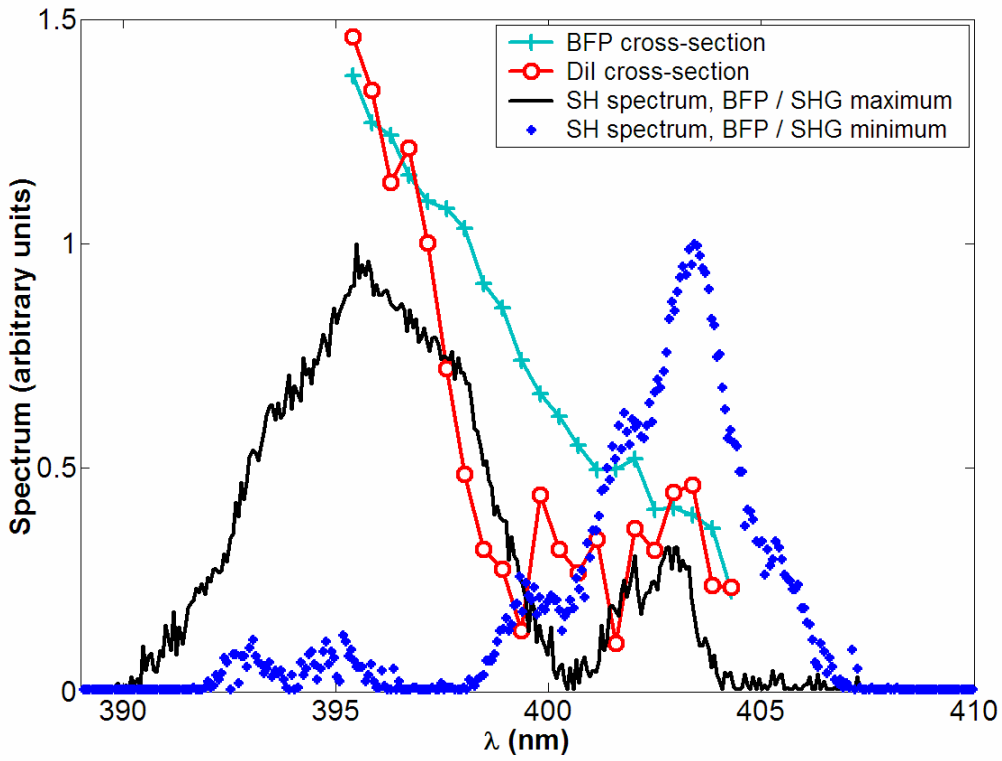

Figure 7.4 Time-domain measured two-photon excitation cross-section spectra of BFP (cyan line) and DiI (red line) with second harmonic power spectra of the optimal pulses for maximization (black line) and minimization (blue asterixes) of the ratio of BFP two-photon fluorescence to SHG.

Clearly, maximization tunes $S_2(\omega)$ to regions where the BFP cross-section ratio is maximal, whereas the minimization algorithm converges in the opposite direction. As second-harmonic tuning is best performed with arbitrary, rather than mere 4th order polynomial phase control, it becomes clear why the GA result improves drastically at the algorithmic switch at generation 30 (Figure 7.3a).

The $\sigma^{(2)}(\omega)$ interpretation also explains the robustness of the control of the BFP / DiI two-photon fluorescent ratio. The two-photon excitation cross-section spectrum for DiI shows a much sharper spectral feature, almost a cliff, near the 400 nm second harmonic. Published literature confirms that this feature continues below the range of accuracy of the time-domain measurement limited by our fundamental laser bandwidth.[38,39] Thus, tuning $S_2(\omega)$ will affect the DiI two-photon fluorescence more significantly than for a typical fluorophore.

That second-harmonic spectral tuning accounts for our result implies that the problem can be reduced to second-order perturbation analysis[17,36], and photon-photon interferences are the fundamental mechanism of control. Despite control of two-photon fluorescence from BFP, at our laser fluences near 0.5 mJ/cm^2 (2 x 10^{15} 800 nm photons / cm^2), control of the two-photon excited state wave packet of BFP probably does not contribute significantly. This is consistent with the observations of Bardeen and colleagues in YFP, another GFP mutant. Specifically, they found that they could control two-photon fluorescence via reduced stimulated emission by appropriately chirping the pulse, but only with order of magnitude higher photon fluence than we employ[40]. Indeed, it is to be expected that such a pump-dump scheme can only meet with success in far from linear fluorescence, in the saturation region we avoid in our experiments.

4. Conclusions

We have seen that a multiplicative fitness parameter in a genetic algorithm optimization of phase-only pulse shaping enables control of the two-photon fluorescence of BFP. There is no evidence of significant physical changes in BFP from our control attempts, and the signal level is maintained at least at the level of the unshaped pulse, both of which may empower the use of BFP in applications such as quantitative FRET. The difficulty of the control problem is underscored by the weakening of the result with a phase search space increased by any of the following: increased number of frequency bins; added ability of amplitude modulation in the algorithm; and not applying a temporal window constraint for the phase-shaped pulse. Further, presence of increased scattered light and the resultant departure from quadratic scaling of the BFP signal channel with I_{ref} completely blocks convergence of the algorithm. A simple ratiometric fitness parameter is also insufficient to control BFP. Despite the difficulty of the problem, the result is consistent with the simple interpretation of second-harmonic spectral tuning to appropriately match our time-domain measured two-photon excitation cross-sectional spectrum. This implies that control of photon-photon interferences, rather than the excited state wave packet, is responsible for the result. Therefore the GA probably did not achieve significant control of the excited state dark isomerization pathway. However, investigations of shaped resonant one-photon excitation have met with success in control of complex molecules at weak excitation[41], and therefore may offer the key to brightening BFP.

References

1. Tsien RY. The green fluorescent protein. Annu Rev Biochem 1998;67:509-544.
2. Truong K, Ikura M. The use of FRET imaging microscopy to detect protein-protein interactions and protein conformational changes in vivo. Curr Opin Struct Biol 2001;11(5):573-578.
3. Xu X, Gerard AL, Huang BC, Anderson DC, Payan DG, Luo Y. Detection of programmed cell death using fluorescence energy transfer. Nucl Acids Res 1998;26(8):2034-2035.
4. Pollok BA, Heim R. Using GFP in FRET-based applications. Trends Cell Biol 1999;9(2):57-60.
5. Squier J, Muller M. High resolution nonlinear microscopy: A review of sources and methods for achieving optimal imaging. Review of Scientific Instruments 2001;72(7):2855-2867.
6. Kawano H, Nabekawa Y, Suda A, Oishi Y, Mizuno H, Miyawaki A, Midorikawa K. Attenuation of photobleaching in two-photon excitation fluorescence from green fluorescent protein with shaped excitation pulses. Biochemical and Biophysical Research Communications 2003;311(3):592-596.
7. Mauring K, Deich J, Rosell FI, McAnaney TB, Moerner WE, Boxer SG. Enhancement of the fluorescence of the blue fluorescent proteins by high pressure or low temperature. J Phys Chem B Condens Matter Mater Surf Interfaces Biophys 2005;109(26):12976-12981.
8. Kummer A, Wiehler J, SchÃ¼ttrigkeit T, Berger B, Steipe B, Michel-Beyerle M. Picosecond Time-Resolved Fluorescence from Blue-Emitting Chromophore Variants Y66F and Y66H of the Green Fluorescent Protein. ChemBioChem 2002;3(7):659-663.
9. Mena M, Treynor T, Mayo S, Daugherty P. Blue fluorescent proteins with enhanced brightness and photostability from a structurally targeted library. Nat Biotech 2006;24(12):1569-1571.
10. Voityuk A, Michel-Beyerle M-E, Rosch N. Structure and rotation barriers for ground and excited states of the isolated chromophore of the green fluorescent protein. Chemical Physics Letters 1998;296(3-4):269-276.
11. Weber W, Helms V, McCammon A, Langhoff P. Shedding Light on the Dark and Weakly Fluorescent States of Green Fluorescent Proteins. Proceedings of the National Academy of Sciences of the United States of America 1999;96(11):6177-6182.
12. Toniolo A, Olsen S, Manohar L, MartÃ-nez TJ. Conical intersection dynamics in solution: the chromophore of Green Fluorescent Protein. Faraday Discuss 2004;127:149-163.

13. Hasegawa J-Y, Fujimoto K, Swerts B, Miyahara T, Nakatsuji H. Excited states of GFP chromophore and active site studied by the SAC-CI method: Effect of protein-environment and mutations. Journal of Computational Chemistry 2007;28(15):2443-2452.

14. Mauring K, Krasnenko V, Miller S. Photophysics of the blue fluorescent protein. Luminescence and Optical Spectroscopy of Condensed Matter - Proceedings of the 2005 International Conference on Luminescence and Optical Spectroscopy of Condensed Matter, 2005 International Conference on Luminescence and Optical Spectroscopy of Condensed Matter 2007;122-123:291-293.

15. Rabitz H, Hsieh M, Rosenthal C. Quantum Optimally Controlled Transition Landscapes. Science 2004;303(5666):1998-2001.

16. Tkaczyk ER, Mignot A, Ye JY, Majoros I, Baker JR, Norris TB. Increasing two-photon fluorescence signals by coherent control. In: Periasamy A, So PTC, editors; 2006. p 165-174.

17. Brixner T, Damrauer NH, Kiefer B, Gerber G. Liquid-phase adaptive femtosecond quantum control: Removing intrinsic intensity dependencies. The Journal of Chemical Physics 2003;118(8):3692-3701.

18. Wachter RM, King BA, Heim R, Kallio K, Tsien RY, Boxer SG, Remington SJ. Crystal structure and photodynamic behavior of the blue emission variant Y66H/Y145F of green fluorescent protein. Biochemistry 1997;36(32):9759-9765.

19. Kaplan D, Tournois P. Theory and performance of the acousto optic programmable dispersive filter used for femtosecond laser pulse shaping. Journal de Physique IV 2002;12:69-75.

20. Verluise Fdr, Laude V, Huignard J-P, Tournois P, Migus A. Arbitrary dispersion control of ultrashort optical pulses with acoustic waves. J Opt Soc Am B 2000;17(1):138-145.

21. Trebino R, Delong K, Fittinghoff D, Sweetser J, Krumbugel M, Richman B, Kane D. Measuring ultrashort laser pulses in the time-frequency domain using frequency-resolved optical gating. Review of Scientific Instruments 1997;68(9):3277-3295.

22. Weiner A. Effect of group velocity mismatch on the measurement of ultrashort optical pulses via second harmonic generation. Quantum Electronics, IEEE Journal of 1983;19(8):1276-1283.

23. Ogilvie J, Kubarych K, Alexandrou A, Joffre M. Fourier transform measurement of two-photon excitation spectra: applications to microscopy and optimal control. Opt Lett 2005;30(8):911-913.

24. Bellini M, Bartoli A, HÃ¤nsch TW. Two-photon Fourier spectroscopy with femtosecond light pulses. Opt Lett 1997;22(8):540-542.

25. Naganuma K, Mogi K, Yamada H. General method for ultrashort light pulse chirp measurement. Quantum Electronics, IEEE Journal of 1989;25(6):1225-1233.

26. Trebino R. Frequency-Resolved Optical Gating: The Measurement of Ultrashort Laser Pulses; 2002.

27. Siegman AE. Lasers. American Journal of Physics 1987;55(9):862.

28. Pearson BJ, White JL, Weinacht TC, Bucksbaum PH. Coherent control using adaptive learning algorithms. Physical Review A 2001;63(6):063412.

29. Fittinehoff DN, Walker BC, Squier JA, Toth CS, Rose-Petruck C, Barty CPJ. Dispersion considerations in ultrafast CPA systems. Selected Topics in Quantum Electronics, IEEE Journal of 1998;4(2):430-440.

30. Tkaczyk E, Rivet S, Canioni L, Santran S, Sarger L. Moment-based Description for Assumption-free Single-shot Measurement of Femtosecond Laser Pulse Parameters via Two-photon-induced Photocurrents. 2006. p 67-71.

31. Birge RR. Two-photon spectroscopy of protein-bound chromophores. Accounts of chemical research 1986;19(5):138.

32. Laarmann T, Shchatsinin I, Singh P, Zhavoronkov N, Gerhards M, Schulz CP, Hertel IV. Coherent control of bond breaking in amino acid complexes with tailored femtosecond pulses. The Journal of Chemical Physics 2007;127(20).

33. Brixner T, Damrauer NH, Niklaus P, Gerber G. Photoselective adaptive femtosecond quantum control in the liquid phase. Nature 2001;414(6859):57-60.

34. Brixner T, Kiefer B, Gerber G. Problem complexity in femtosecond quantum control. Chemical Physics 2001;267(1-3):241-246.

35. Walowicz KA, Pastirk I, Lozovoy VV, Dantus M. Multiphoton Intrapulse Interference. 1. Control of Multiphoton Processes in Condensed Phases. J Phys Chem A 2002;106(41):9369-9373.

36. Meshulach D, Silberberg Y. Coherent quantum control of multiphoton transitions by shaped ultrashort optical pulses. Phys Rev A 1999;60:1287-1292.

37. Cao J, Che J, Wilson KR. Intrapulse Dynamical Effects in Multiphoton Processes: Theoretical Analysis. J Phys Chem A 1998;102(23):4284-4290.

38. Xu C, Zipfel W, Shear J, Williams R, Webb W. Multiphoton fluorescence excitation: New spectral windows for biological nonlinearÂ microscopy. PNAS 1996;93(20):10763-10768.

39. Xu C, Webb WW. Measurement of two-photon excitation cross sections of molecular fluorophores with data from 690 to 1050 nm. Journal of the Optical Society of America B Optical Physics 1996;13:481-491.

40. Bardeen CJ, Yakovlev VV, Squier JA, Wilson KR. Quantum Control of Population Transfer in Green Fluorescent Protein by Using Chirped Femtosecond Pulses. J Am Chem Soc 1998;120(50):13023-13027.

41. Prokhorenko VI, Nagy AM, Miller RJD. Coherent control of the population transfer in complex solvated molecules at weak excitation. An experimental study. J Chem Phys 2005;122:4502.

CHAPTER 8
CONCLUSIONS

From the initial biological motivations for laser pulse optimization in flow cytometry, we have delved into the world of genetic algorithms and touched on other potential applications of laser pulse shaping. Here we consider the relation of the body of results in this doctoral work to possible future improvements and directions.

1. Biological Investigations by Multiphoton Flow Cytometry

Recent studies have focused attention on detecting and quantifying absolute numbers and dynamics of circulating cells in cancer and inflammation to determine disease prognosis, identify potential therapeutic targets, and monitor the response to therapy (reviewed in [1,2]). To better understand normal and pathologic regulation of circulating cells, it is necessary to develop techniques that allow sensitive, long-term real-time monitoring of multiple populations of cells *in vivo*. Multiphoton approaches have proven to be very useful for noninvasive microscopy applications. Studies of the viability of embryos through two-photon microscopy, but not confocal are a prime example[3].

As described in Chapter 2, we have created an innovative two-color two-photon flow cytometer that accomplishes these experimental objectives. Using this system, we were able to perform simultaneous two-color detection of multiple circulating cell lines *in vivo*, which has not been accomplished with previous techniques for *in vivo* flow cytometry. Many unique studies are possible with the novel two-photon approach to *in vivo* flow cytometry. Investigations with red blood cells (RBCs) showed that an abundant population of cells can be monitored for periods of greater than two weeks, thereby establishing that the system can detect single cell events at high counting rates over extended periods of times. This is enabled by the limitation of multiphoton

absorption to the interrogated region, reducing potential collateral damage to tissues outside of the vessel lumen. Interrogating populations of hematopoietic cells, such as RBCs or leukocytes, could provide new insights into normal physiology or disease processes, as well as serving as an internal standard for hemodynamics and perfusion. For example, if the dynamics of a cell population, such as RBCs, are well known, this provides a statistically reliable internal control of the interrogated blood volume per unit time, if more than one detection channel is available (as in our unique multiphoton system).

Variations in measurements during the RBC experiment emphasize the importance of multiple channel detection. While single channel *in vivo* flow cytometry is sufficient for a qualitative analysis of circulating cell dynamics, it is generally limited by variations in event counts in repeated experiments. Between separate times of detection, blood flow velocity at the measurement site may vary. This occurs on a short time-scale due to pulsatile flow, but also on a longer time scale due to drift in the positioning of the laser focus. This can be caused when the anesthetized mouse changes position slightly, which results in the laser focusing on a site closer to the wall of the vessel, where blood flow velocity is lower. Further, physiological conditions can be highly variable between experiments, whether examining the same or a different mouse. These factors are compounded by statistical fluctuations when small sample sets are acquired for studies of rare circulating cells. Without a means to determine the volume and total events sampled over a given time interval, these issues will complicate the analyses of populations of cells in mice using single color flow cytometry.

With multicolor, two-photon *in vivo* flow cytometry, different populations of cells can be compared simultaneously in a single animal with a single laser source, overcoming many variables intrinsic to *in vivo* experiments. In particular, we used this technique to quantify two populations of breast cancer cells in the same mouse and demonstrated intrinsic differences in the dynamics of these cells in the circulation. Because we can monitor multiple cell populations in the same animal, two-photon flow cytometry greatly reduces experimental variability related to animal-to-animal differences in perfusion. We expect that further studies will allow us to interrogate functions of specific molecules implicated in metastatic breast cancer, such as the

chemokine CXCL12 and its receptor CXCR4[4]. These types of studies may improve our understanding of circulating cancer cells and the progression to metastatic disease. These would also facilitate the *in vivo* testing of new compounds targeted against specific molecules or pathways. For example, the five fold increase of targeting to live cancer cells we demonstrated when dendrimers are conjugated to Herceptin (trastuzumab) is an initial step in this direction.

One challenge to *in vivo* cytometry is the small number of labeled cells passing through the blood vessel in the detection region. Using the simultaneous injection of labeled RBCs as a reference control for focal point optimization will enable far more reliable experiments on rare event circulation dynamics. One solution to increase the statistical power of the measurements would be to access larger blood vessels with higher flow rates, thereby increasing the number of detected cells; this should be enabled by the ability of the femtosecond NIR laser source to penetrate much deeper through biological tissue than a continuous wave laser in visible region for one-photon excitation[5], and to potentially reduced photodamage to surrounding tissue for extended monitoring.

We anticipate that two-photon flow cytometry will greatly enhance our ability to interrogate circulating cells in pre-clinical models of cancer and other diseases. For example, we envision that this technology can be used to investigate 1) changes in gene expression in circulating cells through imaging probes injected into mice or genetically-engineered cell lines with fluorescent reporters; and 2) analyze effects of specific adhesion molecules in trafficking of cancer or immune cells using genetically-engineered mice. These studies will be aided by technical advances such as the real-time imaging of blood vessels to monitor and control the position of the laser beam throughout the experiment and the development of approaches to label specific cells *in vivo*, rather than *ex vivo*.

2. Enhancing Sensitivity of Multiphoton Flow Cytometry

Traditionally, the major limitation on optical detection methods has been the average power that can be delivered to the sample at focus without damage. If *in vivo* flow cytometry is to be used for extended monitoring periods for rare event detection, it is critical to minimize the power delivery to the sample while maintaining high signal levels. We have demonstrated in Chapter 3 that an extended cavity oscillator is a useful modification to enhance fluorescent signal from live biological samples in a two-photon flow cytometer at fixed power.

The extended cavity investigation and associated simulations also granted insight into the nature of two-photon detection in our flow system. We observed the anticipated four-fold signal enhancement in a flowing fluorescent dye solution with square-law power scaling. However, the signal for flowing fluorescent microspheres obeyed a sub-square power law, which is understood as a geometrical effect. For increasing excitation intensity, the detectable two-photon excitation region becomes larger, subsuming more dim events. Similar geometrical effects, though less pronounced, would similarly affect the power-scaling of detection signal for any multiphoton or even single photon fluorescence detection scheme whereby the entire capillary cross-sectional area is not uniformly excited above threshold. The model also predicts our experimentally verified lack of correlation in signal strength between two fluorophores with differing spatial distributions. The highly nonlinear detection curves for two-photon flow cytometry result in a critical detection threshold, where even a modest improvement in signal via innovations such as an extended cavity laser can dramatically enhance the sensitivity of the system. GFP-expressing cells were chosen for detection explicitly for this reason: due to their emission in the highly absorbing region of blood, overlapped as well with blood's autofluorescence, they lie at the threshold of detection for single cell *in vivo* measurements.

It is conceivable that some further advantage could be gained from improved detectors which improve the signal-to-noise of the system. For the next generation multiphoton cytometry under construction, we have already purchased photon-counting

PMTs which are orders of magnitude less responsive to scattered excitation light while maintaining sensitivity to visible photons.

The significantly improved sensitivity of the two-photon flow cytometer with the extended cavity oscillator laser excitation source could open new avenues of biomedical investigation. Enhanced ability to detect GFP in whole blood will further empower cancer metastasis investigations in mouse tumor models. Enhanced sensitivity to shorter wavelength dyes will also assist the ultimate goal of noninvasive *in vivo* human monitoring.

3. Physical Aspects of Tailored Pulse Control

With the ultimate goal of improving our flow cytometry application with enhanced molecular specficity, we have developed and tested a genetic algorithm (GA) to control two-photon fluorescence of dyes relative to second-harmonic generation (SHG) or to two-photon fluorescence of another dye. The algorithm converges predictably to optimal pulse shapes which in the time-frequency view are complementary for maximization or minimization of the ratio of two-photon signals. When the ratio itself is used directly as the fitness parameter of the GA, experiments generally converged to the lowest permissible limit of signal levels for maximum discrimination. This problem was solved with a multiplicative fitness parameter, which ensured signal levels of the optimized pulse comparable to or exceeding the unshaped pulse.

3.1 Mechanism of control

Most of the two-photon fluorescence control results are explainable simply in terms of second harmonic spectral tuning of the excitation laser pulse to the relative minimum or maximum of the two-photon excitation cross sections, as confirmed by the acousto-optic time domain measurement for successfully and unsuccessfully discriminated dye pairs. We also noted that the amount of noise we measured in the runs of the algorithm had a significant impact on the degree of control achieved. It is interesting that in the instances of lowest noise, where the highest degree of control was achieved, there is a pulse train nature to the optimal pulses as well. This includes most of the low-field experiments in Chapter 4 that benefited from a very steady home-built oscillator source, but also the rhodamine B vs SHG experiment in Chapter 5. These findings are consistent with coherent control results of other groups[6] and might indicate ture control control of excited state wavepackets beyond mere manipulation of photon-photon interferences. For example, if a specific vibration is important to the control, an integral number of vibrational periods between the pulses in the series enables buildup of coherent population to exclusively populate one Raman level[7]. This “true control” result can be somewhat elusive, for example another repetition of the rhodamine B vs SHG experiment of Chapter 5 resulted in substantially weaker discrimination, and no pulse train character in the time-frequency viewed pulse.

Now we turn our attention to some practical considerations on how the degree of control achieved can be enhanced.

3.2 Laser stability

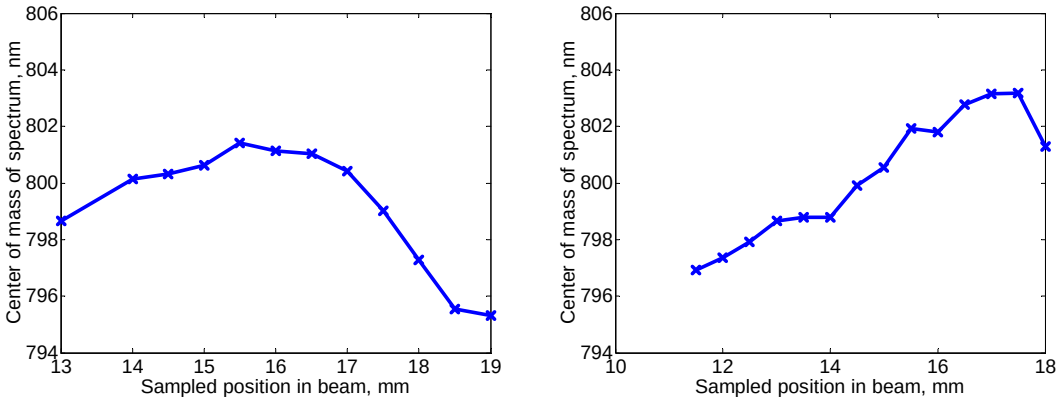

Figure 8.5 Spatial chirp of RegA at compressor output. Variation of the spectrum center wavelength relative to horizontal (left) or vertical (right) position. Spectrum was measured with an ocean optics spectrometer as a slit was translated in front of it. (October 23, 2007).

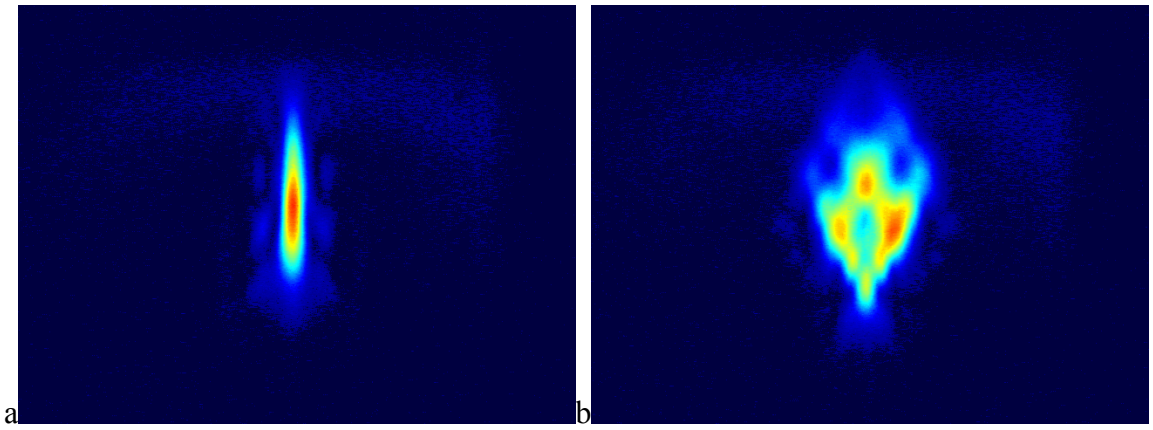

Figure 8.6 SHG-FROG traces of compressed (left) and chirped RegA output pulse revealing phase distortions at the output.

We have seen the degree of dependence of discrimination on noise in the GA run, and further the elusive nature of the pulse train solutions. To achieve superior results and more of the "true coherent control" in continuations of this work, careful attention needs to be paid to the stability of the laser. In the work of Chapter 3, we discovered that enclosing the laser beam significantly improved the stability of the extended cavity laser. Additional beam tubes in the coherent control experimental setup should similarly improve the results with protection from air currents and dust. However, the greatest

serious source of noise in most of these experiments was the newly purchased RegA laser itself. There was a significant spatial chirp measured at its output (Figure 8.5), often manifesting itself as distorted SHG-FROG traces of the shaped pulses (Figure 8.6), despite a TeO_2 crystal compensating the known angular chirp of Dazzler. Improving these issues would not only improve the GA for coherent control, but also the time-domain two-photon cross-section measurement.

3.3 High field control

While simple maximization of fluorescence efficiency converged to transform-limited pulses in the lower-field experiments, irrespective of sample, this was not the case in the high field experiments of Chapter 4, and SHG in fact decreased during vast improvement in fluorescence signal. This correlates with finding of Bardeen *et al.*[8], who only in the higher field regime achieved significant coherent control. Intuitively, it is necessary to build up a significant population in the excited state before being able to control it. One of the key assumptions of the second-order perturbation analysis presented in the introduction (which does not explain manipulation of the excited wave packet's time evolution) is limited ground state depletion.

Work at higher fields will require many special experimental considerations. For example, the nonlinear index of common solvents like DMSO has already ruined many experiments because of the confounding white light generation which masks fluorescence. One also has to consider optical breakdown and bubble generation, which may affect excitation of the sample as well as fluorescence collection. Detector saturation, including the 5 V limit of the DAQ board (translating to less than 2 Vrms) has to be rigorously excluded to confirm the onset of ground state depletion as the mechanism responsible for a saturated two-photon signal. This probably means moving to very dilute dye solutions which are harder to align due to the lack of fluorescence detectable with the eye. Standard Newport cuvette mounts purchased for the system will help with this goal by enabling a concentrated reference solution to confirm alignment. These cuvette mounts also significantly reduce the angular range over which fluorescence is collected. Lower f# focusing lenses could also benefit this line of work. One approach for example might be to use the newly built single-photon counting coherently controlled flow cytometry system as the data acquisition method for high field control experiments,

which will enable higher photon fluences as well as replenishment of the sample to completely exclude photobleaching effects. New GA fitness parameters should also be explored in the high field experiments, especially if an experiment is to compare a saturated two-photon excitation process to unsaturated SHG, for the power- and chirp-scaling reasons outlined in the previous 3 chapters of this work. For example, the simple product of fluorescence and SHG signals would prevent convergence to either extreme range of the power, and would require only trivial modifications to the existing GA software.

From a practical perspective, the ability to apply fields strong enough to approach population inversion seem impractical for *in vivo* applications which initially motivated this work. However, if further exploration bears out our observation that significant control results are achieved in the low noise, high field regime, *ex vivo* application such as multiphoton flow cytometry with high molecular selectivity will nevertheless emerge.

3.4 Alternative control approaches

A fundamental limitation to the approach of second-harmonic spectral tuning is the requirement for significant differences in the spectral shape of the two-photon excitation cross-sections of the dyes of interest within the limited bandwidth of the excitation laser, which is generally a small fraction of the bandwidth of the visible spectrum, even for pulses less than 50 fs long. A potential solution to this problem is to combine pulse shaping with an optical parametric amplifier (OPA) to broaden the possible excitation range.

For coherent control not relying on spectral harmonic tuning, the limited bandwidth of the laser is less of an issue. In theory, the GA as implemented should have been able to match the exciting field to wavepacket coherences up to one or two picoseconds. We are still trying to control at least a third-order interaction however, even in the event that only one off-resonance additional infrared photon is required to manipulate the electronic state excited by the two initially absorbed photons. Lower-order interactions are much more likely, and this may be the reason that so much of the literature on control of quantum phase of the excited wavepacket relies on single-photon processes. Thus, tuning an OPA into the visible for excitation or subsequent manipulation of the wavepacket may be a more successful approach for significant

control. Indeed, investigations of shaped resonant one-photon excitation have met with success in control of complex molecules, even at weak excitation[6,9].

A dual-pulse approach to the problem of discrimination, where one pulse is used to excite the fluorophore, and a second is used for additional manipulation, may in fact be the most successful approach for our purposes . In practice, as vibrational coherences may have dephasing times up to several picoseconds[10], this approach may enable manipulation of an excited electronic state beyond the pulse-shaping capabilities on a single pulse. In fact, in what can be considered a "pump-*pump*" experiment, Courvoisier and colleagues were able to deplete fluorescence from bacteria by up to 50%.[11,12]

4. Possible Applications of Pulse Shaping Work

Tailored pulse shapes could potentially provide a large degree of molecular specificity to enhance numerous fluorescence applications. Here we consider multiphoton microscopy, cancer diagnosis and treatment, quantitative measurements of spectrally similar dyes, and enhanced investigations of protein interactions with Förster resonance energy transfer (FRET).

4.1 Second-harmonic tuning for microscopy

Multiphoton microscopy has already enjoyed application of second-harmonic spectral tuning to perform various feats, including: enhanced pH sensing, reduced damage, and differentiating two- from three-photon processes. This has been achieved through scattering media on lifeless tissue, but even *in vivo*[13-15]. Our method of pulse shaping could further this trend. Firstly, the multiplicative fitness parameter of our genetic algorithm is able to achieve significant discrimination without a drop in signal of the favored fluorophore, which improves the signal-to-noise ratio so important to microscopy. Additionally, speed of acquisition is advantaged by an acousto-optic programmable dispersive filter, where the exciting pulse phase can be rapidly modulated. Compared to the standard liquid crystal pulse shaping for selective excitation, the Dazzler enables reduction of typical switching times of tens of milliseconds[16,17] into the submillisecond regime.

4.2 Cancer diagnosis and therapy

If enough molecular specificity is attained, tailored pulse shapes may become a clinical technology, for example in minimally invasive fiber optic needle biopsies of breast cancer to monitor response to dendrimer-targeted therapy[18]. Failure of our initial direct attempts to ascertain conjugation to the most relevant molecules, herceptin and dendrimers, is not surprising considering the two-photon excitation spectra we measured. Successful discrimination with our method requires a strong electronic coupling reflected in a change of two-photon excitation spectrum occurring precisely within the bandwidth of the two-photon excitation source. This is evidenced in the case of discrimination of phalloidin-bound from free Texas Red dye, which were predicted to have this feature[19,20],

confirmed by our own acousto-optic time domain measurement. Another example of a strong interaction with a dye would be an antibody binding to the dye. In the future we hope to exploit this to develop molecular assays for precise detection of binding events. For these technologies and even herceptin- or dendrimer conjugates, the alternative coherent control approaches described earlier in this chapter could enable significant improvement in sensitivity.

The discrimination of fluorescence from SHG via pulse-shaping alone could have clinical value. The research highlight of a recent *Nature Medicine* paper shows the relevance of SHG to different tumor types[21]:

> "Most tumours have a dense extracellular matrix that inhibits drug diffusion and serves as a barrier to drug delivery. One of the key components of this barrier is a dense collagen meshwork, although the structure and content of the collagen networks varies between tumour types. Brown et al. have used a non-invasive imaging technique to quantify its density in vivo, allowing researchers to estimate the penetrability of tumours to molecular therapeutics.
>
> Brown et al. used a principle called second harmonic generation (SHG) — an intrinsic fluorescent signal that can be detected without the addition of dyes or other reagents — to obtain high-resolution three-dimensional images of fibrillar collagen in vivo. "

It has already been demonstrated that the ratio of autofluorescent signal to SHG helps delineate basal cell carcinoma (BCC) from normal surrounding tissue[22], and the species comprising autofluorescence of skin have also been investigated[23,24]. Thus, significantly enhanced differentiation of known autofluorescent species in skin from SHG of collagen may some day help surgeons demarcate borders of excision of cancerous tissue in real time. An initial experiment with our system to test applicability might be to enhance detection of fluorescent beads in a cellulose mesh, which would produce an SHG background. Once this succeeds, flavoproteins with established two-photon fluorescence features[25] can be imaged within different structures of fibroblast-secreted collagen matrices engineered to mimick different tissue structures with cell patterning techniques[26]. Next, premalignant or malignant tissue samples can be used. Finally, potential enhancements by shaped pulses for photo-activation of delta-amino levulinic acid (ALA) for photodynamic therapy (PDT) can be investigated, which has already met success in treatment of BCC[27] and is rapidly being applied to numerous other cancers including of the colon[28,29].

4.3 Quantitative measurements with pulse shaping, including FRET

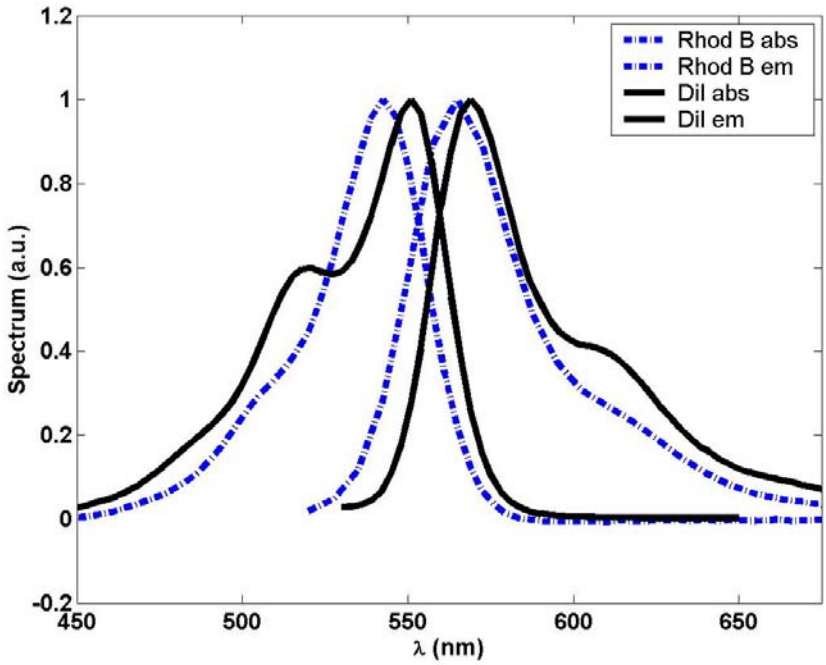

Figure 8.7 Absorption and emission spectra of rhodamine B and DiI[30,31].

In Chapter 6, we demonstrated our ability to control the two-photon fluorescence ratio to nearly a factor of three of rhodamine B and DiI, a dye pair which is practically indistinguishable to traditional one-photon excitation and emission spectroscopy (Figure 8.7). This enabled quantification of a mixture of the two dyes, when done immediately after mixing. Unfortunately, the initial validation attempt to quantify a series of mixtures produced unpublishable data due to the low levels of rhodamine B detected (Figure 8.8), which we suspect is due to a chemical reaction. This was evidenced by significantly lower fluorescence from the 20 μM mixture of rhodamine B with 10 μM DiI in DMSO than 10 μM rhodamine B in DMSO alone at the end of the measurement.

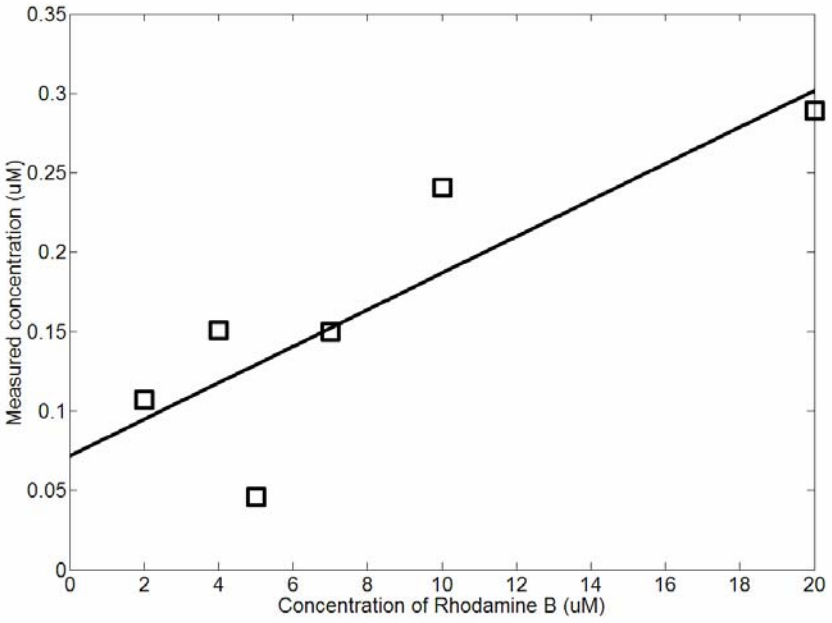

Figure 8.8 Tailored-pulse measured versus actual concentration of rhodamine B in a mixture with 10 µM DiI in DMSO.

Repetition of this experiment or other pairs of dyes indistinguishable by one-photon will be an excellent further demonstration of the power of this technique. One example which might be useful to this end is the ER-Tracker dye which has already been purchased from Molecular Probes, and has a promising sharp spectral feature in the two-photon excitation spectrum at our operating wavelength[19] and is designed for cell labeling.

Another quantitative technique which could be advanced with tailored pulses is the study of protein interactions with FRET. As discussed in Chapter 1, BFP has been very useful in seminal work in this area but has limitations that could be addressed with pulse-shaping, as shown in Chapter 7. It seems unlikely that we will be able to improve the photobleaching rate of BFP with tailored pulse shapes, as Bardeen and colleagues found that the photobleaching rate of a related mutant, YFP, likely has a thermal origin. In the saturated excitation region, boosting or decreasing the fluorescence signal by optimal pulse shapes has no effect on the photobleaching rate, ruling out an excited-state photoreaction mechanism. Future attempts to improve the quantum yield of BFP for eventual application in tailored-pulse-shaped FRET will be improved by a greater

physical understanding of the excited state dynamics of BFP and how they might be controlled by the optimal pulses. The next step in this investigation is computational chemistry of the excited state of BFP, coupled with experimental work to determine the relative weight of the multiple different exponential decay pathways of BFP under different optical excitation fields. Ideally, optimal pulses will change the distribution of states which are excited, resulting in different weights for different lifetimes. A streak camera may be useful to begin this research, but a detailed understanding will require sub-picosecond resolution, and may benefit from two-dimensional spectroscopic methods that have already met with success in examining processes as fundamental as photosynthesis[10,32,33].

5. Coherently Controlled Cytometry

Work to combine multiphoton cytometry and pulse shaping, the two fundamental technologies of this dissertation, is already well underway. We have built a functioning prototype (Figure 8.9), which we hope will enable many new types of investigations to be performed.

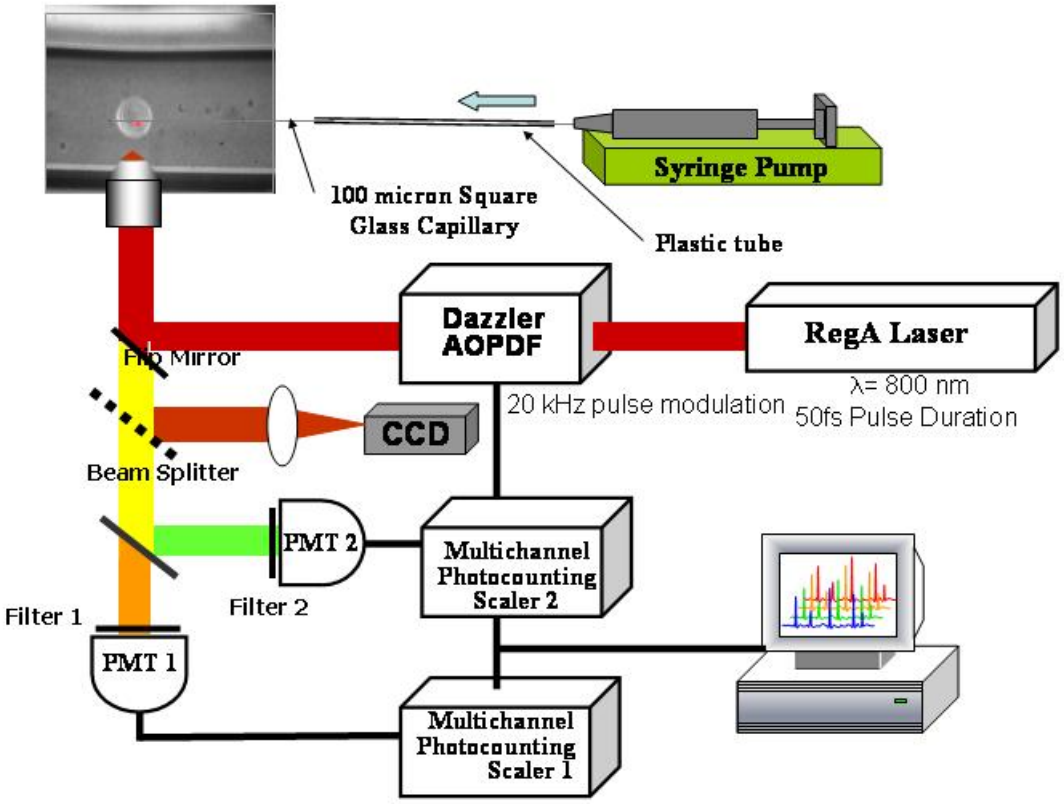

Figure 8.9 System for cytometry with shaped laser pulses.

It should be possible to excite a single cell with multiple pulse shapes as it flows through the focus of the laser beam. For example, under a typical flow rate of 0.36 mL/hour, the total expected transit time per 10 μm cell in the 100 μm square glass capillary is 1 ms. Thus the 20 kHz dazzler repetition rate would be predicted to allow the cell to experience on the order of ten total pulse shapes. In practice, the cell does not necessarily pass through the two-photon interrogation region at its widest point, and our earlier experiments on live cells have shown typical median full-width at half maximum

(FWHM) of flowing labeled cells of 0.1 ms to 0.3 ms, which would still permit at least two to six pulse shapes per cell. The number of actual data points acquired per pulse shape will be limited by the signal-to-noise ratio (SNR) of the fluorescent signal, which for example in PBS has been high enough previously to allow bin sizes of 41 μs in the case of DiI cell detection in PBS. With a 76-MHz or 20-MHz oscillator laser excitation source, this translates into thousands of laser pulses per data point, but only about 5 regeneratively amplified pulses (for our 250 KHz system, assuming 50% duty cycle of the dazzler).

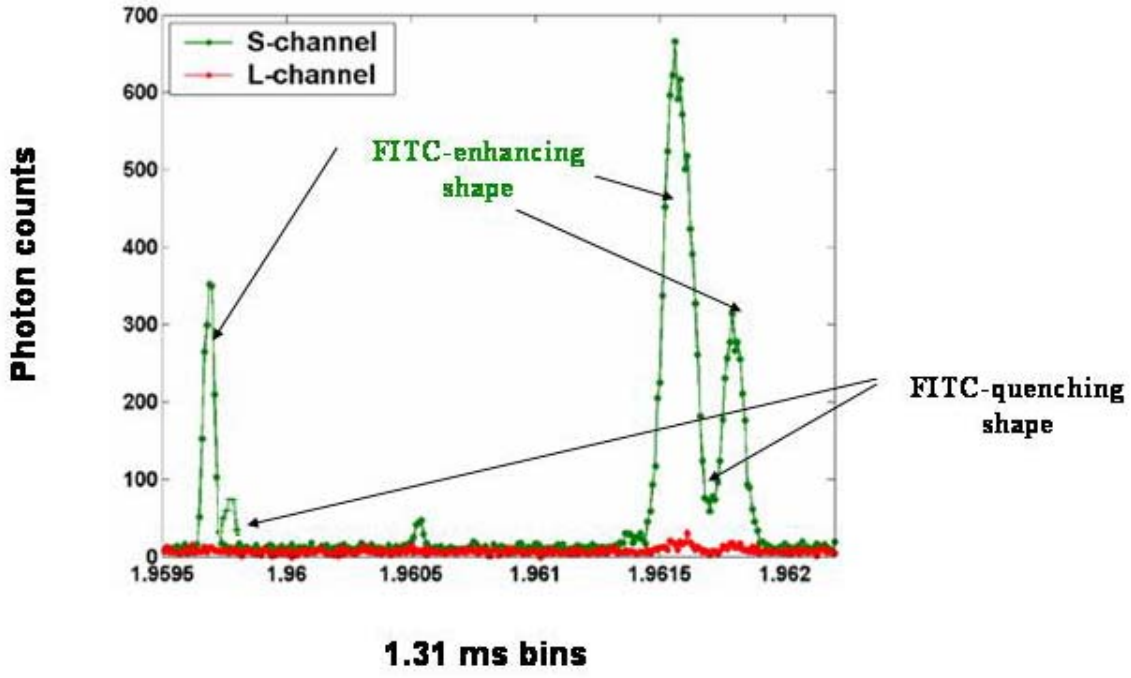

Figure 8.10. Anticipated signal from singly-labeled cell, such as a G5-FITC-Her2Ab-labelled Her2-overexpressing SKBR3 cell, in the slow flow rate limit. The FITC signal appears in the short channel.

Figure 8.10 shows the anticipated signal from a singly-labeled cell flowing through the laser focus under pulse shape modulation synchronous with detection. The slow flow rate provides the high SNR enabling several data points to be taken per cell flowing by. Note that the fluorescent signal is not expected to drop to background levels for the fluorescence-quenching pulse. If a cell is dual-labeled with two dyes that are detected in the same emission channel, coordinated pulse shape modulation and detection

will still enable identification of the amount of either dye present. For example, expected data for an eGFP and FITC dual-labeled cell is shown in Figure 8.11a. Figure 8.11b shows the same experiment if the cross-labeled dye is detected in a different channel, for example the lipophilic membrane dye DiI, which has a very different TPE spectrum near 800 from eGFP.

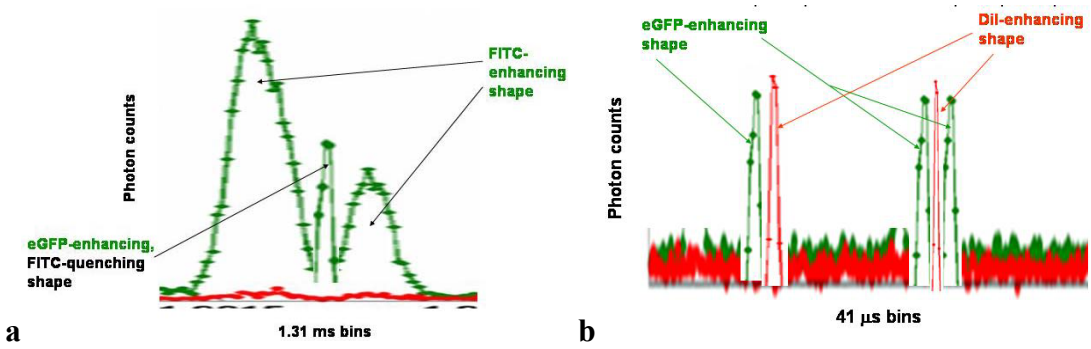

Figure 8.11. (a) Anticipated data for SKBR3 cell dual-labeled with eGFP and her2-internalized G5-FITC in the high SNR limit of slow flow. (b) Anticipated data at faster flow rate in short and long detection channels for dual-labeled eGFP / DiI cells.

Initial work with this system should include biological application of the quanititative measurement technique of Chapter 6 to determine the amount of DiI under variable labeling conditions in a series of cells cross-labeled with DiD. Different samples can have varying concentrations of DiI applied to the cells. Alternatively, as Chapter 3 shows that the number of detected cells has more meaning than the intensity, we may try to vary the number of dual-labeled cells spiked into a DiD cell mix to determine the ability of pulse-shaping to quantify this. Rhodamine B has been shown to accumulate selectively in mitochondria at low concentrations, and rhodamine 6G and rhodamine B have been shown to accumulate in the endoplasmic reticulum of cells at higher concentrations[34-36]. As we have also been able to successfully control these two dyes, they will represent interesting targets.

Following these experiments, we will launch an investigation into the possibilities of coherently-controlled *in vivo* flow cytometry. In the end, we hope that tailored pulse shaping will find application to probe noninvasively at a molecular level, the nature of circulating inflammatory and cancer cells detected with our novel system.

References

1. Luster A, Alon R, von Andrian U. Immune cell migration in inflammation: present and future therapeutic targets. Nature Immunology 2005;6(12):1182-1190.
2. Goon PK, Boos CJ, Stonelake PS, Lip GY. Circulating endothelial cells in malignant disease. Future Oncol 2005;1(6):813-820.
3. Squirrell JM, Wokosin DL, White JG, Bavister BD. Long-term two-photon fluorescence imaging of mammalian embryos without compromising viability. Nat Biotechnol 1999;17(8):763-767.
4. Luker K, Luker G. Functions of CXCL12 and CXCR4 in breast cancer. Cancer Lett 2006;238(1):30-41.
5. Gu M, Gan X, Kisteman A, Xu MG. Comparison of penetration depth between two-photon excitation and single-photon excitation in imaging through turbid tissue media. Applied Physics Letters 2000;77:1551.
6. Prokhorenko VI, Nagy AM, Miller RJD. Coherent control of the population transfer in complex solvated molecules at weak excitation. An experimental study. J. Chem. Phys. 2005;122:4502.
7. Dudovich N, Oron D, Silberberg Y. Single-pulse coherently controlled nonlinear Raman spectroscopy and microscopy. Nature 2002;418(6897):512-514.
8. Bardeen CJ, Yakovlev VV, Squier JA, Wilson KR. Quantum Control of Population Transfer in Green Fluorescent Protein by Using Chirped Femtosecond Pulses. J. Am. Chem. Soc. 1998;120(50):13023-13027.
9. Prokhorenko VI, Nagy AM, Waschuk SA, Brown LS, Birge RR, Miller RJ. Coherent control of retinal isomerization in bacteriorhodopsin. Science 2006;313(5791):1257-1261.
10. Nagy A, Prokhorenko V, Miller R. Do we live in a quantum world? Advances in multidimensional coherent spectroscopies refine our understanding of quantum coherences and structural dynamics of biological systems. Carbohydrates and glycoconjugates / Biophysical methods 2006;16(5):654-663.
11. Courvoisier Fc, Boutou Ve, Wood V, Bartelt A, Roth M, Rabitz H, Wolf J. Femtosecond laser pulses distinguish bacteria from background urban aerosols. Applied Physics Letters 2005;87(6).
12. Courvoisier F, Boutou V, Guyon L, Roth M, Rabitz H, Wolf J-P. Discriminating bacteria from other atmospheric particles using femtosecond molecular dynamics. Coherent Control of Photochemical and Photobiological Processes 2006;180(3):300-306.
13. Ogilvie JP, D D, Solinas X, Martin JL, Beaurepaire E, Joffre M. Use of coherent control for selective two-photon fluorescence microscopy in live organisms. Optics Express 2006;14:759-766.

14. Dela Cruz J, Lozovoy V, Dantus M. Coherent control improves biomedical imaging with ultrashort shaped pulses. Coherent Control of Photochemical and Photobiological Processes 2006;180(3):307-313.

15. Schelhas L, Shane J, Dantus M. Advantages of ultrashort phase-shaped pulses for selective two-photon activation and biomedical imaging. Nanomedicine: Nanotechnology, Biology and Medicine 2006;2(3):177-181.

16. Pastirk I, Dela Cruz JM, Walowicz KA, Lozovoy VV, Dantus M. Selective two-photon microscopy with shaped femtosecond pulses. Optics Express 2003;11:1695.

17. Delacruz JM, Pastirk I, Lozovoy VV, Walowicz KA, Dantus M. Multiphoton Intrapulse Interference 3: Probing Microscopic Chemical Environments. J. Phys. Chem. A 2004;108(1):53-58.

18. Thomas TP, Patri AK, Myc A, Myaing MT, Ye JY, Norris TB, Baker JR. In Vitro Targeting of Synthesized Antibody-Conjugated Dendrimer Nanoparticles. Biomacromolecules 2004;5(6):2269-2274.

19. Bestvater F, Spiess E, Stobrawa G, Hacker M, Feurer T, Porwol T, Berchner-Pfannschmidt U, Wotzlaw C, Acker H. Two-photon fluorescence absorption and emission spectra of dyes relevant for cell imaging. J Microsc 2002;208(Pt 2):108-115.

20. Spiess S, Bestvater B, Heckel-Pompey A, Toth T, Hacker H, Stobrawa S, Feurer F, Wotzlaw W, Berchner-Pfannschmidt U, Porwol P and others. Two-photon excitation and emission spectra of the green fluorescent protein variants ECFP, EGFP and EYFP. Journal of Microscopy 2005;217(3):200-204.

21. Novak K. Measuring the matrix. Nat Rev Cancer 2003;3(6):394-394.

22. Lin S-J, Jee S-H, Kuo C-J, Wu R, Jr., Lin W-C, Chen J-S, Liao Y-H, Hsu C-J, Tsai T-F, Chen Y-F and others. Discrimination of basal cell carcinoma from normal dermal stroma by quantitative multiphoton imaging. Opt. Lett. 2006;31(18):2756-2758.

23. Laiho L, Pelet S, Hancewicz T, Kaplan P, So P. Two-photon 3-D mapping of ex vivo human skin endogenous fluorescence species based on fluorescence emission spectra. Journal of Biomedical Optics 2005;10(2).

24. Tkaczyk E, Laiho L, So P. Deconvolution of Skin Images with Multivariate Curve Resolution. Medical Devices and Biosensors, 2007. ISSS-MDBS 2007.; 2007. p 36-43.

25. Huang S, Heikal A, Webb W. Two-Photon Fluorescence Spectroscopy and Microscopy of NAD(P)H and Flavoprotein. Biophys. J. 2002;82(5):2811-2825.

26. Gu W, Zhu X, Futai N, Cho B, Takayama S. From the Cover: Computerized microfluidic cell culture using elastomeric channels and Braille displays. Proceedings of the National Academy of Sciences 2004;101(45):15861-15866.

27. Svanberg K, Andersson T, Killander D, Wang I, Stenram U, Andersson-Engels S, Berg R, Johansson J, Svanberg S. Photodynamic therapy of non-melanoma malignant tumours of the skin using topical delta-amino levulinic acid sensitization and laser irradiation. The British journal of dermatology 1994;130(6):743-751.

28. Eker C, Montan S, Jaramillo E, Koizumi K, Rubio C, Andersson-Engels S, Svanberg K, Svanberg S, Slezak P. Clinical spectral characterisation of colonic mucosal lesions using autofluorescence and delta Â aminolevulinic acid sensitisation. Gut 1999;44(4):511-518.

29. Endlicher E, Knuechel R, Hauser T, Szeimies RM, Scholmerich J, Messmann H. Endoscopic fluorescence detection of low and high grade dysplasia in Barrett's oesophagus using systemic or local 5-aminolaevulinic acid sensitisation. Gut 2001;48(3):314-319.

30. Du H, Fuh R-CA, Li J, Corkan LA, Lindsey JS. PhotochemCAD: A Computer-Aided Design and Research Tool in Photochemistry. Photochemistry and Photobiology 1998;68(2):141-142.

31. Invitrogen. http://probes.invitrogen.com/servlets/spectra. Invitrogen Website; 2008.

32. Brixner T, Stenger J, Vaswani H, Cho M, Blankenship R, Fleming G. Two-dimensional spectroscopy of electronic couplings in photosynthesis. Nature 2005;434(7033):625-628.

33. Cowan ML, Ogilvie JP, Miller RJD. Two-dimensional spectroscopy using diffractive optics based phased-locked photon echoes. Chemical Physics Letters 2004;386(1-3):184-189.

34. Terasaki M, Reese TS. Characterization of endoplasmic reticulum by co-localization of BiP and dicarbocyanine dyes. J Cell Sci 1992;101(2):315-322.

35. Arregui C, Balsamo J, Lilien J. Impaired Integrin-mediated Adhesion and Signaling in Fibroblasts Expressing a Dominant-negative Mutant PTP1B. J. Cell Biol. 1998;143(3):861-873.

36. Rashid F, Horobin RW. Interaction of molecular probes with living cells and tissues. Part 2. Histochemistry and Cell Biology 1990;94(3):303-308.